

Annual Report 2013

October 2014

Karlsruhe Nano Micro Facility (KNMF)



Dr. Jürgen Mohr, Dr. Susan Anson, Thomas Schaller

A colour version of this report is available for download
on the KNMF website: www.knmf.kit.edu/annualreports.php

KIT – University of the State of Baden-Wuerttemberg and
National Research Center of the Helmholtz Association

Karlsruhe Institute of Technology (KIT)
Karlsruhe Nano Micro Facility (KNMF)
Hermann-von-Helmholtz-Platz 1
76344 Eggenstein-Leopoldshafen
Germany

Phone: +49(721)608-23123
Fax: +49(721)608-26273
Email: knmf-useroffice@kit.edu

Table of Contents

KNMF – A RESEARCH INFRASTRUCTURE OFFERING OPEN ACCESS TO MICRO AND NANO TECHNOLOGIES AND EXPERTISE TO ACADEMIC AND INDUSTRIAL USERS	7
TECHNOLOGIES OFFERED	7
ACCESS AND USE OF KNMF.....	8
KNMF – A RESEARCH FACILITY- OUTLOOK 2014	10
USER COMMITTEE	10
IN-HOUSE ACTIVITIES / RESULTS FROM INTERNAL USERS.....	12
ELECTRON BEAM LITHOGRAPHY (EBL)	12
NANOACTUATORS (C. LAY).....	12
SUB-WAVELENGTH GRATING WAVEGUIDES (KIRA KÖHNLE)	13
REFERENCES	14
DEEP X-RAY LITHOGRAPHY (DXRL).....	15
RESIST CHARACTERISATION FOR A SIMPLIFIED FABRICATION OF HIGH QUALITY X-RAY MASKS	15
REFRACTIVE X-RAY LENSES (MICHEL KLUGE, DANIEL LAMAGO, ARNDT LAST, FELIX MARSCHALL, HARALD VOGT)	16
CRLS WITH VARYING APERTURE REALIZED	16
X-RAY PRISM LENSES.....	17
NEW RESIST MATERIAL FOR X-RAY GRATING FABRICATION (ALEXANDRA KARBACHER, FRIEDER KOCH, DANAYS KUNKA, JAN MEISER, PASCAL MEYER).....	17
INCREASING THE GRATINGS AREA (ALEXANDRA KARBACHER, FRIEDER KOCH, DANAYS KUNKA, JAN MEISER, PASCAL MEYER)	18
STRATEGIC THEMES.....	19
REFERENCES	20
DIRECT LASER WRITING (DLW).....	21
PROCESS DEVELOPMENT	21
CANTILEVERS FOR ACTUATORS (C. LAY)	23
STRATEGIC THEMES.....	23
FURTHER COLLABORATION OUTSIDE KIT IN INTERNAL PROJECTS:.....	24
REFERENCES	24
3D DIRECT LASER WRITING (3D-DLW)	25
PHOTONIC WIRE BONDS (T. HOOSE)	25
3D POLYMER WAVEGUIDES (H. H. D. NGUYEN)	26
STRATEGIC THEMES.....	27
FURTHER COLLABORATION OUTSIDE KIT IN INTERNAL PROJECTS:.....	27
REFERENCES	28
LASER MATERIAL PROCESSING (LMP).....	29
LASER MOULDING FOR FABRICATION OF MICRO- AND NANOSTRUCTURED COMPONENTS	30
LASER GENERATION OF CAPILLARY STRUCTURES.....	30
FS-LASER STRUCTURING OF LiFePO ₄ CATHODE MATERIAL.....	31
STRATEGIC THEMES.....	32
FURTHER COLLABORATION OUTSIDE KIT IN INTERNAL PROJECTS:.....	33
REFERENCES	33
INJECTION MOULDING (µIM).....	34
POLYMERIC FRACTAL SCAFFOLDS IN BIOTECHNOLOGY	34

BIO-INSPIRED NANOSTRUCTURED COMPONENTS REPLICATED BY MICRO INJECTION (COMPRESSION) MOULDING.....	35
MICRO POWDER INJECTION MOULDING (MICROPIM)	35
BENCHMARKING OF DIFFERENT MICRO INJECTION MOULDING MACHINE LAY-OUTS	35
STRATEGIC THEMES.....	36
FURTHER COLLABORATION OUTSIDE KIT IN INTERNAL PROJECTS:.....	36
REFERENCES	36
HOT EMBOSSING/COMPRESSION MOLDING (HE).....	37
NANOIMPRINT SYSTEMS	37
NEW MATERIALS: HOT EMBOSSING OF PURE TEFLON PTFE	38
NEW MATERIALS: HOT EMBOSSING OF SHAPE MEMORY POLYMERS	38
TECHNOLOGY IMPROVEMENTS: HOT PULLING PROCESS	39
TECHNOLOGY IMPROVEMENTS: HIERARCHICAL HOT EMBOSSING	40
STRATEGIC THEMES.....	41
REFERENCES	41
FOCUSED ION BEAM (FIB).....	43
ADVANCED ELECTRON MICROSCOPY TO CHARACTERIZE THE HIERARCHICAL THREE-DIMENSIONAL MORPHOLOGY OF POROUS SOLIDS.....	43
PREPARATION OF SOLID STATE BATTERIES FOR IN-SITU TEM INVESTIGATIONS.....	44
CREEP CAVITATION STUDIES IN 9Cr MARTENSITIC STEEL FOR POWER PLANTS	45
STRATEGIC THEMES.....	45
FURTHER COLLABORATION OUTSIDE KIT IN INTERNAL PROJECTS:.....	46
REFERENCES	46
DIP-PEN NANOLITHOGRAPHY (DPN) AND POLYMER PEN LITHOGRAPHY (PPL).....	47
MULTIPLEXED BIOMIMETIC LIPID MEMBRANES ON GRAPHENE.....	47
MICRO-ARRAYING ON POROUS POLYMER SUBSTRATES	48
ON-CHIP MICROLASERS FOR BIOMOLECULAR DETECTION.....	49
MULTIPLEXED POLYMER PEN LITHOGRAPHY.....	50
STRATEGIC THEMES.....	50
REFERENCES	51
THIN FILM TECHNOLOGIES (TFT)	52
MICROSTRUCTURE AND HARDNESS OF REACTIVELY R.F. MAGNETRON SPUTTERED Cr-V-O THIN FILMS	52
FURTHER COLLABORATION OUTSIDE KIT IN INTERNAL PROJECTS:	54
REFERENCES	54
DRY ETCHING CLUSTER USING RIE(ICP) / RIBE	55
INTRODUCTION (A. MUSLIJA)	55
HIGH ASPECT RATIO X-RAY GRATINGS (A. MUSLIJA).....	56
SOI DEVICE LAYER THINNING BY REACTIVE ION ETCHING CRYO PROCESS (CH. LAY)	57
FABRICATION OF ULTRA COMPACT PLASMONIC DEVICES (S. MÜHLBRANDT).....	58
DRY ETCHING OF GLASS (D. HÄRINGER).....	59
REFERENCES	60
TRANSMISSION ELECTRON MICROSCOPY (TEM).....	61
DENSITY CHANGES IN SHEAR BANDS OF A METALLIC GLASS DETERMINED BY CORRELATIVE ANALYTICAL TRANSMISSION ELECTRON MICROSCOPY.....	61
IMPACT OF SONICATION PRETREATMENT ON CARBON NANOTUBES: A TRANSMISSION ELECTRON MICROSCOPY STUDY	62
CONTROLLED SYNTHESIS OF THORIUM AND URANIUM OXIDE NANOCRYSTALS	63

WHOLE-CELL ANALYSIS OF LOW-DENSITY LIPOPROTEIN UPTAKE BY MACROPHAGES USING STEM TOMOGRAPHY	64
IN-SITU AND EX-SITU TEM ELECTROCHEMICAL STUDIES OF NEW BATTERY SYSTEMS.....	65
STRATEGIC THEMES.....	67
FURTHER COLLABORATION OUTSIDE KIT IN INTERNAL PROJECTS:.....	67
REFERENCES	67
ATOMIC FORCE MICROSCOPY (AFM).....	69
SET-UP OF A LARGE-AREA ATOMIC FORCE MICROSCOPE	69
STRATEGIC THEMES.....	71
FURTHER COLLABORATION OUTSIDE KIT IN INTERNAL PROJECTS.....	71
REFERENCES	72
X-RAY PHOTOELECTRON SPECTROSCOPY (XPS)	73
BIOMIMETIC POLYMER-SWITCHING SYSTEM ON GOLD SURFACES.....	73
SOLUTION PROCESSED ORGANIC LIGHT EMITTING DIODES (OLEDs)	74
R.F. MAGNETRON SPUTTERED LI-MN-O THIN FILMS FOR LI-ION BATTERIES.....	76
STRATEGIC THEMES.....	77
FURTHER COLLABORATION OUTSIDE KIT IN INTERNAL PROJECTS:.....	77
REFERENCES	77
SINGLE CRYSTAL X-RAY DIFFRACTION (SCXD)	78
CRYSTAL STRUCTURE IDENTIFICATION OF METAL CHALCOGENIDE CLUSTER COMPOUNDS (WEN YU, XIAOXUN YANG)	78
STRUCTURAL ANALYSIS OF LARGE MOLECULAR AGGREGATES	78
STRUCTURAL ANALYSIS OF MONO- OR POLY-NUCLEAR IRON AND RARE EARTH METAL COMPOUNDS	79
ANALYSIS OF MULTINUCLEAR METAL COMPLEXES WITH MACROCYCLIC LIGANDS	79
FURTHER COLLABORATION OUTSIDE KIT IN INTERNAL PROJECTS:.....	79
REFERENCES	79
AUGER ELECTRON SPECTROSCOPY (AES).....	80
DESIGN PARAMETERS OF OUR EQUIPMENT	80
MEASUREMENT POSSIBILITIES OVERVIEW.....	81
DIFFUSION DETECTION BY LINE MEASUREMENTS.....	81
ELEMENT MAPPING AT GRAIN BOUNDARIES.....	82
REFERENCES	82
BULK AND TRACE ANALYSIS (BTA)	83
FURTHER COLLABORATION OUTSIDE KIT IN INTERNAL PROJECTS / COLLABORATION IN IN-HOUSE RESEARCH.....	85
REFERENCES	85
LA-ICP-MS	87
SHORT TECHNOLOGY DESCRIPTION/OVERVIEW AND MAIN FEATURES (EQUIPMENT CAPABILITIES).....	87
TECHNOLOGICAL UPGRADES IN 2013	87
REFERENCES	88
THIN FILM CHARACTERISATION (TFC).....	89
LI-ION BATTERY CATHODE MATERIALS	89
FURTHER COLLABORATION OUTSIDE KIT IN INTERNAL PROJECTS:	91
REFERENCES	91
KNMF LABORATORY FOR SYNCHROTRON RADIATION.....	92

INFRARED AND HARD X-RAY SPECTROSCOPY, X-RAY DIFFRACTION – IR1, IR2, PDIFF, XAS, AND X-SPEC	
BEAMLINES	92
NANOSTRUCTURE FORMATION MECHANISMS DURING SPUTTER DEPOSITION	93
REFERENCES	94
SOFT X-RAY SPECTROSCOPY AND SPECTROMICROSCOPY – WERA.....	95
REFERENCES	96
PUBLICATION LIST	97
USER REPORTS	112
LIST OF CONTRIBUTORS	112
FINAL REPORTS AS SUBMITTED BY THE USERS	115

KNMF – a research infrastructure offering open access to micro and nano technologies and expertise to academic and industrial users

KNMF is a leading user facility operating on regional, national, European and global levels. We aim to provide optimal user support by offering a state-of-the-art portfolio of micro and nano structuring and characterisation technologies which can often be individually adapted to suit user needs. The close proximity of the in-house research at KIT; ensures that the latest advances in application focussed scientific knowledge and state-of-the-art the technology development are available to our users. We are a collaboration-oriented facility, where our technology experts work together with our users to achieve the desired results.

During 2013 more than 140 users have benefited from the opportunity to access advanced nano and micro structuring and characterisation facilities at KNMF: Our annual budget, excluding investments, of 916T€ is rewarded by excellent scientific and technological advances made by our users in different nano and micro technology related fields. This impact is demonstrated by around 270 publications acknowledging KNMF in referenced journals more than 110 of these arose during 2013.

Technologies offered

KNMF was launched in 2009 by coordinating a complementary portfolio of technologies and expertise located in seven institutes at KIT into three virtual laboratories which work closely together.

- KNMF laboratory for micro- and nanostructuring (opened in 2009)
- KNMF laboratory for microscopy and spectroscopy (opened in 2010)
- KNMF laboratory for synchrotron characterisation (opened in 2012)

The latter laboratory offers the unique possibility to combine traditional characterisation methods for micro/nano characterisation with synchrotron based methods at one location.

In 2013 in total 23 technologies were available to users. The on-going investment programme has enabled the commissioning of several new technologies, adding the possibility e.g. to access 3D direct laser writing, (3D-DLW), direct laser writing (DLW), single crystal X-ray diffractions (SCXD) and ToF-SIMS which were each made available to users during the year.

It is not only the single technology which makes KNMF of interest for external user. The possibility to combine the technologies offered by KNMF to complex process chains and characterisation clusters allows the execution of user requests in a more comprehensive manner. This is demonstrated by external and in-house user projects described in the following chapters.

By the end of 2015 KNMF will offer a total 34 technologies with machine time of roughly 75,000 hours per year not including the beam-time of the ANKA beam-lines. The number of personnel (scientists, technicians) will increase to more than 50 persons.

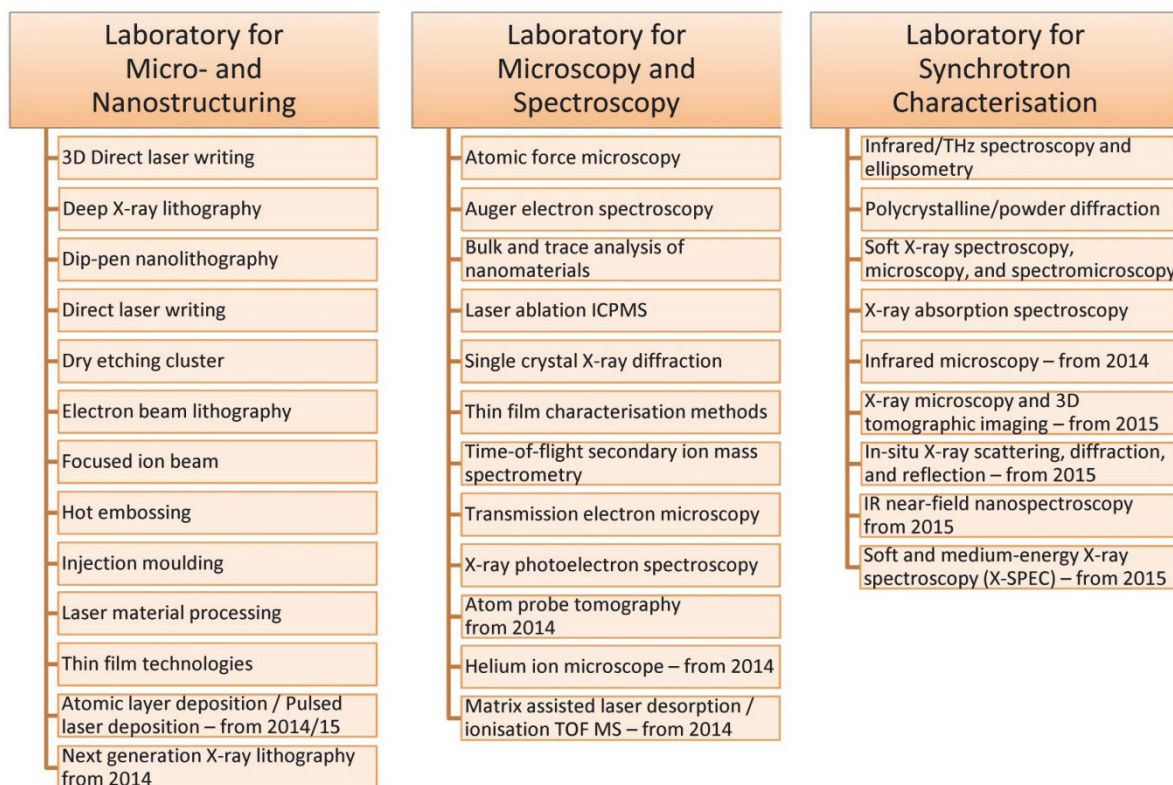


Fig. 1: Portfolio of the KNMF including planned technologies

Access and use of KNMF

Users from all types of organisation can access KNMF. No fee access, for work intended for publication is possible *via* a straightforward peer review process. Two calls per year are published and proposals are evaluated immediately after the close of the call by an independent peer review board (PRB). For user projects linked with public funded and already reviewed external collaborative projects, e.g. European, BMBF, DFG projects the proposal submission is simplified and, as long as the activities are in-line with KNMFs portfolio and strategy, the PRB usually accepts the decisions made by the respective independent review panels. Users can submit four types of proposals: If preferred, a proprietary service is available, on individual terms.

- standard (duration up to 6 months),
- long-term (duration up to 2 years),
- proprietary (full cost recovery, not peer reviewed, publication of results not required),
- fast-track (for small and urgent tasks upon decision of the KNMF head, review by PRB *a posteriori*).

Users are encouraged to contact the user office or the technical experts prior to proposal submission to discuss all open issues and to define a feasible work-plan. This usually results in well-written proposals and increases the chance for acceptance during the review process.

Full details of how to access KNMF can be found under <http://www.knmf.kit.edu/>.

KNMF receives an average of just over 90 proposals per call (Fig. 2). KNMF is still in the implementation phase. In 2013 the annual use by external users was 46%. In 2014 it is expected to reach more than 50%.

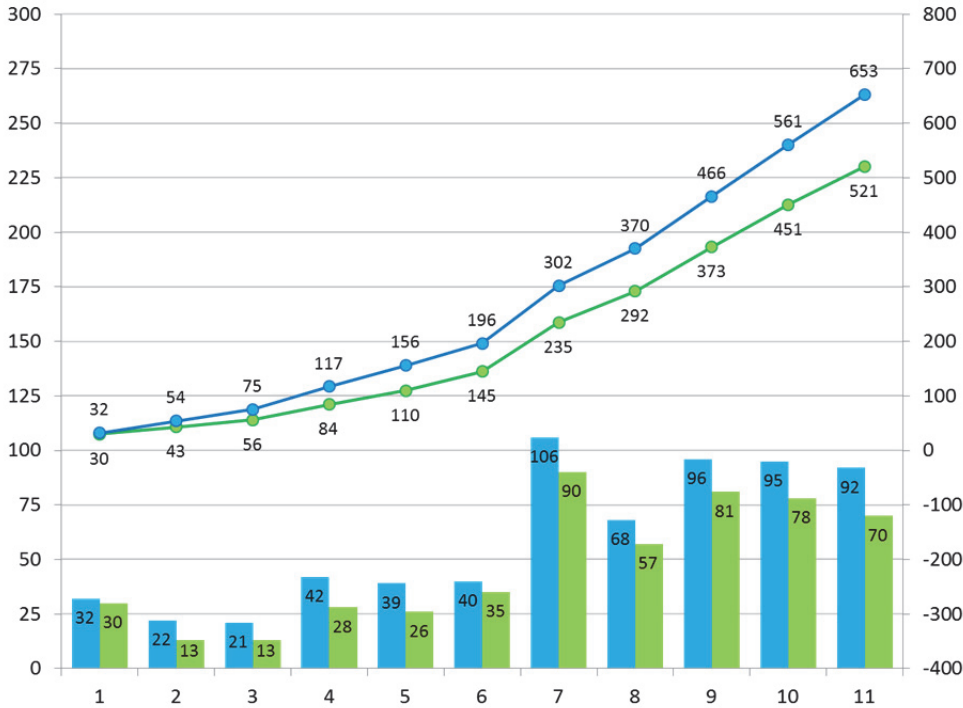


Fig 2. Numbers of proposals submitted and accepted per Call

Whilst the majority of users come from academia, 23% of users are from industry; this figure represents both no fee and proprietary industrial users (Fig. 3). More than 40% of our users come from outside Germany, whereas 15% are from outside Europe. This demonstrates that KNMF’s technology portfolio and competence is recognised as having global relevance and also enables international groups to benefit from and contribute to the scientific developments at KNMF. (Fig. 4)

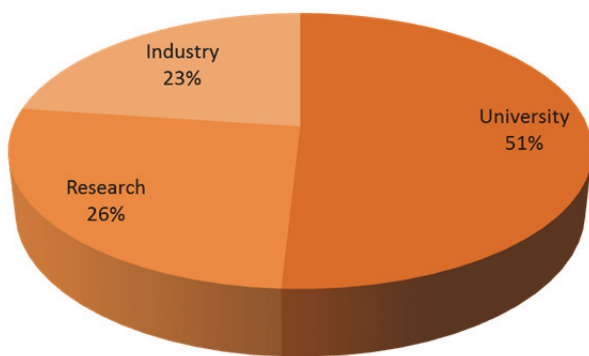


Fig. 3 Type of organisation of users

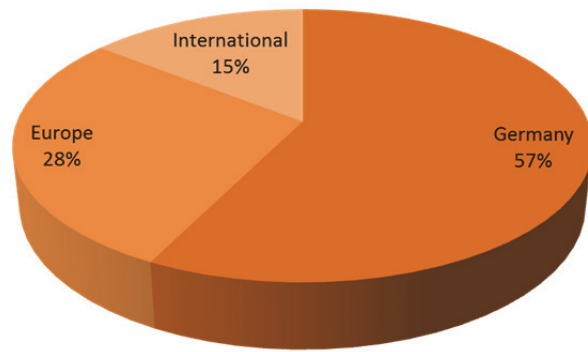


Fig. 4 Geographical origin of users

KNMF’s technologies are relevant to a broad range of application areas, usually our users do not simply request access to a specific technology but require solutions to achieve particular goals. Such projects need a very close interaction between KNMF staff and the user for pre-preparation of the project and post-processing of the project results. The ideas of the users are indeed beneficial for KNMF in that they often challenge the state-of-the-art of the skills and stimulate the further development of the technologies relevant to the user community. The application areas relevant to our users are presented in Figure 5.

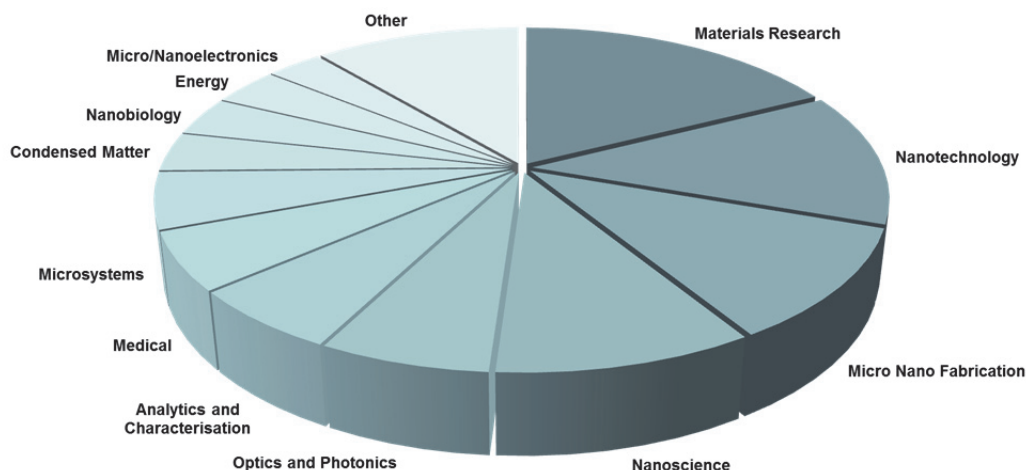


Fig. 5 Application areas relevant to KNMF user proposals

KNMF – a research facility- outlook 2014

At the close of 2013 KNMF was approaching a milestone in its development; an international review scheduled for February 2014, would evaluate the progress and planning of KNMF to receive the status of a Helmholtz Research Infrastructure. The formal recommendations of the review are expected in November 2014.

The key ingredient for KNMF's technical competence is that it builds on technologies and skills developed in the Helmholtz Programme Science and Technology of Nanosystems (STN) which ensures a continuous development of the expertise in micro- and nanotechnologies. Future developments are proposed in the areas of multi-scale structuring and correlative characterisation. Development work on processes for printing technologies occurring within the programme STN may also become available within KNMF

In view of strategic development KNMF has identified some strategic R&D topics which address complex research challenges and warrant long term collaboration ("public-public" partnerships). These public-public-partnerships are being established along the value chain with partners responsible for fundamental scientific research, methodology studies, instrumentation and innovative application oriented developments. The virtual institute "New X-ray analytic methods for material science" (VI-NXMM) is a first realisation of this concept. It started from the X-ray imaging activities in medical applications brought to KNMF by Prof. Pfeiffer's group (Technical University Munich) and was further complemented by external (EMPA, CAU, HZG) and internal partners (IAM-WK, IPS, ANKA) with a focus on materials analysis. Additional public-public partnerships are under discussion e.g. teratronics or micro patterning in the frame of battery development.

User Committee

The user committee represents all KNMF users; elections are held every two years and the most recent election was December 2013. We welcome Prof. John F. Corrigan to the committee, and express our gratitude to Dr. Erik Bründermann who retired from the committee in 2013. The user committee gives also advice to the future development of KNMF's technology portfolio, and represented the users at the evaluation in February 2014. Elected members are:

Newly elected

Prof. John F. Corrigan, University of Western Ontario, Canada

Re-elected

Prof. Sven Achenbach (Chair), University of Saskatchewan, Canada

Prof. Florian Banhart, University of Strasbourg, France

Prof. Jost Göttert, Hochschule Niederrhein, Krefeld, Germany

Prof. Lorenz Kienle, University of Kiel, Germany

Dr. Karen Lienkamp (Co-Chair), University of Freiburg, Germany

Retiring member

Dr. Erik Bründermann, Ruhr-University of Bochum, Germany

In-house Activities / Results from Internal Users

Electron Beam Lithography (EBL)

Peter-J. Jakobs

E-beam-lithography is operated in KNMF by the Institute of Microstructure Technology (IMT) for the fabrication of highly accurate structures in the nano- and microscale. We use a state of the art Vector Beam-tool from Vistec for 6" Substrates with **Ultra High Resolution** and **Extrem Wide Field** (VB6UHR-EWF), this means we can expose an area of 1310 x 1310 μm^2 and a resolution 1.25 nm - without moving the substrate. We tune in to two different ways. One way is to realize a pattern in extreme thick resist (3200 nm) for intermediate masks with an aspect ratio up to 10, only very few working groups are doing this worldwide. The other way is to expose very small patterns, down to about 20 nm (this depends on substrate stack). In 2013 we gained experience with two negative resists. Process chains using these resists will be offered to KNMF users. Below you will find two selected R&D activities which have been performed in 2013.

Nanoactuators (C. Lay)

Nano-scale actuators consisting of a free-standing bilayer of ferromagnetic shape memory alloy (FSMA) and silicon with critical lateral dimensions of 250 nm are designed, nanofabricated and characterized *in-situ* in a scanning electron microscope (SEM). Upon Joule heating and cooling, fully reversible nano-actuation in out-of-plane direction of up to 4 % of actuator length is observed.

We fabricate our structures by using Silicon on Insulator (SOI) wafers with a device layer of 500 nm and a buried oxide of 4 μm as a starting material (Fig. 1a). Then a polymethyl metacrylate photoresist is deposited and exposed by electron beam lithography (Fig. 1b). After development of the resist, a reactive ion etching (RIE) cryo process is used to create Si double beam cantilevers with rectangular sidewalls and a minimum width of 150 nm (Fig. 1c). After removing the photoresist, an additional RIE cryo etching step is used to reduce the silicon device layer thickness down to 200 nm while retaining the bimorph structure's geometry. Free-standing cantilever structures (shown in Fig. 2) are obtained by wet etching the buried oxide SiO_2 layer with hydrofluoric acid (Fig. 1d). After this, a Ni-Mn-Ga layer of 200 nm thickness is deposited by DC magnetron sputtering at 500°C. As can be seen in Fig. 3, sidewall deposition causes a total increase in width of 100 nm.

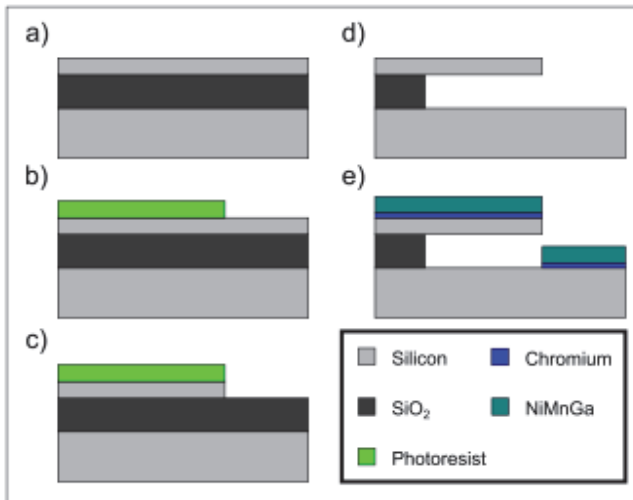


Fig. 1: Process flow for the fabrication of Ni-Mn-Ga/Si bimorph structures.

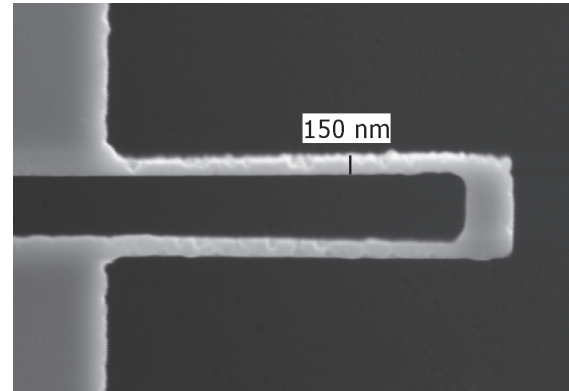


Fig. 2: SEM Micrograph of a free-standing silicon double beam; with width, thickness and length $0.15 \times 0.35 \times 3.5 \mu\text{m}^3$.

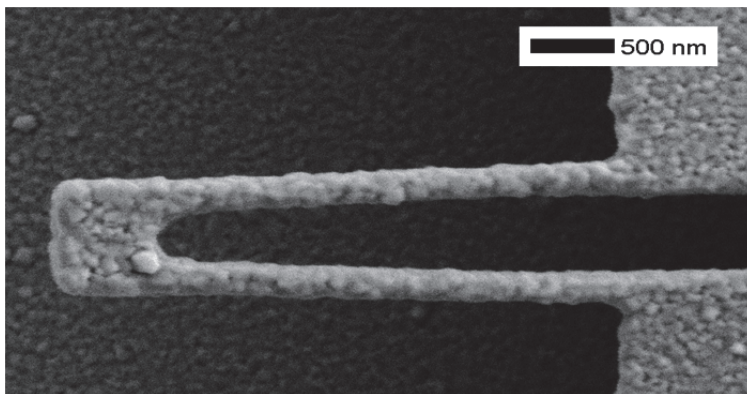


Fig. 3: SEM Micrograph of a free-standing Ni-Mn-Ga bimorph with dimensions of $0.25 \times 0.55 \times 3.5 \mu\text{m}^3$ in width, thickness and length, respectively. The thickness values for Si and Ni-Mn-Ga are 350 nm and 200 nm, respectively.

Sub-wavelength Grating Waveguides (Kira Köhnle)

Silicon-organic hybrid (SOH) modulators offer high-speed modulation of light (@1550 nm wavelength) up to 50 GHz. They are key components for optical interconnects and short-reach telecommunication links. While state-of-the-art devices exploit carrier-injection or carrier-depletion in p-n-junctions, recent publications have shown that the combination of SOI waveguides with organic electro-optic (EO) cladding materials are a better solution in terms of modulation speed and energy efficiency [1,2]. In view of the fabrication of such modulators, a process was developed to fabricate silicon waveguides with electrodes on a silicon-on-insulator (SOI) substrate with 250 nm device layer thickness and 3 μm buried oxide (BOX) thickness.

The developed process uses markers which are defined in an electron beam lithography step with PMMA 950K resist and then dry etched by cryogenic silicon process. These topological markers must be of high quality, because they are used for the alignment of the subsequent EBL steps. In the first electron beam lithography step the waveguides are defined in ma-N 2401 resist and then transferred to the silicon layer by cryogenic dry etching. After stabilizing

the cryogenic, SF_6 gives a suitable etch time as well as repeatable and good results for silicon layers which are etched down to the BOX.

In the second electron beam lithography step the electrodes are defined in a PMMA mask. Subsequently gold is deposited on the developed PMMA and a lift-off process is performed. The result can be seen in Fig. 4. This process could be used successfully to fabricate an SOH phase modulator using sub-wavelength grating (SWG) waveguides.

The above mentioned process will expand the KNMF EBL portfolio and will be offered at the beginning of next year. Alignment accuracy will be determined soon. Preliminary results confirm that the accuracy is better than 100 nm in both horizontal and vertical direction, see Fig. 5.

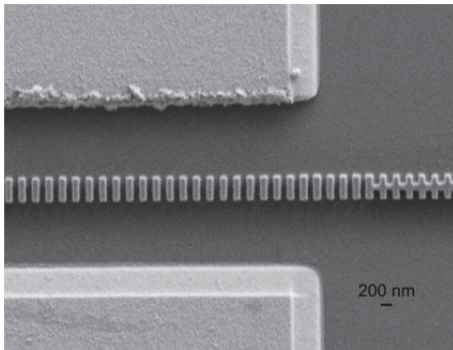


Fig. 4: SEM image: Silicon waveguide on a substrate with silica surface with gold electrodes on both sides of the waveguide.

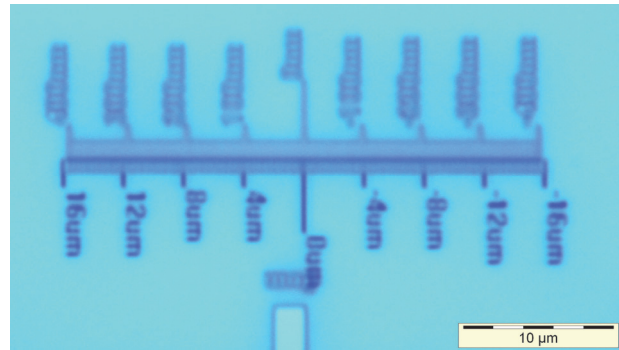


Fig. 5: Light microscope image: Excellent alignment of multiple layers. Alignment is better than 100 nm.

References

- [1] R. Palmer, L. Alloatti, D. Korn, P. Schindler, M. Baier, J. Bolten, T. Wahlbrink, M. Waldow, R. Dinu, W. Freude, C. Koos, J. Leuthold, *IEEE Photonics Technol. Lett.* 25 (2013)1226-1229.
- [2] D. Korn, P. Robert, Yu H., P. Schindler, L. Alloatti, M. Baier, R. Schmogrow, W. Bogaerts, S. Selvaraja, G. Lepage, M. Pantouvaki, J. Wouters, P. Verheyen, J. Van Campenhout, Chen B., R. Baets, P. Absil, R. Dinu, C. Koos, W. Freude, Wolfgang, J. Leuthold, *Opt. Exp.* 21 (2013), 13219-13227.

Deep X-ray Lithography (DXRL)

Martin Börner, Birgit Hübner, Barbara Matthis, Daniel Münch, Franz Josef Pantenburg, Christin Straus, Julia Wolf

Three beamlines at the synchrotron source ANKA are operated in KNMF by the Institute of Microstructure Technology (IMT) for fabrication of high aspect ratio microstructures (HARMST). Litho I and Litho II are open to users, Litho III is under commission up to 2015 to allow upscaled fabrication for multiscale dimensions. The in-house research focuses both on process improvement and optimization as well as on the fabrication of new and innovative HARMST. In this report we will highlight a selection of R&D activities which have been performed during 2013 on resist development and on X-ray optics.

Resist Characterisation for a simplified Fabrication of High Quality X-ray Masks

Deep X-ray lithography requires high quality X-ray lithography masks. Currently these masks are fabricated by soft X-ray copying of an e-beam mask using a photosensitive resist named PMMA A11. In view of reducing the processing time and simplifying the process, a new resist system named AR-P 6510.17 (Allresist) was studied. Spin-parameters, exposure parameters and the parameters for the development process were evaluated. For the evaluation of the spin-parameters a corresponding rotation speed range from 150 to 400 rpm was chosen. The dose variation was carried out starting with 0,1 kJ/cm³. For the upper limit 4,5 kJ/cm³ was chosen to estimate the exposure conditions and the development time was varied between 15 minutes and two hours for the fabrication of gratings [1]. The following parameters were evaluated as an optimum for the achievement of 60µm (+/-3µm) thick microstructures:

Spin coating:

First step: Duration: 180 sec Ramp: 150 Rotation Speed: 325 rpm

Second step: Duration: 10 sec Ramp: 450 Rotation Speed: 450 rpm

Exposure:

Bottom dose: 4,0 J/cm³; Top dose: 13,5 J/cm³

Development:

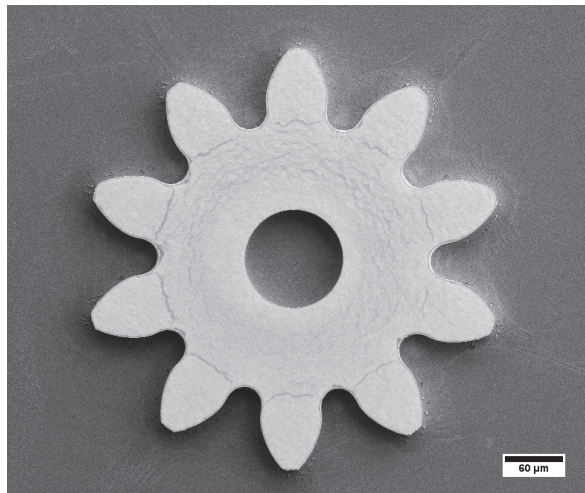
Time: 60 min. GG; 20 min. BDG; 10 min. H₂O.

We observed that one of the main advantages of the AR-P 6510.17 resist system is the possibility to process resist films in 65 µm thickness, by keeping the standard mask quality, within just one single coating step. Previously it was necessary to apply three coating steps to achieve a resist height of about 50 µm.

Subsequently, the quality of the structures was investigated with a special test layout. Several line width measurements were used to make a comparison between the two resist systems PMMA A11 and AR-P 6510.17. Thus, an additional working mask with the Liga 2.0 design [2] was manufactured. This layout consists of structures that are relevant for industry like gear wheels. Inner and outer diameters of the wheels were measured as well as the form tolerance, e.g. for a designed diameter of 200.0 µm corresponding gold absorbers with a diameter of around 198.5 µm could be achieved. To compensate the loss in diameter, the design data for the mask fabrication can easily be adopted.

Also the investigation of the structures with a SEM showed no significant differences between the structures fabricated with these two resist systems (Fig. 1).

Fabricated with AR-P 6510.17



Fabricated with PMMA A 11

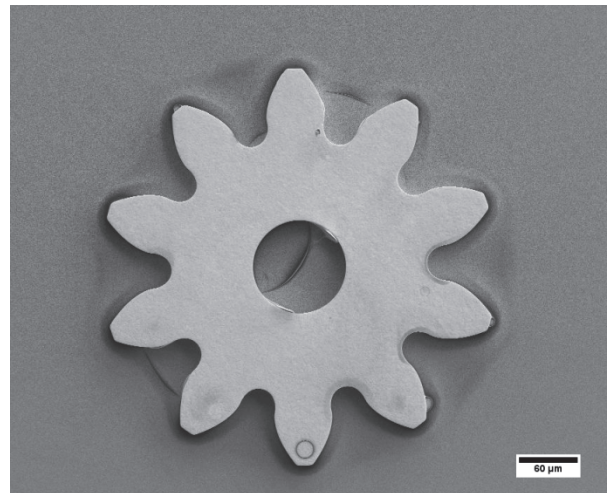


Fig. 1: Selected SEM pictures for comparison

In conclusion three different layouts for various applications for the two resist systems were investigated. It could be proved that the new resist system is useful for all these applications.

Refractive X-ray lenses (Michel Kluge, Daniel Lamago, Arndt Last, Felix Marschall, Harald Vogt)

Several optical components are needed to set up enlarging X-ray optical systems such as X-ray microscopes,. These are mainly imaging lenses and illumination optics. We aim to design systems for photon energies above 15 keV and up to about 40 keV. In this range refracting X-ray lenses are well suited, as the material does not absorb too strongly and at the same time the refracting effect is still sufficiently large [3].

In 2013 refractive X-ray optics have been fabricated using Deep X-ray Lithography (XRL). These optics have been characterized at beamlines at ANKA, PETRA III, ESRF and Spring-8.

CRLs with varying aperture realized

With respect to an increased photon density in the outermost areas (“s” in Fig.2) the layout of compound refractive X-ray lenses (CRLs) has been improved. It was shown that lenses with larger entrance and exit apertures and smaller apertures in the centre have better optical properties for full field microscopy. Relating to the German word for “waist”, these lenses were called “Taille”-lenses.

With these lenses the intensity distribution and the spatial resolution of full field microscopy images are more homogeneous over the total field of view (Fig 3). The effect of vignetting in the corners of the images is clearly reduced. At the same time the field of view can be increased, compared to constant aperture CRLs.

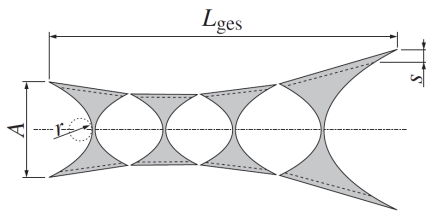


Fig. 2: CRL with varying apertures

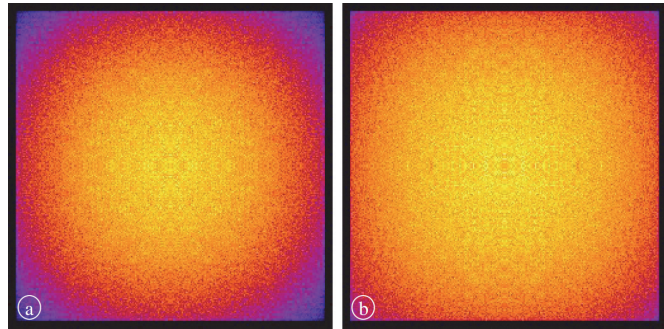


Fig. 3: Image intensity distribution for a) CRL with constant aperture b) "Taille"-CRL

The imaging resolution in a full field X-ray microscopy was improved to better 200 nm (per line & space period). Further process development will result in improved illumination optics and imaging optics specially designed respectively for use at ANKA PETRA III in 2014.

X-ray Prism Lenses

To be able to realize spot sizes of less than 10 μm using high aperture 1D lenses a new concept was followed which combines rows of prisms with compound refractive X-ray lenses (CRLs). Rows of prisms with 10 μm to 20 μm edge length are used to change the direction of the X-rays towards the illuminated spot and a few parabolic lens elements are added to each row of prisms to focus the micro beam further down (Fig. 4 and Fig. 5). In this way focal spot sizes clearly below the prism size should become feasible. To realize a lens opening of more than 150 μm , the prisms needed to be fabricated in this height. To prevent a collapse of the structures due to capillary forces these structures were freeze dried.

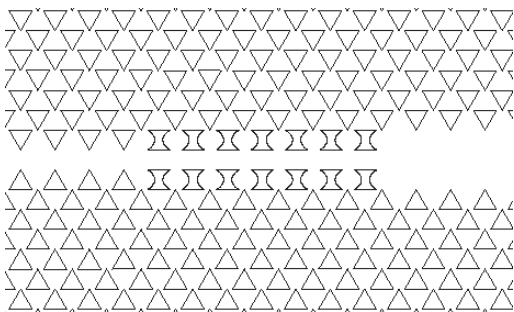


Fig. 4: X-ray Prism Lens including parabolic lens elements (scheme)

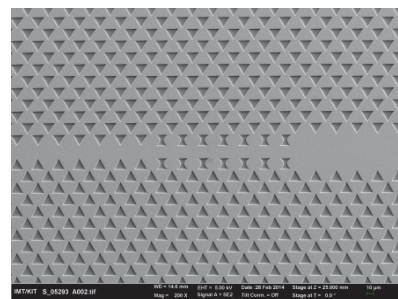


Fig. 5: SEM picture of a DXRL mask for fabrication of new X-ray prism lenses with parabolic lens elements

New resist material for X-Ray Grating fabrication (Alexandra Karbacher, Frieder Koch, Danays Kunka, Jan Meiser, Pascal Meyer)

Grating based X-ray Differential Phase Contrast Imaging (DPCI) is a promising technique exploiting not only the absorption, but also the phase shift and scattering of X-Rays going through matter. It requires high aspect ratio grating structures in order to keep the set-up compact while measuring at photon energies >30 keV. We develop these structures using X-ray lithography and subsequent electroplating.

As the image quality in a DPCI setup is directly related to the structure quality of the gratings used, it is crucial to have a defined procedure to evaluate the structure quality when

changing parameters, e.g. trying out a new resist formulation. We therefore set up a characterization methodology consisting of three steps: contrast evaluation of the resist, evaluation of the lithographic performance using different grating periods and characterization of the final grating structures in terms of visibility and homogeneity [4].

We used this methodology to compare resist formulations that were developed in collaboration with Micro Resist Technology GmbH. Preliminary results show a considerable increase in contrast and good structure quality with a new resist formulations compared to standard SU-8 photoresist (Fig. 6). The contrast could be increased from about 3 J/cm³ to more than 5 J/cm³. Unfortunately the material still lacks some inhomogeneity and further studies are needed to stabilize the resist performance.

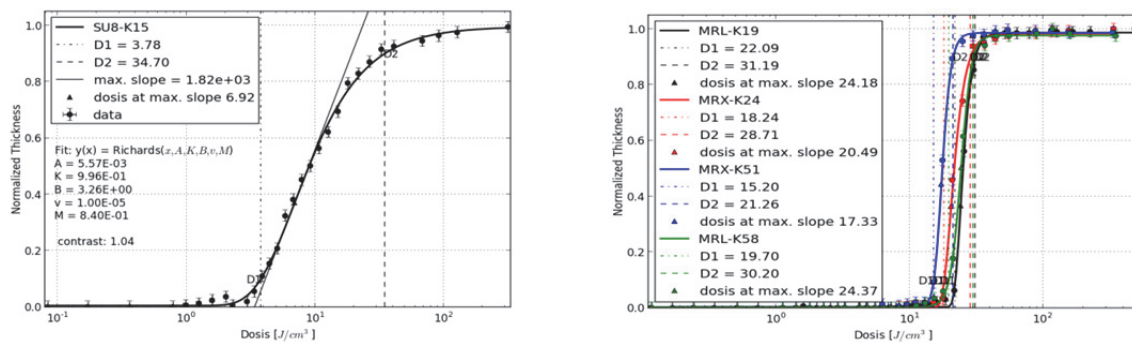


Fig. 6: Contrast Curves for SU-8 (left) and newly developed resist formulations (right)

Increasing the gratings area (Alexandra Karbacher, Frieder Koch, Danays Kunka, Jan Meiser, Pascal Meyer)

The field of view of an X-ray DPCI setup directly scales with the area of the gratings. In order to image large objects, such as a human torso, one needs gratings with an area of up to 400x400 mm. In fabrication, we are currently limited to 70 mm diameter, which translates to a square of about 50 mm edge length. To overcome this limit, we have developed a stitching technique. After going through the X-ray lithography and electroplating steps, the unstructured areas of the wafer are cut away using a saw. The resulting square gratings are then merged on a carrier substrate to form a larger grating.

The gap between two grating tiles on the carrier substrate should not be larger than 50 μm , in order to only affect one pixel row in the imaging setup. Furthermore, the angle between the lamellas of neighbouring tiles should be inferior to 0.01° to avoid remaining Moiré fringes that cause difficulties in obtaining the final image (Fig. 7 and Fig. 8). The carrier substrate should have a low X-ray absorption and high mechanical stability.

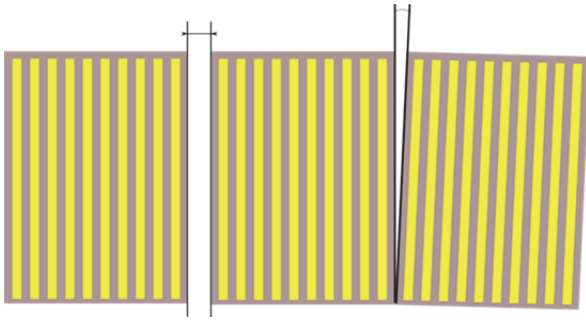


Fig. 7: Challenges of stitching (gap and angle)

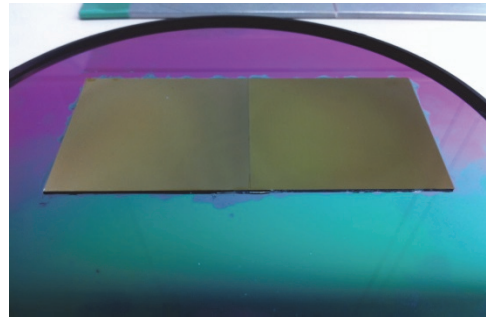


Fig. 8: Two stitched gratings to achieve an active area of 50 x 100 mm²

A proof of concept was done using a 6" Si-wafer with a thickness of 625 μm as carrier substrate. It provided high mechanical stability and reasonable low X-ray absorption for high energy (>35 keV) imaging, but still introduces too much additional absorption in the low energy domain which is not tolerable in the clinical application. Therefore, further studies are necessary to set-up an optimized process for large area stitched gratings which also fulfils the request of high transmission [5].

Fig. 9 shows a dark field image. In the middle of the picture the stitching effect could be seen. It affects only one row of pixels. That corresponds to a lateral resolution of 172 μm (pixel size). The picture of an aortic valve was taken in an X-ray tube setup at TU Munich with an energy of 27keV.

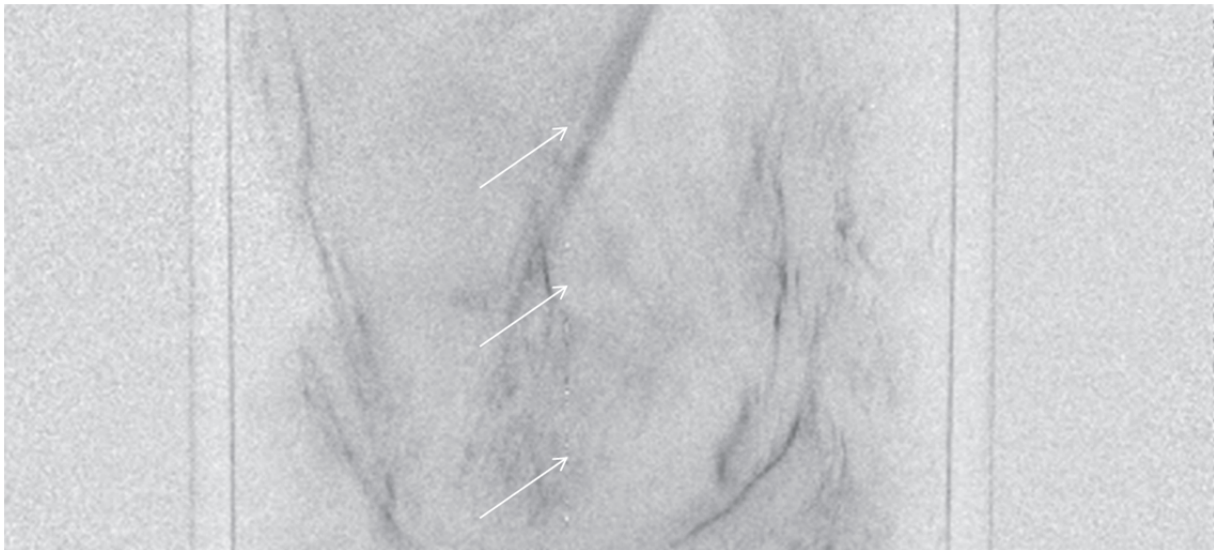


Fig. 9: Arrows indicate the disturbances of the joints suggestively

Strategic Themes

The X-ray optics activities at KIT are outstanding due to the structuring possibilities of deep X-ray lithography (XRL), e.g. refractive X-ray lenses made out of SU-8-resist fabricated at KIT/IMT show the least stray light background of all refractive X-ray lenses due to the non-crystalline polymer material and smooth optical surfaces provided by XRL. Also X-ray gratings are fabricated with the highest aspect ratio world-wide. To underline this strategic importance we set-up the Virtual Institute "New X-ray analytic Methods in Material science" (VI-NXMM, see www.roentgenbildgebung.de). Additionally there are collaborations with

ESRF, APS, SPring-8, Institute for X-ray Microscopy, Würzburg. This together with the on-site expertise from colleagues at ANKA, and the activities in the programme STN results in a very strong competence in this area.

References

- [1] J. Wolf "Herstellung und Charakterisierung von Röntgenarbeitsmasken mit einem neuen Resistsystem", KIT/IMT as well as Fachschule für Technik Fachrichtung Chemietechnik der Carl-Engler-Schule Karlsruhe, 2014
- [2] Jochen Heneka „Neues LIGA2.X Verfahren zur industriellen Fertigung von hochpräzisen Kunststoff-Mikrobauteilen“, Proceeding Mikrosystemtechnik Kongress 2013 Aachen, ISBN 978-3-8007-3555-6, 306 – 308 as well as KIT Presseinformation 091/2013
- [3] F. Marschall „Entwicklung eines Röntgenmikroskops für Photonenenergien von 15 keV bis 30 keV“, dissertation, KIT/IMT, to be published 2014
- [4] Kunka, D., Mohr, J. et al. (2013). "Characterization method for new resist formulations for HAR patterns made by X-ray lithography." *Microsystem Technologies*. doi:10.1007/s00542-013-2055-x
- [5] J. Meiser, et al. "Increasing the field of view of x-ray phase contrast imaging using stitched gratings on low absorbent carriers", *Proc. SPIE 9033, Medical Imaging 2014: Physics of Medical Imaging*

Direct Laser Writing (DLW)

Klaus Bade, Stefan Hengsbach

Direct Laser Writing allows patterning of SU-8 (Epoxy) and AZ-Resists due to a wavelength of 355 nm. Resist thicknesses are in the range of several hundred nm up to 100 μm . The lateral resolution is 1 μm for thin resist layers. Due to high precision stages scanning speeds 35 mm^2/min are achieved. this allows a 100 mm wafer to be written in approx. 4 h. The maximum substrate size is 150 mm wafer format (square or circular). The height difference in the writing area should be less than 50 μm . Reflective substrate surfaces have to be covered with an antireflective coating to avoid standing wave patterns in the sidewalls.

DLW was first offered to users in 2013. The laser writer is a commercial machine, but in our case differs from the standard with respect to the wavelength of the laser and newly developed software for machine control and layout handling. The software allows a better organization of layout, documentation, layout arrangement and a better alignment on the substrate. The autofocus is independent from substrate materials because a pneumatic system is used.

DLW is a fast maskless patterning method which complements the e-beam. The layout can be rapidly transformed into the pattern which is particularly beneficial for prototyping or single features. DLW is often used as a patterning method for etch-masks used in Deep Reactive Ion Etching (DRIE).

Combination of 2D and 3D Direct Laser Writing [1] is possible, which extends the applicability of the 2D-DWL.

Process Development

Beside the standard application of thin resist film patterning we are working on processes for higher structures and larger aspect ratios. Further, the manufacturing of X-ray masks is an important topic. Results from a feasibility study are presented below.

High Structures

Typically 2D DLW is used for patterning of thin resist layers for example in photo mask fabrication. Our work shows the possibility to pattern thicker resists (Fig. 1 and 2) up to very high resist structures of 400 μm . For this transparent photoresists are needed, in this case an epoxy type negative resist is used. With AZ-type resists heights are limited because of higher absorption. Typically, ranges below 6 μm are tested up to now in the latter. Sidewall profiles are not as steep as in e-beam-, and X-ray lithography, because the Gaussian beam width changes with distance away from the focal spot volume.

Applications of these high structures are for example micro-fluidic chips.

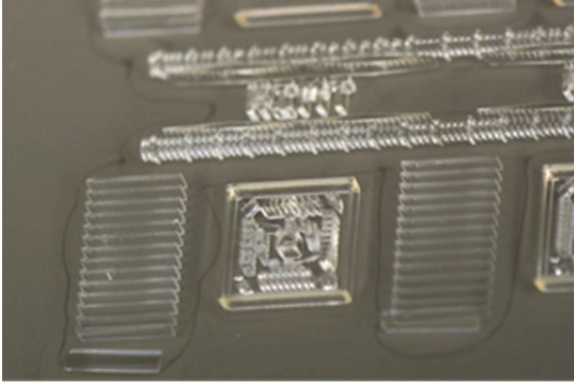


Fig. 1: Test pattern with a height of 400 µm.

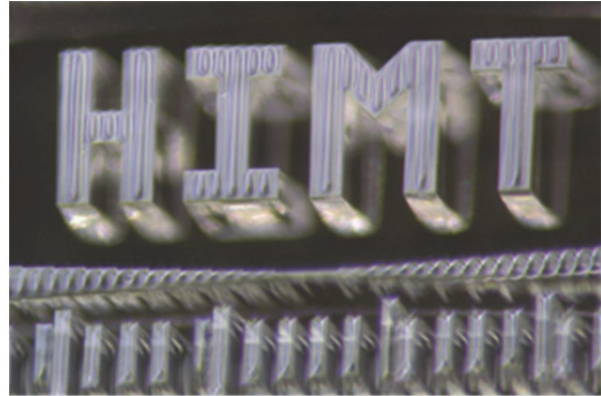


Fig. 2: Detail of Fig. 1. The streaks on the surface are due to the writing method of the laser writer. This effect also the sidewall quality of the wall below the text.

Decreasing the width of structures leads to high aspect ratio structures. In fig. 3 a tall micro cylinder with a height of 70 µm with an approximate aspect ratio of 7 is shown. The aspect ratio is dependent on structure geometry. Typically an aspect range of 4 is achievable for a larger range of structure sizes. The sidewall is sloped as discussed above. In some applications this is beneficial for example for mould inserts used in hot embossing.

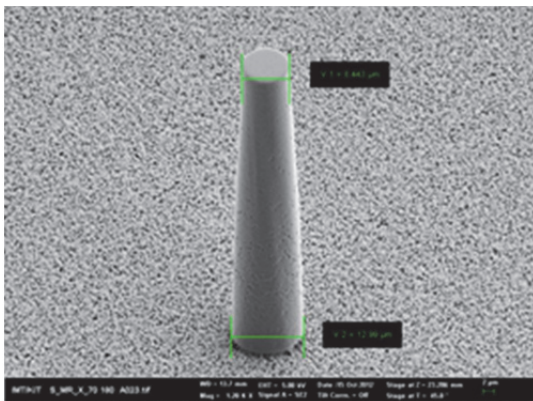


Fig. 3: High aspect ratio column with a height of 70 µm made out of epoxy-type negative resist. Porosity can be due to a higher dose in the bottom region.

X-ray Mask Fabrication

X-ray masks are important tools to fabricate high aspect ratio structures. X-ray masks consist of a transparent carrier membrane and a gold absorber. The laser written resist pattern is transformed in the gold pattern by gold electroplating. Normally, e-beam written resist structures are used. Here we demonstrate the feasibility to use DLW in the case of coarser structures which could be patterned with the laser writer. The advance of DLW is a shorter writing time.

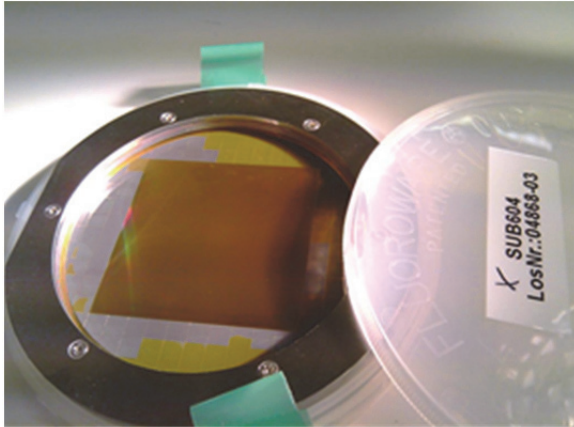


Fig. 4: X-ray mask. The square area (60 mm x 60 mm) is the gold structure area.

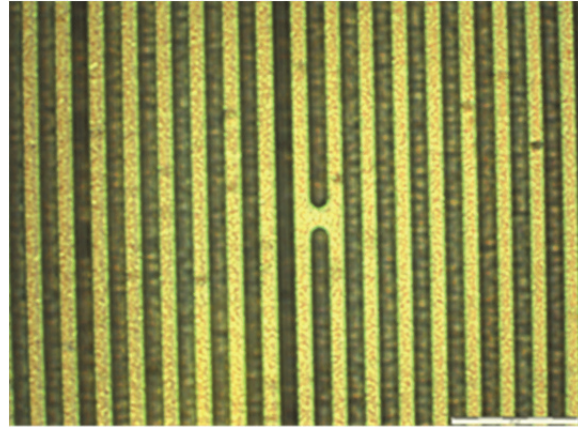


Fig. 5: Detail of fig. 4 shows a gold grating with a period of 5.4 μm .

Cantilevers for Actuators (C. Lay)

In this project the target is the prototyping of cantilever structures for actuators. The final cantilevers width is in the nm range leading to nano actuators. For that ebeam writing is necessary. To avoid long development time, a faster prototyping method is beneficial to define the process for cantilever manufacture. Here, DLW defines the etch-mask for the following RIE process to etch Si which lead to freestanding cantilevers (Fig. 6). In fig. 7 the motion of such a bimorphic cantilever by heating is shown as overlay of the cooled and heated state of the actuator.

In contrast to the examples described above, the AZ-type positive resist allows the finest line width, using our current write head, of 2 μm . Smaller line widths down to 1 μm can, in principle, be achieved by using a different write head [1].

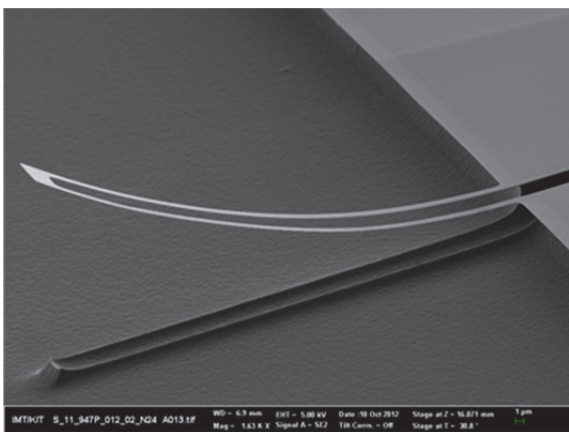


Fig. 6: Double beam generated with patterning a RIE mask layer by DLW. Beam width is 2 μm

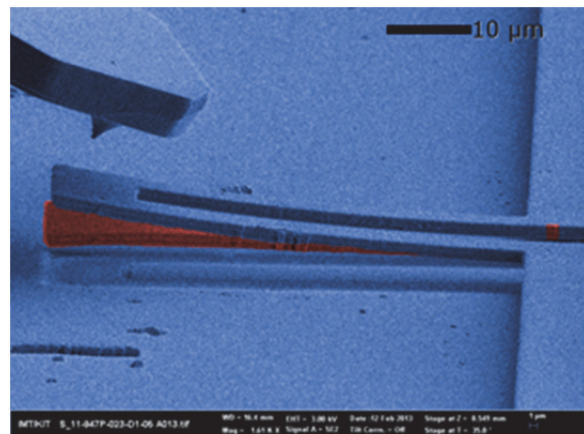


Fig. 7: Overlay SEM pictures of a heated and cooled cantilever illustrating its motion. The cantilever is a bimorph Si/NiMnGa,

Strategic Themes

none

Further Collaboration outside KIT in internal projects:

none

References

[1] S Hengsbach, A Diaz Lantada, Rapid prototyping of multi-scale biomedical microdevices by combining additive manufacturing technologies, Biomed Microdevices, DOI 10.1007/s10544-014-9864-2

[2] Data sheet DWL 66+ Heidelberg Instruments

[www.himt.de/files/Factsheet_Download/HIMT Fact Sheet DWL 66+.pdf](http://www.himt.de/files/Factsheet_Download/HIMT_Fact_Sheet_DWL_66+.pdf)

3D Direct Laser Writing (3D-DLW)

Klaus Bade, Stefan Hengsbach

With 3D direct laser writing 3D objects with feature sizes down to 200 nm can be written on a substrate. The method relies on two-photon absorption in a tightly focussed laser spot (voxel). By scanning the laser spot in the resist, 3D objects are generated. Mostly acrylic photoresists (negative) are applied. Focussing is done by microscope objectives where the objective could also be immersed into a liquid resist (Dip-in, DiLL) which allows refractive index matching.

The equipment allows three different writing modes:

- Piezo stages: x,y-writing area is 300 μm x 300 μm with additional 300 μm in z-direction. Each coordinate can be addressed independently, which allows vectorial writing.
- Hybrid stages: larger x,y-writing area 100 mm x 100 mm by combination of motor stage and piezo drive for accuracy on long distances. Movement in z-direction is performed with the above mentioned piezo drive.
- Galvoscan: In 2014 the 3D Direct Laser Writing system will be upgraded with a galvoscan unit. It allows a faster writing speed in the x,y-plane with a writing field: rectangular 140 μm x 140 μm or circular with 200 μm diameter, leading to smaller writing times. Larger areas can be obtained by stitching of several fields. Movement in z-direction is performed with the above mentioned piezo drive.

The 3D direct laser writing was offered the first time in 2013 for users.

Photonic Wire Bonds (T. Hoose)

Very fast communication between various chips requires the ability to shift from electronic to optical connections. Therefore photonic wire bonds (PWB) are intensively investigated [1]. To generate 3D PWBs 3D-laser writing with DiLL (fig. 1) can be successfully applied as demonstrated in fig. 2. The challenge consists in the connection SOI-waveguides with dimensions in the micro range. These waveguides are part of optical chips and need to be coupled with low loss.

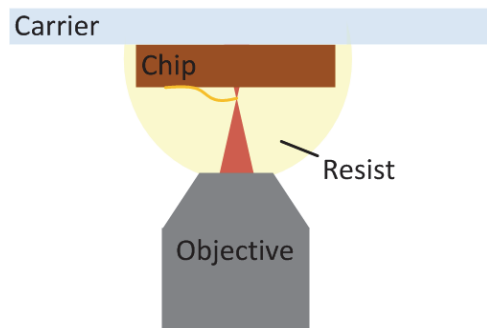


Fig. 1: DiLL, objective is immersed into liquid resist.

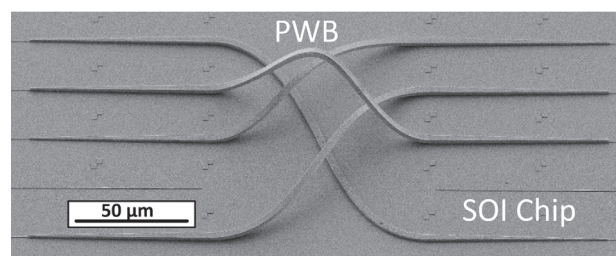


Fig. 2: SEM picture of photonic wire bonds between SOI waveguides for experimental characterization of losses for PWB with different trajectories.

To realize such photonic wire bond the two coupling ports are determined *via* the camera of the lithography system. The design of the PWB is then calculated based on these 3D coordinates of the coupling ports. By moving the focussed laser beam through the calculated volume the PWB is written into the resist. Here, Dip-in Lithography (DiLL) with acrylic based resist is used. The focusing objective is dipped into the liquid resist which allows refractive index matching. Two-photon absorption enables a truly 3D-structure to be written in space as can be seen in fig. 2. The benefits are low coupling losses and optimized wave guiding. The measurements reveal average insertion losses of 1.1 dB for a 70 μm -long and of 0.7 dB for an 80 μm -long taper, both with an uncertainty of ± 0.8 dB (fig. 3).

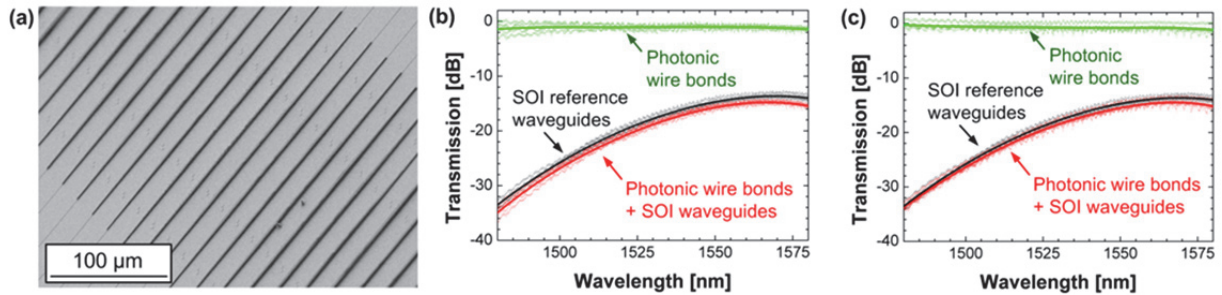


Fig. 3: Reproducibility tests of PWB prototypes linking two SOI waveguides on the same chip. (a) We have fabricated 40 nominally identical wire bonds with connected to different inverse SOI taper structures and investigated the insertion losses. (b) Measured insertion losses for a set of 5 nominally identical PWB connected to 70 μm -long inverse tapers. The insertion loss amounts to (1.1 ± 0.8) dB. (c) Measured insertion losses for a set of 5 nominally identical PWB connected to 80 μm -long inverse tapers. The insertion loss amounts to (0.7 ± 0.8) dB. The results show that PWB structures can be fabricated with reproducible low insertion loss. [2]

3D Polymer Waveguides (H. H. D. Nguyen)

This activity aims on the fabrication of integrated 3D polymer waveguides over large distances of several centimetres which are also of strong interest for intra chip and chip to board connections. In contrast to the above described photonic wire bonds air objectives (fig. 3) are applied. The resulting wave guide is embedded in the solid resist layer. The written pattern is not developed but an additional diffusion process of low-index monomers is necessary for final functionality [3].

In 2013 the work concentrated on the qualification of a specialized resist material for optimal refractive index differences in a confined region of the resist layer. Straight waveguides were generated to learn about resolution and measuring wave guide properties in modified new resist materials on epoxy basis. The resist is negative and the crosslinking is induced by acid (H^+) generated by the 2-photon absorption in the focus volume (Voxel).

In fig. 3a several parallel waveguides are shown from top. In the cross section (fig. 4b) the written waveguide core within the resist layer is shown.

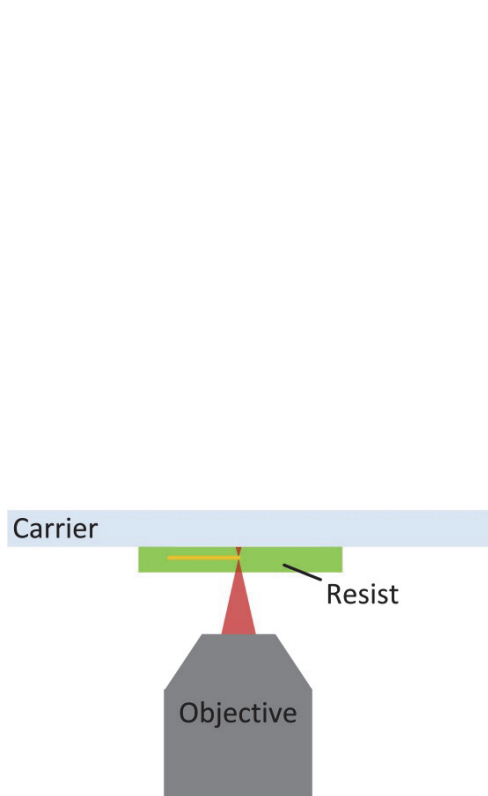


Fig. 3: Principle of 3D laser writing with an air objective in solid resist

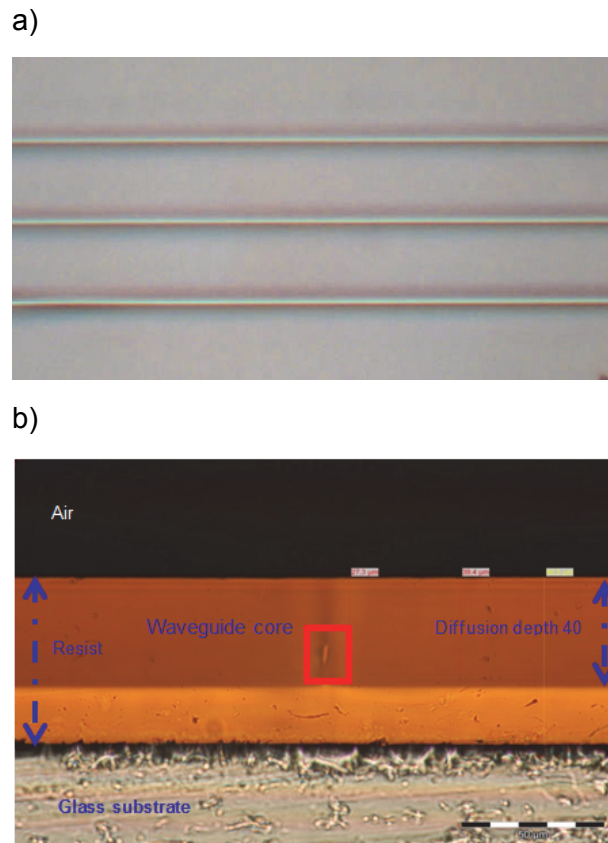


Fig. 4: a) Sample with photopolymer with laser power of 42 mW and writing speed of 200 $\mu\text{m/s}$

b) Cross-section showing the volume voxel where the photopolymerization occurred in the resist layer. Furthermore, the diffusion zone is visible.

High index contrast between the core and the cladding of 0.013 has been achieved. By adjusting the writing speed and laser intensity for the laser writing, it is possible to fabricate symmetric square-shaped waveguides with adjustable core dimensions in the range of 5 μm – 12 μm . The measured near field pattern showed a single-mode Gaussian profile with mode field dimensions of 6.1 μm x 7.5 μm [4].

Strategic Themes

- Multi-method processing for multi-scale structuring and patterning on arbitrary shaped surfaces, e.g. 3D DLW combined with other lithography methods or replication techniques will serve the need for e.g. fluidic devices with surfaces functionalized by nano structures needed in biological analysis systems (lab-on-chip) or cell growing containers. Also optical structures can benefit from these technological developments.
- 3D laser writing is also seen as one of the core technologies in the development of optical interconnects.

Further Collaboration outside KIT in internal projects:

none

References

- [1] N Lindenmann, G Balthasar, D Hillerkuss, R Schmogrow, M Jordan, J Leuthold, W Freude, and C Koos, Photonic wire bonding: a novel concept for chip-scale interconnects, *Optics Express* 20 16 (2012) 17667
- [2] C. Koos, W. Freude, N. Lindenmann; S. Koeber, T. Hoose, M. R. Billah, Three-dimensional two-photon lithography: an enabling technology for photonic wire bonding and multi-chip integration, *Proc. SPIE 8970, Laser 3D Manufacturing*, 897008 (March 6, 2014); doi:10.1117/12.2044327
- [3] D H H Nguyen, K Kaleta, S Hengsbach, U Ostrzinski, K Pfeiffer, U Hollenbach, and J. Mohr, Three-dimensional buried polymer waveguides via femtosecond direct laser writing with two-photon absorption, *Proc. SPIE 9130, Micro-Optics 2014*, 91300N (May 2, 2014)
- [4] Duc H. H. Nguyen, Stefan Hengsbach, Kerstin Kaleta, Ute Ostrzinski, Karl Pfeiffer, Uwe Hollenbach, Jürgen Mohr, Three-dimensional on-board optical Interconnects enabled by femtosecond direct laser writing in polymer, *Proc. DGaO, 115th Annual Conference, 2014* (to be published).

Laser Material Processing (LMP)

**W. Pfleging, H. Besser, N. Kandora, R. Kohler, M. Mangang, J. Pröll,
P. Severloh, P. Smyrek, M. Torge**

The Institute of Applied Materials - Applied Materials Physics (IAM-AWP) offers the following laser material processing technologies in KNMF:

- Short pulsed UV excimer lasers (pulse duration 4-6 ns) operating at 193 nm and 248 nm are suitable for laser structuring and modification processes on micrometer and nanometer scale, especially for thin films and polymers. Within 2014 all excimer laser sources will be up-graded to modern and long-life-time 1000 Hz systems in order to reduce processing times and enhance process stability.
- High power diode laser operating at 940 nm is applied for recently developed laser moulding of micro- and nanostructured components, laser annealing of thin films and laser transmission welding for microstructured and transparent polymers. Within 2014 an upgrade of the diode laser system and workstation is planned in order to enable large area material processing (600 x 600 mm²).
- In 2013 the new ultrafast and high repetition laser machining system has already been used in several KNMF projects and is so far the most deployed laser for the micro- and nanostructuring of multimaterial systems. Three wavelengths (1030nm, 515nm, 343nm), high laser repetition rates (up to 2 MHz), tuneable pulse durations (300 fs-10 ps) and the combination of the ultrafast laser with a tuneable nanosecond fibre laser (pulse length 4 ns-200 ns, wavelength 1064 nm) are unique specifications for laser material processing in one single workstation. In mid of 2013 the workstation was upgraded with a Synchronized Scanner and Motion Module in order to enable high dynamic laser processing (scanner optics and movement of positioning stages at the same time) of structure designs with outer dimensions of up to 300 x 300 mm².
- In 2013 a new highly flexible Laser Induced Breakdown Spectrometry (LIBS) system (FiberLIBSscientific FLSC0105, Fig. 1) with an optical detection spectrum range from 230 nm – 790 nm was installed. LIBS can be used in two ways:
 - 1) any sample can be analysed for elemental and isotopic composition (depth profiling, element mapping, Fig. 2)
 - 2) real-time control of ultrafast laser micromachining processes.Due to the broad spectrum range it is possible to also detect hydrogen (656 nm), oxygen (777nm) and lithium (671 nm) easily. Rapid chemical mapping and depth profiling by LIBS enables quick quality control and identification and characterization of possible defects. A software package based on principal component analysis (PCA) and partial least squares (PLS) regression helps distinguish and identify complex organic and inorganic samples.

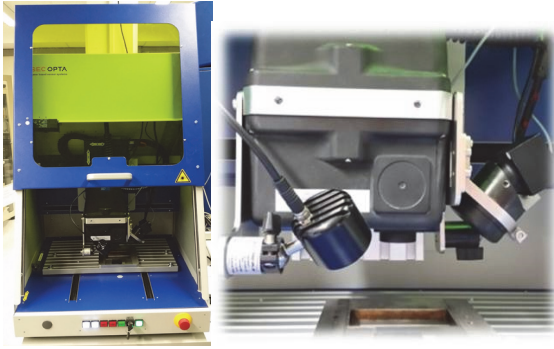


Fig. 1: Experimental set-up of LIBS, overview (left) and detail view of processing chamber (right)

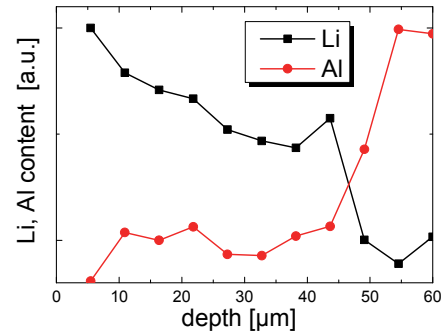


Fig. 2: LIBS depth profile of a NMC electrode (post-mortem analysis)

The in-house research is focused on the development of new laser-assisted processes with special focus on polymers and battery materials. The following R&D activities have been performed in 2013.

Laser moulding for fabrication of micro- and nanostructured components

Laser moulding is a novel polymer moulding process developed in cooperation with KIT-IAM-AWP, KIT-IMT and KIT-LTI. The process to mould thermoplastic polymers has been enhanced to provide a new and highly efficient and flexible method for the fabrication of micro and nano-structures. During testing, moulds with micro- and nanostructures of silicon, glass or nickel were used. PMMA nano gratings with different periods down to 195 nm were produced for the realization of organic semiconductor distributed feedback (DFB) laser sources. Another success in 2013 was the realization of SERS (Surface-enhanced Raman scattering) substrates consisting of arrays of metal coated cyclic olefin copolymer nanopillars (diameter sizes ranging from 60 nm to 260 nm and pillar gaps down to 10 nm).

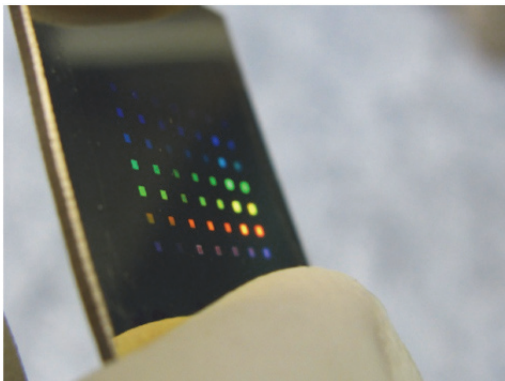


Fig. 1: Nanogratings in COC fabricated via Laser Moulding (IMT/IAM-AWP)

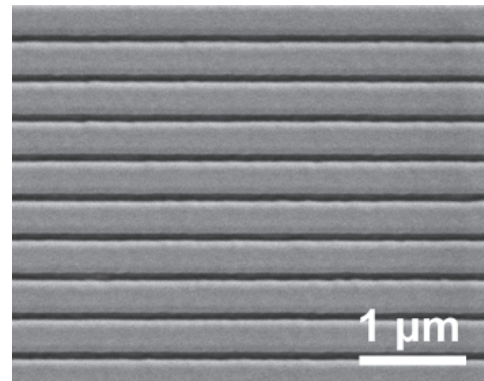


Fig. 2: SEM image of grating structures (400 nm) fabricated by Laser Moulding

Laser generation of capillary structures

For lithium-ion cells with pouch cell geometries (electrode size: 5x5 cm²) as well as for smaller battery sizes (electrode diameter: 12 mm) a laser patterning process for electrodes has been developed in order to significantly improve the lithium-ion battery performance for high charging and discharging currents (charging/discharging time ≤ 1 hour). The capacity

retention and cell life-time is significantly improved for cells with laser modified electrodes in comparison to unmodified electrodes (e.g., lithium manganese oxide (LMO), Fig. 3). Besides an enhanced electrolyte wetting behaviour of laser modified electrodes, a laser-generated increase in active surface area significantly contributes to an improved battery performance which was assigned to enhanced Li-ion diffusion kinetics. The laser-assisted generation of capillary microstructures (Fig. 4) in composite electrode materials (LMO) made of binder, conductive agents and active material was investigated using cost efficient short pulse fiber laser radiation with a wavelength of 1064 nm and pulse duration of 200 ns. The ablation process was realized via polymer (binder) vaporization without thermal impact on the active material. The key parameters (e.g., aspect ratio, structure size, surface topography) for most efficient electrolyte wetting behaviour were identified. With this approach, a cost efficient battery manufacturing for long life-time cells is possible.

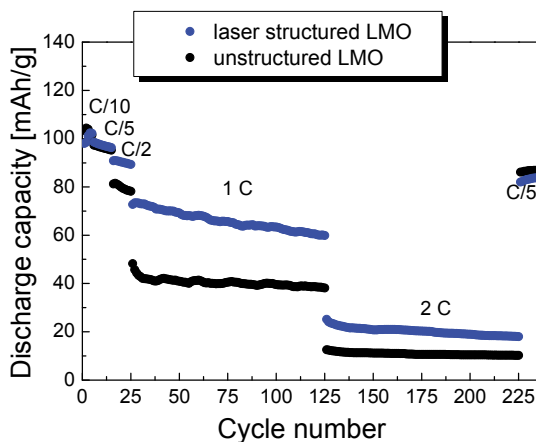


Fig. 3: Specific discharge capacities of LMO pouch cells for cells with structured and unstructured electrodes.

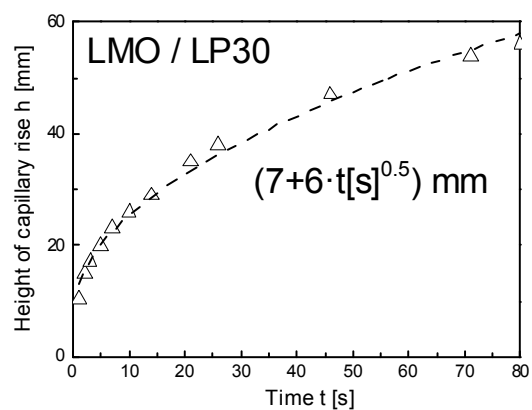


Fig. 4: Height of capillary rise as function of the wetting time for laser-structured LMO cathodes (capillary diameter 72 μm) using LP30 electrolyte.

fs-laser structuring of LiFePO₄ cathode material

The influence of the laser pulse width for patterning of composite battery materials was studied in more detail. For this purpose, laser processing of LiFePO₄ with femtosecond, picosecond and nanosecond laser radiation has been performed focusing on the optimization of ablation efficiency and processing speed. The laser pulse duration has been varied in the range of 200 ns to 350 fs. Droplet formation on the surface of LiFePO₄ composite material could be reduced with decreasing pulse length indicating a decrease of thermal impact using ultrafast laser radiation. For laser pulse durations of 350 fs and 10 ps the ablation depth could be increased by a factor of 2.6 (Fig. 5). Galvanostatic cell tests using laser structured LiFePO₄ electrodes show a significant improvement in specific capacity for laser structured electrodes whereby pulse lengths in the fs-regime have been applied for the structuring process (Fig. 6).

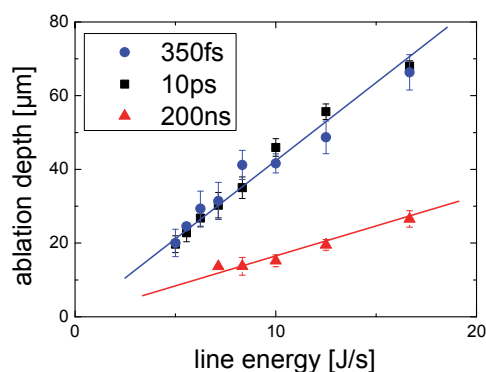


Fig. 5: Ablation depth of LiFePO_4 as function of laser line energy for different laser pulse lengths (repetition rate 200 kHz, average laser power 10 W)

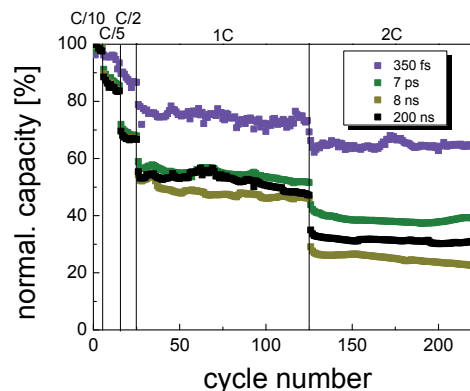


Fig. 6: Normalized discharge capacity as function of cycle number for LiFePO_4 cells with structured electrodes

Strategic Themes

The Laser Materials Processing Group (IAM-AWP) is specialised in laser processes for surface functionalization and micro-/nano-structuring. For the application area of “lithium-ion-batteries” the complete battery process chain, from electrode coating, laser processing, laser structuring, laser cutting, and through to battery assembly and electrochemical battery characterisation has been established. An outstanding expertise in the field of advanced laser processes for energy storage materials has been developed. Laser surface structuring of electrode materials enables a significant improvement of battery performance (battery life-time, enhanced cycle retention at high charging/discharging currents) due to a significant improvement of electrolyte wetting of electrode materials as well as an enhancement of lithium-ion diffusion properties. For this pioneering work of further developing the lithium-ion pouch cell manufacturing process, the renowned “SPIE 2014 Green Photonics Award” has been awarded to the Laser Materials Processing Group (IAM-AWP). In cooperation with external partners new materials, laser printing technologies and battery degradation mechanisms are currently under investigation. External partners are: Manz Automation AG (laser cutting), Sihl GmbH (separator material), Princeton University (Correlation of surface topography and mechanical properties during electrochemical cycling), Naval Research Laboratory Washington (Laser-printed electrodes / all-solid state microbatteries), KIST – Korean Institute of Science and Technology (study of degradation mechanisms; new electrode materials).

The combination of laser processes (3D structuring, surface modification, transmission welding) and print technologies is rather new. In October 2012 a European project (EU-SMARTLAM-Project, FP7, Smart Production of Microsystems based on laminated polymer films) was launched to investigate the combination of laser and printing technologies for the development of polymeric micro devices. Within SMARTLAM, the Laser Materials Processing Group (IAM-AWP) is responsible for the integration and development of laser processing technologies. External partners within the consortium are: Micrux AG (microfluidic chips), DesignLED (LED-devices), PROFACTOR (product development), Neotech Services (AerosolJet Technology), FhG-IPA (micro production technologies).

Further Collaboration outside KIT in internal projects:

Paul Scherrer Institut (PSI), University of Birmingham, University of Cardiff, IREPA LASER, VITO - Lasercentrum Vlaanderen, ATL Lasertechnik GmbH, Coherent Inc., Daimler AG

References

- [1] J. Pröll, P.G. Weidler, R. Kohler, A. Mangang, S. Heissler, H.J. Seifert, W. Pfleging, W. Comparative studies of laser annealing technique and furnace annealing by X-ray diffraction and Raman analysis of lithium manganese oxide thin films for lithium-ion batteries, *Thin Solid Films* 531 (2013) 160-171
- [2] R. Kohler, J. Proell, M. Bruns, S. Ulrich, H.J. Seifert, W. Pfleging, Conical surface structures on model thin-film electrodes and tape-cast electrode materials for lithium-ion batteries, *Applied Physics A* 12 (1) (2013) 77-85
- [3] R. Kohler, J. Proell, M. Bruns, T. Scherer, H.J. Seifert, W. Pfleging, Laser-induced self-organizing surface structures on cathode materials for lithium-ion batteries, *SPIE Vol. 8608* (2013) 860806- 1-6
- [4] J. Proell, R. Kohler, M. Bruns, V. Oberst, P.G. Weidler, S. Heißler C. Kübel, T. Scherer, R. Prang, H.J. Seifert, W. Pfleging, Thin film passivation of laser generated 3D micro patterns in lithium manganese oxide cathodes, *SPIE Vol. 8608* (2013) 860807- 1-10
- [5] A. Singh, W. Pfleging, M. Beiser, C. Khan Malek, Transparent thin thermoplastic biochip by injection-moulding and laser transmission welding, *Microsystem Technologies* 19 (2013) 445–453
- [6] W. Pfleging, R. Kohler, I. Südmeyer, M. Rohde, "Laser Micro and Nano Processing of Metals, Ceramics, and Polymers" in *Laser-Assisted Fabrication of Materials*, Jyotsna Dutta Majumdar and Indranil Manna (Eds.), Springer-Verlag ISBN 3642283594 (2013) 319-374
- [7] M. Dickerhof, D. Kimmig, S. Scholz, C. Wögerer, R. Adamietz, W. Pfleging, An additive manufacturing and e-printing based approach for flexible scalable manufacturing of Microsystems, In: Azcárate, Sabino (Ed.), Singapore: Research Publishing (2013) 288-291, DOI 10.3850/978-981-07-7247-5 407
- [8] W. Pfleging, R. Kohler, J. Pröll, Elektrodenmaterial für Lithium-Ionen-Batterien und Verfahren zu seiner Herstellung, Patentschrift, DE 10 2011 120 893 B3 2013.03.07
- [9] W. Pfleging, O. Baldus, A. Baldini, Method for joining plastic workpieces, EP1758729 B1

Injection moulding (μ IM)

**Volker Piotter, Klaus Plewa, Jochen Heneka, Elvira Honza
Alexander Klein, Tobias Müller**

Injection moulding offers decisive advantages for the manufacturing of nano- and micro components, in particular the following benefits should be mentioned:

- a wide range of processible polymers, metals, and ceramics
- very high economic efficiency in medium and large-scale fabrication
- complex shaped 3D parts (singular items or large bodies + nanostructures)

The latter might be singular items or large bodies with nano- or microstructures on the surface, [1]. In both cases very high geometric accuracies and smallest tolerances can be achieved using e.g. LIGA-fabricated mould inserts [2]. In addition to the replication of polymers, powder injection moulding (MicroPIM) allows for the micro fabrication of components made of a large variety of metals or ceramics [3, 4]. Having reached a reliable status, further special variants like two-component injection moulding and in-mould-labelling offer reduced mounting expenditures and production of multi-functional devices.

Polymeric fractal scaffolds in biotechnology

The main task of this project was to validate the use of fractal surfaces to promote cell motility and to achieve controlled growth. To obtain statistically significant results, application of replicative processes for obtaining series of identical scaffolds was necessary.

For this purpose a production chain starting with polymer masters made by stereolithographic methods (AM: Additive Manufacturing) which had to be replicated by galvanofarming was developed. The metallic structures were used as mould inserts for polymer replication by injection moulding. Some hundred replicas made of PMMA and PC have been produced. For each step the suitable materials and appropriate parameters had to be determined.

The project had been performed in close cooperation with the IMT (hot embossing and galvanofarming). Although a standard parameter set had been used the project opened a new method to obtain mould inserts by additive manufacturing. Thus it corresponded to the approaches for combining IM and AM (see below "benchmarking of different micro-injection moulding machine lay-outs).

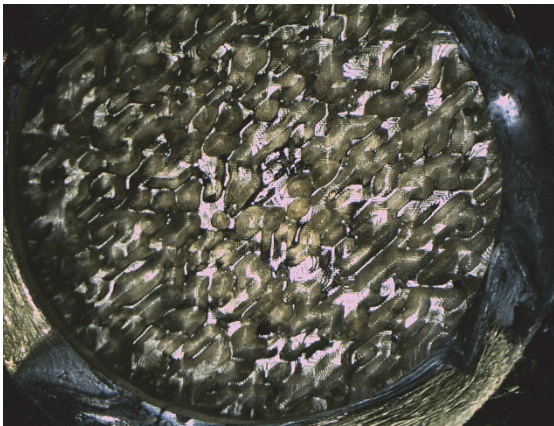


Fig. 1: Microscopic view of the mold insert used for replication by injection molding

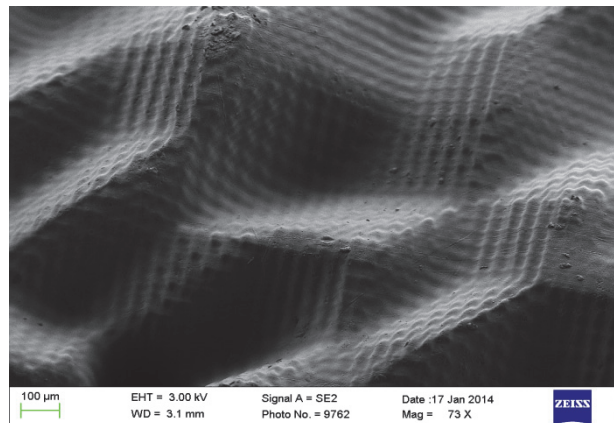


Fig. 2: SEM figure of polymer part (PMMA) with randomly shaped structures

Bio-inspired nanostructured components replicated by Micro Injection (Compression) Moulding

The goal of this project was to establish the replication of bulk-volume devices endowed with nano-structured surfaces. Ommatidia (moth-eye) structures had been chosen as demonstrator for which the related mould inserts were made by Focused Ion Beam (FIB).

Replication was performed by either unaltered micro-injection moulding or injection compression moulding (MicroICM). Both variants were additionally featured with tool evacuation and variothermal temperization.

The project verified the capability of MicroI(C)M to replicate features far in the submicron range even if the structure centerline is not in parallel with the direction of demoulding. Additionally, the utilisation of FIB-made mould inserts has been demonstrated.

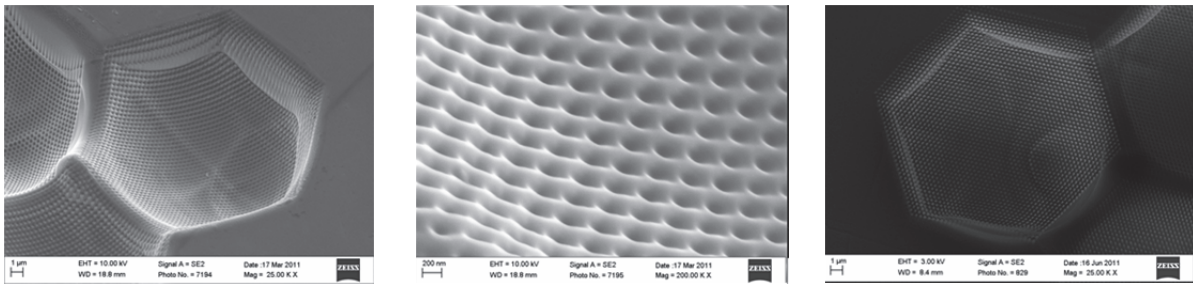


Fig. 3: SEM figures of a FIB-made mould insert (left) and polymer part (PMMA) with nano-sized moth-eye structures

Micro Powder Injection Moulding (MicroPIM)

The range of processible materials had been extended to now cover 440C steel with outstanding high hardness of up to 62HRC. Such values, of course, can only be achieved by a subsequent hardening step. Thermal treatment (precipitation hardening) was also applied for the more common 17-4PH steel which led to an increase in tensile strength from 690 MPa up to ca. 1000 MPa.

Benchmarking of different Micro Injection Moulding Machine Lay-outs

Injection moulding machines specially designed for micro replication first entered the market approximately 15 years ago. Recently however, the trend is towards more flexible units which cover an extended range of shot volumes and clamping forces. For example, the Microsystem 50 machine design which is used at KIT has been superseded by the so-called MicroPower machine series which operates with higher clamping forces and allows the mounting of either micro or conventional injection units.

The question arose if these new generation machines can compete with the former ones designed for micro replication performance without any compromises. To investigate this matter, a moulding series had been carried out on both Microsystem 50 (at KIT) and MicroPower (at the manufacturer) units using the same materials and micro sample test tools. The shot volume and injection parameters had been defined as well as the achieved material densities. Final examination is currently running, nevertheless, it turned out that the Microsystem design achieves better results for all materials tested. It appears that a lower micro-replication performance is the price for enhanced operating flexibility.

Strategic Themes

Additive Micro Manufacturing of Metals and Ceramics

To complete the entire chain from prototyping through to small, medium, and large series manufacturing, it is the aim to offer future customers a “full service-package” for metal and ceramic products. For this purpose special powder-filled polymers have to be developed which can be processed by AM shaping equipment but further allow for subsequent debinding and sintering. Additive manufacturing technologies need to be improved to enable structure sizes for metals and ceramics below 20µm to be obtained. This requires the procurement of a 3D-LCM printer with special-focused lenses, and the creation of a data base to enable the correct choice of material and process capabilities in the context of the requested piece numbers. This will enable the determination of the optimal solution for particular customer demands.

Hybrid Additive and Injection Moulding Manufacturing

Following the goal to establish a process for high-efficient manufacturing of individualized micro parts the advantages of both technologies, i.e. the geometrical flexibility and individual design capability of additive manufacturing with the high economic efficiency of Micro Injection Moulding shall be combined. Required AM-systems have to be purchased. The challenge is one step higher as the one described above: Binder systems suitable for both shaping processes (AM+IM) have to be developed. Further on, subsequent co-debinding and co-sintering procedures need to be developed. Currently, application for third-party funding for set-up of pilot line and production of demonstrators is under preparation.

Further Collaboration outside KIT in internal projects:

HGF-internal project: Development of Ceramic Nozzles for Femtosecond Laser Applications

HGF partner: Center for Free-Electron Laser Science at DESY (Hamburg)

Development of ceramic nozzles to be used in experiments with X-ray free-electron lasers. Such nozzles are required to generate a strongly focused liquid jet of the analysis sample perpendicular to the beam of intense femtosecond pulses of X-rays at the LCLS. KIT will bring in its knowledge on manufacturing ceramic micro components [2, 3] to provide reproducibly accurate nozzles.

References

[1] Y Nazirizadeh, K Plewa et al. „Sensitivity optimization of injection-molded photonic crystal slabs for biosensing applications”, OPTICAL MATERIALS EXPRESS: Vol. 3, No. 5 (2013) 556-565.

[2] V Piotter, E. Honza, A. Klein, T. Mueller, K. Plewa, J. Prokop „Replication Processes for Metal and Ceramic Micro Parts”, Proc HARMNST Conference, Berlin, (2013) 240-241, and Microsyst Technol, DOI 10.1007/s00542-013-2045-z.

[3] V. Piotter, E. Honza, A. Klein, T. Mueller, K. Plewa: High-Grade Micro Components Produced by Variants of Powder Injection Moulding; Proc. of Euro PM 2013, Gothenburg, published by EPMA, ISBN 978-1-899072-41-5, Vol. 1 (2013) 293-298.

[4] V Piotter, E Honza, A Klein, T Mueller, K Plewa „Examinations on the production of micro and precision PIM-parts”, Proc 2013 Int Conference on Powder Metallurgy & Particulate Materials, Chicago, published by MPIF, ISBN 978-0-9853397-3-9 (2013) on CD.

Hot Embossing/Compression Molding (HE)

Matthias Worgull, Alexander Kolew

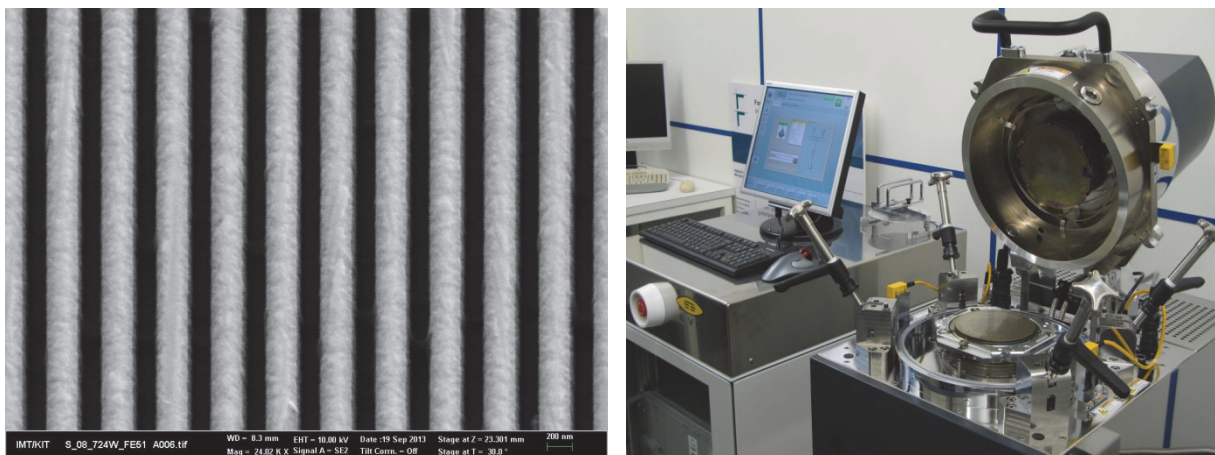
The laboratory for micro replication comprises different technologies, for the surface structuring of thermoplastics and other mouldable materials, like hot embossing, thermal nanoimprint, UV nanoimprint, microthermoforming, hot pulling, and related technologies. Most of the processes offered within KNMF have been invented within the department so user enquiries requiring modifications and adaptation of the technologies can be addressed. We are continuously developing and improving new processing variants of embossing technologies as well as alternative materials which enable us to accommodate challenging user needs for replication of micro and nano structures [1]

During 2013 the hot embossing equipment was moved into a new laboratory which allows a better coordination and interaction of the different hot embossing systems. By this strongly interconnected processes like surface patterning by hot embossing, film stretching by micro thermoforming and packaging by thermal bonding processes can be performed within a short time frame and limitations arising from materials transfer and temperature drops are also minimised.

Nanoimprint Systems

The recently installed nanoimprint system EVG510 (Fig. 1) with two structuring units was validated for small-scale nano-imprint lithography on silicon wafers. This process is the base for the combination of thermal surface structuring of thin thermoplastic films at wafer scale with the surface structuring of UV-curing photoresist materials. Compared to standard Nanoimprint systems the advanced technology allows applying pressure during UV curing.

Using the nanoimprint equipment it has been possible to demonstrate the coating of polymer on silicon wafer surfaces with thickness between a few tens of nanometre up to several tens of microns, whereas hot embossing is more suitable for layer thickness from several tens of micron upwards. Current research has enabled the successful replication of nanostructures with structures sizes from several tens of nanometres.



a) SEM image of a thermal nano imprint of PMMA done with the EVG 510 Nanoimprint machine

b) open thermal unit for moulding nanostructures on the wafer scale

Fig. 1: EVG 510 Nanoimprint machine with thermal and UV Curing unit

New Materials: Hot Embossing of pure Teflon PTFE

The hot embossing system was adapted to high temperature thermal micro replication in order to assist with a user request to surface structure pure Teflon PTFE. By use of nickel tools with high aspect ratio PTFE a variety of patterns were structured using a variation of process parameters and conditions for each nickel tool. Whereas PTFE could not be replicated by injection moulding or extrusion processes hot embossing is now capable to produce micro feature on this highly chemically resistant material. [2]

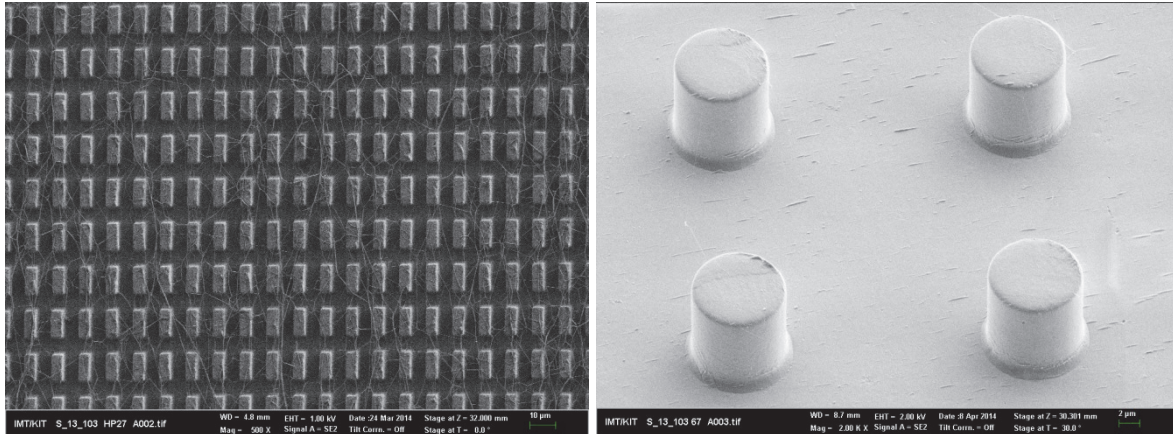


Fig. 2: (P. Thanh) Hot **embossed** microstructures in PTFE with different patterns by process variation

New Materials: Hot Embossing of Shape Memory Polymers

In addition to the improved functionality of surface structured parts by pattern design further valorization can be given by smart materials and functional materials.[3] Shape memory polymers are such materials and offer not only new applications by surface structuring but also allow for a shape change from a temporary shape into a predefined permanent shape. The shape memory effect can be used in micro-systems for demoulding otherwise non-demouldable microstructures by self-demoulding tools. This effect can also be applied locally by local heating using electric wires or laser heating. The utilisation of this principle has also been demonstrated for switching optical diffractive structures as shown in fig. 3.

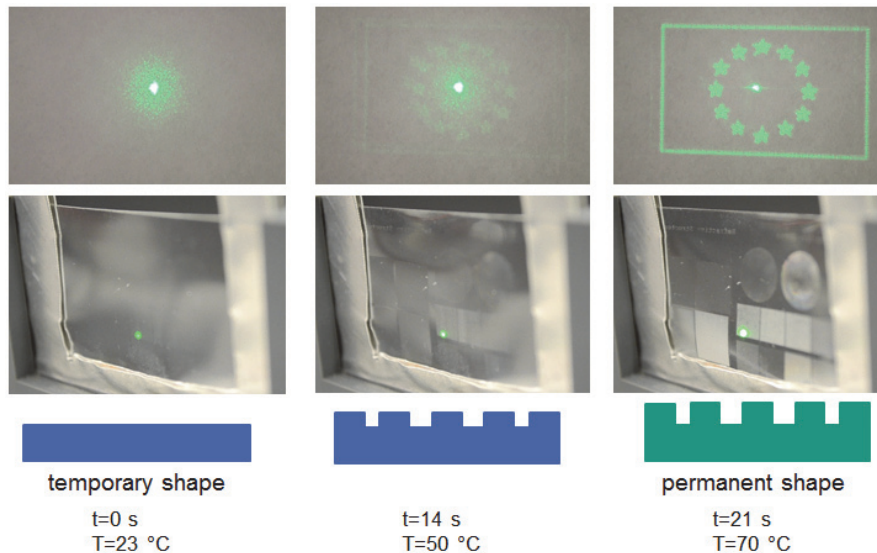


Fig. 3: Switching of diffractive optical structures using shape memory polymers. Due to the switch between two states of the polymer diffractive structures appears if the temperature increases. In a first step the permanent structure (optical grating) is embossed at high moulding temperature. In a second step the temporary structure is embossed at lower temperature (in this case a polished plate – the structure disappear). This state remains at room temperature. If finally the temperature increases again the permanent structure appear and the optical grating is visible.

Technology Improvements: Hot Pulling Process

Hot embossing can be modified to overcome limitations of replicating high aspect ratio structures by utilising the adhesive characteristics of molten polymers. With the hot pulling process (fig.) high aspect ratio nano- and micro-structures were achieved which cannot be replicated by conventional replication processes. The main difference between the hot pulling and classical hot embossing processes are in the applied temperature windows and tool requirements. In hot pulling; instead of solidifying the material before demoulding by cooling the tool, the temperature of the mould insert is maintained above the material's softening temperature. While separating the mould insert, the viscous material elongates due to adhesion to the inner sidewalls of the cavities. Hence, roughness and even undercuts of the cavities of the mould insert are beneficial for high aspect ratios. Since demoulding forces are required in hot pulling, higher stiction can be achieved e.g. by etching the sidewalls of the mould insert's cavities [4].

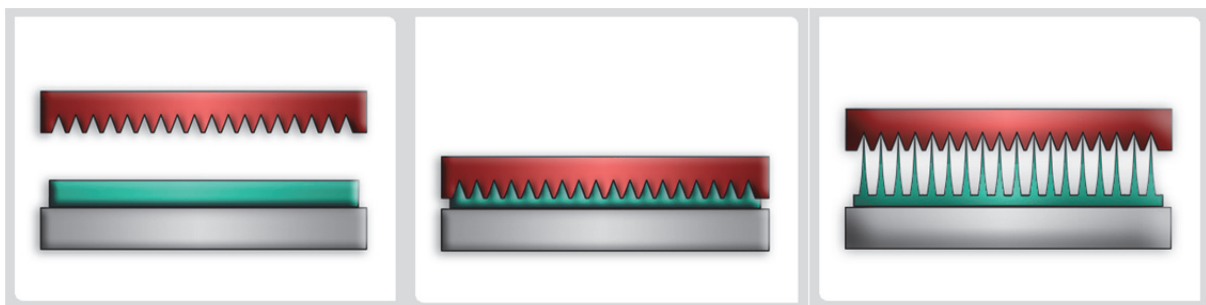


Fig. 4: Scheme of hot pulling of microstructures using the modified hot embossing process. The process bases on a pulling of a molten thermoplastic polymer at a temperature above the glass transition temperature.

Using the process of hot pulling, polymer surfaces with hairs in the size range of 100-300 nm were fabricated. The so called “nanofur” (Figure 5) shows superhydrophobic and oleophilic behaviour which will be investigated further for applications in water-oil separation [5].

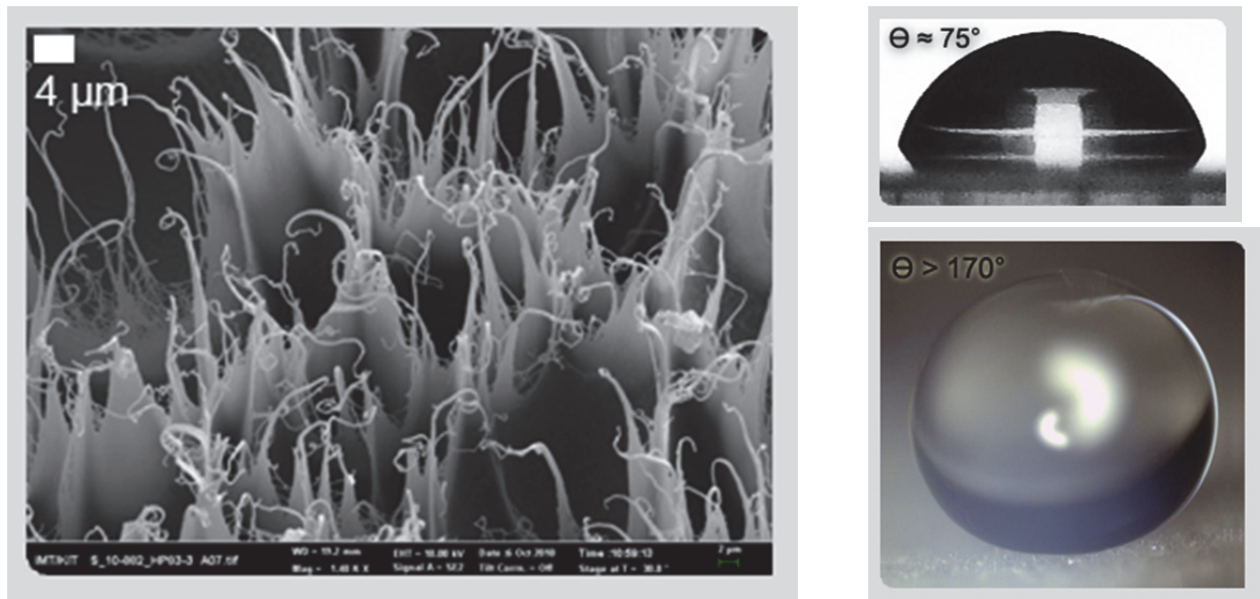


Fig. 5: Hot pulled microstructures in PC and the respective wetting behaviour. With the so called “nano fur” the contact angle increases significant. In this example the contact angle for Polycarbonate increase form intrinsic 75° to 170° .

Technology Improvements: Hierarchical Hot Embossing

Hot embossing and pulling techniques can be combined to allow the fabrication of hierarchical micro- and nano-structures (Figure 6). By utilizing demoulding forces we can replicate nanopillars with high aspect ratio (AR of 10) and small diameters (200 nm). Furthermore, we draw a dense nanofur with either defined or random design. Introducing an electromechanical sensor system we have subsequently fabricated a threefold hierarchical structure. Using these replication techniques tiny hairs for bio-inspired designs can be realized with short cycle times and high scalability [6].

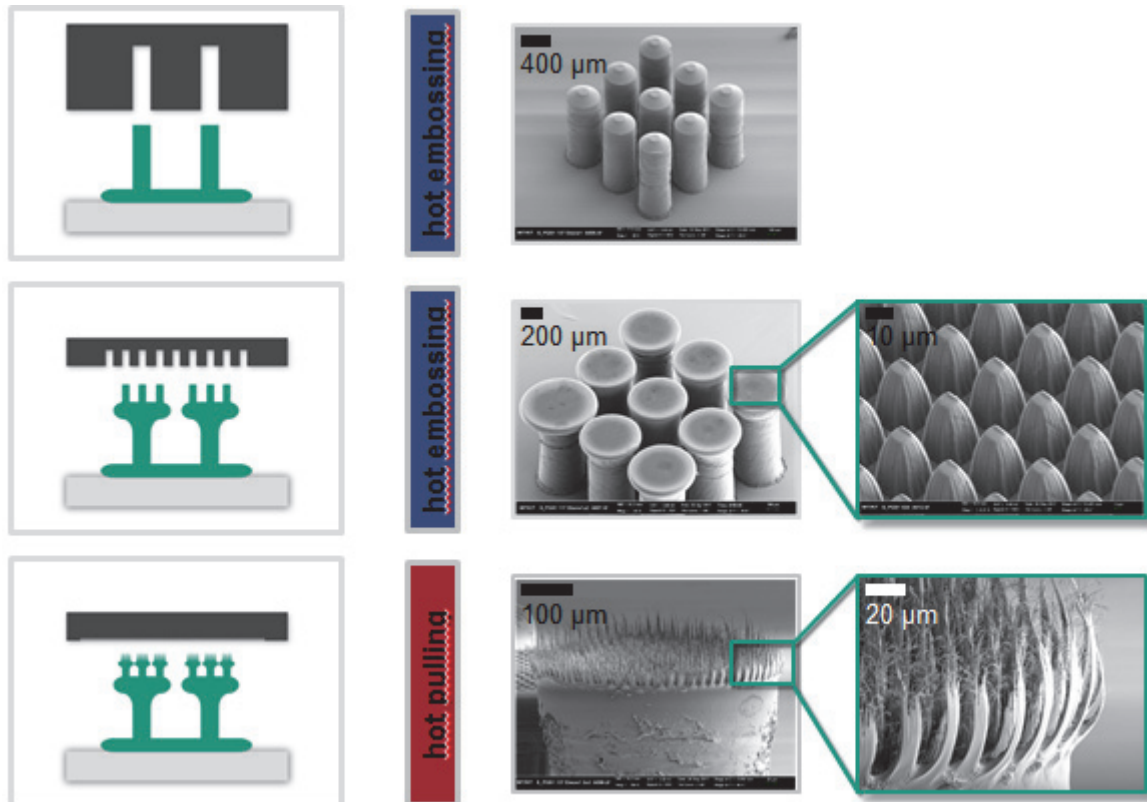


Fig. 6: (M. Röhrig) Fabrication of three layer hierarchical structures by a combination of hot embossing and hot pulling. In a first step the first layer of structures is replicated by embossing. In a second step a second layer of structures is embossed on top of layer one. The third layer on top of layer two was achieved by hot pulling. By the hot pulling process the structures of layer two merges to the structures of layer three.

Strategic Themes

The improvement of the micro moulding equipment for hot embossing, micro-thermoforming and nanoimprinting offers unique technologies for a large range of applications. The installation Hot Embossing/Compression Moulding [HE] at KNMF is worldwide outstanding in terms of maximum moulding temperatures (up to 650 °C), moulding areas (up to 250 mm diameter), moulding forces (up to 1000 kN), lowest hot embossing cycle times (a few minutes). HE also offers the highest flexibility, with double sided moulding, through hole fabrication, multi component hot embossing, and widest process combinations of hot embossing with microthermoforming as well as thermal nanoimprint with UV-nanoimprint.

With these replication technologies additional functionality can be integrated into micro systems either by functionalization by defined surface structures e.g. for change of wetting behaviour and adhesion or by structuring of intrinsic functional materials like shape memory polymers.

References

- [1] A. Kolew, M. Heilig, M. Schneider, D. Münch, R. Ezzat, N. Schneider, M. Worgull, Hot embossing of transparent high aspect ratio micro parts, *Microsystem Technologies*, 2014, Volume 20, Issue 10, Page 1967-1973
- [2] M. Worgull, M. Schneider, N. Schneider, A. Kolew, *Advances In Material Variety For Hot Embossing*, NNT conference, 2013, Barcelona

- [3] M. Worgull, M. Schneider, M. Röhrig, T. Meier, M. Heilig, A. Kolew, K. Feit, H. Hölscher, J. Leuthold, Hot embossing and thermoforming of biodegradable three-dimensional wood structures, *RSC Adv.*, 2013, 3, 20060-20064,
- [4] M. Röhrig, M. Schneider, G. Etienne, F. Oulhadj, F. Pfannes, A. Kolew, M. Worgull, H. Hölscher, Hot pulling and embossing of hierarchical nano- and micro-structures, *J. Micromech. Microeng.* 2013, 23, 105014
- [5] M. Kavalenka, A. Hopf, M. Schneider, M. Worgull, H. Hölscher, Wood-based microhaired superhydrophobic and underwater superoleophobic surfaces for oil/water separation, *RSC Adv.*, 2014, 4, 31079-31083
- [6] M. Röhrig, M. Mail, M. Schneider, H. Louvin, A. Hopf, T. Schimmel, M. Worgull, H. Hölscher, Nanofur for Biomimetic Applications, *Adv. Mater. Interfaces*, 2014, 1: 1300083

Focused Ion Beam (FIB)

**Torsten Scherer, Robby Prang, Aaron Kobler, Mohammed Hamed,
Kiran Chakravadhanula, Christian Kübel**

A FEI Strata 400S DualBeam FIB is operated in KNMF by the Institute of Nanotechnology (INT) as a universal tool for nanostructure characterization and processing. In addition to structural characterization by in plane- and cross-sectional analysis using SEM and EDX as well as 3D imaging by slice&view techniques, the FIB is used extensively for nanostructuring of materials, especially for high-quality TEM sample preparation in combination with the newly installed Fischione NanoMill, which is essential for high-end structural characterization in the TEM. Furthermore, in-house developments focus on establishing mechanical testing of nanomaterials using various straining and bending geometries inside the FIB and on optimizing the sample preparation for in-situ mechanical and electrical testing inside the TEM.

A new Zeiss Auriga 60 DualBeam FIB has been ordered as a new high-end addition to the Strata 400S and has been installed beginning of 2014. It provides a high resolution of 2.5 nm at 30KV for FIB processing and can also be operated at low voltages of 500V to minimize surface damage. It is equipped with an EDX and EBSD detector as well as a high-vacuum transfer chamber for inert transfer between a sputter system, the FIB and a glove box.

A selection of the in-house R&D activities performed in 2013 is described below.

Advanced Electron Microscopy to Characterize the Hierarchical Three-Dimensional Morphology of Porous Solids

Hierarchical porous silica in monolithic form is used in chromatography and heterogeneous catalysis as an alternative to other fixed bed structures. Their distinctly bimodal pore size distribution is essential to the performance of silica monoliths as solid support. A continuous network of macropores (~2 μm) enables liquid transport at high flow rates without necessitating high pressures, while the nanometre-sized mesopores provide the high surface area for sufficient contact between chemicals and the stationary phase (for separation or catalysis) immobilized on the fixed bed.

Beyond a superficial characterization of the two pore categories, the monolith's disordered pore structure remained largely unknown until recently, when the macropore space has been accessed by confocal laser scanning microscopy. For the much smaller mesopores nothing beyond pore size data from bulk methods, e.g. mercury intrusion porosimetry and nitrogen physisorption is available at present. However, an accurate and quantitative morphological characterization would be needed to tailor the morphological properties of mesoporous adsorbents for their intended use.

Here we demonstrate the reconstruction and characterization of the complete morphology of a silica monolith, from macropores to mesopores, by combining FIB slice&view techniques and high-resolution STEM tomography. Based on the three-dimensional reconstruction we performed a comprehensive statistical analysis to extract key structural parameters relevant to mass transport at the macropore and mesopore level. The reconstructed model is also the starting point for simulations of flow, mass transport, sorption and reaction which aim at a fundamental understanding of the morphology-transport relationships of hierarchically structured, disordered materials as a basis to improve morphological features responsible for separation efficiency and catalytic activity. [1]

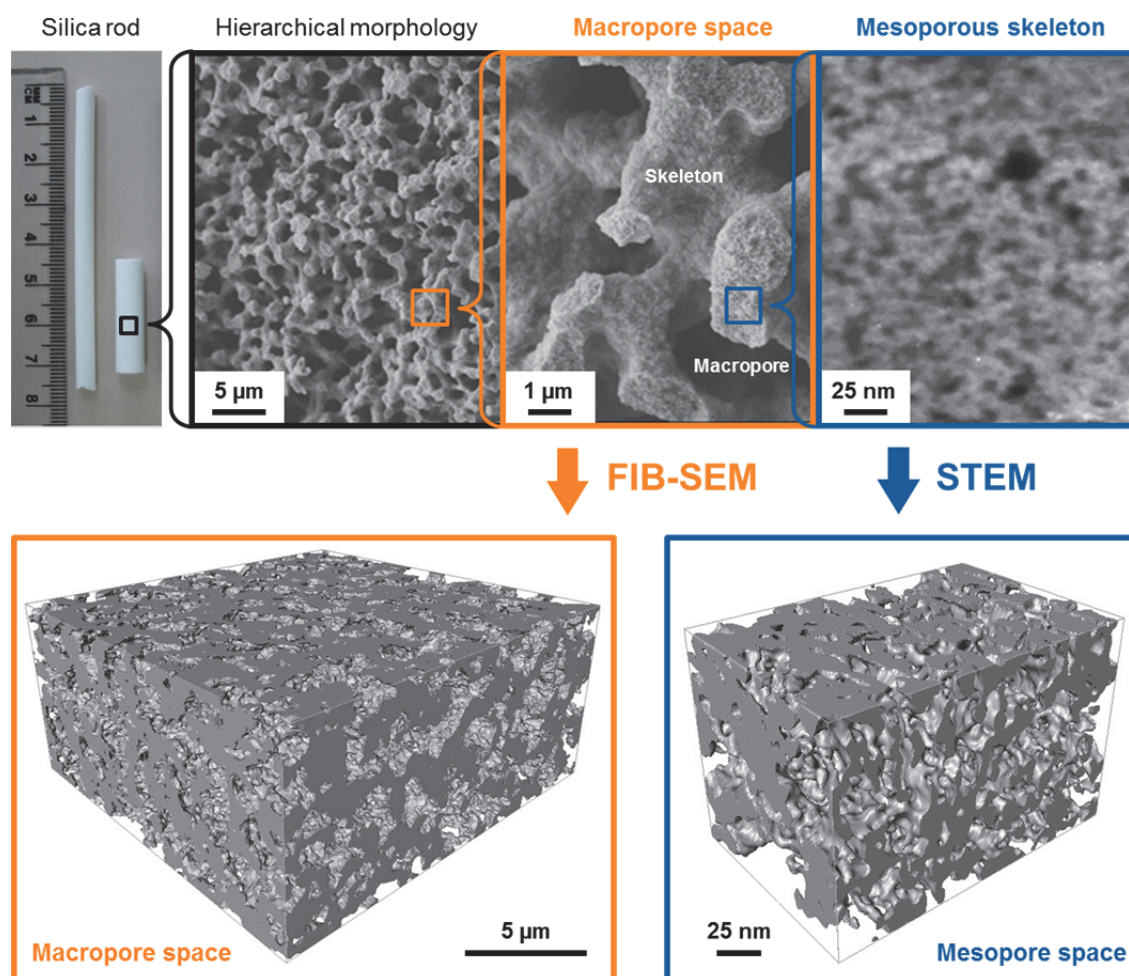


Fig. 1: Characterization of the hierarchical structure combining FIB-SEM and HAADF-STEM tomographic techniques to build a 3D model.

Preparation of Solid State Batteries for In-situ TEM Investigations

Lithium ion batteries (LIBs) are used as secondary energy/power sources for portable electronic devices and in transportation. However, the low energy density of current state-of-the-art LIBs with layered Li transition metal oxides as cathode, such as LiCoO_2 or LiFePO_4 , limits extensive practical applications. Alternative battery systems are researched widely and recently the principle of a secondary battery based on a fluoride ion shuttle to replace lithium has been demonstrated, which could theoretically provide high energy densities. Understanding the design principles and optimization of these new battery systems requires a good knowledge of the structure and the basic processes in these materials. To directly see and understand the processes during electrochemical cycling of battery systems, in-situ TEM is one of the few techniques able to provide direct structural and compositional information at the nanoscale. However, preparation of the necessary nano- to micron sized battery setups and contacting them in the TEM is challenging.

We have been optimizing the FIB preparation for in-situ electrochemical studies of solid state batteries in the TEM. For a $\text{Cu/La}_{0.1}\text{Ba}_{0.9}\text{F}_{2.9}/\text{MgF}_2$ fluoride battery system (Fig. 2), we have been able to produce the first battery setup that could be (partially) reversibly charged (Fig. 3) and discharged in the TEM and the structural changes could be followed.

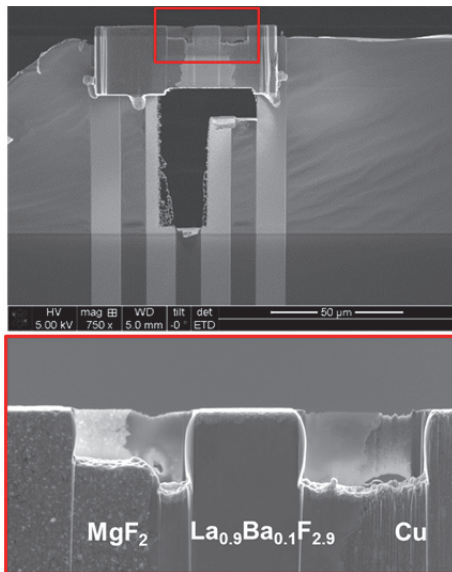


Fig. 2: SEM image of the electrically contacted FIB lamella of a Cu/La_{0.9}Ba_{0.1}F_{2.9}/MgF₂ battery.

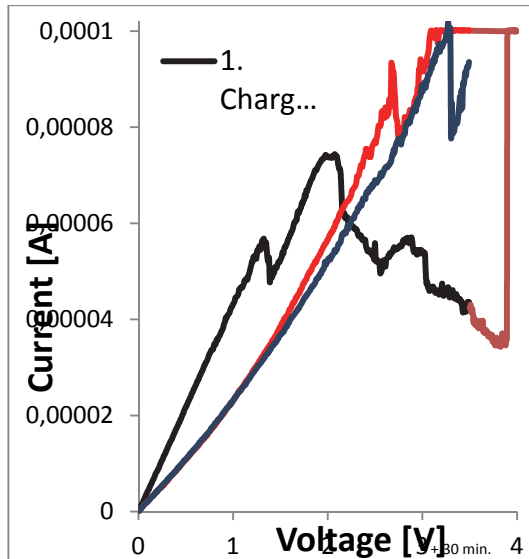


Fig. 3: Charging and discharging of the battery inside the TEM.

Creep cavitation studies in 9Cr martensitic steel for power plants

Creep rupture of materials under service conditions heavily depends on the formation and growth of cavities, motivating the characterization and modelling of the cavitation process scientifically as well as from an industrial point of view. In the present work, creep cavities are investigated in P91 steel creep loaded for up to 10000 hours at 650°C. FIB-SEM techniques have been employed to investigate the cavities in detail. Size distributions from 2D investigations have been converted into 3D distributions and compared to actual 3D results obtained by FIB slice&view reconstruction. The tendency of interlinking in creep cavities to form cracks is characterized using the nearest neighbour distances. Another focus is laid on the interaction of the cavities on laves phases and M₂₃C₆ precipitates, identified with EDX and BSE. It is shown that transverse grain boundaries, laves phase and grain boundary triple points are found to be preferential site for cavity nucleation.

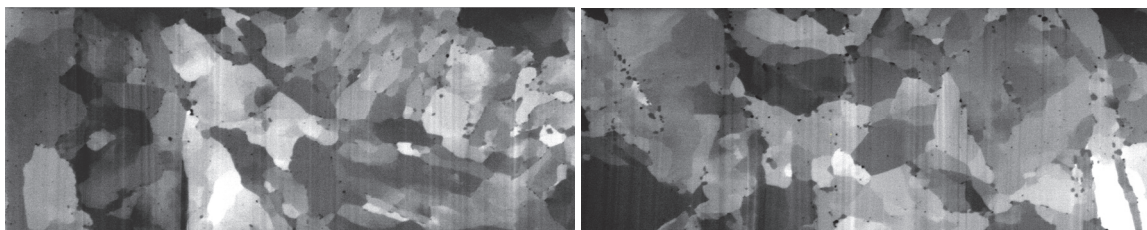


Fig. 4: SEM cross-section images of a slice&view series illustrating the grain, precipitate and pore structure of the steel sample.

Strategic Themes

A long-term strategic development for FIB together with TEM, HIM, XPS, ToF-SIMS, DPN and laser material processing will focus on multi-method correlative processing and characterization providing correlative analysis using reference markers and optical guidance maps as well as an inert transfer between selected installations.

Further Collaboration outside KIT in internal projects:

TU Darmstadt, Helmholtz Institute Ulm, Uni Wien

References

[1] D. Stoeckel, C. Kübel, K. Hormann, A. Hölzel, B.M. Smarsly, U. Tallarek "Morphological Analysis of Disordered Macro–Mesoporous Solids Based on Physical Reconstruction by Nanoscale Tomography", *Langmuir* (2014) submitted.

Dip-Pen Nanolithography (DPN) and Polymer Pen Lithography (PPL)

Michael Hirtz, Sylwia Sekula-Neuner, Harald Fuchs

Our group, stationed at the Institute for Nanotechnology (INT), offers access to two high-end dip-pen nanolithography (DPN) platforms (DPN 5000 and NLP 2000). With these platforms we provide DPN and related techniques as polymer pen lithography (PPL) or spotting with microchannel cantilevers to KNMF users. In DPN, a fine tip as also used in atomic force microscopy is coated with a chemical ink and then brought into contact with a substrate to transfer the ink onto the surface, similar to the way a quill writes, though here with size and precision in the nanoscale. The more advanced set-ups developed in the last decade now feature the use of arrays of tips (instead of a single tip) which allow a bigger through-put and large area covering by the parallelization of the lithographic process. By the use of so called "inkwells" (microfluidic chips that match the feature sizes of the cantilever arrays) it is possible to deliver different inks to each particular cantilever in such an array, allowing for multiplexed writing (i.e. the integration of different inks in one process step and within the same pattern with high registry). The main strengths of DPN are the possibility of arbitrary pattern generation (maskless, direct write) in combination with high resolution (sub-micron- to nanoscale, depending on the specific ink/substrate system), mild process conditions and multiplexing. In PPL, instead of the single silicon cantilever or cantilever array as in DPN, a polymer stamp (moulded in a silicon master produced by anisotropic etching) featuring some 10.000 pyramidal tips over an area of about 1 cm² is used for pattern generation. By introducing these kinds of stamps that feature precise control over the stage movement in x-, y- and z-direction, into our DPN platforms, we can combine the best features of microcontact printing (μ CP, large area, inexpensive consumables) with that of DPN (high resolution, high spatial control, arbitrary patterns), yielding new and improved ways for advanced micro- and nanoscale surface patterning. We recently established a facile strategy for allowing multiplexed printing with PPL, which offers very promising application routes and is described below.

Multiplexed biomimetic lipid Membranes on Graphene

Graphene has attracted much attention for use as the basis of sensor devices. For tuning the specificity and biological compatibility of graphene, specific functionalization of the pristine graphene is desired. By the application of L-DPN, we could demonstrate the direct writing of tailored phospholipid membranes on graphene [1]. The phospholipids exhibit higher mobility on graphene compared with the commonly used silicon dioxide substrate, therefore leading to very well-spread uniform membranes. By applying the multiplexing capabilities of DPN, phospholipid membranes of different functionalities in close proximity to each other could be achieved. These membranes are stable in aqueous environments and electronic doping of graphene by charged phospholipids could be observed, as well as specific binding of proteins to a target hapten on a lipid. The results offer a route for non-covalent immobilization of various functional groups on graphene for applications in biosensing and biocatalysis by the means of L-DPN.

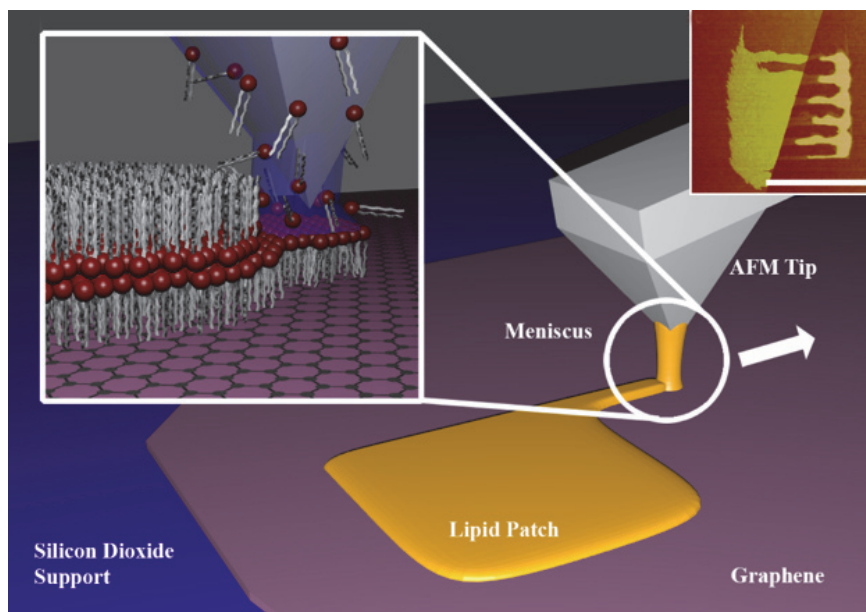


Fig. 1: Scheme of the writing process of lipid membranes onto graphene. The inset on the top right shows an lipid patch written half part on graphene (left) and half part on silicon oxide (right) to demonstrate the difference in spreading under same writing conditions. Scale bar is 5 μ m.

Micro-Arraying on Porous Polymer Substrates

Spotting for arraying applications is of great interest in medical testing and screening. While generally spot sizes of hundreds of μ m are still common in commercial application, miniaturization of these arrays is beneficial in regard to material consumption and needed sample volumes. However, especially the low micrometer (rather than nanometer) scale is relevant for current applications, since smaller features will hinder the readout in current standard fluorescence setups. In this size range, achievable e.g. by spotting with microchannel cantilevers, the broadly used substrate types for larger scale arrays (as e.g. nitrocellulose or nylon membranes) show non-homogeneous features, due to their large and varying pore size structure (Figure 2). In contrast, nanoporous HEMA polymer shows high pattern fidelity in this size range and can be used for functional sensing microarrays [2].

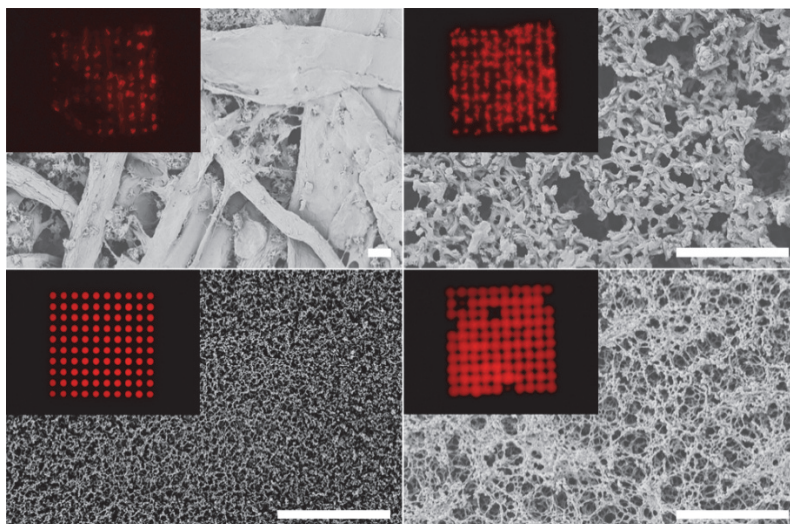


Fig. 2: Fluorescent microarrays printed on different porous substrates. SEM images of the specific substrate in the background have a scale bar 10µm, insets show the microarrays with a dot pitch of 50µm. The advantage in pattern fidelity when printing on the HEMA polymer (bottom left) is obvious when compared to paper (top left), nylon membrane (top right) and nitrocellulose (bottom right).

On-chip Microlasers for biomolecular Detection

Passive photonic whispering gallery mode microresonators (goblet structures) have shown interesting and promising properties for diverse sensing applications. For biomolecular recognition, we functionalized the rim of microresonator structures by L-DPN with different lipid mixtures. By this method, solely the light-guiding circumference of pre-fabricated poly(methyl methacrylate) resonators were coated with a multifunctional molecular ink. This functional ink provides at the same time the gain material for lasing and the sensor for selective binding of target molecules. This allows for a direct and flexible realization of on-chip microlasers, which can be utilized as biosensors in optofluidic lab-on-a-chip applications. The binding of the target molecule (in our demonstration experiment the protein streptavidin) is then accompanied by a shift in the lasing resonance frequency (Fig. 3). The shift magnitude and time response is dose dependent and demonstrates how this setup can be used for sensitive and specific detection of bio-molecules in liquid.

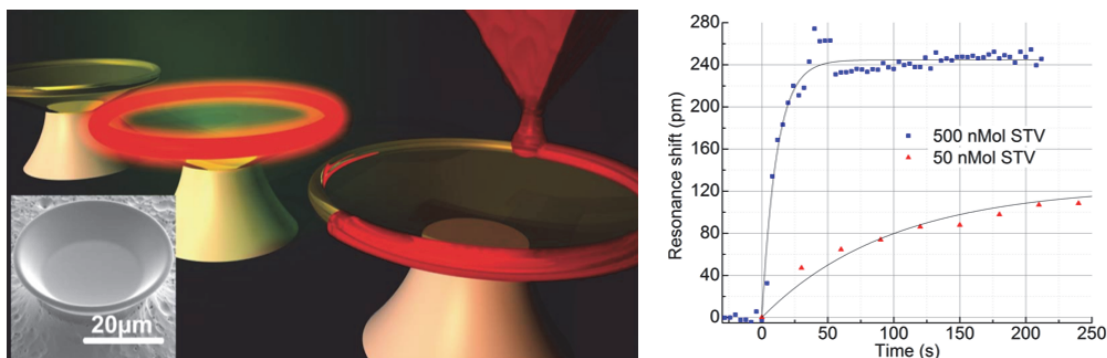


Fig. 3: Microresonance goblet structures are functionalized very specifically on the rim of the resonator structure by L-DPN (left). The inset shows a scanning electron microscopy image of a goblet structure. The shift in lasing resonance in dependence of analyte concentration and time is shown on the right.

Multiplexed Polymer Pen Lithography

Multiplexing is the application and integration of more than one component in an interdigitated pattern. Though this is highly desirable for a vast number of biological and biomedical applications, it is still a challenge to fabricate microscale and subcellular patterns in a multiplexed fashion, especially if large area coverage is demanded at the same time. To address this issue in polymer pen lithography (PPL), we developed a new writing strategy allowing for facile multiplexing in microscale patterns. Instead of trying to bring together the inks closely on the PPL stamp, in this strategy, whole sections of the stamp are inked in one component and stamped one after the other. By the virtue of a large range positioning stage, the different ink patterns can be overlaid so precisely that multiplexing is enabled while full pattern flexibility of PPL is preserved. This patterning strategy offers a wide range of relevant pattern sizes especially for the work of cell biologists and biochemists while featuring easy pattern generation and adjustment, the use of only biofriendly, nontoxic chemicals, and mild processing conditions. Sample multiplex patterns containing differently labelled lipids are shown in Figure 4. The applicability of the technique for cell culture applications was shown by selective cell adhesion studies and neural guidance on a multi-component pattern [4].

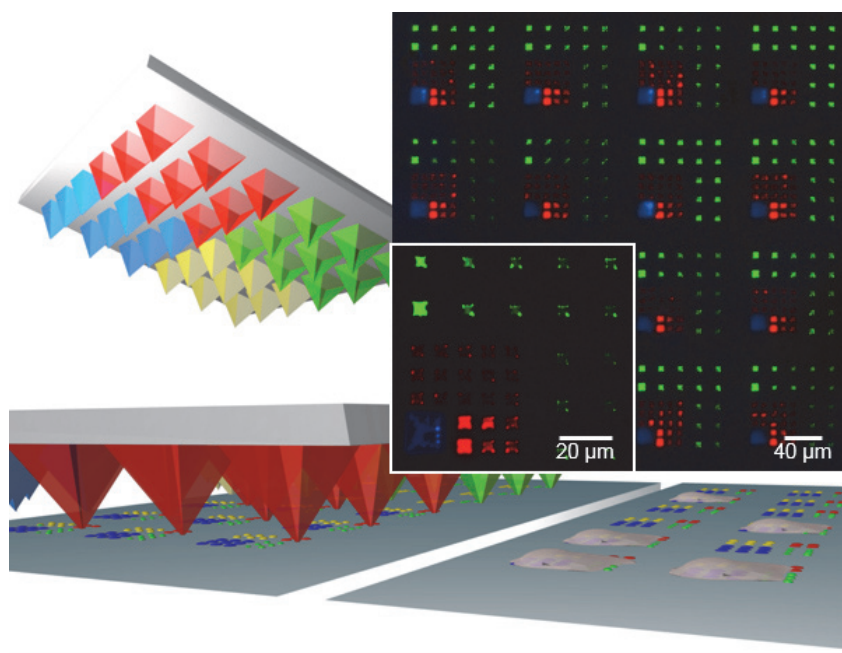


Fig. 4: Scheme of multi-colour PPL printing. The inset shows actual printed interdigitated microstructures with three different fluorescently labelled lipid mixtures.

Strategic Themes

Our installations offer a wide range of additive surface lithography options with special emphasis in bioactive surfaces and sensor functionalization. We can provide users with tailored solutions based on a variety of patterning and coupling chemistry options depending on the specific experimental need. Additionally, we demonstrated that we are not be limited to flat sample surface geometry but can also address three dimensional prestructures and perform site-selective and precisely registered functionalization to devices. Examples of ongoing work in these areas are our activities on functionalizing graphene in collaboration with groups from INT (Krupke, Danneau), international partners from Manchester [1, 5] and collaborations with the Pernice group (INT) on the functionalization of opto- and

optomechanical circuits. This also demonstrates the possibility for processing chains within KNMF as currently demonstrated in our joint user project with the Pfleging group (IAM) to functionalize the area around laser drilled holes and laser surface modifications for the use in patch clamp setups. In regard to our biological research, we also continue our strong internal collaborations with the Cato (ITG) and Bastmeyer (ZOO, CS) groups which also brings expertise back to ongoing user projects with cell culture aspects. Complementary to the biological research there are also ongoing and emerging collaborations in material research (Levkin group, ITG) and printable electronics (Hahn group, INT).

References

- [1] M. Hirtz, A. Oikonomou, T. Georgiou, H. Fuchs and A. Vijayaraghavan "Multiplexed biomimetic lipid membranes on graphene by dip-pen nanolithography", *Nat. Commun.* 4 (2013) 2591
- [2] M. Hirtz, M. Lyon, W. Feng, A. E. Holmes, H. Fuchs and P. A. Levkin "Porous polymer coatings as substrates for the formation of high-fidelity micropatterns by quill-like pens", *Beilstein J. Nanotechnol.* 4 (2013) 377-384
- [3] U. Bog, T. Laue, T. Grossmann, T. Beck, T. Wienhold, B. Richter, M. Hirtz, H. Fuchs, H. Kalt and T. Mappes "On-chip microlasers for biomolecular detection via highly localized deposition of a multifunctional phospholipid ink", *Lab Chip* 13 (2013) 2701-2707
- [4] F. Brinkmann, M. Hirtz, A. M. Greiner, M. Weschenfelder, B. Waterkotte, M. Bastmeyer and H. Fuchs "Interdigitated Multicolored Bioink Micropatterns by Multiplexed Polymer Pen Lithography", *Small* 9 (2013) 3266-3275
- [5] A. Felten, B. S. Flavel, L. Britnell, A. Eckmann, P. Louette, J.-J. Pireaux, M. Hirtz, R. Krupke and C. Casiraghi "Single- and Double-Sided Chemical Functionalization of Bilayer Graphene", *Small* 9 (2013) 631-639

Thin Film Technologies (TFT)

Stefanie Spitz, Harald Leiste, Michael Stüber

Thin films can be deposited on 2- and 3-dimensional substrates for the development of new materials and the modification and enhancement of surfaces. Different facilities are operated within KNMF at the Institute for Applied Materials (IAM-AWP). The PVD-processes are magnetron sputtering, arc ion plating and PVD/CVD-hybride processes. In the scope of these facilities thin films of different compositions and properties can be developed in terms of mechanical, magnetic, electrical or optical applications. The R.F. and DC-magnetron processes in the non-reactive and reactive mode are open to users, beside other deposition methods, and allow complete new system properties. The in-house research focuses on process improvement and optimization as well as on the fabrication of new materials and concepts. The following R&D activities were performed in 2013.

Microstructure and hardness of reactively r.f. magnetron sputtered Cr-V-O thin films

The deposition of the Cr-V-O thin films was done with a Leybold Z550 PVD coating machine using a segmented chromium-vanadium (Cr-V) target to realize a deposition dependent composition of the films to the Cr-Zr-O or the V-Al-C-N system [1, 2, 3]. As demonstrated for other materials combinations, the realization of such an experimental combinatorial approach enables the deposition of Cr-V oxide thin films with a large variation of composition, i.e. from Cr-rich to V-rich, in one deposition process. The segmented target was made of two metal pieces, cut from circular plates of pure chromium and vanadium (each 75 mm diameter, 6 mm thick, purity: 99.95 % and 99.87 %).

The thin films were deposited on mirror-polished cemented carbide substrates with a geometry of 12 mm x 12 mm x 5 mm. Prior to deposition, all substrates were cleaned in an ultrasonic bath in acetone and plasma etched in a pure Ar (6.0) atmosphere at a pressure of 0.5 Pa and substrate bias of -200 V.

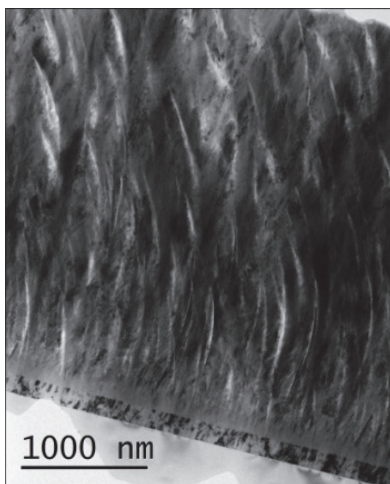


Fig. 1: TEM analysis of a cross-section sample of a Cr-V-O thin film with 3.7 at.% V concentration; bright field image.

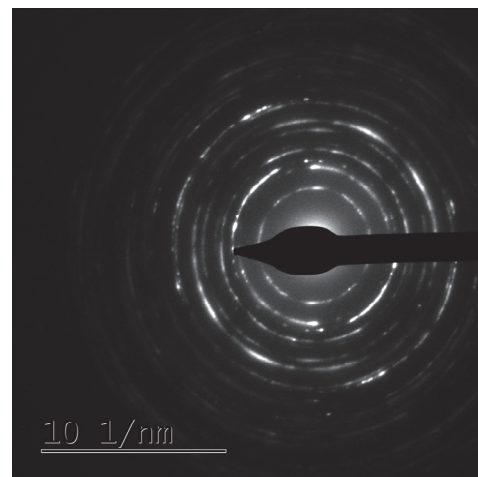


Fig. 2: TEM analysis of a cross-section sample of a Cr-V-O thin film with 3.7 at.% V concentration; SAED image, indicating a single-phase solid solution $(\text{Cr},\text{V})_2\text{O}_3$ corundum structure.

The deposition rate was determined for all Cr-V-O thin films. Thin films, placed below the Cr part of the segmented Cr-V target exhibit values of 22 nm/min to 27.2 nm/min, resulting in a total film thickness from 3.3 μm to 4.1 μm . Thin films deposited under the V part of the segmented target exhibit lower deposition rates between 21.1 nm/min and 17.6 nm/min resulting in a total film thickness of 3.2 μm and 2.6 μm .

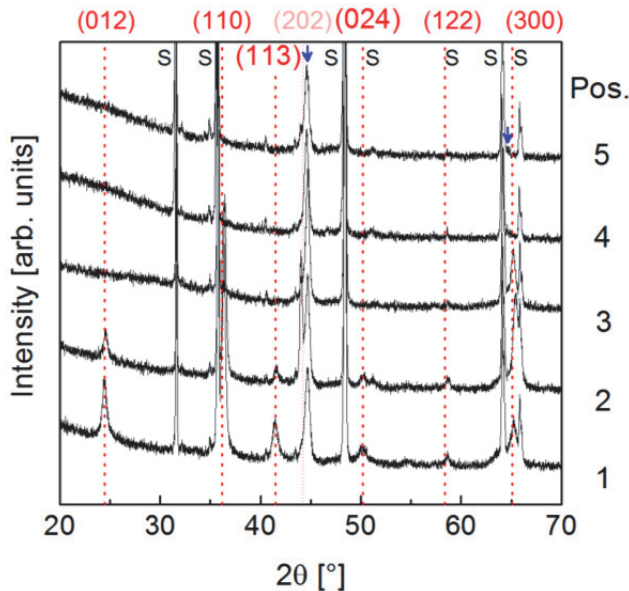


Fig. 3: XRD patterns of Cr-V-O thin films deposited at zero volt substrate bias. Cr-rich films deposited in sample positions 1, 2 and 3 are nanocrystalline, while V-rich films deposited in sample positions 4 and 5 are X-ray amorphous. The index “S” refers to substrate related XRD reflexes, whereas the arrows denominates XRD reflexes attributed to the Cr interface layer (PDF No. 6-694). Reflexes marked by dashed lines refer to Cr_2O_3 (PDF No. 38-1479).

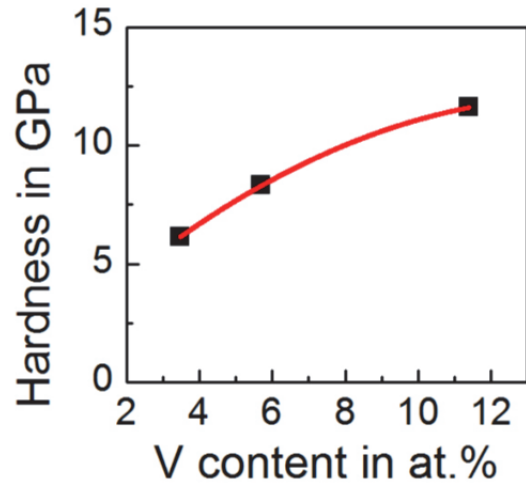


Fig. 4: Values of the indentation hardness of solid solution $(\text{Cr,V})_2\text{O}_3$ thin films in corundum structure in dependence on the V content of films deposited at 0 V substrate bias.

The elemental compositions of the Cr-V-O thin films were determined by EPMA. Thin films deposited in sample positions below the Cr part of the segmented target show high Cr contents of 34.3 at.% and low V contents between 3.7 at.% and 6.0 at.%. Accordingly, thin films deposited in sample positions below the V part of the segmented target exhibit high V contents of 21 at.% and lower Cr contents of 10 at.%. The oxygen content of the Cr-V-O thin films is higher for V-rich films, and a significant trend is visible. The metal/oxygen concentration ratio $(\text{Cr}+\text{V})/\text{O}$ is relatively close to 0.66 (which is characteristic of an metal/oxygen concentration ratio of 2/3), indicated by an oxygen concentration of about 61 at.% in case of Cr-rich thin films. In case of V-rich thin films, the metal/oxygen concentration ratio is close to 0.5. The sum of contaminants measured (i.e. contamination of the films with Ar, N and C) is always below 1.3 at.%.

TEM analyses were done on selected cross-sectional samples only (Fig. 1, 2). The microstructure of the Cr-V-O thin films was systematically evaluated by means of XRD. The XRD patterns of the Cr-V-O thin films are presented in Fig. 3. The index “S” refers to substrate related XRD reflexes, whereas the arrows mark XRD reflexes attributed to the Cr interface layer at 44.6° and 64.4° (according to PDF No. 6-694). Reflexes marked by dashed lines refer to XRD reflexes of pure Cr_2O_3 . As a result, the Cr-rich films (deposited in sample

positions 1, 2 and 3) below the segmented target are nanocrystalline which can be deduced from the FWHM of the reflexes, while V-rich films (deposited in sample positions 4 and 5) are X-ray amorphous. In conclusion, we suggest that these Cr-rich Cr-V-O thin films are grown in a single-phase solid solution $(\text{Cr,V})_2\text{O}_3$ structure with moderate deviations from the perfect 2:3 stoichiometry. The grain size of these films obviously decreases with increasing V content, indicated by the increasing FWHM of the reflexes.

The indentation hardness values obtained by microindentation are displayed in Fig. 4. The indentation hardness of the nanocrystalline Cr-V-O films increases in general with increasing V concentration. Thus, a solid solution hardening effect could be postulated, possibly superimposed by a texture and grain size effect. Hardness values of 11.6 GPa for films with 10.7 at.% V were measured. The films with highest Cr concentration (deposited in sample position 1) show a hardness value of about 6 GPa. All amorphous Cr-V-O thin films, obtained in sample positions 4 and 5 at high V concentrations, show hardness values around 5 GPa. Identical trends are found for the values of the reduced Young's modulus. The nanocrystalline, corundum structured thin films exhibit values between 166 GPa and 234 GPa, which are increasing with increasing V concentration, whereas the amorphous films show values between 120 – 140 GPa.

Further Collaboration outside KIT in Internal Projects:

Universities of: Bochum, Kiel, Kaiserslautern, Aachen, Uppsala (Sweden), Linköping (Sweden), Coimbra (Portugal)

Companies: Walter, Gühring, Balzers, Rockwell Collins

Research Centers: FHG-IMW Freiburg, KIST (Korea), AIN Pamplona (Spanien)

References

[1] S. Spitz, M. Stueber, H. Leiste, S. Ulrich and H. J. Seifert, Surf Coat Tech, 237 (2013) 149

[2] S. Spitz, M. Stueber, H. Leiste, S. Ulrich and H. J. Seifert, Thin Solid Films, 548 (2013) 143

[3] B. Krause, S. Darma, M. Kaufholz, S. Mangold, S. Doyle, S. Ulrich, H. Leiste, M. Stüber and T. Baumbach; J. Appl. Cryst. (2013). 46, 1064

Dry Etching Cluster using RIE(ICP) / RIBE

Alban Muslija, Christian Lay, Sascha Mühlbrandt, Daniel Häringer, and Manfred Kohl

Introduction (A. Muslija)

A dry etching cluster from Oxford Instruments, utilising a RIE / ICP (System: Plasmalab100 with a ICP380 source) and a RIBE (System Ionfab 300) process chamber, is operated in KNMF by the Institute of Microstructure Technology (IMT) for fabrication of Si, SiO₂, SiN and Si₃N₄ microstructures as well as various metal structures (Ti, Cr, Au).

The most frequent and important application during the last 3 years is without doubt the RIE/ICP Silicon Cryo Process. In several long term external and internal projects, this technology is crucial for the fabrication of the silicon devices needed for many nano-photonics and -plasmonic applications. Several process improvements have been made during the course of 2013 to improve the performance of this complex low temperature process towards even smaller, smoother and more vertical structures in the nm range. The smallest lateral dimensions that can actually be performed with the RIE/ICP and the RIBE technology are about 70 nm for silicon and silicon oxide and, only 45 nm for gold (using the lift-off-process). In terms of high aspect ratios we fabricated structures with aspect ratios up to 15.

A special feature of the dry etching cluster is the Ionfab 300 Plus RIBE tool (RIBE: Reactive Ion Beam Etching) used for structuring of special metal alloys, in particular magnetic alloys consisting of Ni, Co, Fe, shape memory alloys (NiTi) and ferromagnetic shape memory alloys (NiMnGa). The in-house research focuses on process development and optimization as well as on the fabrication of complete nano devices.

A major improvement has been made on the cluster during 2013 with the installation of an additional gasline (HBr) for the RIE/ICP chamber. Compared with the "classic" SF₆/O₂ Cryo Process for silicon structures in the μm and nm range, etching with HBr is characterized by an up to 10 times lower etch-rate (~100 nm/min). This allows much better control of the etching depth, especially in case of very shallow structures in the nm range, and makes this process the favoured one e.g. when nanoplasmonic devices on silicon on insulator (SOI) are requested.

In terms of special designs, e.g. the etching of large areas vs. very small masked surfaces, the implementation of a new negative resist (ma-N2401) in the EBL process proved to be very useful for the following RIE processes. Thus, very tall silicon pillars measuring only 120 nm in diameter and 1,5 μm in height, have been etched accurately via the silicon cryo process using this negative resist (Figure 1 and 2).

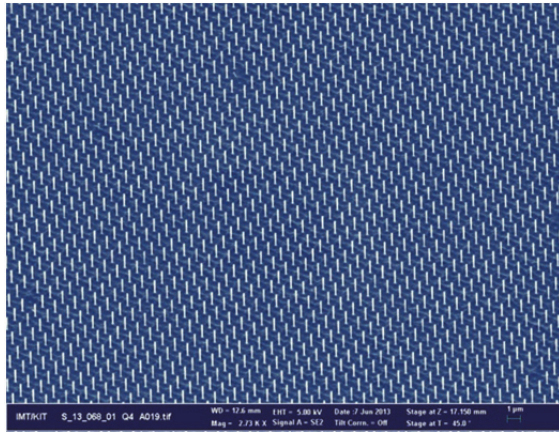
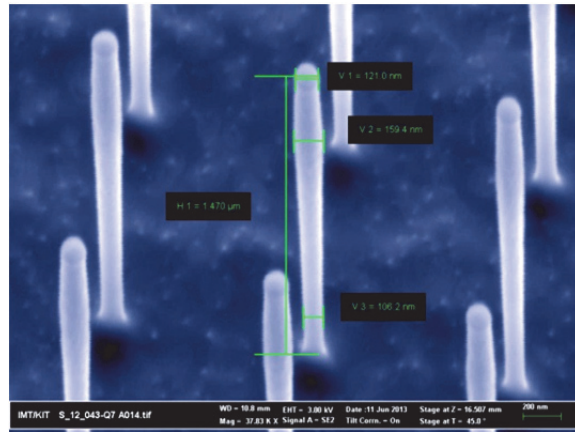


Fig. 1: Array of silicon nanopillars on a very large area



Critical dimensions of the nanopillars: height = 1,5 µm, width = 120 nm, -> AR=12,5

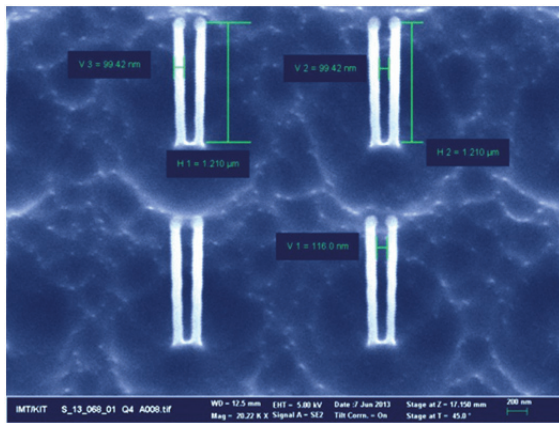
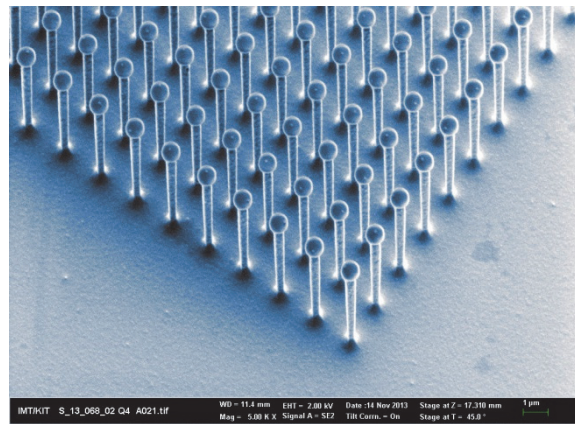


Fig. 2: Double-pairs of nanopillars, height = 1,2 µm, width = 100 nm -> AR = 12



Interesting artefact at a height of 2,5 µm: remaining resist "hats" on the top of the pillars, while the silicon underneath has been under etched

High Aspect Ratio X-Ray Gratings (A. Muslija)

In addition to the well-known fabrication of X-Ray gratings using the LIGA technology, we developed the Silicon Cryo Process for the fabrication of high aspect ratios with structure depths up to 30 µm. A typical X-Ray grating with a period of 5.4 µm was etched using a 1 µm thick oxide layer as the main etch resist. Figures 3 and 4 show the cleaved grating intersection.

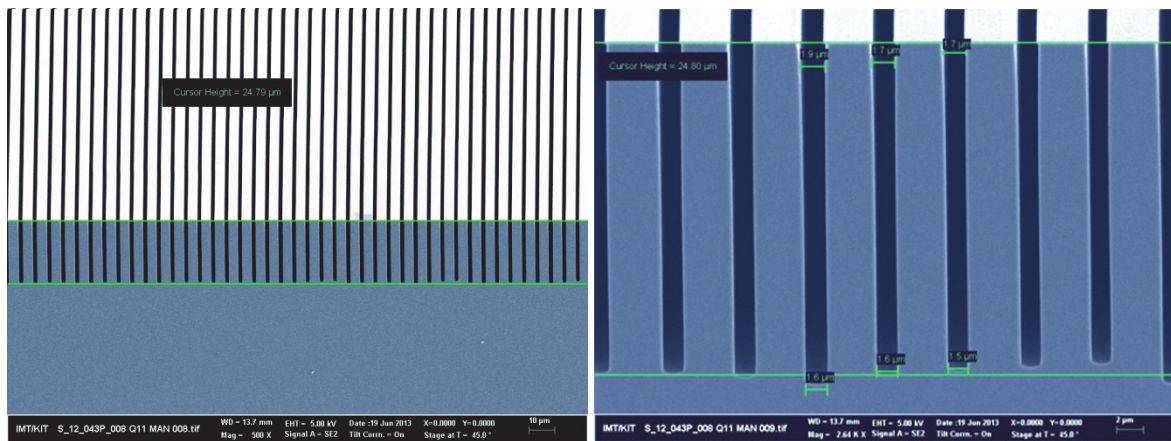


Fig. 3: X-Ray Gratings in Silicon - height = 25 μm , gap width = 1,6 μm -> AR > 15

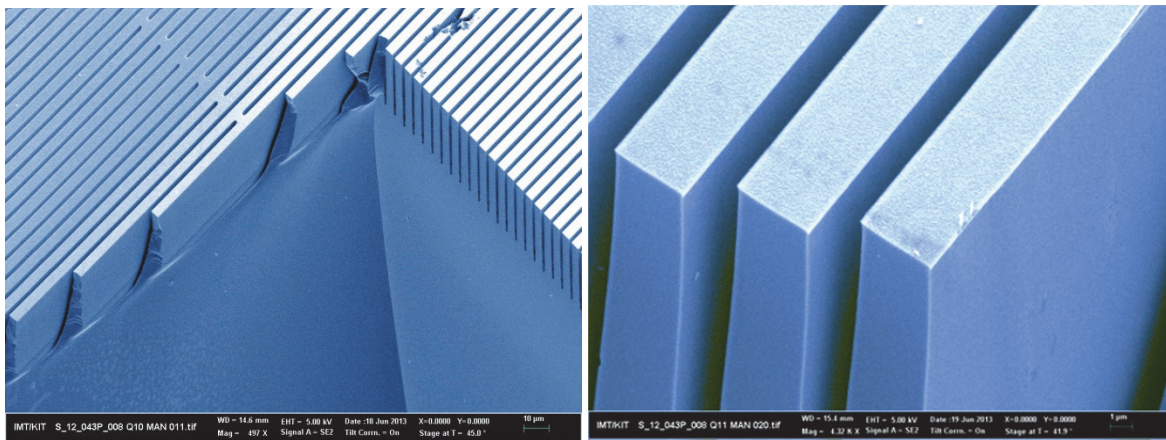


Fig. 4: Superior sidewall quality of the X-Ray gratings etched with the Silicon Cryo Process

SOI device layer thinning by reactive ion etching cryo process (Ch. Lay)

The fabrication and evaluation of nano actuators based on a shape memory alloy/silicon bimorph scheme requires a greater variety in silicon device layer thickness for the testing of actuators with different SMA/Si thickness ratios. Generally, and contrary to industrial applications, scientific use of SOI wafers requires only low quantities, but greater variety in SOI parameters such as device layer thickness. The high anisotropy of reactive ion etching, specifically the silicon cryo-etching process, allows us to thin the device layer to the desired dimensions.

We fabricate silicon double beam cantilevers with minimum feature sizes of 100 nm. A SOI wafer with a nominal silicon device layer thickness of 500 nm is coated with PMMA photoresist and exposed by electron beam lithography. After development, a reactive ion etching cryo process is used to structure the silicon device layer. The remaining photoresist is removed. Fig. 5 shows one of the double beam cantilevers fabricated in this way. It can be seen that the passivating effect of the cryo process results in rectangular sidewalls, and that the actual device layer thickness is 750 nm. After this, a second cryo etch is performed. As there is no more photoresist on the substrate, the etch process reduces structure height while sidewall passivation preserves the rectangular profile. While the process decreases structure height by 400 nm, as can be seen in Fig. 6, lateral loss caused by etching is only 25 nm.

Thus, thinning of SOI wafer structures allows for a quick and cost effective tailoring of the device layer thickness.

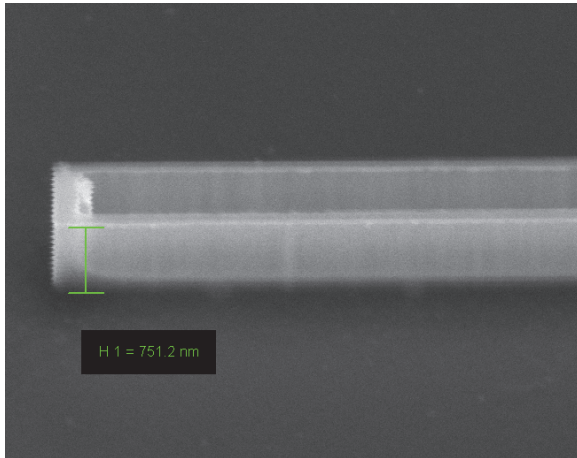


Fig. 5: SEM image of a silicon double beam structure on top of the buried oxide layer of an SOI wafer. The nominal device layer thickness of the SOI wafer is 500 nm, while the SEM image indicates a thickness of 750 nm. Scale bars in the image have been corrected for tilt.

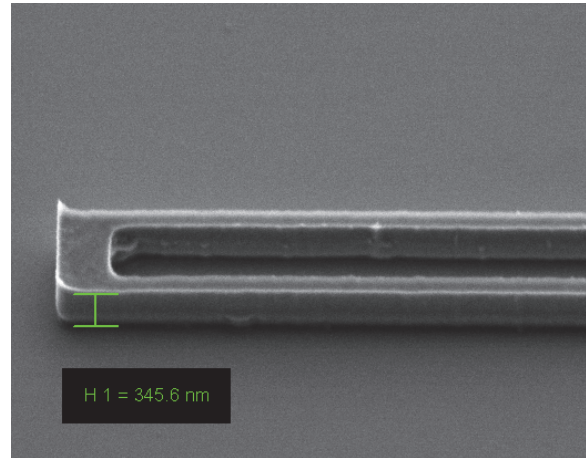


Fig. 6: After a second cryo-etch process without resist mask, device layer thickness is decreased by 400 nm with a lateral etch attack of 25 nm.

Scale bars in the image have been corrected for tilt.

Fabrication of Ultra Compact Plasmonic Devices (S. Mühlbrandt)

Integrated high-speed plasmonic devices are key components of future optical transmission links. The field confinement and enhancement in plasmonic structures allow accessing highly non-linear light-matter interaction. At the same time, the usually small device lengths on the micron scale make RC-limitations negligible. Plasmonic devices are therefore expected to operate at unprecedented electrical bandwidths. A main challenge in the fabrication of on-chip active plasmonic devices, such as photo diodes, is to simultaneously provide coupling of the plasmonic domain to photonic and electronic domains on-chip. In this respect, asymmetric plasmonic MSM waveguides are of special interest for photo diodes based on internal photoemission (IPE). They consist of a sub-100 nm semiconductor core and different metal claddings on the sidewalls without direct contact. Such structure enables a high electric field inside the plasmonic waveguide by applying an external voltage while keeping charge carrier drift times low. The two different metal layers are used for adjustment of potential energy levels. However, fabrication of such an asymmetric multi-material junction with smooth sidewalls poses a considerable technological challenge due to limitations of spatial resolution in lithography and subsequent physical vapor deposition (PVD) steps.

The new fabrication process is demonstrated for silicon-on-insulator chips with 340 nm silicon device layer, which are thermally oxidized to create an 80 nm thick oxide layer. Rectangular silicon nanowires with a top oxide layer are prepared using electron beam lithography and anisotropic RIE-ICP etching steps. Positive resist is spun on top of the chip. Subsequent electron beam lithography opens the plasmonic sections and defines the contour of the electrodes for external electronics. The resist layer serves as a mask for an isotropic etching step with SF₆. The SF₆ only attacks the sidewalls of the opened waveguide sections and leaves the oxide unharmed. As a result, the uppermost oxide layer is undercut as depicted in Figure 7. Due to the isotropic nature of this etching step, the surface roughness of the silicon is well below the metal grain size of about 40 nm. Lateral

thicknesses of the nanowire of 70 nm can be achieved. In a further step, the undercut oxide serves as a hard mask for metallization under grazing incidence from either side of the nanowire with different metals. Under such condition, an asymmetric MSM junction is created without a shortcut [Figure 8].

This processing is not restricted to metals. In principle, any desired layer sequence can be achieved, given that the materials can be directionally deposited. The scalability of the process allows fabrication of lambda-scale, active plasmonic devices [Figure 9].

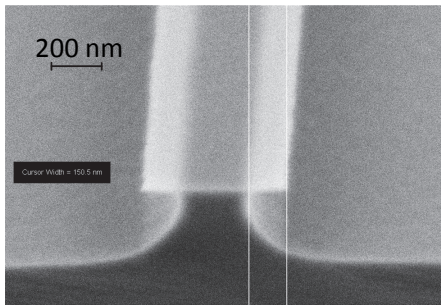


Fig. 7: Front view of the waveguide structure consisting of an undercut SiO_2 hard mask on silicon. Isotropic etching with SF_6 is used to undercut the oxide.

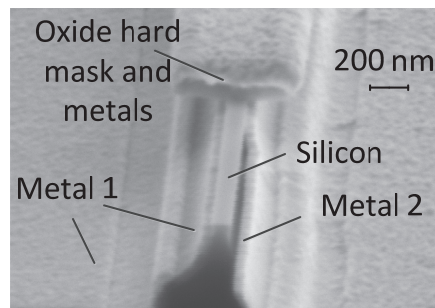


Fig. 8: Front view of the cleaved facet of an asymmetric photo-active MSM junction. Evaporation of metals at grazing incidence creates plasmonic waveguides without shortcuts between the electrodes. The oxide hard mask has partially come off due to cleaving the chip.

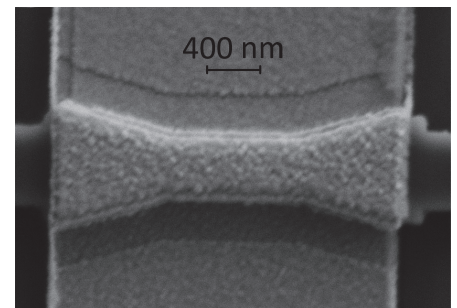


Fig. 9: Top view of an asymmetric MSM plasmonic waveguide coupled to silicon photonic waveguides and electrode pads on an SOI chip. The length of the device is less than $3 \mu\text{m}$.

Dry Etching of Glass (D. Häring)

Glass substrates can be dry-etched using a two-step approach. In a first step a chromium mask is processed with a $\text{He}/\text{O}_2/\text{Cl}_2$ – plasma. This chromium mask is used for the SiO_2 etch process, because of its high resistivity against a CHF_3 - plasma. Etch rates of about 190 nm/min can be reached. As an example a section of a large area pore array is shown in figure 10 A.

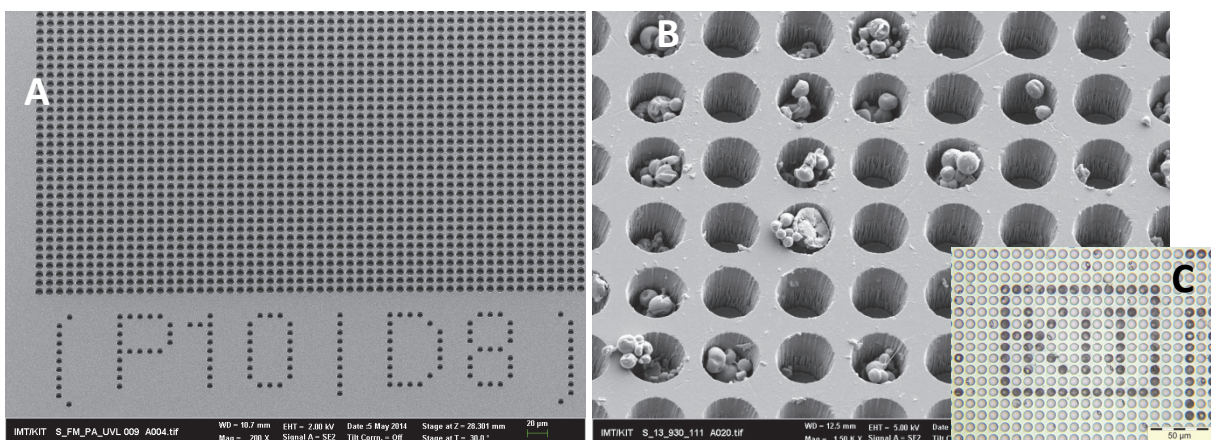


Fig. 10: (A) SEM image of a pore array with 1 million pores dry etched in glass. With a pore diameter of $8 \mu\text{m}$ and a distance of $10 \mu\text{m}$ a density of 1 million pores per square centimeter results. (B) Section of a structured pore array after laser induced particle transfer. (C) Microscope image of a complete particle pattern [1].

These pore arrays are used to make particle patterns by a laser induced particle transfer (see figure 10 B, C). Such particle patterns can be made e.g. with amino acid particles for combinatorial peptide synthesis.

References

[1] Märkle, F., Laserbasierte Verfahren zur Herstellung hochdichter Peptidarrays. PhD Thesis, 2014. Institute of Microstructure Technology, Karlsruhe Institute of Technology.

Transmission Electron Microscopy (TEM)

Christian Kübel, Di Wang, Kiran Chakravadhanula, Eglantine Courtois, Aaron Kobler, Torsten Scherer, Robby Prang, Emma Tröster

An image corrected FEI Titan 80-300 Transmission Electron Microscope (TEM) is operated as part of the KNMF by the Institute of Nanotechnology (INT) for high-end structural characterization in materials sciences using a combination of high resolution imaging in TEM and STEM mode with nanoscale compositional analysis and nanoscale 3D imaging. The TEM is supported by Focused Ion Beam (FIB), which, together with the newly acquired Fischione NanoMill, enables site specific high-quality sample preparation suitable for atomic resolution imaging.

In-house research focuses on optimizing the performance of the existing microscopy techniques and on developing new techniques for *in-situ* mechanical and electrical characterization as well as heating of materials inside the TEM. In addition, in-house research is used for high-end characterization of a range of nanomaterials for HGF and KIT internal partners. A selection of the R&D activities performed in 2013 is described below.

Density changes in shear bands of a metallic glass determined by correlative analytical transmission electron microscopy

Density changes between sheared zones and their surrounding amorphous matrix as a result of plastic deformation in a cold-rolled metallic glass (melt-spun $\text{Al}_{88}\text{Y}_7\text{Fe}_5$) were determined using high-angle annular dark-field (HAADF) detector intensities supplemented by electron-energy loss spectroscopy (EELS), energy-dispersive X-ray (EDX) and nano-beam diffraction analyses. Sheared zones or shear bands were observed as regions of bright or dark contrast arising from a higher or lower density relative to the matrix (Fig. 1). Moreover, abrupt contrast changes, from bright to dark and *vice versa*, were found within individual shear bands. We associate the decrease in density mainly with an enhanced free volume in the shear bands, and the increase in density with concomitant changes of the mass due to compositional variations between the bright and dark part of the shear band. Nanobeam electron diffraction revealed local changes in the order of the shear bands: in the dark part of the shear band, a mixture of amorphous and crystalline/medium range ordered domains were observed (Fig. 2). [1]

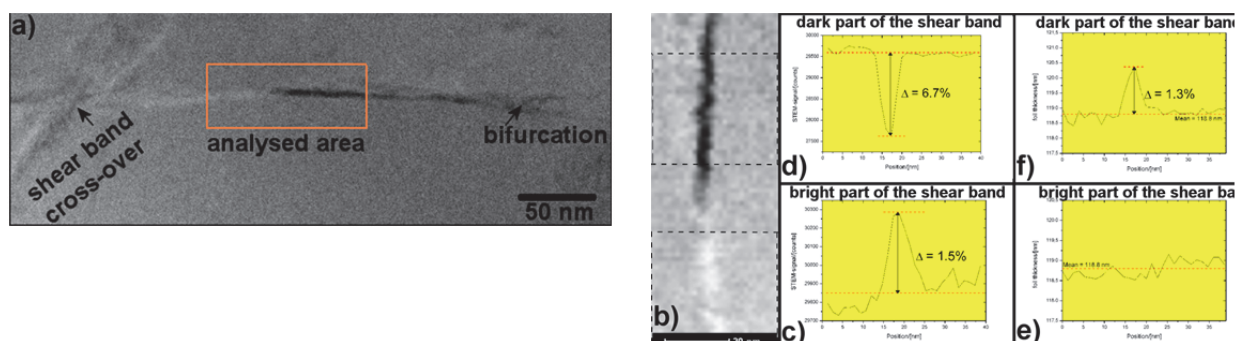


Fig. 1: (a) Z-contrast (HAADF-STEM) image showing characteristic shear bands of a cold-rolled $\text{Al}_{88}\text{Y}_7\text{Fe}_5$ melt-spun ribbon. A cross-over of shear bands is seen on the left side. The horizontal shear band displays a contrast change from bright to dark in the box (analyzed area) and a bifurcation at the end. (b) HAADF image of the analyzed area shown in (a). (c and d) Averaged profiles of the HAADF detector signal of the indicated areas. (e and f) Averaged profiles of the foil thickness of the indicated areas. Images taken from [1].

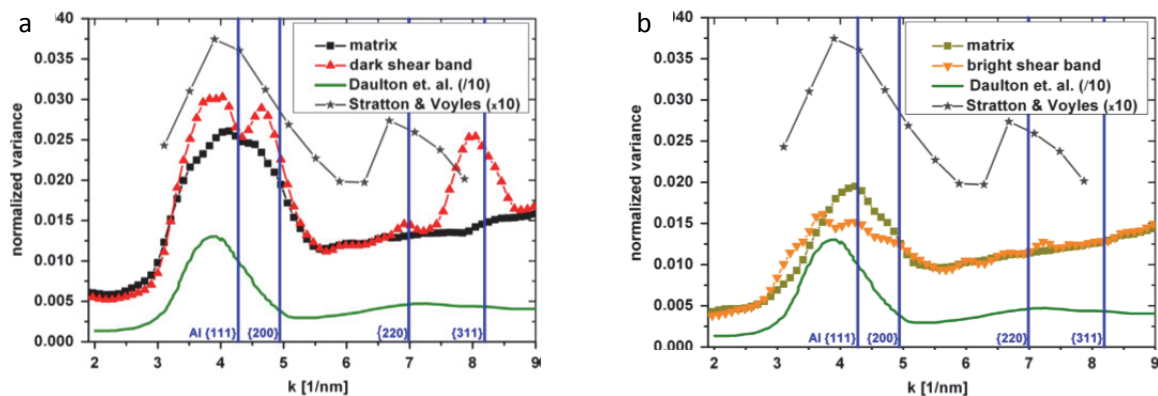


Fig. 2: Results of the NBDP analysis: The averaged normalized intensity variance of different NBDP ensembles (matrix, dark/bright part of the shear band) was calculated following the normalized variance of ring ensemble. For comparison, two data sets of undeformed $\text{Al}_{88}\text{Y}_7\text{Fe}_5$ are plotted as references from the literature. Strong reflections of the Al fcc structure are indicated. Images taken from [1].

Impact of sonication pretreatment on carbon nanotubes: A transmission electron microscopy study

Sonication treatments are commonly used for debundling and dispersing carbon nanotubes (CNTs) in liquid media prior to chemical functionalization. However, this step may lead to the stripping of the outer graphitic layers and the scission of the CNTs, and can therefore have a deleterious effect on the achievable properties of the functionalized CNTs. Thus, knowledge on the structural integrity of the modified CNTs is required to understand its influence on the device performance of hybrid nanocarbon-based composites. This work shows the impact of a sonication pre-treatment on the structure of multi-walled CNTs, and on the role of the induced modifications on the subsequent attachment of ferromagnetic Fe_3O_4 nanoparticles. Decoration of the CNTs with Fe_3O_4 nanoparticles is achieved by a microwave-assisted synthesis route involving the reaction of iron acetylacetonate with 2-pyrrolidinone. Employing a combination of atomic resolution transmission electron microscopy, electron energy-loss spectroscopy, energy-filtered transmission electron microscopy and electron tomography, we provide evidence that significant degradation of the CNT structure takes place during the dispersion process (Fig. 3). Moreover we find that the sp^2 system is more heavily disrupted at the interface between the CNTs and the surface-deposited nanoparticles suggesting that nucleation of Fe_3O_4 preferentially occurs at the nanotube defect sites (Fig. 4). [2]

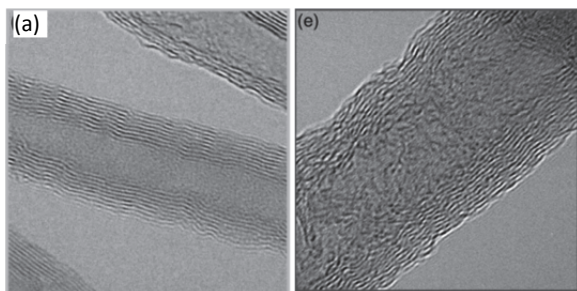


Fig. 3: HRTEM images of a (a) bare-untreated MWCNT, (b) bare-sonicated MWCNT revealing stronger disorder in the graphite lattice of the sonicated:MWCNTs. Images taken from [2].

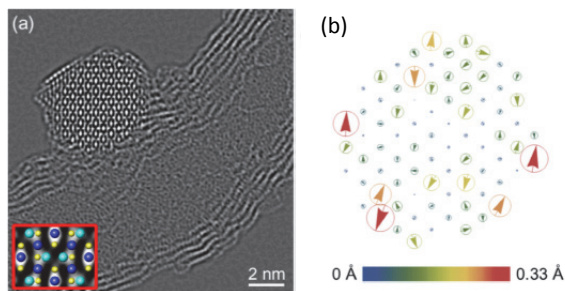


Fig. 4: (a) Reconstructed phase image of a MWCNT/ Fe_3O_4 interphase. Inset: magnified view of a unit cell from the particle with overlaid model of the Fe_3O_4 structure along along $[1\ 0\ 1]$ showing the (light and dark blue) Fe and (yellow) O columns. (b) Displacement map illustrating no clear displacement pattern of the atomic columns. The vector magnitudes are given by the color scale. Images taken from [2].

Controlled Synthesis of Thorium and Uranium Oxide Nanocrystals

Very little is known about size and shape effects on the properties of actinide compounds. As a consequence, the controlled synthesis of well-defined actinide-based nanocrystals constitutes a fundamental step before studying their corresponding properties. Here, we report on the non-aqueous surfactant-assisted synthesis of thorium and uranium oxide nanocrystals. The final characteristics of thorium and uranium oxide nanocrystals can be easily tuned by controlling a few experimental parameters such as the nature of the actinide precursor and the composition of the organic system (e.g., the chemical nature of the surfactants and their relative concentrations). Additionally, the influence of these parameters on the outcome of the synthesis is highly dependent on the nature of the actinide element (thorium versus uranium). By using optimised experimental conditions, monodisperse isotropic uranium oxide nanocrystals (Fig. 5) with different sizes (4.5 and 10.7 nm) as well as branched nanocrystals (overall size ca. 5 nm), nanodots (ca. 4 nm) and nanorods (with ultra-small diameters of 1 nm) of thorium oxide were synthesised (Fig. 6) and characterized in detail by high-resolution TEM and STEM. [3,4]

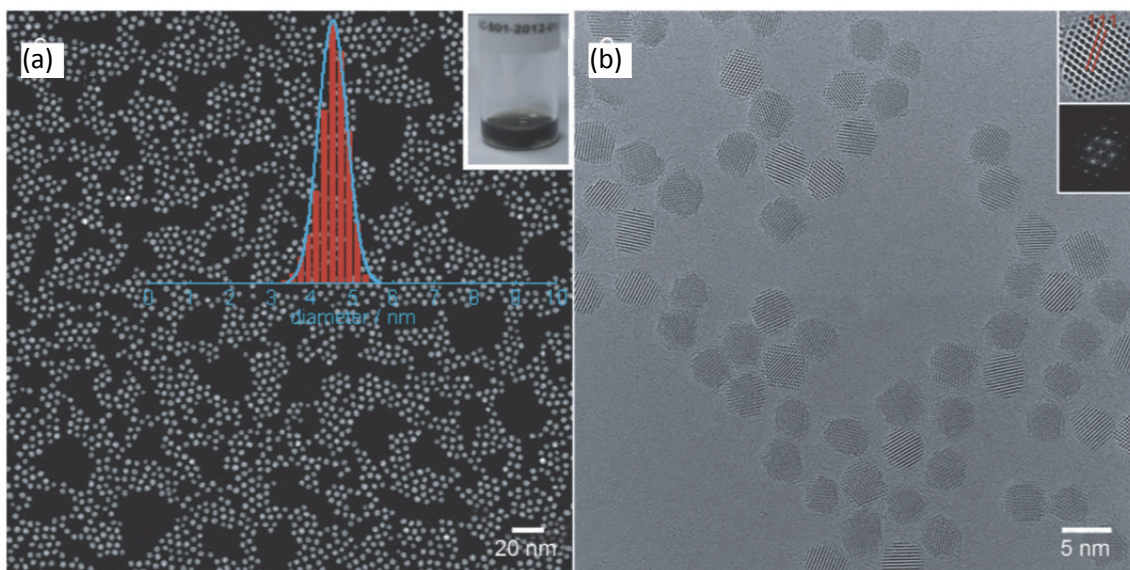


Fig. 5: STEM (a) and TEM images (b) of uranium oxide nanocrystals synthesised in BnOBn/OA/OAm with $\text{UO}_2(\text{acac})_2$ as starting uranium precursors. Images taken from [3].

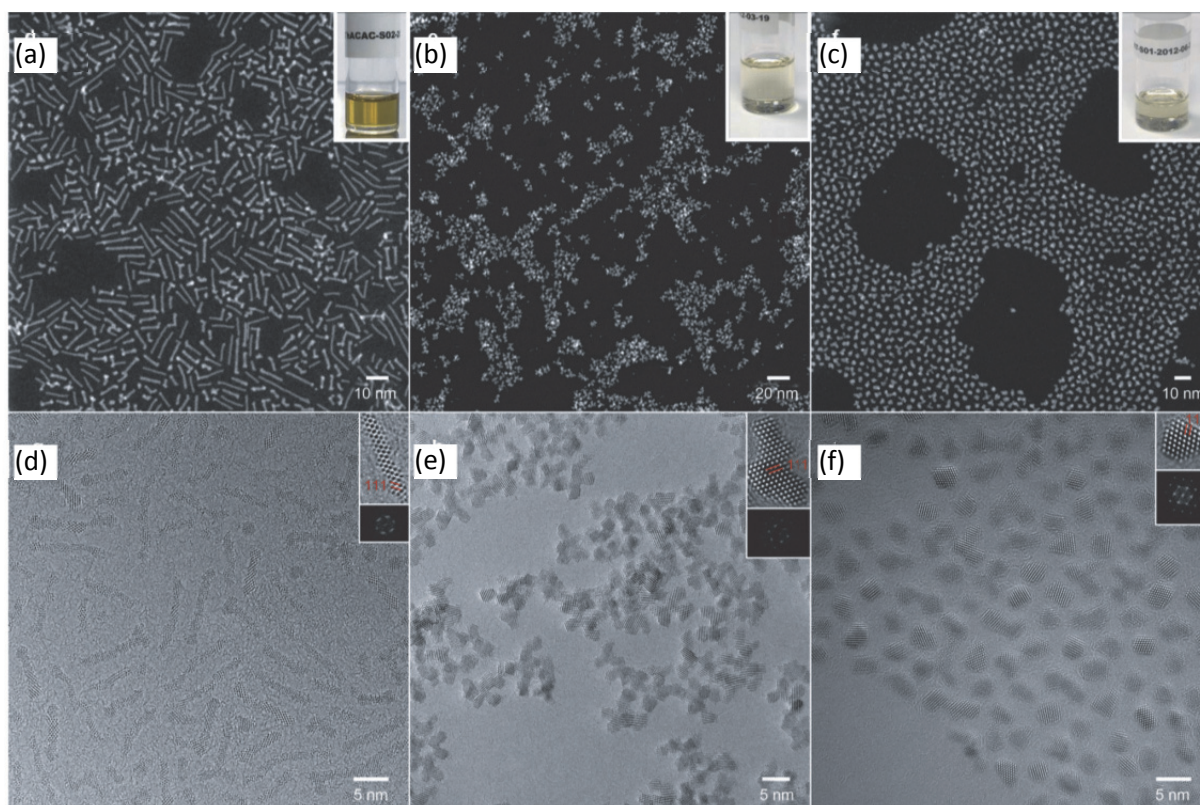


Fig. 6: TEM and STEM images of thorium oxide nanocrystals synthesised in BnOBn/OA/N(Oct)₃/OP(Oct)₃ with various thorium precursors: a,d) $[\text{Th}(\text{acac})_4]$, b,e) $[\text{Th}(\text{OAc})_4]$ and c, f) $\text{Th}(\text{NO}_3)_4 \cdot 5\text{H}_2\text{O}$. Insets in (a–c) show the thorium oxide nanocrystals dispersed in toluene. Insets in (d–f) show HRTEM images and their corresponding FFTs. Images taken from [3].

Whole-Cell Analysis of Low-Density Lipoprotein Uptake by Macrophages Using STEM Tomography

Nanoparticles of heavy materials such as gold can be used as markers in quantitative electron microscopic studies of protein distributions in cells with nanometer spatial resolution. Studying nanoparticles within the context of cells is also relevant for nanotoxicological

research. Here, we report a method to quantify the locations and the number of nanoparticles, and of clusters of nanoparticles inside whole eukaryotic cells in three dimensions using scanning transmission electron microscopy (STEM) tomography. Whole-mount fixed cellular samples were prepared, avoiding sectioning or slicing (Fig. 7). The level of membrane staining was kept much lower than is common practice in transmission electron microscopy (TEM), such that the nanoparticles could be detected throughout the entire cellular thickness. Tilt-series were recorded with a limited tilt-range of 80° preventing excessive beam broadening occurring at higher tilt angles. The 3D locations of the nanoparticles were nevertheless determined with high precision using computation. The obtained information differed from that obtained by conventional TEM tomography data since the nanoparticles were highlighted while only faint contrast was obtained on the cellular material. Similar as in fluorescence microscopy, a particular set of labels can be studied. This method was applied to study the fate of sequentially up-taken low-density lipoprotein (LDL) conjugated to gold nanoparticles in macrophages. Analysis of a 3D reconstruction revealed that newly up-taken LDL-gold was delivered to lysosomes containing previously up-taken LDL-gold thereby forming onion-like clusters (Fig. 8). [5]

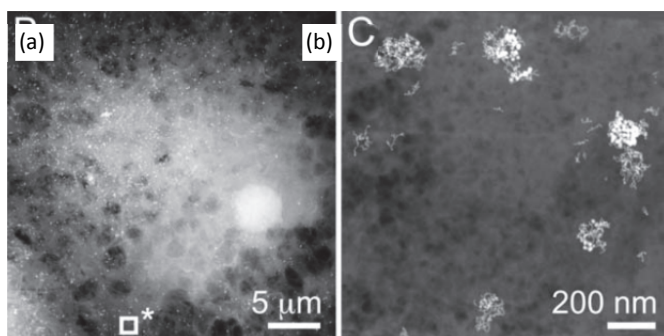


Fig. 7: Scanning TEM (STEM) images recorded of whole-mount macrophage cells. (a) Nucleus and section of cell containing many gold nanoparticles. (b) Image from a tilt-series showing gold nanoparticles of different sizes, recorded as a magnification of 115,000x. The location of this image is shown as square with * in (a). Images taken from [5].

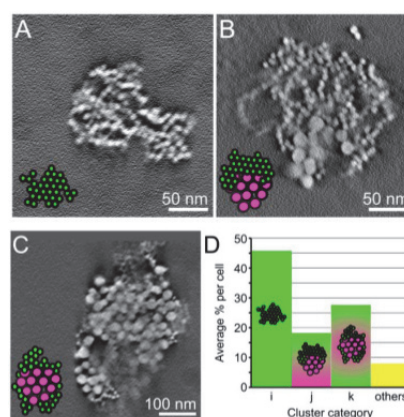


Fig. 8: Quantitative characterization of the three main types of clusters formed after sequential incubation with large, and small LDL gold nanoparticles. (a–c) Representative images of the three main categories of clusters. (d) Population of each cluster type in an average thickness of 0.73 ± 0.29 mm. Images taken from [5].

In-Situ and ex-situ TEM electrochemical studies of new battery systems

Lithium ion batteries (LIBs) are used as secondary energy/power sources for portable electronic devices and in transportation. However, the low energy density of current state-of-the-art LIBs with layered Li transition metal oxides as cathode, such as LiCoO_2 or LiFePO_4 , limits extensive practical applications. Alternative battery systems are researched widely and one potential solution to achieve higher energy densities is utilization of higher oxidation states in the transition metals. Cathodes based on conversion reactions, which involve multi-electron redox reactions, appear to be potential candidates and theoretically deliver a high specific capacity [6, 7, 8]. Another option is the use of different transfer ions, e.g. recently the principle of a secondary battery based on a fluoride ion shuttle to replace the lithium has been demonstrated, which could theoretically provide high energy densities.

Transmission electron microscopy at different charging states has been used to characterize the structure and morphology of different LiF/Fe/C conversion electrodes (fig. 9) and enabled a correlation with the electrochemical performance. For example, it could be shown that the graphitic shell around the iron nanoparticle is crucial to maintain the nanostructure during electrochemical cycling. Looking at cathodes materials formed by reaction of graphite fluoride (CF_x) with $Fe(CO)_5$, EELS analysis (fig. 9) revealed the formation of more graphitic matrix with lower F/C ratios ($x = 0.5$), which resulted in stable capacity of 150-200 mAh/g for more than 150 cycles, whereas high F/C ratios ($x = 1-1.1$) resulted in cathodes with a higher initial capacity, but which were lacking cyclic stability. [7]

To directly see and understand the processes during electrochemical cycling of battery systems, *in-situ* TEM techniques are under development. In addition to the challenges of producing a working battery with nanoscale dimensions, the electron beam sensitivity of a lot of typical LIB materials is limiting this approach. Therefore, we have been looking into alternative systems and initial partially reversible *in-situ* TEM electrochemical results for charging and discharging a $La/La_{0.1}Ba_{0.9}F_{2.9}/BiF_3$ battery have been obtained (Fig. 10) as an example for a fluoride shuttle system.

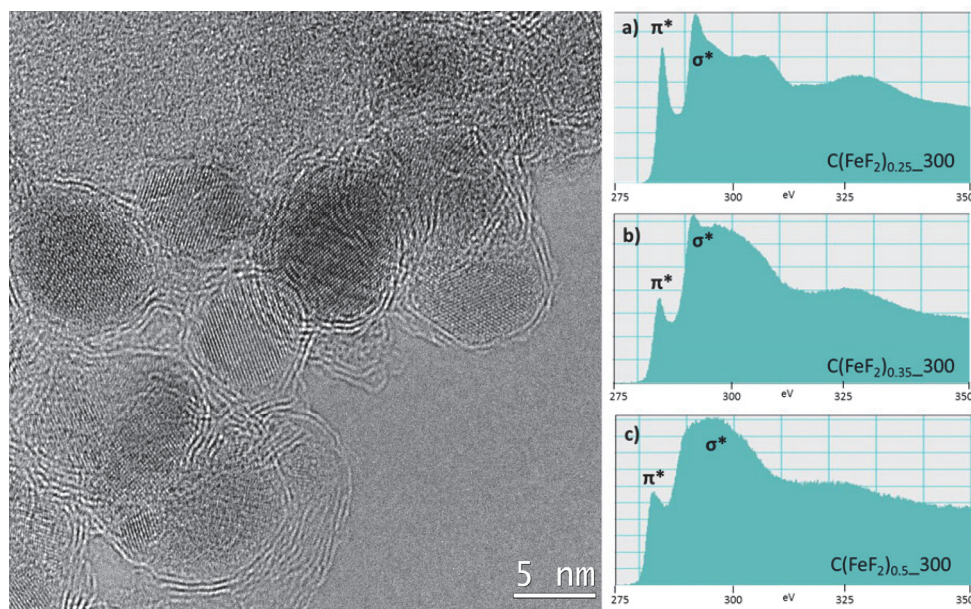


Fig. 9: Ex-situ TEM investigation of the structure of LiF/Fe/C conversion electrodes: left) core/shell structure of the Fe/C nanoparticles produced by thermal decomposition of ferrocene; right) EELS spectra showing the transition from graphitic to amorphous for the carbon matrix formed during reaction of $Fe(CO)_5$ with CF_x at different concentrations. Images taken from [7].

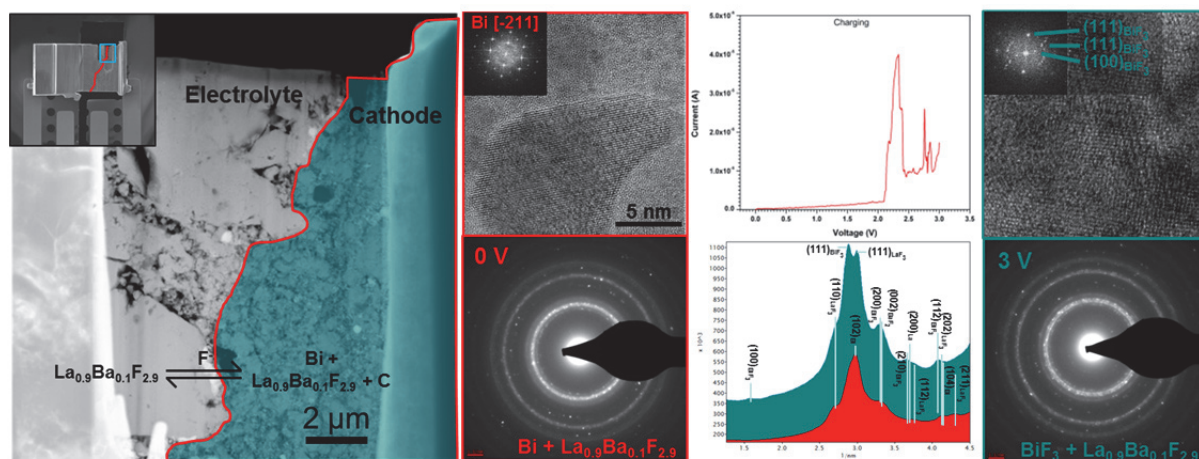


Fig. 10: *In-situ* TEM electrochemical investigation of a La/La_{0.9}Ba_{0.1}F_{2.9}/BiF₃ battery: The oxidation of the Bi in the cathode to BiF₃ can be followed *in-situ* by electron diffraction and in HRTEM.

Strategic Themes

For a close correlation between structure and materials properties, *in-situ* TEM techniques provide an essential link at the nano scale. Over the last years, we have successfully developed the combination of *in-situ* mechanical testing with crystal orientation mapping to quantitatively follow structural changes during plastic deformation as revealed by grain boundary movement, grain rotation or the formation of CSL boundaries *in/between* grains.

We will also continue to further develop other *in-situ* TEM techniques to follow structural changes during cooling, heating, electrical testing and electrochemical reactions with a special focus on *in-situ* electrochemistry to study battery materials.

A long-term strategic development for TEM together with FIB, HIM, XPS, ToF-SIMS, DPN and laser material processing will focus on multi-method correlative processing and characterization providing correlative analysis using reference markers and optical guidance maps as well as an inert transfer between selected installations.

Further Collaboration outside KIT in internal projects:

TU Darmstadt, University of Ulm, University Leiden

References

- [1] H. Rösner, M. Peterlechner, C. Kübel, V. Schmidt, G. Wilde "Density changes in shear bands of a metallic glass determined by correlative analytical transmission electron microscopy", *Ultramicroscopy*: Volume 142, (2014) 1-9.
- [2] M.D. Rossell, C. Kübel, G. Ilari, F. Rechberger, D. Koziej, M. Niederberger, R. Erni "Impact of sonication pretreatment on carbon nanotubes: a transmission electron microscopy study", *Carbon*: Volume 61, (2013) 404-411.
- [3] D. Hudry, C. Apostolidis, O. Walter, T. Gouder, E. Courtois, C. Kübel, D. Meyer "Controlled Synthesis of Thorium and Uranium Oxide Nanocrystals", *Chem. Eur. J.*: Volume 19, Issue 17, (2013) 5297-5305.
- [4] D. Hudry, C. Apostolidis, O. Walter, T. Gouder, A. Janssen, E. Courtois, C. Kübel, D. Meyer "Synthesis of Transuranium-Based Nanocrystals via the Thermal Decomposition of Actinyl Nitrates", *RSC Advances*: Volume 3, (2013) 18271-18274.

- [5] J.-P. Baudoin, W. G. Jerome, C. Kübel, N. de Jonge "Whole-cell Analysis of Low-Density Lipoprotein Uptake by Macrophages using STEM Tomography", PLoS ONE: Volume 8, Issue 1 (2013) e55022.
- [6] M.A. Reddy, B. Breitung, V.S.K. Chakravadhanula, C. Wall, M. Engel, C. Kübel, A.K. Powell, H. Hahn, M. Fichtner "CFx Derived Carbon-FeF₂ Nanocomposites for Reversible Lithium Storage", Adv. Energy Mater.: Volume 3, Issue 3 (2013) 308-313.
- [7] B. Breitung, M. A. Reddy, V.S.K. Chakravadhanula, M. Engel, C. Kübel, A. K. Powell, H. Hahn, M. Fichtner "Influence of particle size and fluorination ratio of CFx precursor compounds on the electrochemical performance of C-FeF₂ nanocomposites for reversible lithium storage", Beilstein J. Nanotechnology: Volume 4, (2013) 705-713.
- [8] R. Prakash, K. Fanselau, S. Ren, T.K. Mandal, C. Kübel, H. Hahn, M. Fichtner "A facile synthesis of a carbon-encapsulated Fe₃O₄ nanocomposite and its performance as anode in lithium-ion batteries", Beilstein J. Nanotechnology: Volume 4, (2013) 699-704.

Atomic Force Microscopy (AFM)

Hendrik Hölscher, Tobias Meier, Richard Thelen

Since the invention of atomic force microscopy (AFM) in the 1980s it has become a versatile tool used in, e.g., nanoscale metrology, biosensing, maskless lithography and high density data-storage. The experimental set-up of an AFM is based on a simple idea [1]. It detects forces acting between a sample surface and a sharp tip that is mounted on a soft leaf spring (the so-called cantilever). A feedback system, which controls the vertical z-position of the tip on the sample surface, keeps the deflection of the cantilever (and thus the force between tip and sample) constant. Moving the tip relative to the sample of the surface by means of piezoelectric drives, the actual z -position of the tip is recorded as a function of the lateral position with very high precision. The obtained data represent a map of equal forces which can be interpreted as the surface topography.

The AFM tools in KNMF have been complemented by a large-area AFM which allows us to image samples with scan sizes up to nearly 1 mm². Beside this large scan-size this home-built systems has several other advantages which allow us to provide the KNMF users with many options to analyse their samples.

Set-up of a Large-Area Atomic Force Microscope

Most commercial AFM are limited to scan sizes of 100 µm x 100 µm. However, frequent requests from the KNMF users urged us to set-up a large area AFM which allows scans up to 800 µm x 800 µm and features many other options (self-sensing cantilever [2], non-magnetic set-up, advanced optical access of the sample as well as open software for the AFM controller). As large scan ranges normally interfere with high lateral resolution, a new concept of a small area, high resolution scanner nested on the large area scanner is successfully demonstrated.

An integrated optical microscope for coarse navigation on the sample is implemented. A schematic of the optical setup is shown in Fig. 1a. Using an infinity-corrected microscope objective and an ocular lens allow to illuminate the sample and focus the laser beam on the cantilever with the same objective. Using the microscope objective to focus the laser also simplifies the adjustment of the laser beam deflection setup because the complete optical microscope can be moved instead of adjusting the laser. As a result, the focal spot of the laser is fixed towards the field of view of the optical microscope and the laser is aligned to the cantilever when the cantilever is at a specific position in the optical image. To block scattered light inside the optical path of the laser from the camera, a red mirror is used to couple the laser beam into the objective. As the mirror reflects only light with wavelengths longer than 600 nm, all light from the laser is either reflected towards the objective or the laser itself. The cantilever is tilted toward the optical axis of the microscope and acts as a mirror for the laser beam. As the cantilever gets deflected, the angle of the cantilever tilts towards the incident laser beam and consequently the reflection angle changes. As the reflected beam is divergent (due to the focusing of the microscope objective), it is refocused to the position sensitive photo-detector by a tilting mirror.

A wavelength shorter than the reflection edge of the red mirror was chosen to illuminate the sample and polarizing optics are useful to suppress stray light within the optical path of the microscope. In contrast to the laser, the light of the illumination has first to illuminate the sample, be reflected at the sample and the reflected light has to pass the complete

microscope to the camera. By using polarized light for illumination, a polarizing beam-splitter can be used to reflect all the light from the light source of the illumination towards the sample. By passing a $\lambda/4$ -plate, the polarization direction gets rotated by 45° . After being reflected on the sample, the light passes the $\lambda/4$ -plate again and the polarization is rotated again by 45° . The polarization of the reflected light is now rotated by 90° towards the incident light from the light source. Therefore, the beam-splitter is completely transparent to light reflected from the sample which can pass towards the camera.

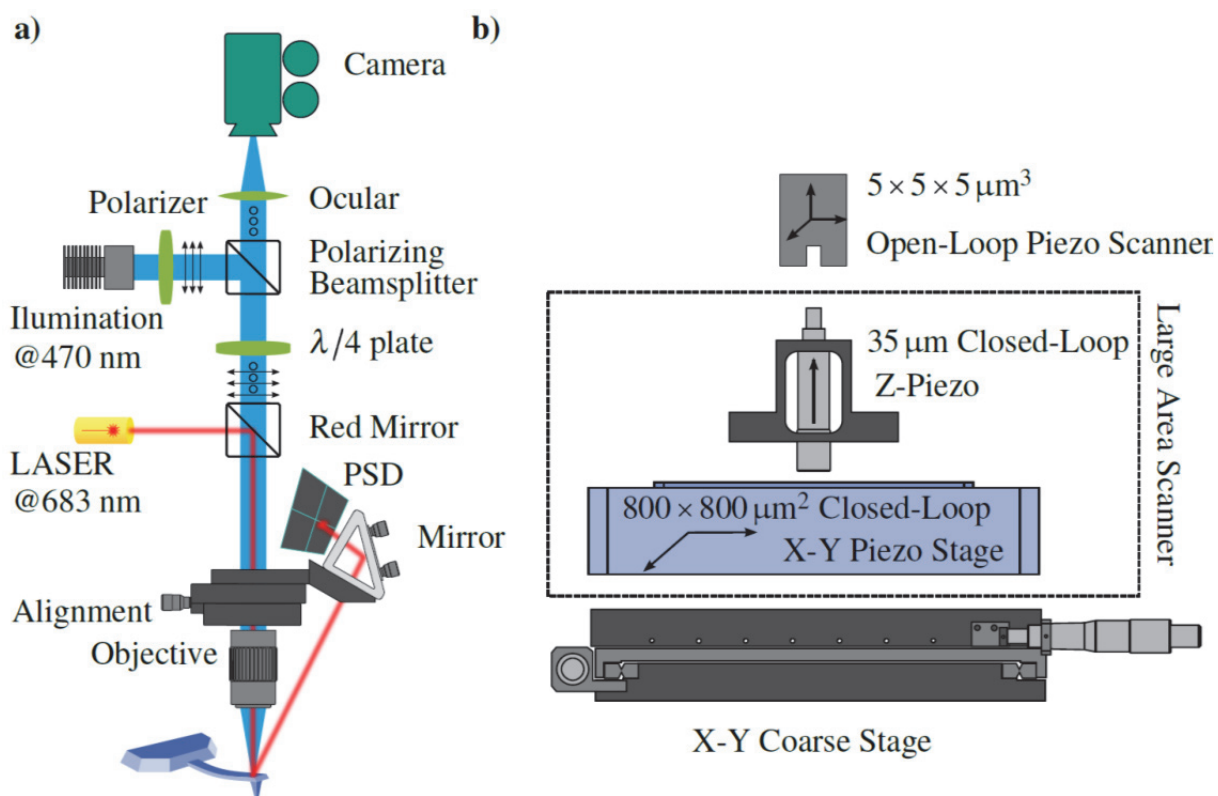


Fig. 1: a) Optical setup of the beam deflection read-out on the large area AFM. The laser is focused with an optical microscope objective on the backside of the cantilever. The reflected beam is focused on the PSD with a tilting mirror to align the beam towards the PSD. The illumination of the sample is done at a different wavelength than the laser wavelength to decouple laser and illumination by selective mirrors in the microscope and filters at the PSD. To reduce stray light within the optical microscope, polarizing optics for the illumination allow a directed transmittance of the microscope image. b) To realize both high lateral resolution and a large field of view, a high resolution open loop scanner is nested on a large area closed loop scanner. For coarse positioning of the sample, the entire scanner can be moved with respect to the cantilever and optics.

The AFM is operated with a commercial AFM controller (ARC2-biPolar by Asylum Research). The controller can directly drive open-loop piezo scanners, because of its integrated high voltage amplifier, as well as closed-loop scanners with an attached high voltage amplifier and closed-loop controller. As the AFM set up in this work is equipped with two independent scanners to combine both, a large field of view and a high spatial resolution, this feature allows driving both scanners directly. As the large area scanner is mechanically stable, it can be used to carry a second small area scanner with a higher spatial resolution and better dynamic properties. Using an AFM with multiple scanners allows both, a large field of view and a high spatial resolution. In Fig. 2, the potential of such an instrument is demonstrated. By scanning a calibration grating structure with structural details on length scales spanning from hundreds of micrometre to less than 200 nm and a feature height of 22 nm, the

topography of the sample can be investigated on all length scales. For a first overview of the sample, the maximum scan size can be used and sequentially zoomed into the region of interest. As the desired magnification level results in a scan size below the maximum scan range of the high resolution scanner, the scan position can be held with the large area scanner while the sample is scanned with the small area scanner enabling further zoom steps. Thereby, the instrument can span over three orders of magnitude in scan range which makes it a unique tool for micro- and nanomechanical analysis.

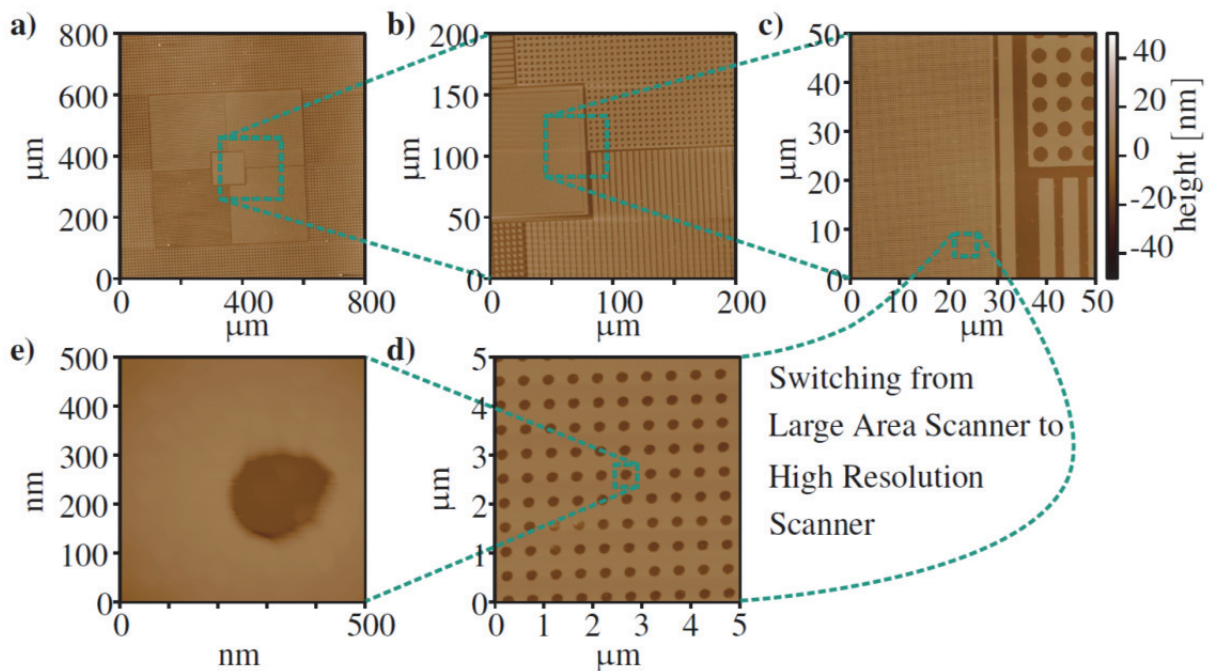


Fig. 2: Large area scanning with switching to the small area scanner for high resolution. All 5 pictures were taken on a SiO_x calibration grating with various feature sizes. **(a)** An $800 \mu\text{m} \times 800 \mu\text{m}$ overview image of the structure was taken before the scan size was reduced to $200 \mu\text{m} \times 200 \mu\text{m}$ in **(b)**. In **(c)** the scan size was reduced again to $50 \mu\text{m} \times 50 \mu\text{m}$. After switching to the high resolution scanner **(d)** and **(e)** show $5 \mu\text{m} \times 5 \mu\text{m}$ and $500 \text{nm} \times 500 \text{nm}$ images of the smallest feature sizes of the calibration grating. The nested scanner which can span over 3 orders of magnitude in scan range makes this instrument a versatile tool for micro and nanomechanical analysis.

Strategic Themes

Atomic force microscopy enables the imaging of surface properties down to the atomic scale. The imaging of single atoms, molecules, and defects is possible using the so-called non-contact atomic force microscopy technique (NC-AFM) in ultra-high vacuum (UHV) at low temperatures. Recent studies showed that this high resolution is also possible in liquids. The main requirement for successful atomic-scale imaging is the ability to acquire images of surfaces with extremely low noise and defined conditions over extended periods of time. Key to success is the signal-to-noise ratio and the preparation of clean samples as well as sharp and well defined tips. Therefore, our current research focusses on the improvement these issues together with the development of new imaging modes.

Further Collaboration outside KIT in internal projects

Dr. Dirk Meyners and Prof. Dr. Eckhard Quandt, Christian-Albrechts University of Kiel

Dr. Andreas Günther and Prof. Dr. József Fortágh, University of Tübingen

Dr. Daniel Ebeling and Prof. Dr. André Schirmeisen, University of Giessen

Prof. Dr. Santiago Solares, University of Maryland

Dr. Bernd Gotsmann, Dr. Heike Riel, IBM Zürich

Prof. Dr. Udo D. Schwarz, Yale University

References

[1] H. Hölscher, "Atomic Force Microscopy and Spectroscopy". In: Dynamical Force Spectroscopy and Recognition (ed. by A. R. Bizzari and S. Cannistraro), Taylor & Francis, pp. 51-91 (2012)

[2] Ali Tavassolizadeh, Tobias Meier, Karsten Rott, Günter Reiss, Eckhard Quandt, Hendrik Hölscher, and Dirk Meyners. Self-sensing atomic force microscopy cantilevers based on tunnel magnetoresistance sensors. Applied Physics Letters 102, 153104 (2013)

X-ray Photoelectron Spectroscopy (XPS)

Michael Bruns, Vanessa Trouillet

X-ray photoelectron spectroscopy (XPS) is the most widely used surface analysis technique to provide both quantitative atomic concentration and chemical state information of the detected elements. X-ray irradiation of surfaces results in the emission of photoelectrons whose energies are characteristic of their constituting elements. The information depth is approximately 5–7 nm. Angle-resolved XPS offers non-destructive resolution of structures within the XPS sampling depth, e.g. layer ordering, composition and thickness can be determined. Moreover, XPS can be utilized for sputter depth profiling to characterize thin films and multilayer systems by quantifying matrix-level elements as a function of depth.

In Mai 2013 a glove-box was attached to the K-Alpha XP spectrometer to enable atmosphere-contact-free sample transport and load into the spectrometer. In September 2013 complementary time-of-flight secondary ion mass spectrometry (ToF-SIMS) was opened for KNMFs *Call 11*.

The in-house research focuses on surface analytical characterization of (polymer)modified surfaces based on a number of cutting-edge projects within the Barner-Kowollik group, on energy storage materials in collaboration with the Pfleging, Ulrich, and Indris teams, and on organic light emitting diodes with the Colsmann group. In all cases XPS was used as one of the few characterization methods which give precise information of the molecular composition of the modified surfaces.

Biomimetic Polymer-Switching System on Gold Surfaces

Mussel adhesives feature the ability to attach to a wide range of materials, such as metals, wood, glass and even Teflon. The combination of synthetically mimicked mussel adhesives and the well-known principles of modular ligation (i.e. *Click*) chemistry provide opportunities for defined and orthogonal surface modifications, which can be accomplished on a broad variety of materials.

In this work the use of a biomimetic precursor molecule is presented, which performs an autopolymerization process under aqueous maritime conditions on important surfaces, such as gold substrates, and which possesses the capability to operate as a *switch* for the covalent linkage and delinkage of polymer chains equipped with an appropriate diene group.

To prove the successful step-wise functionalization of the gold surfaces XPS was chosen as a powerful tool to provide information on chemical binding states in a non-destructive manner. In particular, the increase and decrease of C 1s intensity ratios of C-O to C-C bonds prove the successful Diels-Alder (DA) and retro-Diels-Alder (rDA) reaction of dopamine-maleimide-PEG on gold surfaces (fig. 1a and b). The DA reaction does not seem to proceed to full conversion, possibly associated with the steric requirements of the polymer coil. [1]

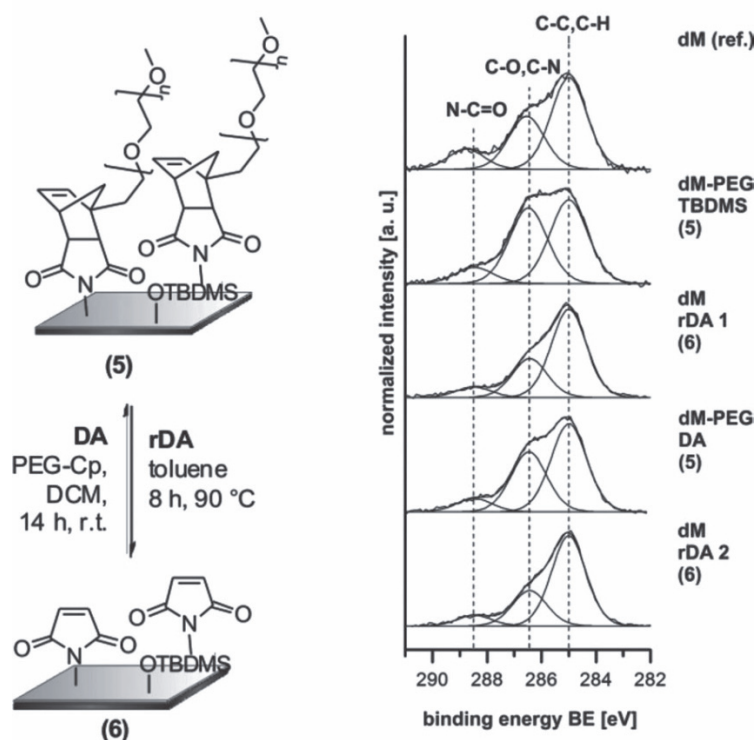


Fig. 1a: Schematic representation of DA and rDA reactions of dM-PEG on the surface of a gold substrate (left) and corresponding C 1s spectra (right). dM (reference) illustrates the surface attachment of pure dM on the gold substrate.

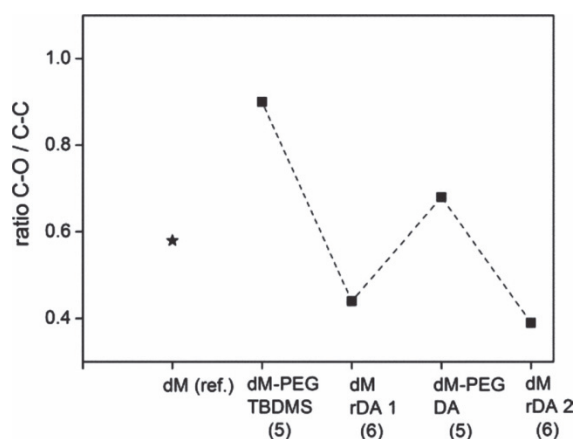


Fig 1b: C 1s intensity ratios of components assigned to C–O and C–C bonds. The DA/rDA system is depicted in squares and a dashed line, while the ratio for pure dM (reference) on the surface is labeled with an asterisk.

Solution Processed Organic Light Emitting Diodes (OLEDs)

Solution processing of organic semi-conductor devices is one of the key technologies towards low-cost optoelectronic devices. State-of-the-art OLEDs are mostly fabricated by thermal evaporation because these processes allow the stacking of different functional layer on top of each other. In contrast, solution deposition (printing and coating) is ruled by solvent limitations. One approach to deposit solution-processed metal oxides, like WO_3 , as a high-work function hole-injection layer is investigated by a facile precursor route from, tungsten(V)ethoxide or tungsten(VI)ethoxide, respectively. After conversion the achieved WO_3 layers are nearly insoluble.

The W 4f XP spectra in fig. 2 (left) together with the corresponding O 1s spectra (Data not shown) prove doubtlessly that sol-gel processed WO_3 layers using different precursors have the same stoichiometry as CVD deposited WO_3 layers. Moreover, XPS sputter depth profiles reveal adventitious carbon at the WO_3 surface only, shown exemplarily for the $\text{W}(\text{OEt})_5$ layer on ITO in fig. 2 (right). The absence of organic compounds throughout the WO_3 layer indicates full conversion of the precursor. [2]

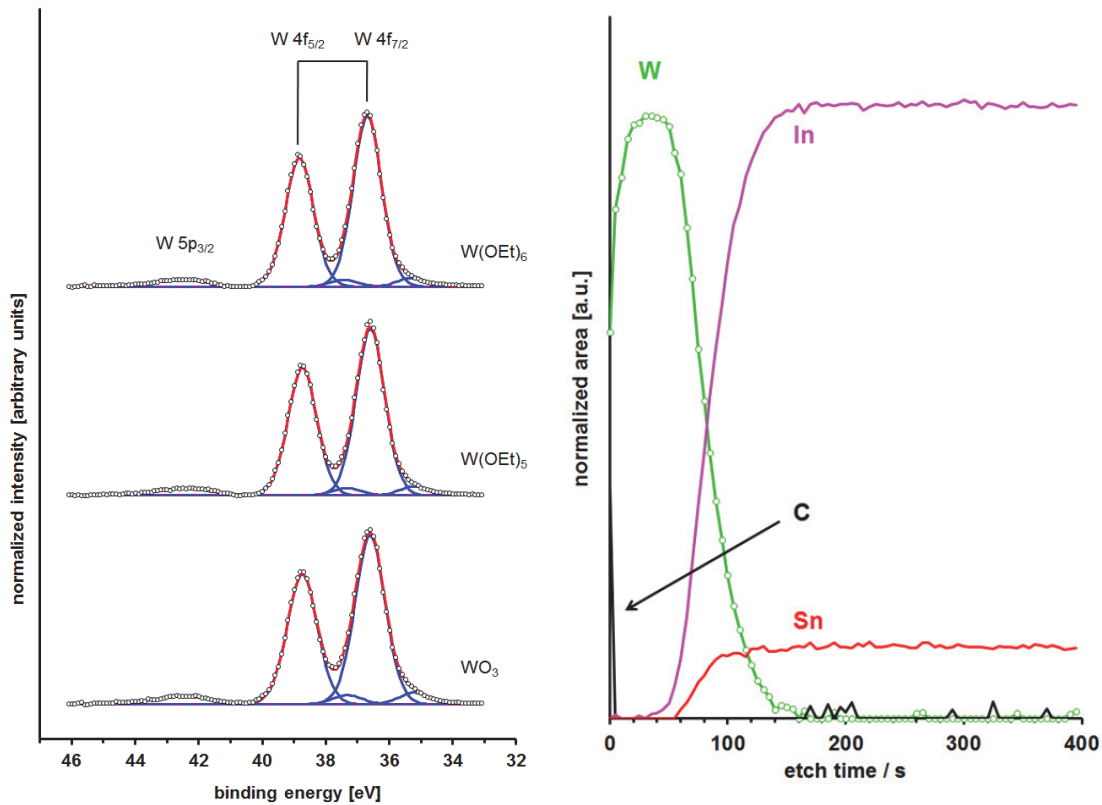


Fig 2: XPS W 4f spectra of the solution processed $\text{W}(\text{OEt})_5$ and $\text{W}(\text{OEt})_6$ based layers in comparison to the evaporated WO_3 reference (left) and XPS sputter depth profiles of a $\text{W}(\text{OEt})_5$ layer on ITO (right).

Another issue when designing new OLED architectures is the determination of the work function of different functional layers and layer systems. Again XPS is one of the few methods to achieve the desired information. The data for the layer and layer systems are depicted in fig. 3. The work functions were calculated from the X-ray photon energy ($\text{AlK}\alpha = 1486.6 \text{ eV}$) and the low kinetic energy spectrum cut-off of the respective sample.

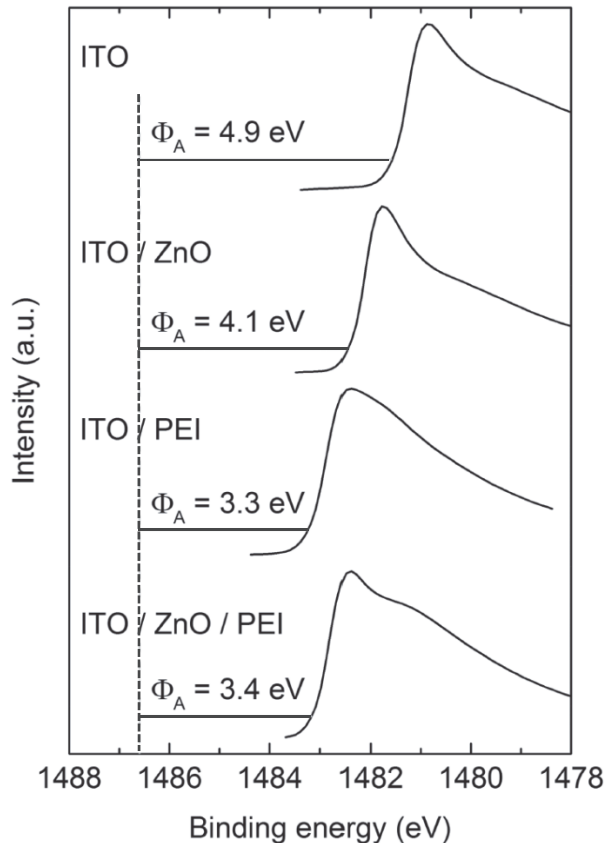


Fig. 3: Work functions of ITO, ITO/ZnO, ITO/PEI and ITO/ZnO/PEI electrodes as determined by XPS measurements. (PEI = polyethyleneimine). The energy scale was referenced to the sample's Fermi level = 0 eV.

R.F. Magnetron Sputtered Li-Mn-O Thin Films for Li-Ion Batteries

Most of the currently available lithium-ion batteries operate with toxic and highly flammable liquid electrolytes bearing risks of leakage, ignitability and undesirable side-reactions. To overcome these problems a very promising approach is the development of all-solid-state-LIBs by means of thin-film technology. Such batteries consist of a solid multilayer stack of cathode, electrolyte and anode thin films of about 3 μm overall thickness. Here we focus on the surface analytical characterization of environmental friendly Li-Mn-O based thin film cathodes fabricated by means of combined R.F. magnetron sputtering.

X-ray photoelectron spectroscopy (XPS) provides the chemical composition of the topmost layer in a non-destructive manner. The in-depth distribution of the film constituents was studied by XPS and time-of-flight secondary mass spectrometry (ToF-SIMS) sputter depth profiling. Special care was taken to guarantee atmosphere-contact-free sample transport and handling using the glove-box directly attached to the XPS spectrometer and the ToF-SIMS transport vessel. The XPS sputter depth profiles of a pristine Li-Mn-O thin film deposited onto an Au/stainless steel substrate depicted in fig. 4 evidences a uniform multilayer system with sharp interfaces. Due to a strong crosstalk of Au $5p_{3/2}$ and Fe 3p peaks the Li 1s profile was cut at the Li-Mn-O/Au interface. This procedure is justified by the corresponding Li^+ ToF-SIMS sputter depth profile in fig. 4. Quantitative XPS data were used to calibrate the ToF-SIMS results. In conclusion, only the combination of complementary XPS and ToF-SIMS allows for quantitative information on the uniformity and stoichiometry of Li-Mn-O thin films. [4]

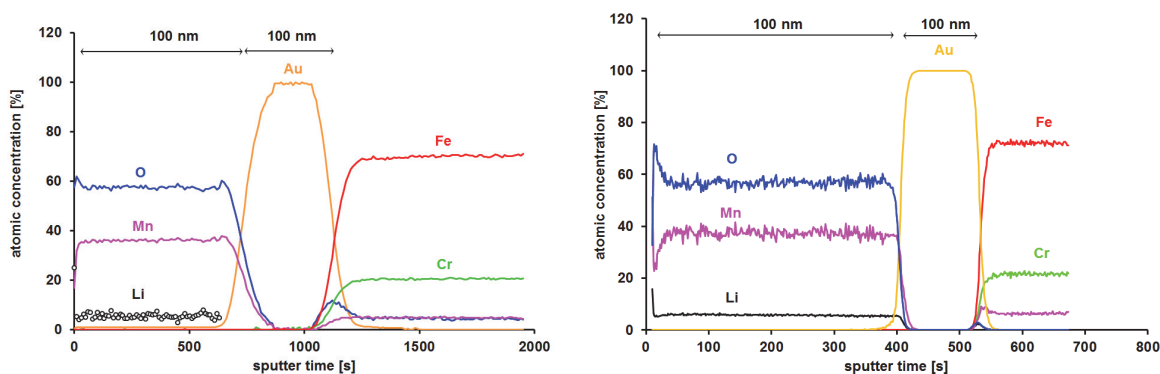


Fig 4: XPS (left) and ToF-SIMS (right) sputter depth profiles of a pristine Li-Mn-O thin film deposited onto an Au/stainless steel substrate. ToF-SIMS data were calibrated using XPS results.

Strategic Themes

It is the goal to offer and use correlative characterization tools to be able to provide a full picture of materials, layers and structures to be characterized. Thus, we have added time-of-flight secondary ion mass spectrometry (ToF-SIMS) as new technology complementary to XPS to the portfolio of characterization methods. In a mid to long term view sample transfer without environmental influence will be established between the different technologies.

In a scientific based collaboration with the Thermo Fisher Scientific Application Lab, East Grinstead, UK, the method is continuously updated due to our role as K-Alpha Demo-Lab for Thermo Fisher Scientific (since 2009). This is also demonstrated by commonly organizing the 4th International Workshop on XPS (June 25-27, 2014).

Further Collaboration outside KIT in internal projects:

B. Holländer, Peter Grünberg Institute (PGI-9), Forschungszentrum Jülich: *Rutherford Backscattering Spectrometry (RBS)*.

References

- [1] C. M. Preuss, A. S. Goldmann, V. Trouillet, A. Walther, C. Barner-Kowollik, Biomimetic Dopamine-Diels–Alder Switches, *Macromol. Rapid Commun.*, 34 (2013) 640–644.
- [2] S. Höfle, M. Bruns, S. Strässle, C. Feldmann, U. Lemmer and A. Colsmann, Tungsten oxide buffer layers fabricated in an inert sol-gel process at room-temperature for blue organic light emitting diodes, *Adv. Mater.*, 25 (2013) 4113–4116.
- [3] S. Höfle, A. Schienle, M. Bruns, U. Lemmer and A. Colsmann, Enhanced electron injection into inverted polymer light emitting diodes by combined solution processed zinc oxide / polyethylenimine interlayers, *Adv. Mater.*, 26 (2014) 2750–2754.
- [4] M. Bruns, J. Fischer, H. Ehrenberg, H.-J. Seifert, and S. Ulrich, ToF-SIMS and XPS Characterization of R.F. Magnetron Sputtered Li-Mn-O Thin Films for Li-Ion Batteries, ECASIA 13, October 13 - 18, 2013 Cagliari, Italy.

Single Crystal X-ray Diffraction (SCXD)

Andreas Eichhöfer, Olaf Fuhr, Dieter Fenske

Single crystal X-ray diffraction (SCXD) is a method of determining the arrangement of atoms within a crystal, in which a beam of X-rays strikes a crystal and causes the beam of light to spread into many specific directions. During 2013 the new Pilatus 300K detector was delivered and installed. It allows for shorter measurement times and an improvement of the quality of the data. In detail: absence of readout noise and dark current enables best possible data; a sharp point-spread function of one pixel results in excellent resolution of closely spaced reflections and maximizes signal-to-noise ratio; short readout times in the millisecond range allow continuous data collection and minimize acquisition times; a high dynamic range practically eliminates detector overloads.

A selection of in-house R&D activities performed in 2013 is described below.

Crystal structure identification of metal chalcogenide cluster compounds (Wen Yu, Xiaoxun Yang)

A multitude of metal chalcogenide cluster compounds containing the elements Cu, Ag or Au were measured. Their crystal structures could be solved from datasets obtained at different temperatures using the two available X-ray sources/wavelengths:

- a. Reactions of bi- or tetra-dentate phosphanes with [AuCl(tht)] yielded new crystalline Au complexes. These were used to synthesize polynuclear Au compounds containing up to 14 metal atoms. Within these reactions the formation of new kinds of ligands which are the result of substitution reactions was observed. The ligand conversions seem to be the result of an activation of the initial ligands within the coordination sphere of gold. The structures of all new gold compounds were determined by single crystal X-ray diffraction. These results were a significant part of the PhD thesis of Mrs. Wen Yu (corporate graduation under supervision of Prof. S. Dehnen (Marburg) and Prof. D Fenske (KIT)). Manuscripts for publication in peer reviewed journals of these results are in preparation.
- b. Metal thiolates of the elements copper and silver were reacted with various bidentatephosphane ligands. The structures of the crystalline products (either isolated clusters or 1-, 2- or 3D-frameworks) were determined by X-ray diffraction. These results were a significant part of the PhD thesis of Mrs. Xiaoxun Yang (Lehn Institute of Functional Materials, Sun Yat-Sen University, China). Manuscripts for publication in peer reviewed journals of these results are in preparation.

Structural analysis of large molecular aggregates

The compound $C_{55}H_{60}N_{12}O_{10}$ (**L**), which is known for more than a decade, has been found, in the solid state as well as in solvents of low polarity at room temperature, to exist not as the monomer previously characterized, but to undergo a remarkable self-assembly into a complex supramolecular species. The solid state molecular structure, determined by X-ray crystallography, revealed that it is a highly organized hexameric entity L_6 of capsular shape, built on two sets of three monomolecular components, linked through hydrogen bonding interactions. Collaboration with the group of Prof. J.-M. Lehn (University Strasbourg); manuscript submitted 2013 and published 2014.

Structural analysis of mono- or poly-nuclear iron and rare earth metal compounds

The research activity of the Functional Molecular Nanostructures Group (Prof. M. Ruben) at the Institute of Nanotechnology in Karlsruhe is oriented towards the design of functional nano-systems by state-of-the-art organic/inorganic synthesis and supramolecular self-assembly techniques. For the characterization of these new compounds single crystal X-ray analysis is an essential tool. Within the project to build supramolecular spintronic units several structures of mono- or poly-nuclear iron and rare earth metal compounds were determined. Manuscripts are in preparation; part of them submitted or already accepted.

Analysis of multinuclear metal complexes with macrocyclic ligands

Within the field of supramolecular chemistry the research of the group of M. Stadler (INT) deals with the synthesis and properties of trinuclear macrocyclic complexes, of tetranuclear grid-like complexes (interesting for their self-assembly process and magnetic properties) and of helical complexes (interesting as models of ion channels). The X-ray crystallography is of particular importance for the studies because a) of the absence of structural models for the species b) of their structural complexity (of which elucidation requires methods like NMR and X-ray diffraction) c) of the necessity of structural data (distances, angles) to be correlated with their properties and d) of the possible diversity of their mode of assembly (depending on anions, metal, solvent). Preliminary determinations of the structures of several multinuclear metal complexes with macrocyclic ligands have been performed. The publication of the data requires further investigation.

Further Collaboration outside KIT in internal projects:

University Marburg, Lehn Institute of Functional Materials, Sun Yat-Sen University, University Strasbourg

References

There have been no publications related to internal projects with KNMF acknowledgement in 2013. Several publications are under preparation or already issued in 2014.

Auger Electron Spectroscopy (AES)

Tobias Weingärtner, Thomas Bergfeldt

An Auger electron spectrometer (Physical Electronics 680 Xi Auger Nanoprobe) is operated in KNMF by the analytical group of the Institute of Applied Materials - Applied Material Physics (IAM-AWP).

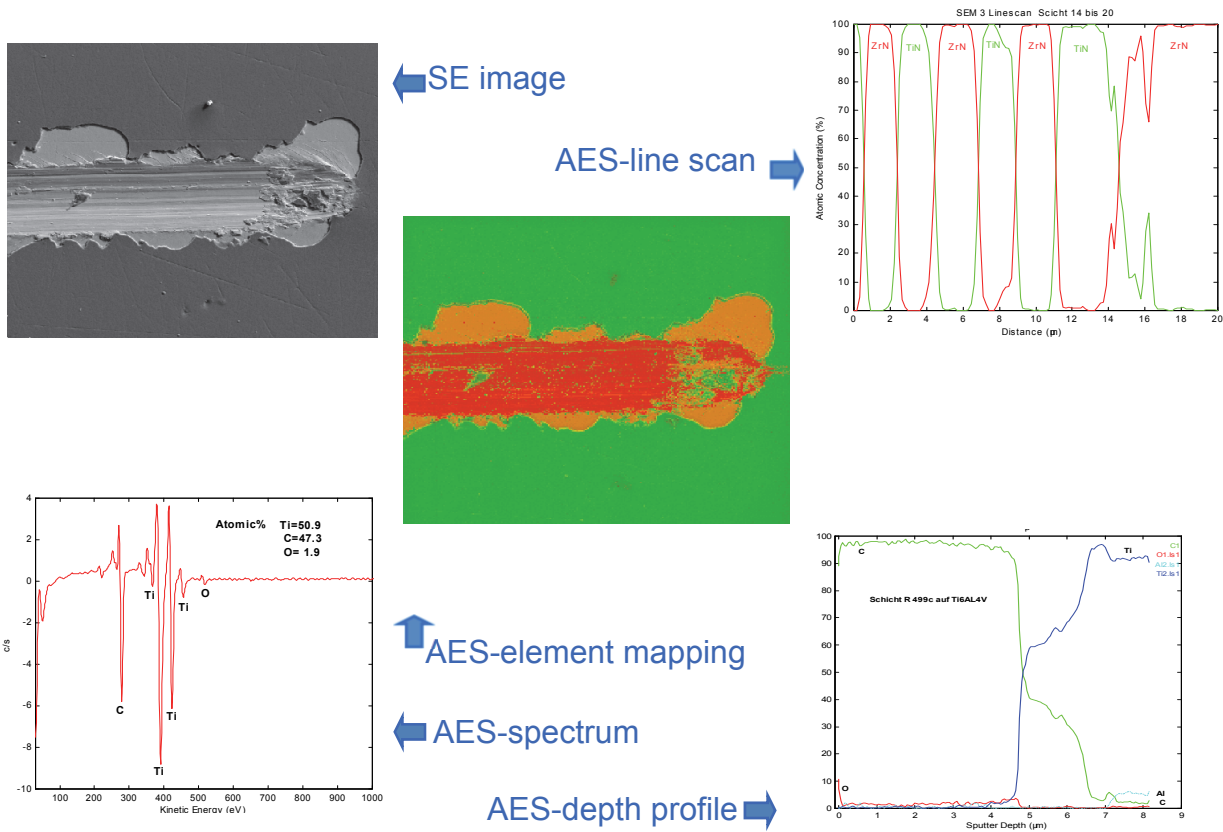
Design Parameters of our equipment

Auger electron spectroscopy (AES) provides information about the composition and to some extent also the chemical state, within nanometer sized solid and vacuum stable, conductive materials. In combination with Ar ion sputtering and Zalar rotation depth profiles to 1000 nm are available.

Semi-quantitative analysis of elements from Li through to U is possible by including sensitivity factors and quantitative analysis standards in the calculation. The practical detection limit ranges from 0.5 to 5 at%. The element distribution is shown by point and area analysis, linescans, depth profiles and element mappings. The practical lateral resolution begins at 24 nm and the depth resolution varies between 0.5 to 5 nm depending on the energy of the Auger electrons. The spot of the low energy ion gun has a size of about 0.5 mm. *In-situ* fracture of samples with liquid N₂ cooling can be used for grain boundary analysis.

In this year the instrument was upgraded with a High Energy Resolution Optic (HERO) and a new SE-Detector. The HERO improves the Auger-electron energy resolution from the AES. So for example it is now possible to differentiate between Al-metal and Al-oxide. The new SE-Detector has improved the sensitivity, the contrast and the S/N ratio of the SE image.

Measurement possibilities overview



The following examples illustrate the capability of the AES investigations.

Diffusion detection by line measurements

For one group at the Institute for Photon Science and Synchrotron Radiation (IPS) it was essential to know how deep oxygen diffuses in a Ti material, while they try out a new surface modification by laser treatment. Fig. 1 shows a SEM picture of a cross sectioned Ti material and Fig. 2 gives the corresponding line measurement. The oxygen diffusion can be seen as trend of the red curve in Fig. 2. In the illustrated example oxygen infiltrated the Ti material down to ca. 100µm.

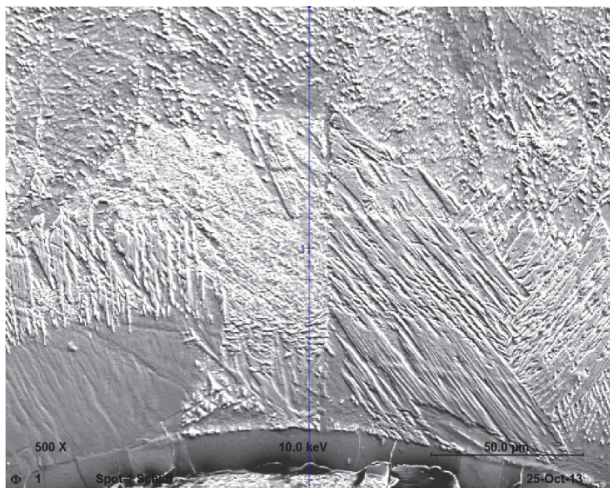


Fig. 1: SEM cross section of laser treated Ti

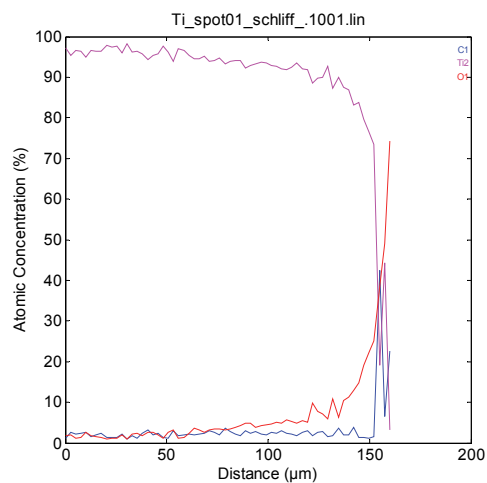


Fig. 2: Line measurement from bulk to surface

Element mapping at grain boundaries

A group at IAM-WPT investigates the design and development of divertor-parts for future fusion power plants. Tungsten, with its physical properties, is a very interesting material to be used for Plasma Facing Components. One of the methods which are used to determine the quality of the designed and machined tungsten components is to fracture a specimen in the ultra-high vacuum chamber of the AES. The fresh fracture surface can be measured immediately without the influences of normal atmosphere. The following pictures show a fracture surface of a tungsten specimen. In Fig. 6 the elemental mapping of La is shown. In this measurement the La allocation in a sintered tungsten bolt should be cleared.

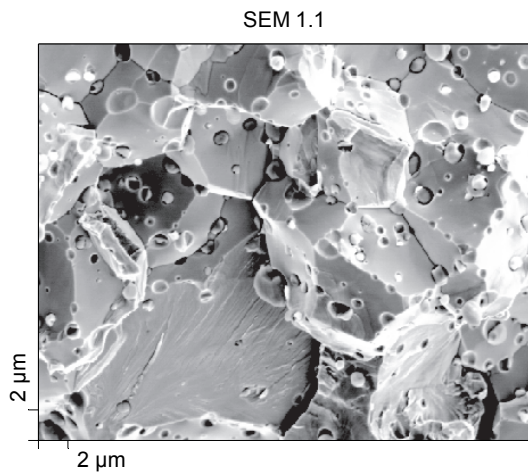


Fig. 5: SEM of a La doped W, fracture surface

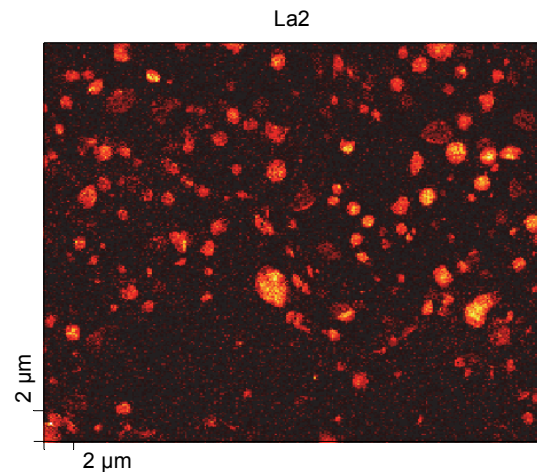


Fig. 6: La particles at the fracture surface

References

- [1] Zupanic, F.; Markoli, B.; Naglic, I.; Weingärtner, T.; Meden, A.; Boncina, T.; Phases in the Al-Corner of the Al-Mn-Be System, *Microscopy and Microanalysis* 19, 2013, 1308-1316

Bulk and Trace Analysis (BTA)

Thomas Bergfeldt

For the chemical characterization of materials five different analytical instruments are operated for the KNMF by the analytical group of the Institute of Applied Materials - Applied Material Physics (IAM-AWP).

X-Ray Fluorescence Spectrometry, XRF (S4 Pioneer, Bruker-AXS) is a non-destructive method for quick qualitative and semi-quantitative analysis. In combination with reference materials it is also a precise quantitative element determination. In samples like powders, solids, paste, films and liquids with sizes of 10 to 50000 μm elements from F to U can be analyzed in the concentration range from ppm to 100 % depending on the atomic mass.

Atomic or Optical Emission Spectrometry by Inductively Coupled Plasma, ICP-AES or ICP-OES (OPTIMA 4300 DV, Perkin-Elmer) is widely used in inorganic analysis of aqueous solutions and metals, oxides, nitrides, carbides etc. dissolved by acids. Simultaneous measurement of all elements except noble gas, halogens, hydrogen, oxygen and nitrogen can be conducted. The element concentrations range from below 1 $\mu\text{g/g}$ to 50 % in solids and < 0.001 to 100 mg/L in liquids. Reference or matrix matched standard solutions enable precise element determinations.

Mass Spectrometry by Inductively Coupled Plasma, ICP-MS (7500ce, Agilent) is the preferred analytical method for isotope and ultra trace analysis of aqueous and acid solutions. The quadrupole mass spectrometer equipped with off-axis Omega lenses and an octopole Reaction System (ORS) to eliminate polyatomic interferences covers the mass range from 6 to 260 u, Li to U. Depending on the sensitivity and number of isotopes the quantification limits vary from 1 ng/g to 1000 $\mu\text{g/g}$ in dissolved solids or < 0,001 to 1000 $\mu\text{g/L}$ in aqueous solutions.

Carrier Gas Heat Extraction, CGHE (TC600, LECO) is one of few reference methods to determine oxygen and nitrogen. Solid samples are heated in a graphite crucible in a metal bath up to 2600°C with He as carrier gas. Released CO and CO₂ are detected by IR and N₂ by thermal conductivity. The concentrations range from < 0.1 $\mu\text{g/g}$ to 50 %.

In a **Carbon-Sulfur-Analyzer** (CS600, LECO) solid samples are combusted in a high frequency furnace under oxygen flow and the formed CO₂ and SO₂ are detected by IR-cells. C and S concentrations range from 5 $\mu\text{g/g}$ to 100 %.

In 2013 a lot of different intern research issues for KNMF and the HGF program STN had taken place.

One important task was the investigation of TiO₂Au nanoparticles and their accurate proportions. A new method for the chemical digestion had to be found and the quantification was carried out with the ICP-MS for Au and ICP-OES for Ti.

Hybrid Type	Method	Au %									
Au-1/TiO ₂ A	Theory	0.1	0.25	0.5	1	2	5	10	20	50	
	Experiment (ICP-MS)	0.09	0.19	0.42	0.87	1.81	4.61	9.71	19.35	43.47	
Au-1/TiO ₂ B	Theory	0.10	0.25	0.5	1	2	5	10	20	50	
	Experiment (ICP-MS)	0.13	0.47	0.74	1.53	2.78	6.89	13.51	24.77	58.58	

Table 2: Comparison of calculated and ICP-MS measured Au/Ti ratios for Au-1/TiO₂A and Au-1/TiO₂B hybrids. Miljevic, M.; et al. *Advanced Functional Materials*, 24(2014) pp.907-915.

A new topic was the chemical analysis of different organic electrolytes, such EMC, DMC or DME which are used in batteries. In this context we have looked for different elements like Li, S, Mn, Ni etc. This usually involved a very small quantity of solution for analysis, this was difficult to handle. The newly developed method included the oxidation of the electrolyte with nitric acid and hydrogen peroxide by 433 K in a microwave.

To control and verify the results the analytical group works with a substantial quality management. We work analog to the requirements of ISO/IEC 17025 for analytical laboratories, take part at round robin tests (GDMB), calibrate with certified reference materials, inspection of measuring and testing equipment and document every data.

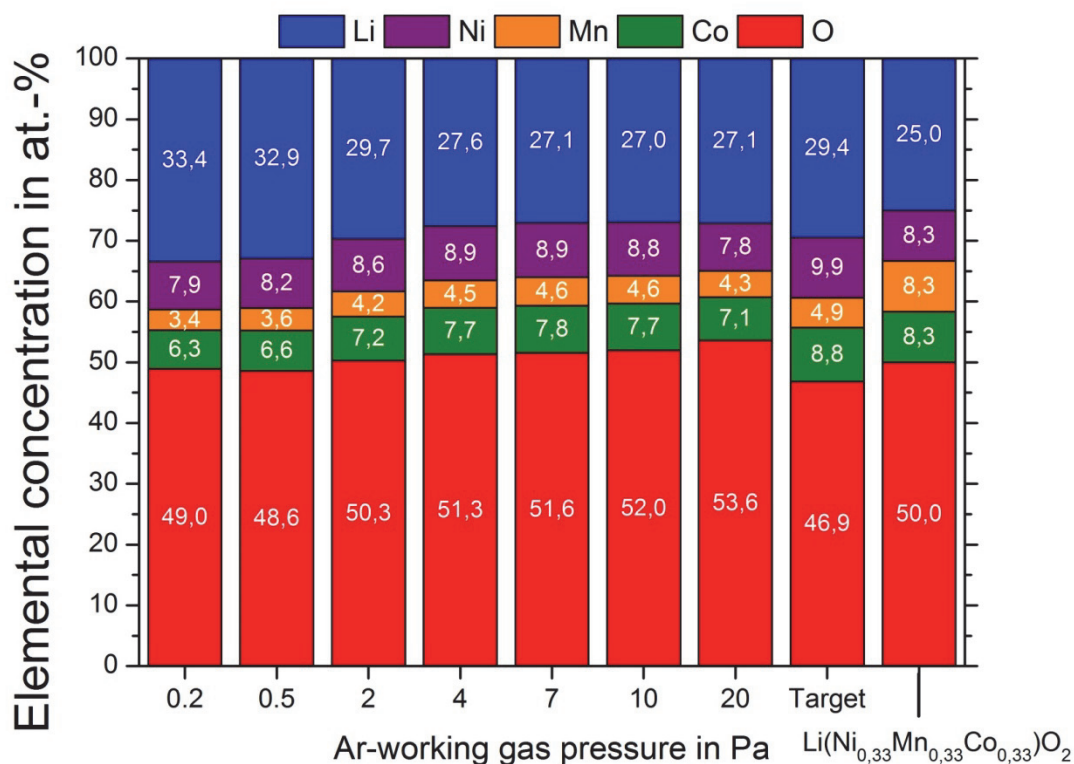


Fig. 1: Constitution and microstructure of magnetron sputtered Li-Ni-Mn-Co-O thin film cathodes for lithium-ion batteries as a function of working gas pressure. Marc Strafela, KIT

Further Collaboration outside KIT in internal projects / Collaboration in in-house research

The Bulk and Trace Analysis group is not only part of KNMF. There are many other activities and co-operations with other research groups in the KIT and abroad. The following list gives a short overview about topics and co-operations in 2013.

HGF programme Fusion:

- Determination of main compounds and impurities in ceramic breeding blanket
- Chemical analysis of ODS alloys
- Impurities in PbLi in the liquid metal corrosion loop PICOLLO

HGF programme Nuclear:

- Chemical analysis of Zr

HGF programme REUN and EE:

- Determination of elements from filters deposits of an experiment by REGA (Research Entrained-flow GASifier). This is part of a Humboldt stipendium research in the institute of ITC
- Chemical analysis of raw material for Celitement a new hydraulic binder. Celitement is a foundation of the Schwenk group, Karlsruhe Institute of Technology (KIT), and scientists of KIT

Co-operation with other institutes in KIT:

- Chemical analysis of material from catalyzer (ITCP)
- Stoichiometric of Ti and Au in TiO₂ and Au Nano particles in buffer solution (DFG-Centre for Functional Nanostructures).
- Chemical analysis of dust from different towns in China (IMG)
- Chemical analysis of Li and S in organic solutions from LiS-batteries (BELLA)
- Chemical analysis of steel and refractory metals (IAM-WK)
- Co in Cyclohexan (IMVT)

Project with BMU:

- Chemical analysis of Ba in different solutions from test stations by the institute of IKET (KIT). This is part of the project "Scaling and outgassing in geothermal sites – influence factors, kinetic, inhibitors and technical actions"

References

[1] Cupid, D.M.; Lehmann, T.; Bergfeldt, T.; Berndt, H.; Seifert, H.J. Investigation of the lithium-rich boundary of the Li_{1+x}Mn_{2-x}O₄ cubic spinel phase in air. *Journal of Materials Science*, 48(2013) S.3395-3403

[2] Fischer, J.; Adelhelm, C.; Bergfeldt, T.; Chang, K.; Ziebert, C.; Leiste, H.; Stüber, M.; Ulrich, S.; Music, D.; Hallstedt, B.; Seifert, H.J. Development of thin film cathodes for lithium-ion batteries in the material system Li-Mn-O by r.f. magnetron sputtering. *Thin Solid Films*, 528(2013) S.217-223

[3] Gotcu-Freis, P.; Pfleging, W.; Mangang, M.; Bergfeldt, T.; Prill, M.; Markus, T.; Seifert, H.J. Electrochemical studies using GITT in cells with 3D structured intercalation cathode materials.

3. Statustreffen des Helmholtz Portfolios 'Elektrochemische Speicher im System - Zuverlässigkeit und Integration', Karlsruhe, 11.-12. Dezember 2013

[4] Canic, T.; Baur, S.; Bergfeldt, T. Einflussparameter auf die Barytausfüllungen aus Geothermalwasser. Geothermie Kongress 2013, Essen, 12.-14. November 2013

[5] Issac, I.; Heinzmann, R.; Kaus, M.; Zhao-Karger, Z.; Gesswein, H.; Bergfeldt, T.; Chakravadhanula, V.S.K.; Kübel, C.; Hahn, H.; Indris, S. Synthesis and electrochemical performance of nanocrystalline $\text{Al}_0.4\text{Mg}_0.2\text{Sn}_0.4\text{O}_{1.6}$ and $\text{Al}_0.25\text{Mg}_0.38\text{Sn}_0.38\text{O}_{1.5}$ investigated by in situ XRD, $^{27}\text{Al}/^{119}\text{Sn}$ MAS NMR, ^{119}Sn Mössbauer spectroscopy, and galvanostatic cycling. *Journal of Materials Chemistry A*, 1(2013) S.13842-13852

[6] Lepple, M.; Adam, R.; Cupid, D.M.; Franke, P.; Bergfeldt, T.; Wadewitz, D.; Rafaja, D.; Seifert, H.J. Thermodynamic investigations of copper oxides used as conversion type electrodes in lithium ion batteries. *Journal of Materials Science*, 48(2013) S.5818-5826

LA-ICP-MS

Thomas Bergfeldt, Tobias Weingärtner

A Laser Ablation (UP 193 FX, New Wave) – Inductively Coupled Plasma – Mass Spectrometry (7500 ce, Agilent) is operated in KNMF by the analytical group of the Institute of Applied Materials - Applied Materials Physics (IAM-AWP).

Short technology description/Overview and Main Features (Equipment Capabilities)

LA-ICP-MS is a sensitive analytical method (0,000001 – 100%) for rapid multi-element (Li - U except C, N, O, F, Cl) determination in the trace and ultra-trace range of different solid sample materials, technical products and even biological samples (biological samples can't be analyzed in this laboratory). A small area (\varnothing 10 – 200 μm) of the sample is vaporized in laser plasma by focused laser radiation and transported with argon or helium in the inductively coupled plasma ion source of an ICP-MS. There the material is atomized, ionized, accelerated into the mass spectrometer and separated according the mass/charge ratio and energy/charge ratio and detected by electron multipliers.

The main advantage of LA-ICP-MS is that samples are investigated not under vacuum but in atmospheric pressure and electrically conductive as well as non-conductive material can be investigated and be analyzed in the concentration range from ppm to 100 % depending on the atomic mass.

Technological upgrades in 2013

To increase the measurement possibilities some modifications has been made to the instrument in 2013. The transportation gas has been changed from argon to helium and a complete new set of cones and lenses have been bought for the ICP-MS. So it is now possible to change between ICP-MS measurement with liquids from an Autosampler and LA-ICP-MS measurement with solid samples from the sample chamber of the laser with fewer cross contamination risks.

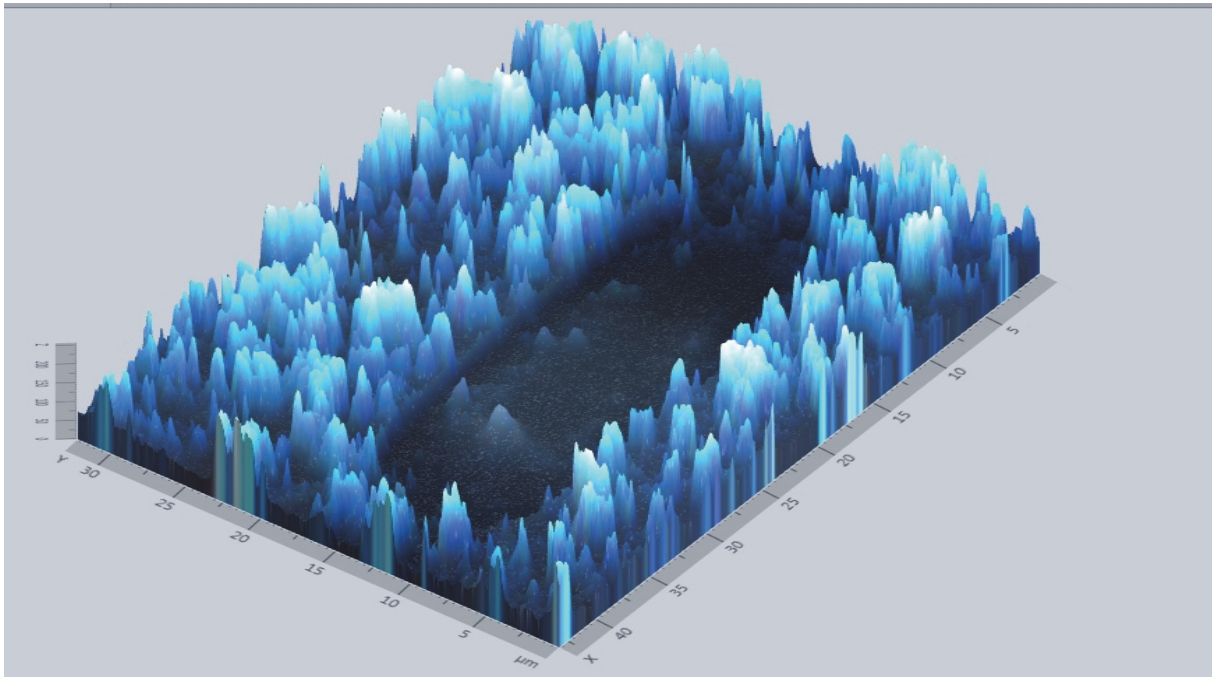


Fig. 1: 3D View from car finish on a car aluminum panel sheet after ablation. [1]

Figure 1 shows the ablation of a blue car finish on a car aluminum panel sheet under a Zeiss microscope. The blue part are the unaffected part of the car finish and the black rectangle is the ablate area.

Further technical work began in 2013 and will be completed in Spring 2014 to investigate the accurate quantification possibilities of the LA-ICP-MS Comparison. -- So far it is only possible to measure element ratios or semiquantitative measurements with the LA-ICP-MS with a measuring inaccuracy larger than 25 %. In liquids the measuring inaccuracies are less than 5 %. So far it could be shown that in line scans RSD values less than 2 % can be reached and the repeatability of the same measurements on different days is very good.

References

[1] Ciske Faber, Benjamin Stephan, Entwicklung einer Laserablation - Induktiv gekoppeltes Plasma – Massenspektroskopie (LA-ICP-MS) Multielementmethode zur qualitativen Bestimmung von Verunreinigungen in verschiedenen Materialien unter Verwendung von Helium als Trägergas. Techniker Arbeit an der Technischen Fachschule in Ludwigshafen (2013).

Thin Film Characterisation (TFC)

Monika Rinke, Julian Fischer

For the thin film characterization different measurement setups are operated within KNMF at the Institute for Applied Materials (IAM-AWP) to analyse the composition, structure, properties and behaviour of thin films. The focus of the characterization is on the microstructure (by XRD and Raman spectroscopy), the mechanical and the magnetic properties of thin films.

Li-ion battery cathode materials

During the last years, extensive research has been carried out to develop advanced lithium including metal oxides as positive electrodes for lithium-batteries. Their use as insertion electrodes for rechargeable 4 V lithium batteries is favoured because of their diffusion pathways for Li ions and high energy density (due to the combination of high capacity and high voltage). Today most commercially available lithium ion batteries are still based on the toxic and expensive LiCoO₂ as a standard cathode material. Especially Li-Mn-oxides are ideal as high-capacity Li-ion battery cathode materials by virtue of their low toxicity and low costs (high natural abundance of Mn). However, there remain several key material issues such as the structural stability over several hundreds of cycles, which need to be solved.

Raman spectroscopy is a well suited technique for the characterization of the local structure in transition metals. Since Raman microscopy is an optical spectrometry, it has several characteristics very well suited to the study of these electrode materials for lithium ion batteries.

- Raman experiments can be performed without sample preparation
- under careful excitation conditions the analysis is nondestructive, the analysis causes neither damage nor alteration
- good spatial resolution: it is possible to focus the excitation beam on a very small spot, whose diameter depends on the selected laser wavelength and the aperture of the objective, typically <1 μm .

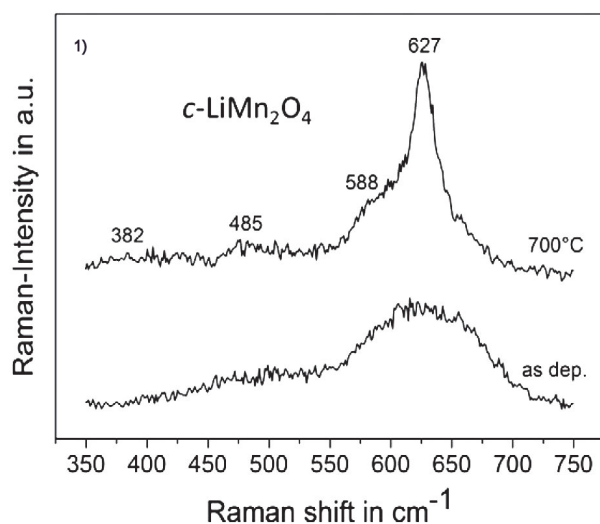


Fig. 1: Raman spectra of films as deposited with

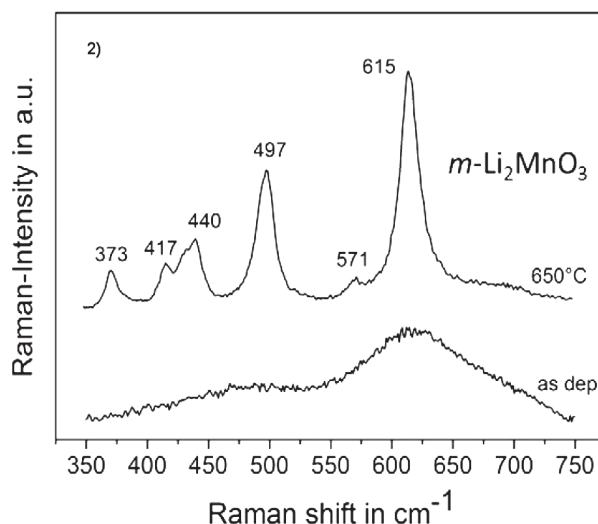


Fig. 2: Raman spectra of films as deposited with

a LiMn_2O_4 -target (16 Pa/100 W) and annealed in air at 700°C (film thickness: $1.6\ \mu\text{m}$).

a Li_2MnO_2 -target (4 Pa/100 W) and annealed in air at 650°C (film thickness: $1.0\ \mu\text{m}$).

While vibrational spectroscopy cannot give the detailed structural information available from high quality diffraction data, it is sensitive to the local environments of lithium and transition metal cations in the oxide lattice. The number, frequency, and relative intensities of the vibrational bands depend upon both coordination geometries and bond strengths and thus are very sensitive to the crystal symmetry, coordination geometry, and oxidation states.

A careful examination of the data allows the determination of various features such the local distortion, the phase evolution during lithium insertion-extraction, and the structural modification towards amorphization, etc.

Different lithium manganese oxide thin films have been synthesized by nonreactive r.f. magnetron sputtering in combination with well-defined post deposition annealing processes [1]. For the first time all three Li–Mn–O microstructures (spinel, monoclinic and orthorhombic) were synthesized by one upscalable thin film deposition method. All three structures were well distinguished by Raman spectroscopy and XRD.

The elemental investigation analysis of films sputtered with a LiMn_2O_4 target revealed a composition in the range of a stoichiometric LiMn_2O_4 compound, whereas the films, which were sputtered with a Li_2MnO_2 target mainly showed compositions close to Li_2MnO_3 . In both cases annealing in air produced the crystal structure, which was expected from the stoichiometry before annealing which means spinel and monoclinic respectively.

The corresponding Raman spectra of the as deposited and the annealed film (700°C) can be seen in Fig. 1 and 2. Whereas the spectrum of the as deposited material show a broad band near $630\ \text{cm}^{-1}$, the spectrum of the annealed layer exhibit the characteristic shape of a cubic spinel phase and of the monoclinic Li_2MnO_3 , respectively.

The Raman spectrum of LiMn_2O_4 is dominated by a strong and broad band at approximately $627\ \text{cm}^{-1}$. It is viewed as the symmetric Mn-O stretching vibration of MnO_6 octahedrons, assigned to the A_{1g} symmetry. Its broadness is related with the cation/anion bond lengths and polyhedral distortion occurring in LiMn_2O_4 .

The intensity of the shoulder peak at $582\ \text{cm}^{-1}$ of the F_{2g} mode may be attributed to the Mn^{4+} -O bonding vibration and could help to obtain information on the lithium stoichiometry of the film after annealing. A band with a medium intensity appears at approximately $485\ \text{cm}^{-1}$, which has the F_{2g} symmetry. Two low-wavenumber bands having a weak intensity are observed at approximately 428 and $382\ \text{cm}^{-1}$. They have the E_g - and F_{2g} -symmetry, respectively.

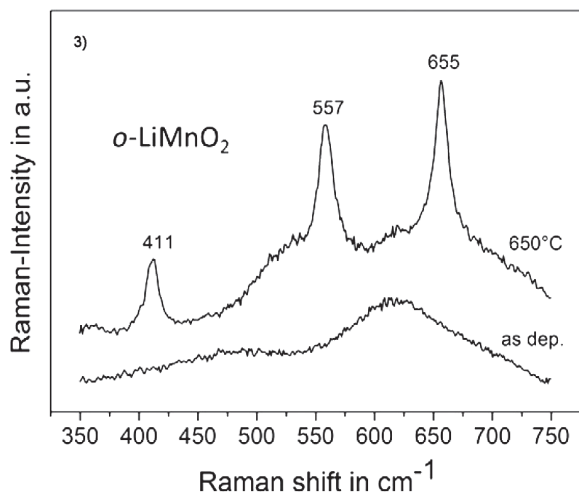


Fig. 3: Raman spectra of films as deposited with a Li_2MnO_2 -target (4 Pa/100 W) and annealed in vacuum at 700°C (film thickness: 1.4 μm).

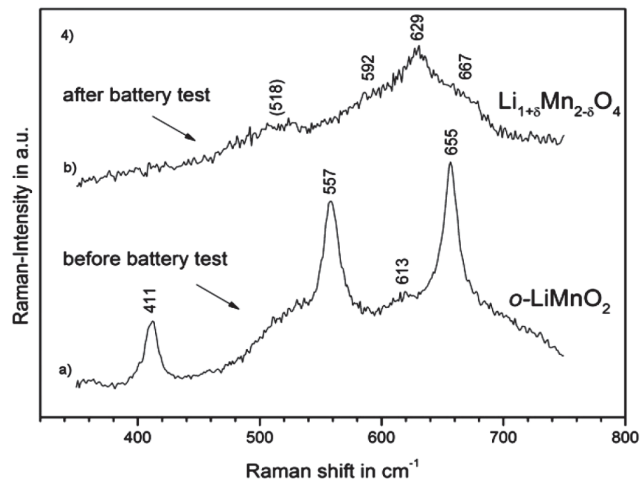


Fig. 4: a) Raman spectrum of the $o\text{-LiMnO}_2$ before the electrochemical tests. b) Post mortem analysis of the cycled $o\text{-LiMnO}_2$ cathode shows Raman signals of the cubic $\text{Li}_{1+\delta}\text{Mn}_{2-\delta}\text{O}_4$ spinel structure after battery test.

At 650 °C six distinct Raman bands can clearly be seen at 373, 417, 440, 497, 571 and 615 cm^{-1} . The spectrum matches the results obtained by Julien and Massot, very well (Mater. Sci. Eng. B 100 (2003) 69) on powder samples and shows some special features, which are characteristic of the Li_2MnO_3 phase. Especially the small signal at $\sim 571 \text{ cm}^{-1}$ and the double band at around 417/440 cm^{-1} can easily be identified.

The deposited spectrum in Fig. 3 is the same that in Fig. 2. After annealing to 650 °C in vacuum, the spectrum shows three bands at the Raman shift positions of 655 cm^{-1} , 557 cm^{-1} and 411 cm^{-1} , which could all be attributed to the $o\text{-LiMnO}_2$ phase.

The cathodes of orthorhombic- LiMnO_2 thin films were cycled in half cells against metallic lithium [2]. They showed a cycle induced transformation into the cubic lithium manganese oxide spinel structure during the first cycles. The transformation of the films was confirmed by in-situ cyclic voltammetry measurements and ex-situ Raman spectroscopy (Fig. 4).

Further Collaboration outside KIT in Internal Projects:

Universities of: Bochum, Kiel, Kaiserslautern, Aachen, Uppsala (Sweden), Linköping (Sweden), Coimbra (Portugal)

Companies: Walter, Gühring, Balzers, Rockwell Collins

Research Centers: FHG-IMW Freiburg, KIST (Korea), AIN Pamplona (Spanien)

References

[1] J. Fischer et al., Thin Solid Films 528 (2013) 217.

[2] J. Fischer et al., Thin Solid Films 549 (2013) 263.

KNMF Laboratory for Synchrotron Radiation

Infrared and hard X-ray spectroscopy, X-ray diffraction – IR1, IR2, PDIFF, XAS, and X-SPEC Beamlines

T. Baumbach, S. Doyle, B. Gasharova, C. Heske, B. Krause, S. Mangold, Y.-L. Mathis, D. Moss, A.-S. Müller, and L. Weinhardt

ANKA, the national German synchrotron radiation facility at KIT, is engaged in the KNMF activities of its Laboratories for Microfabrication and Synchrotron Characterization. ANKA provides dedicated user service for the Nanoscience and Microtechnology user communities. Beamtime is accessible *via* the proposal portals of the KNMF (in particular in combination with other KNMF technologies) and of ANKA, and beamtime allocation is based on a peer-review process.

In 2013, the pool of ANKA beamlines accessible *via* the KNMF proposal portal included infrared/THz spectroscopy and ellipsometry (IR1 beamline), polycrystalline/powder X-ray diffraction (PDIFF beamline), and X-ray absorption spectroscopy (XAS beamline). Furthermore, the commissioning of the IR2 beamline (infrared/THz microspectroscopy) was completed and user operation commenced. X-SPEC, a future beamline in the soft and hard X-ray regime for X-ray spectroscopy and *in-situ* studies, was designed and ordered. In the following, the various beamline capabilities and their upgrades in 2013 will be briefly discussed, and a science application of an off-normal sputter deposition study will be presented.

The **IR1 and IR2 beamlines** feature classical synchrotron radiation and edge radiation from a bending magnet and offer infrared/THz spectroscopy, microspectroscopy, and ellipsometry capabilities. The experimental stations at both beamlines are based on FTIR spectrophotometers (Bruker IFS 66v/S), covering a spectral range from 4 to 10,000 cm^{-1} with a spectral resolution down to 0.1 cm^{-1} , and equipped with high-sensitivity detectors and appropriate beam-splitters for all spectral ranges.

The ellipsometry set-up at IR1 runs under vacuum and features an optimized bolometer detector and a liquid He cryostat. Coherent THz emission can be exploited when the ANKA accelerator is operated in low- α mode, resulting in an extremely intense beam in the 5 – 50 cm^{-1} spectral range.

The newly accessible IR2 experimental station exploits the brilliance advantage of synchrotron light to offer infrared/THz microspectroscopy at measurement spot sizes down to the diffraction limit. The vacuum spectrophotometer is complemented by a Bruker IRscope II infrared microscope with single-element and imaging detectors, including a liquid He cooled bolometer for the far IR spectral range down to 100 cm^{-1} . A selection of microscope objectives is available for measurements in transmission, reflection, grazing incidence, and ATR sampling geometry.

The **XAS beamline** features X-ray absorption spectroscopy (XAS) on a dipole magnet source. Besides standard XAS measured in transmission (detection limit ~5%) and fluorescence (detection limit 1 mmol/L) modes, the beamline offers a “Quick XAS” mode, allowing scans as fast as 30 seconds. Grazing incidence XAS provides surface sensitivity in the 50 nm range. The XAS beamline spans the energy range from 2.4 to 27 keV, covering the K-edges from S to Cd, and up to the L-edge of U. Upgrades performed in 2013 focused

on the installation of an experimental table with high load capacity and 6 degrees of freedom. Further on-going upgrades will allow highly reproducible (better than 10 μm) and fast exchange of sample holders.

The **PDIFF beamline** is primarily used for hard X-ray diffraction investigations of bulk polycrystalline materials under varying *in-situ* conditions, utilizing various combinations of detectors and sample-environmental chambers. Various transmission and reflection diffraction geometries are possible, and samples in various forms can be measured (capillaries, flat plates, pellets, and thin films). In addition, the beamline offers the possibility of high-resolution powder diffraction for detailed structural investigations, residual stress and texture measurements, albeit with reduced options for *in-situ* observations.

In 2013 a wide variety of investigations were performed at the beamline for the elucidation of the relationship between crystal and supramolecular structure and materials functionality. Examples from current research projects, with particular focus on micro- and nano-properties, include *in-situ* studies on the influence of grain size, grain boundaries and stacking faults on the deformation mechanics in thin multilayer films, *in-situ* observation of strain development in pearlitic steel wires, and the *in-situ* characterization of phase composition in Li-ion battery materials during charge/discharge cycling. Technical developments at the PDIFF beamline in 2013 have included the installation of a motorized linear stage for the large CCD camera and the commissioning of a setup for repeated cyclic measurement of multiple battery-cells during charging/discharging processes.

The portfolio of beamlines available through the KNMF will, in the future, be complemented by the **X-SPEC beamline**. X-SPEC will cover a broad energy range (approx. 80 eV to 15 keV), bringing together soft and hard X-rays in one beamline, and combining them with cutting-edge spectroscopy techniques. These methods will extend KNMF's spectroscopy portfolio with capabilities such as hard X-ray photoelectron spectroscopy (HAXPES) and resonant inelastic soft X-ray scattering (soft RIXS).

Nanostructure formation mechanisms during sputter deposition

As an example of research conducted within the framework of the KNMF Laboratory for Synchrotron Radiation (in combination with other KNMF facilities), we report on a study of the fundamental structure formation mechanisms during sputter deposition. Off-normal deposition offers very interesting possibilities to tailor the nanostructure of sputter-deposited thin films. The direction of the incoming flux influences the orientation, size, and porosity of columnar structures formed, e.g., by transition metal carbides and nitrides. It can also change the crystallite orientation, leading in the extreme case to the formation of biaxial textures. These textures are of special interest since, for many applications, they offer a cheap alternative to single-crystalline material.

Both the texture and the shape of the columns allow for the control of the mechanical properties of the coating. For the prediction of these properties, a detailed understanding of the growth process is required. In situ X-ray reflectivity, EXAFS and diffraction measurements at the synchrotron give detailed insight into the sputter process [1]. To further deepen the understanding and to arrive at a unique interpretation of the results, however, further correlation with complementary measurement approaches is needed. As shown in Fig. 1, additional data for a VN thin film surface was obtained, utilizing the experimental capabilities to derive pole figure measurements and scanning probe microscopy data.

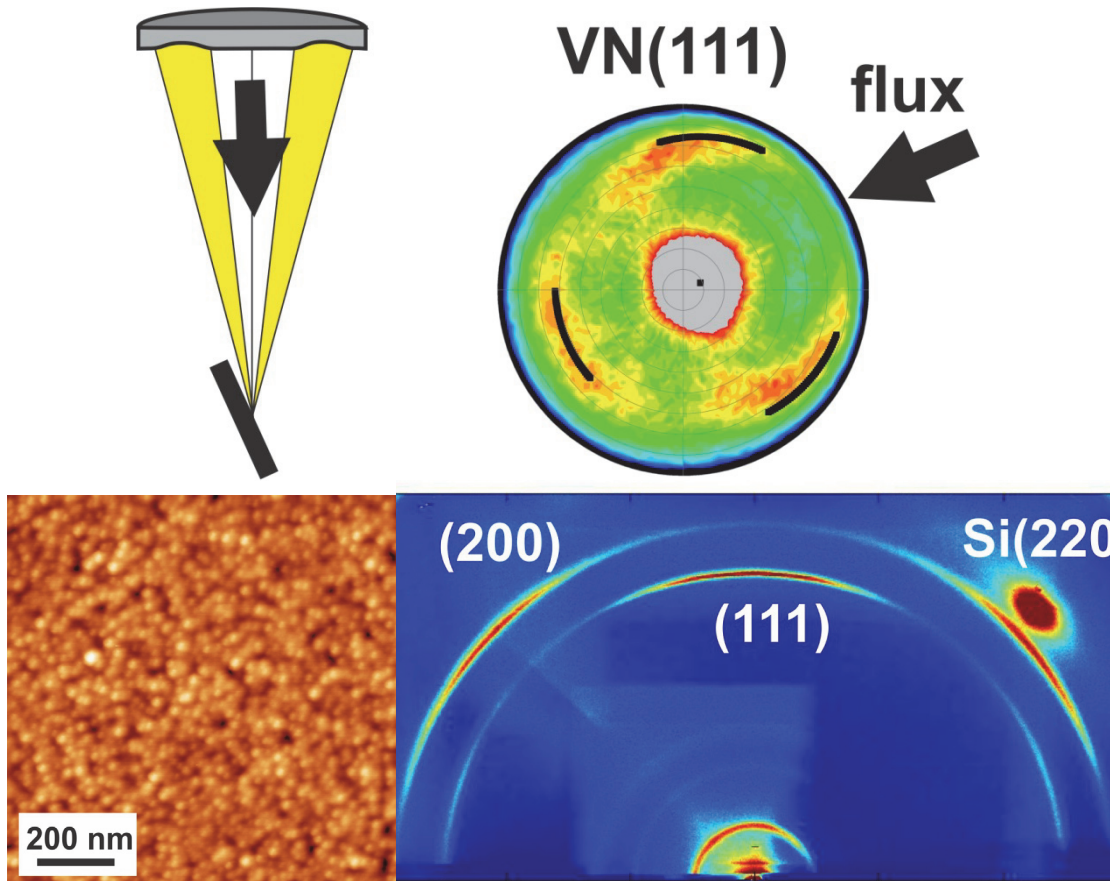


Fig. 1: *Top left:* Sputter geometry for off-normal deposition. *Top right:* Pole figure showing the resulting biaxial texture. *Bottom left:* Non-contact AFM image of a VN thin film surface, *bottom right:* *in-situ* texture measurement.

References

- [1] Krause et al., J. Synchr. Rad. 19 (2012) 216.

Soft x-ray spectroscopy and spectromicroscopy – WERA

P. Nagel, M. Merz, D. Fuchs, Th. Wolf, M.-J. Huang, H. v. Löhneysen, and S. Schuppler

The Institute for Solid-State Physics (IFP) at KIT owns and operates the soft x-ray analytics facility WERA at the synchrotron radiation facility ANKA. WERA is designed for facilitating combinatory studies of the electronic and magnetic structure and microstructure, which have particular promise for strongly correlated, thin-film, and/or nanoscale materials. This is both at the heart of IFP's own activities within the HGF Programme "Science and Technology of Nanosystems" (STN) and those of the external user communities, which can access WERA *via* peer review through the ANKA and KNMF portals and also through the EU project QualityNano.

The soft X-ray analytics facility WERA takes a fully combinatory and integrative approach to studying the microscopic electronic and magnetic structure – (i) by coherently combining important electron spectroscopies (PES, NEXAFS, XMCD; all in a number of variants; XMCD is supplied through a long-term cooperation with the MPI-IS Stuttgart) mutually and also with laterally resolved spectromicroscopy in PEEM (μ -NEXAFS, μ -PES, μ -XMCD); (ii) by organically tying in quasi-*in-situ* sample synthesis in currently 4 preparation chambers, all dedicated to specific techniques including pulsed-laser deposition (PLD), and with UHV sample transfer between end-stations and chambers; and (iii) also by combining radiation sources: bending magnet for more "standard" experiments and covering the full photon-energy range 100 – 1500 eV; undulator (future) for experiments demanding considerably enhanced sensitivity (higher photon flux/flux density) and ultimately also with full polarization control. The resulting cluster of methods and possibilities is unique, and users increasingly appreciate the further insights that this approach and these combinations offer for their experiments.

Within the general thrust of IFP's activities in STN to understand strong electron-electron correlations and related phenomena in condensed matter, current in-house research at WERA concentrates on 3d transition-metal (TM) compounds where electron correlation competes with other interactions on similar energy scales to create phases with novel properties (and susceptible to epitaxial strain imposed by and tunable through the growth process), and on iron-based pnictides whose superconducting properties have posed important challenges in condensed-matter physics as well. User projects performed at WERA cover a large variety of interesting subjects in fundamental and applied science and typically range from microscopic to long-range effects, from molecular order in organic materials to novel magnetic properties, from bulk samples to ultrathin films, and more. The element-specific electronic and magnetic structure of all those materials has been studied by performing electron spectroscopies like NEXAFS, PES, and XMCD and spectromicroscopy (PEEM), and also taking advantage of the possibilities for in-situ sample preparation at WERA. In the following, we briefly touch upon a selection of recent results.

Recently, new aspects of the magnetic exchange mechanism in hole-doped ferromagnetic cobaltates could be clarified with the help of XMCD on epitaxially strained $\text{La}_{0.7}\text{Sr}_{0.3}\text{CoO}_3$ films [1]. O *K* XMCD is directly sensitive to both magnetism and hybridization. An XMCD effect is found only for the energy range of t_{2g} states which thus must participate in the magnetic exchange. Furthermore, the strong strain dependence of the magnetic anisotropy (even with a sign change) indicates a substantial effect of Jahn-Teller distortion, which can occur only in Co^{3+} HS and, thus, corroborates that the magnetic interaction is of the Co^{3+} HS – Co^{4+} HS double exchange (DE) type. The high sensitivity of T_c to the bulk compression, along with the linear correlation between T_c and the strength of the O2p-Co3d hybridization observed in NEXAFS and XMCD, indicates that the double exchange is, however, special in

that it approaches the limit of strong coupling. This is also evident in and can be explained by the small bandwidth of the t_{2g} -derived states. In other words: a new, strong-coupling, t_{2g} -mediated double exchange appears to be at work here, not the plain-vanilla, medium-coupling e_g -based DE generally found in other TM systems such as the manganites.

The exchange interaction of the single spin localized at the central ion of Cu-tetraazaporphyrin molecules deposited on magnetite (100) was shown by XMCD to have clear anisotropic character, indicating that in this system, the Heisenberg model usually used to describe exchange interaction in molecular magnets becomes insufficient. This opens up possibilities for a future control over the spin configuration in single molecular magnets [2]. XPS and NEXAFS helped to understand the depth-dependent molecular orientation when chemically transforming chloroaluminum phthalocyanine, AlClPc, to μ -(oxo)bis(phthalocyaninato)aluminum(III), (PcAl)₂O, on indium tin oxide [3], indicating also that a controlled environment, in particular the presence of some humidity, is necessary for the reaction to take place. Further interesting results include certain aspects of the Kondo effect observed in Gd-doped ZnO, where XMCD shows the dopant to behave entirely paramagnetic [4], and the absence of an XMCD effect for all elements contained in ferromagnetic In₂O₃:Cr, suggesting that the magnetism in this system originates from vacancies [4].

Most fruitful has been the cooperation with the Max-Planck Institute for Intelligent Systems (MPI-IS) Stuttgart (Prof. G. Schütz, PD E. Goering, and coworkers). Their excellent XMCD setup at WERA – fully embedded in the WERA user facilities available through the standard ANKA and KNMF review system – is made almost peerless worldwide by the high sensitivity and particularly by the new, fast-ramp 7 T magnet.

References

- [1] D. Fuchs et al., Phys. Rev. Lett. 111, 257203 (2013).
- [2] J. Klanke et al., Phys. Rev. Lett. 110, 137202 (2013).
- [3] F. Lattayer et al., Anal. Bioanal. Chem. 405, 4895 (2013).
- [4] Y. Li et al., Phys. Rev. B 87, 155151 (2013); J. B. Yi et al. Thin Solid Films 531, 481 (2013).

Publication List

The following list gives details of publications in scientific journals which have resulted from the external and internal use of KNMF installations..

(published in 2013, reported to KNMF by 25th September 2014)

First Author	Title	Citation
Reddy, M. Anji	CFx Derived Carbon-FeF ₂ Nanocomposites for Reversible Lithium Storage	Adv. Energy Mater. 3 (2013) 308-313
Blasco, Eva	Photochemical Generation of Light Responsive Surfaces	Adv. Funct. Mater. 23 (2013) 4011-4019
Nasr, Babak	High-Speed, Low-Voltage, and Environmentally Stable Operation of Electrochemically Gated Zinc Oxide Nanowire Field-Effect Transistors	Adv. Funct. Mater. 23 14 (2013) 1750-1758
de Jonge, Niels	In-situ Deformation Analysis of Nanocrystalline Metals by Quantitative ACOM-STEM	Adv. Imag. Electron Phys. 179 (2013) 172-174
Rodriguez-Emmenegger, Cesar	Controlled Cell Adhesion on Poly(dopamine) Interfaces Photopatterned with Non-Fouling Brushes	Adv. Mater. 25 (2013) 6123-6127
Höfle, Stefan	Tungsten oxide buffer layers fabricated in an inert sol-gel process at room-temperature for blue organic light emitting diodes	Adv. Mater. 25 30 (2013) 4113-4116
Paulöhrl, Thomas	Spatially Controlled Surface Immobilization of Non-Modified Peptides	Angew. Chem.-Int. Edit. 52 (2013) 9714-9718
Duprey, Jean-Louis H. A.	Metal-Locked DNA Three-Way Junction	Angew. Chem.-Int. Edit. 52 4 (2013) 1212-1216
Zhao, Xiangyu	Metal Oxychlorides as Cathode Materials for Chloride Ion Batteries	Angew. Chem.-Int. Edit. 52 51 (2013) 13621-13624
Kohler, Robert	Conical surface structures on model thin-film electrodes and tape-cast electrode materials for lithium-ion batteries	Appl. Phys. A-Mater. Sci. Process. 112 1 (2013) 77-85

First Author	Title	Citation
Zhang, Zhenhao	Cross sections of operating Cu(In,Ga)Se ₂ thin-film solar cells under defined white light illumination analyzed by Kelvin probe force microscopy	Appl. Phys. Lett. 102 (2013) 023903
Tavassolizadeh, Ali	Self-sensing atomic force microscopy cantilevers based on tunnel magnetoresistance sensors	Appl. Phys. Lett. 102 (2013) 153104
Polyakov, M. N.	Microstructural variations in Cu/Nb and Al/Nb nano metallic multilayers	Appl. Phys. Lett. 102 (2013) 241911
Lohmiller, Jochen	The effect of solute segregation on strain localization in nanocrystalline thinfilms: Dislocation glide vs. grain-boundary mediated plasticity	Appl. Phys. Lett. 102 (2013) 241916
Beck, Torsten	High-Q polymer resonators with spatially controlled photo-functionalization for biosensing applications	Appl. Phys. Lett. 102 12 (2013) 121108-1-1211108-3
Witte, Ralf	Evidence for enhanced ferromagnetism in an iron-based nanoglass	Appl. Phys. Lett. 103 (2013) 073106
Thüring, Thomas	X-ray grating interferometry with a liquid-metal-jet source	Appl. Phys. Lett. 103 (2013) 091105
Bick, Jens-Peter	Exchange-stiffness constant of a Nd-Fe-B based nanocomposite determined by magnetic neutron scattering	Appl. Phys. Lett. 103 (2013) 122402
Zanette, Irene	Holotomography versus X-ray grating interferometry: A comparative study	Appl. Phys. Lett. 103 (2013) 244105
Hirtz, Michael	Porous polymer coatings as substrates for the formation of high-fidelity micropatterns by quill-like pens	Beilstein J. Nanotechnol. 4 (2013) 377-384
Kobler, Aaron	Deformation-induced grain growth and twinning in nanocrystalline palladium thin films	Beilstein J. Nanotechnol. 4 (2013) 554-566

First Author	Title	Citation
Prakash, Rajua	A facile synthesis of a carbon-encapsulated Fe ₃ O ₄ nanocomposite and its performance as anode in lithium-ion batteries	Beilstein J. Nanotechnol. 4 (2013) 699-704
Breitung, Ben	Influence of particle size and fluorination ratio of CF _x precursor compounds on the electrochemical performance of C-FeF ₂ nanocomposites for reversible lithium storage	Beilstein J. Nanotechnol. 4 (2013) 705-713
Tischer, Thomas	Spatially Controlled Photochemical Peptide and Polymer Conjugation on Biosurfaces	Biomacromolecules 14 12 (2013) 4340-4350
Rossell, Marta D.	Impact of sonication pretreatment on carbon nanotubes: A transmission electron microscopy study	Carbon 61 (2013) 404-411
Thiele, Cornelius	Electron-beam-induced direct etching of graphene	Carbon 64 (2013) 84-91
Chen, Hsien-Yeh	Vapor-based tri-functional coatings	Chem. Commun. 49 (2013) 4531-4533
Glassner, Mathias	Polymer Surface Patterning via Diels-Alder Trapping of Photo-Generated Thioaldehydes	Chem. Commun. 49 (2013) 633-635
Yameen, Basit	A facile one-pot route to poly(carboxybetaine acrylamide) functionalized SWCNTs	Chem. Commun. 49 (2013) 6734-6736
Hudry, Damien	Controlled Synthesis of Thorium and Uranium Oxide Nanocrystals	Chem.-Eur. J. 19 17 (2013) 5297-5305
Wang, Di	Carbon Supported Gold Nano Catalysts: shape effect in the selective glycerol oxidation	ChemCatChem 5 9 (2013) 2717-2723
Short, Judith M.	Electron cryo-microscopy of meso-tetrakis-(4-sulphonatophenyl)-porphyrin dihydrochloride tubes reveals a helical organisation that explains the origin of their chirality	ChemPhysChem 14 14 (2013) 3209-3214

First Author	Title	Citation
Frank, Nicolas	Formation of an iron phosphine ζ borane complex by formal insertion of BH ₃ into the Fe-P bond	Dalton Trans. 42 (2013) 11252-11261
Xu, Xiaofeng	Selective activation of C-F and C-H bonds with iron complexes, the relevant mechanism study by DFT calculations and study on the chemical properties of hydrido iron complex	Dalton Trans. 42 (2013) 3417-3428
Li, Junye	Selective C-F/C-H bond activation of fluoroarenes by cobalt complex supported with phosphine ligands	Dalton Trans. 42 (2013) 5740-5748
Pillai, Arun Deepak Ramalingom	ALD Growth of PbTe and PbSe Superlattices for Thermoelectric Applications	ECS Transactions 58 10 (2013) 131-139
Nminibapiel, David	Microstructure Analysis of ALD Bi ₂ Te ₃ /Sb ₂ Te ₃ Thermoelectric Nanolaminates	ECS Transactions 58 10 (2013) 59-66
Zhao, Xiangyu	Ge-Cu nanoparticles produced by inert gas condensation and their application as anode material for lithium ion batteries	Electrochem. Commun. 35 (2013) 116-119
Gaass, T.	Iterative reconstruction for few-view grating-based phase-contrast CT - An in vitro mouse model	EPL 102 4 (2013)
Sztrókay, Anikó	Assessment of grating-based X-ray phase-contrast CT for differentiation of invasive ductal carcinoma and ductal carcinoma in situ in an experimental ex vivo set-up	Eur. Radiol. 23 2 (2013) 381-387
Antusch, Steffen	A new fully automatic PIM tool to replicate two component tungsten DEMO divertor parts	Fusion Eng. Des. 88 9-10 (2013) 2461-2465
Alissawi, N.	Effect of gold alloying on stability of silver nanoparticles and control of silver ion release from vapor-deposited Ag-Au/polytetrafluoroethylene nanocomposites	Gold Bull. 46 1 (2013) 3-11

First Author	Title	Citation
Müller, Patrick	New Phosphorus-Containing Quinone Derivatives II: Tri- and Tetraphosphorylated Quinone Derivatives	Heteroatom Chem. 24 4 (2013) 252-262
Steidle, Nicole	Fabrication of Polymeric Microfluidic Devices with Tunable Wetting Behaviour for Biomedical Applications	IEEE Eng. Med. Biol. Mag. (2013) 6659-6662
Palmer, Robert	Silicon-Organic Hybrid MZI Modulator Generating OOK, BPSK and 8-ASK Signals for Up to 84 Gbit/s	IEEE Photonics J. 5 2 (2013)
Palmer, Robert	Low Power Mach-Zehnder Modulator in Silicon-Organic Hybrid Technology	IEEE Photonics Technol. Lett. 25 13 (2013) 1226-1229
Thoma, Petra	Highly responsive Y-Ba-Cu-O thin film THz detectors with picosecond time resolution	IEEE Trans. Appl. Supercond. 23 3 (2013) 2400206
Krüger, Kathrin	Thermal stability of the ferromagnetic in-plane uniaxial anisotropy of Fe-Co-Hf-N/Ti-N multilayer films for high-frequency sensor applications	IEEE Trans. Magn. (2013) 3870-3873
Reitz, Christian	Morphology, Microstructure, and Magnetic Properties of Ordered Large-Pore Mesoporous Cadmium Ferrite Thin Film Spin Glasses	Inorg. Chem. 52 7 (2013) 3744-3754
Zheng, Tingting	Cobalt induced C-H Bond Activation and C8-Arylation of Caffeine with Aryl Bromides	Inorg. Chem. Commun. 30 (2013) 139-142
Huang, Ning	Nickel-heterocumulene complexes stabilized by trimethylphosphine: Synthesis, characterization and catalytic application in organozinc coupling with CS ₂	Inorg. Chim. Acta 394 (2013) 446-451
Kohler, Christian	Effects of ZnO-B ₂ O ₃ addition on the Microstructure and Microwave Properties of Low Temperature Sintered Barium Strontium Titanate (BST) Thick-films	Int. J. Appl. Ceram. Technol. 10 s1 (2013) E200-E209

First Author	Title	Citation
Zupanič, Franc	The experimental investigation of phase equilibria in the Al-rich corner within the ternary Al-Mn-Be system	J. Alloy. Compd. 570 (2013) 125-132
Lazarev, Sergey	Study of threading dislocation density reduction in AlGaN epilayers by Monte Carlo simulation of high-resolution reciprocal-space maps of a two-layer system	J. Appl. Cryst. 46 1 (2013) 120-127
Krause, Bärbel	Composition-dependent structure of polycrystalline magnetron-sputtered V-Al-C-N hard coatings studied by XRD, XPS, XANES and EXAFS	J. Appl. Cryst. 46 4 (2013) 1064-1075
Danilewsky, Andreas	Crack propagation and fracture in silicon wafers under thermal stress	J. Appl. Cryst. 46 4 (2013) 849-855
Lazarev, Sergey	Three-dimensional reciprocal space mapping of diffuse scattering for the study of stacking faults in semipolar (1122) GaN layers grown from the sidewall of an r-patterned sapphire substrate	J. Appl. Cryst. 46 5 (2013) 1425-1433
Zelenina, Anastatia	Structural and optical properties of size controlled Si nanocrystals in Si ₃ N ₄ matrix: The nature of photoluminescence peak shift	J. Appl. Phys. 114 (2013) 184311
Krüger, Kathrin	High-frequency magnetoelastic measurements on Fe-Co-Hf-N/Ti-N multilayer coatings	J. Magn. Magn. Mater. 343 (2013) 42-48
Issac, Ibrahim	Synthesis and electrochemical performance of nanocrystalline Al _{0.4} Mg _{0.2} Sn _{0.4} O _{1.6} and Al _{0.25} Mg _{0.38} Sn _{0.38} O _{1.5} investigated by in situ XRD, ²⁷ Al/ ¹¹⁹ Sn MAS NMR, ¹¹⁹ Sn Mössbauer spectroscopy, and galvanostatic cycling	J. Mater. Chem. 1 (2013) 13842-13852

First Author	Title	Citation
Zhao-Karger, Zhirong	Altered reaction pathways of eutectic LiBH ₄ -Mg(BH ₄) ₂ by nanoconfinement	J. Mater. Chem. A 1 (2013) 3379-3386
Nasr, Babak	Temperature tolerance study of high performance electrochemically gated SnO ₂ nanowire field-effect transistors	J. Mater. Chem. C 1 (2013) 2534-2539
Lepple, Maren	Thermodynamic Investigations of Copper Oxides Used as Conversion Type Electrodes in Lithium Ion Batteries	J. Mater. Sci. 48 17 (2013) 5818-5826
Ivanisenko, Yulia	Observation of shear band formation in nanocrystalline Pd-Au alloy during in situ SEM compression testing	J. Mater. Sci. 48 19 (2013) 6841-6847
Cupid, Damian M.	Investigation of the lithium-rich boundary of the Li _{1+x} Mn _{2-x} O ₄ cubic spinel phase in air	J. Mater. Sci. 48 9 (2013) 3395-3403
Schröder, Melanie	Post-doping via spray-drying: a novel sol-gel process for the batch synthesis of doped LiNi _{0.5} Mn _{1.5} O ₄ spinel material	J. Mater. Sci. 48 9 (2013) 3404-3414
Stemme, Florian	Fabrication and characterization of iron and fluorine co-doped BST thin films for microwave applications	J. Mater. Sci. 48 9 (2013) 3586-3596
Omar, F.	Simulation and Experimental Study of the Effects of Process Factors on the Uniformity of the Residual Layer Thickness in Hot Embossing	J. Micro Nano-Manuf. 1 2 (2013) 021002
Brammer, Marko	Modular Optoelectronic Microfluidic Backplane for Fluid Analysis Systems	J. Microelectromech. Syst. 22 2 (2013) 462-470
Röhrig, Michael	Hot pulling and embossing of hierarchical nano- and micro-structures	J. Micromech. Microeng. 23 10 (2013) 105014
Greiner, Felix	Fabrication techniques for multiscale 3D-MEMS with vertical metal micro- and nanowire integration	J. Micromech. Microeng. 23 2 (2013) 025018

First Author	Title	Citation
Soshnikova, Yulia M.	Starch-modified magnetite nanoparticles for impregnation into cartilage	J. Nanopart. Res. 15 (2013) 2092
Chen, Ruiyong	Structural Evolution of $\text{Li}_2\text{Fe}_{1-y}\text{MnySiO}_4$ ($y=0, 0.2, 0.5, 1$) Cathode Materials for Li-Ion Batteries upon Electrochemical Cycling	J. Phys. Chem. C 117 2 (2013) 884-893
Senna, Mamoru	Transfer and State Changes of Fluorine at Polytetrafluoroethylene / Titania Boundaries by Mechanical Stressing and Thermal Annealing	J. Phys. Chem. C 117 29 (2013) 15272-15278
Vieira , Eliana M. F.	Influence of RF-sputtering power on formation of vertically stacked $\text{Si}_{1-x}\text{Ge}_x$ nanocrystals between ultra-thin amorphous Al_2O_3 layers: structural and photoluminescence properties	J. Phys. D-Appl. Phys. 46 38 (2013) 385301
Mangold, Stefan	Full field spectroscopic imaging at the ANKA-XAS- and -SUL-X-Beamlines	J. Phys.: Conf. Ser. 430 (2013) 012130
Cheng, Yin	Multi-contrast computed laminography at ANKA light source	J. Phys.: Conf. Ser. 463 (2013) 012038
Becker, Sebastian M.	Nanocrystalline Solid Solutions $\text{Al}_y\text{Sn}_{1-y}\text{O}_{2-y/2}$ ($y = 0.57, 0.4$) as Electrode Materials for Lithium-Ion Batteries	J. Power Sources 229 (2013) 149-158
Daschner de Tercero, Maren	Synthesis of in situ functionalized iron oxide nanoparticles presenting alkyne groups via a continuous process using near-critical and supercritical water	J. Supercrit. Fluids 82 (2013) 83-95
Fukui, Hiroshi	Large-aperture refractive lenses for momentum-resolved spectroscopy with hard X-rays	J. Synchrot. Radiat. 20 (2013) 591-595
Gaillard, Mireille	High-resolution transmission electron microscope observations of multi-walled carbon nanotube microstructures grown by plasma enhanced chemical vapor deposition	J. Vac. Sci. Technol. B 31 3 (2013) 031805

First Author	Title	Citation
Scholz, Ferdinand	Studies on Defect Reduction in AlGaN Heterostructures by Integrating an In-situ SiN Interlayer	Jpn. J. Appl. Phys. 52 (2013) 08JJ07
Bog, Uwe	On-chip microlasers for biomolecular detection via highly localized deposition of a multifunctional phospholipid ink	Lab Chip 13 (2013) 2701-2707
Grossmann, Tobias	Polymeric photonic molecule super-mode lasers on silicon	Light: Science & Applications 2 (2013) e82
Zydziaik, Nicolas	Hetero Diels-Alder Chemistry for the Functionalization of Single-Walled Carbon Nanotubes with Cyclopentadienyl End-Capped Polymer Strands	Macromol. Rapid Commun. 34 (2013) 672-680
Yameen, Basit	Conducting Polymer/SWCNTs Modular Hybrid Materials via Diels-Alder Ligation	Macromolecules 46 7 (2013) 2606-2615
Ning, Jiang-li	Tensile properties and work hardening behaviors of ultrafine grained carbon steel and Armco iron processed by warm high-pressure torsion	Mater. Sci. Eng. A 581 (2013) 8-15
Dai, Gaoliang	Reference nano dimensional metrology by scanning transmission electron microscopy	Meas. Sci. Technol. 24 (2013) 085001
Rutishauser, Simon	Fabrication of two-dimensional hard X-ray diffraction gratings	Microelectron. Eng. 101 (2013) 12-16
Chakravadhanula, Venkata Sai Kiran	TEM investigations on FeF ₂ based nanocomposite battery materials	Microsc. microanal. 13 Suppl 2 (2013) 1524-1525
Zupanic, Franc	Phases in the Al-Corner of the Al-Mn-Be System	Microsc. microanal. 19 5 (2013) 1308-1316
Kolew, Alexander	Hot embossing of transparent high aspect ratio micro parts	Microsyst. Technol. (2013)
Greiner, Felix	High aspect ratio metal micro and nano pillars for minimal footprint MEMS suspension	Microsyst. Technol. 19 3 (2013) 425-431

First Author	Title	Citation
Singh, Akanksha	Transparent thin thermoplastic biochip by injection-moulding and laser transmission welding	Microsyst. Technol. 19 3 (2013) 445-453
Maier-Flaig, Florian	Multicolour Silicon Light Emitting Diodes (SiLEDs)	Nano Lett. 13 (2013) 475-480
Maier-Flaig, Florian	Looking Inside a Working SiLED	Nano Lett. 13 8 (2013) 3539-3545
Abdulkin, Pavel	New routes to Cu(I)/Cu nanocatalysts for the multicomponent click synthesis of 1,2,3-triazoles	Nanoscale 5 (2013) 342-350
Knappett, Benjamin R.	Characterisation of Co@Fe ₃ O ₄ core@shell nanoparticles using advanced electron microscopy	Nanoscale 5 (2013) 5765-5772
Abdelaziz, Ramzy	Green chemistry and nanofabrication in a levitated Leidenfrost drop	Nat. Commun. 4 (2013) 2400
Hirtz, Michael	Multiplexed biomimetic lipid membranes on graphene by dip-pen nanolithography	Nat. Commun. 4 (2013) 2591
Li, Jingshi	Four-in-one interferometer for coherent and self-coherent detection	Opt. Express 21 11 (2013) 13293-13304
Siddique, Radwanul Hasan	Theoretical and experimental analysis of the structural pattern responsible for the iridescence of Morpho butterflies	Opt. Express 21 12 (2013) 14351-14361
Weber, Thomas	Increasing the darkfield contrast-to-noise ratio using a deconvolution-based information retrieval algorithm in X-ray grating-based phase-contrast imaging	Opt. Express 21 15 (2013) 18011-18020
Pelzer, Georg	Grating-based x-ray phase-contrast imaging with a multi energy-channel photon-counting pixel detector	Opt. Express 21 22 (2013) 25677-25684
Liu, Xin	Pump spot size dependent lasing threshold in organic semiconductor DFB lasers fabricated via nanograting transfer	Opt. Express 21 23 (2013) 27697-27706

First Author	Title	Citation
Epple, F. M.	Unwrapping differential x-ray phase-contrast images through phase estimation from multiple energy data	Opt. Express 21 24 (2013) 29101-29108
Zhou, T.	Comparison of two x-ray phase-contrast imaging methods with a microfocus source	Opt. Express 21 25 (2013) 30183-30195
Willner, Marian	Quantitative X-ray phase-contrast computed tomography at 82 keV	Opt. Express 21 4 (2013) 4155-4166
Nazirizadeh, Yousef	Sensitivity optimization of injection-molded photonic crystal slabs for biosensing applications	Opt. Mater. Express 3 5 (2013) 556-565
Wu, Siqun	Synthesis and Reactivity of Silyl Iron, Cobalt, and Nickel Complexes Bearing a [PSiP]-Pincer Ligand via Si-H Bond Activation	Organometallics 32 11 (2013) 3227-3237
Xu, Wengang	Acid-Promoted Selective Carbon-Fluorine Bond Activation and Functionalization of Hexafluoropropene by Nickel Complexes Supported with Phosphine Ligands	Organometallics 32 23 (2013) 7122-7132
Daschner de Tercero, Maren	Continuous hydrothermal synthesis of in situ functionalized iron oxide nanoparticles - a general strategy to produce metal oxide nanoparticles presenting clickable anchors	Part. Part. Syst. Charact. 30 3 (2013) 229-234
Velroyen, A.	Microbubbles as a scattering contrast agent for grating-based x-ray dark-field imaging	Phys. Med. Biol. 58 4 (2013) N37
Bao, Zhaohui	Antiferromagnetism in UO ₂ thin epitaxial films	Phys. Rev. B 88 (2013) 134426
Seredin, P. V.	X-Ray Diffraction Studies of Heterostructures Based on Solid Solutions Al _x Ga _{1-x} As _y P _{1-y} : Si	Phys. Solid State 55 10 (2013) 2161-2164
Seredin, P. V.	Photoluminescence Properties of Heavily Doped Heterostructures Based on Al _x Ga _{1-x} As _{1-y} Si _y Solid Solutions	Phys. Solid State 55 10 (2013) 2169-2172

First Author	Title	Citation
Yu, Yiting	The Focusing and Talbot Effect of Periodic Arrays of Metallic Nanoapertures in High-Index Medium	Plasmonics 8 2 (2013) 723-723
Jensen, Torben Haugaard	Imaging of Metastatic Lymph Nodes by X-ray Phase-Contrast Micro-Tomography	PLoS ONE 8 1 (2013) e54047
Baudoin, Jean-Pierre	Whole-cell Analysis of Low-Density Lipoprotein Uptake by Macrophages using STEM Tomography	PLoS ONE 8 1 (2013) e55022
Tapfer, Arne	X-Ray Phase-Contrast CT of a Pancreatic Ductal Adenocarcinoma Mouse Model	PLoS ONE 8 3 (2013) e58439
Meinel, F. G.	Diagnosing and Mapping Pulmonary Emphysema on X-Ray Projection Images: Incremental Value of Grating-Based X-Ray Dark-Field Imaging	PLoS ONE 8 3 (2013) e59526
Malecki, A.	Coherent Superposition in Grating-Based Directional Dark-Field Imaging	PLoS ONE 8 4 (2013) e61268
Saam, T.	Translation of Atherosclerotic Plaque Phase-Contrast CT Imaging from Synchrotron Radiation to a Conventional Lab-Based X-Ray Source	PLoS ONE 8 9 (2013) e73513
Zhang, Zehua	N-H bond activation of 2-aminobenzophenone by trimethylphosphine complexes of nickel and cobalt	Polyhedron 50 1 (2013) 571-575
Zydziaik, Nicolas	Modular Ambient Temperature Functionalization of Carbon Nanotubes with Stimuli-Responsive Polymer Strands	Polym. Chem. 4 (2013) 1524-1537
Eisenblaetter, Joerdis	Polymers with Phosphor Containing Side Chains via Modular Conjugation	Polym. Chem. 4 (2013) 2406-2413
Tanner, B. K.	X-ray diffraction imaging for predictive metrology of crack propagation in 450-mm diameter silicon wafers	Powder Diffr. 28 2 (2013) 95-99

First Author	Title	Citation
Palmer, Robert	Silicon-Organic Hybrid (SOH) Modulator Generating up to 84 Gbit/s BPSK and M-ASK Signals	Proc. IEEE (2013) 1-3
Yaroshenko, Andre	Pulmonary Emphysema Diagnosis with a Preclinical Small-Animal X-ray Dark-Field Scatter-Contrast Scanner	Radiology 269 2 (2013) 427-433
Junginger, Mathias	Crystal structure and chemical composition of biomimetic calcium phosphate nanofibers	RSC Adv. 3 (2013) 11301-11308
Hudry, Damien	Synthesis of Transuranium-Based Nanocrystals via the Thermal Decomposition of Actinyl Nitrates	RSC Adv. 3 (2013) 18271-18274
Zanette, Irene	X-ray grating-based phase tomography for 3D histology	RSC Adv. 3 (2013) 19816-19819
Worgull, Matthias	Hot embossing and thermoforming of biodegradable three-dimensional wood structures	RSC Adv. 3 (2013) 20060-20064
Brinkmann, Falko	Interdigitated Multicolored Bioink Micropatterns by Multiplexed Polymer Pen Lithography	Small 9 19 (2013) 3266-3275
Felten, Alexandre	Single- and Double-Sided Chemical Functionalization of Bilayer Graphene	Small 9 4 (2013) 631-639
Faust, Matthias	Synthesis of nanostructured Pt/oxide catalyst particles by MOCVD process at ambient pressure	Surf. Coat. Technol. 230 (2013) 284-289
Spitz, Stefanie	Phase formation and microstructure evolution of reactively r.f. magnetron sputtered Cr-Zr oxynitride thin films	Surf. Coat. Technol. 237 (2013) 149-157
Fischer, Julian	Development of thin film cathodes for lithium-ion batteries in the material system Li-Mn-O by r.f. magnetron sputtering	Thin Solid Films 528 (2013) 217-223

First Author	Title	Citation
Pröll, Johannes	Comparative studies of laser annealing technique and furnace annealing by X-ray diffraction and Raman analysis of lithium manganese oxide thin films for lithium-ion batteries	Thin Solid Films 531 (2013) 160-171
Issenmann, Daniel	Determination of nanoscale heat conductivity by time-resolved X-ray scattering	Thin Solid Films 541 (2013) 28-31
Fischer, Julian	Structural transformation of sputtered o-LiMnO ₂ thin-film cathodes induced by electrochemical cycling	Thin Solid Films 549 (2013) 263-267
Kobler, Aaron	Combination of in-situ straining and ACOM TEM: a novel method for analysis of plastic deformation of nanocrystalline metals	Ultramicroscopy 128 (2013) 68-81
Gottwald, Eric	Characterization of a chip-based bioreactor for three-dimensional cell cultivation via Magnetic Resonance Imaging	Z. Med. Phys. 23 22 (2013) 102-110
Pfeiffer, Franz	Grating-Based X-ray Phase Contrast for Biomedical Imaging Applications	Z. Med. Phys. 23 3 (2013) 176-185
Fu, Jian	An algebraic iterative reconstruction technique for differential x-ray phase-contrast computed tomography	Z. Med. Phys. 23 3 (2013) 186-193
Hetterich, Holger	Grating-based X-ray phase-contrast tomography of atherosclerotic plaque at high photon energies	Z. Med. Phys. 23 3 (2013) 194-203
Noël, Peter B.	Evaluation of the potential of phase-contrast computed tomography for improved visualization of cancerous human liver tissue	Z. Med. Phys. 23 3 (2013) 204-211
Grandl, Susanne	Evaluation of phase-contrast CT of breast tissue at conventional X-ray sources - presentation of selected findings	Z. Med. Phys. 23 3 (2013) 212-221

First Author	Title	Citation
Anton, Gisela	Grating-based darkfield imaging of human breast tissue	Z. Med. Phys. 23 3 (2013) 228-235
Schwab, Felix	Comparison of Contrast-to-Noise Ratios of Transmission and Dark-Field Signal in Grating-Based x-ray Imaging for Healthy Murine Lung Tissue	Z. Med. Phys. 23 3 (2013) 236-242

User Reports

Following the completion of a user project users are encouraged to publish the results in high ranking scientific journals and to disseminate them at the most relevant conferences with acknowledgement to KNMF. In addition users are expected to submit a report on their work to the KNMF user office. Reports received for work completed until 2013 are given below.

List of contributors

(Reports received by 25th September 2014)

Proposal ID	Proposal Title	Name	Organisation	Country
2011-006-000581	Pioneering Hole-Array IR Blocking Filters for X-ray Astrophysics	Simon Bandler	NASA - Goddard Space Flight Center	USA
2011-007-000757	Ruthenium dissolution and crossover in direct methanol fuel cells	Alexander Schoekel	Freie Universität Berlin	Germany
2012-007-000783	Phase separation in amorphous and partially crystallized SiC _x	Harald Schmidt	Technische Universität Clausthal	Germany
2012-007-000789	The imaging of a new carbon phase by high-resolution electron microscopy	Florian Banhart	Université de Strasbourg	France
2012-007-000810	Multi-period compound gratings with varying component efficiencies for outcoupling enhanced OLEDs	Christian Kluge	Christian-Albrechts-Universität zu Kiel (CAU)	Germany
2012-007-000859	Bimetallic Nanocatalysts: The Gold-Nickel Model System	Adam Fraser	University of Cambridge	United Kingdom
2012-008-000970	Out of Plane High Aspect Ratio Micro Wires as Suspension Elements in Inertial Sensors	Felix Greiner	Technische Universität Darmstadt	Germany
2012-008-000992	Actin Myosin Interaction in Functionally Structured Micro/Nano-Domains	Matias Mosqueira	Ruprecht-Karls-Universität Heidelberg	Germany

Proposal ID	Proposal Title	Name	Organisation	Country
2012-008-001000	A Self-reluctant Against Shear Stress of Anode Materials for High Electrochemical Performance Lithium-Ion Battery	Joong-Kee Lee	Korea Institute of Science and Technology	South Korea
2012-008-001002	Evaluation of Talbot-Lau based X-ray imaging for medical applications	Gisela Anton	Friedrich-Alexander-Universität Erlangen-Nürnberg	Germany
2012-008-001027	3D imaging and analysis of mesopores in hierarchical pore structures by electron tomography	Daniela Stoeckel	Justus-Liebig-Universität Gießen	Germany
2012-009-001164	High-resolution x-ray grating interferometry in a laboratory setting	Anna Burvall	KTH Royal Institute of Technology	Sweden
2013-009-001176	Characterization of binding process of Oligonucleotides, and Lipids on microlithographed TiO ₂ substrates	Ruy Sanz	Nanoate	Spain
2013-009-001195	Micro-machining of a glass coverslip implanted for high resolution imaging of mouse brain	Yajie Liang	Eberhard-Karls-Universität Tübingen	Germany
2013-009-001221	Using FIB-SEM to determine the influence of support morphology on the structure and performance of low-temperature fuel cells	Benedikt Peter	Technische Universität Darmstadt	Germany
2013-010-001305	Replacement of Noble Metal Catalysts for the Hydrogenation of Polar Multiple Bonds	Robert Langer	Philipps-Universität Marburg	Germany
2013-010-001394	Surface texturing for hybrid contact tribological applications	Mengyan Nie	University of Southampton	United Kingdom

Proposal ID	Proposal Title	Name	Organisation	Country
2013-010-001537	Development of 3D topography in laser-printed LiFePO_4 cathodes by femtosecond laser structuring	Alberto Pique	US Naval Research Laboratory	USA
2013-010-001548	Biomimetic lipid-based research platform for studying antibody-membrane interactions	Stefan Zauscher	Duke University	USA
2013-010-001670	TEM observation of the initial growth stage of carbon nanotubes synthesized in low temperature plasmas	Eva Kovacevic	Université d'Orleans	France
2013-011-002529	In-depth profiling of amino acid coupling efficiency on polymeric surfaces	Volker Stadler	PEPperPRINT GmbH	Germany

Final Reports as submitted by the Users

Pioneering Hole-Array IR Blocking Filters for X-ray Astrophysics

Simon Bandler

NASA - Goddard Space Flight Center

USA

Final Report

1. Project goals (max. 1.800 characters):

It was the goal to develop a filter that will effectively block infrared, UV, and optical photons, and transmit soft X-rays (0.1-2.0 keV). The filters should have a net efficiency of ~ 20 -50% all across this low energy band, providing orders of magnitude increase in transmission at the lowest energies. The opening of this soft X-ray band is essential to the future success of x-ray astrophysics.

2. Project results (max. 7.000 characters + figures):

An X-ray mask has been successfully produced by electron beam lithography followed by electroplating. The smallest structures were about 170nm wide compared to 100nm that were anticipated. To this time all attempts to copy the mask structures into negative resist by x-ray lithography were unsuccessful, some final test are still pending. No filters have yet been produced in the project and subsequently no filters were characterized.

3. Publications (please stick to the user guidelines for publications and acknowledgements on www.knmf.kit.edu):

No Papers could be published during the project.

4. Comments (max. 1.800 characters):

Both processing steps turned out more complicated than expected. Work however did progress well and significant processing knowledge was established for both electron beam lithography and x-ray lithography. The collaboration between the proposers and KIT personnel went very well and concepts have been developed that can lead to the successful production of filters. Because of the significant amount of personnel and tool time that went into the project, we have decided to apply for an extension.

Ruthenium dissolution and crossover in direct methanol fuel cells

Alexander Schoekel

Freie Universität Berlin

Germany

Note: Please fill in this report form and save/print it as a PDF file, then upload it to the KNMF proposal submission system. A cover page containing proposal title, proposer name(s), and technologies selected will be added by the system. A link for the download of the complete report as a PDF file will be displayed in the system.

Final Report

1. Project goals (max. 1.800 characters):

Anode and cathode catalysts of direct methanol fuel cells (DMFC) were analyzed in regard to changes induced by ruthenium dissolution. During fuel cell operation ruthenium is dissolved from the platinum-ruthenium anode catalysts and migrates onto the pure platinum cathode catalyst. In order to understand the involved mechanisms, the composition of the ruthenium phases inside the catalysts before and after different operation conditions in a DMFC were analyzed.

2. Project results (max. 7.000 characters + figures):

As expected, the measurement of ruthenium spectra was challenging. The catalysts are carbon supported and therefore high amounts of carbon are present in the samples. The strong overlap of the C1s and Ru3d signal exacerbate the deconvolution of the peaks. The Ru3p signal on the other hand is much weaker and shows a poor signal to noise ratio.

Because the amounts of migrated ruthenium on the cathode catalysts are very low (below 0.05 atom% for most cathode samples), no reasonable data for the Ru3d or Ru3p signals could be obtained.

On the contrary, the ruthenium amount of the anode catalysts is comparably high (25 wt%) and spectra of good quality were obtained. Figure 1 shows the spectra of three anode catalyst samples after treatment in methanol, formic acid and water, respectively.

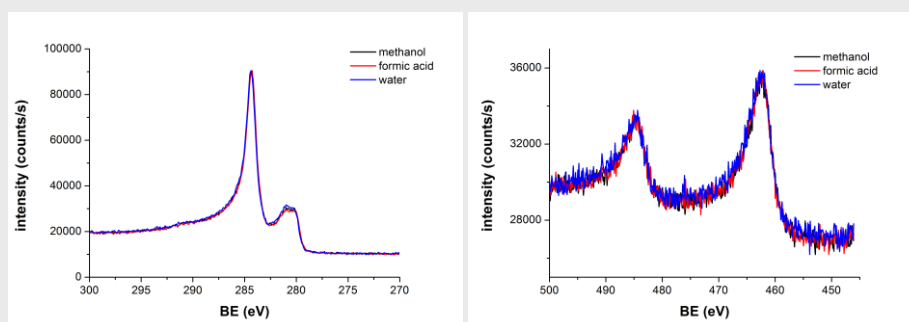


Figure 1: C1s/Ru3d and Ru3p XPS spectra of anode catalysts after treatment in different media.

Interestingly and unexpectedly the spectra obtained for the anode catalysts were almost identical. Also the spectra of anode catalysts after operation under various DMFC conditions (i.e. potentials and operation time) do not show any significant differences as shown in figure 2.

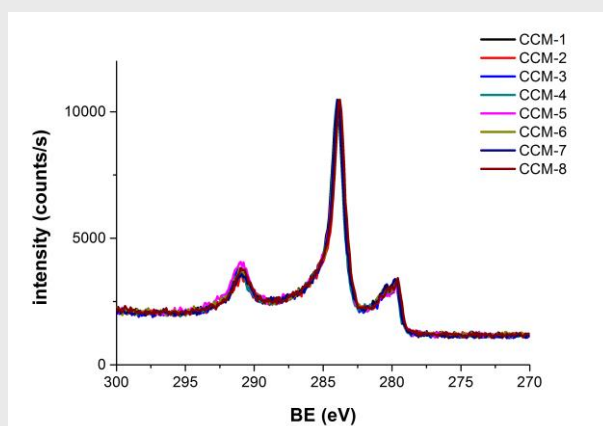


Figure 2: C1s/Ru3d spectra of anode catalyst samples after DMFC operation.

Since complementary analyses on the samples confirm that different amounts of ruthenium were transferred to the corresponding cathode catalyst samples, some differences were expected. Two possibilities seem likely: (1) the amount of dissolved ruthenium is not large enough to have a significant effect on the XPS spectra, (2) the samples 'return' to a similar state, when they are removed from the electrochemical environment inside the DMFC, dried and exposed to vacuum conditions for XPS analysis. Measuring the composition of the anode samples provided the necessary information to correlate our findings from other measurements with findings and proposed mechanisms found in literature.

3. Publications (please stick to the user guidelines for publications and acknowledgements on www.knmf.kit.edu):

"Ruthenium cross-over in direct methanol fuel cells traced by synchrotron X-ray fluorescence spectroscopy", A. Schoekel, D. Batchelor, M. Borchert, M. Bruns, F. Kuppler, C. Roth – *in preparation (2014)*

4. Comments (max. 1.800 characters):

Phase separation in amorphous and partially crystallized SiC_x

Harald Schmidt

Technische Universität Clausthal

Germany

Summary Report

1. Project Objectives (250 words)

Non-stoichiometric $\text{Si}_{1-x}\text{C}_x$ films deposited on adequate substrates are important for various branches of technology like electronics, optoelectronics and photovoltaic. Characteristic applications are window layers in solar cells, insulating layers in thin film transistors, thin film light emitting diodes, color displays, UV detectors, and micro electro-mechanical systems [1-3]. A straightforward research field is the design of silicon quantum dots embedded in an amorphous matrix of silicon carbide for applications as e. g. tandem solar cells [4]. For these applications a fundamental understanding of the formation, growth and modification of nano-crystallites in silicon-rich $\text{Si}_{1-x}\text{C}_x$ is of large importance.

Using magnetron sputtering, high quality amorphous films with reproducible properties can be deposited on various substrates. Annealing at elevated temperatures leads to precipitation and crystallization. Nucleation and growth processes affect the nanostructure of the films. In order to get insight into the nanostructural modifications during crystallization, high resolution TEM measurements are necessary.

During preliminary experiments at KNMF (project 2010-005-000416) Si_2C films on silicon wafer substrates were investigated. The aim of the present project was now to launch a comparative investigation, where Si_2C films are deposited on carbon substrates in order to investigate the substrate dependence of the nanostructural modifications during crystallization [5].

[1] G. Ambrosone et al., Thin Solid Films 403 (2002), 349.

[2] G. Foti, Appl. Surf. Sci. 184 (2001), 20.

[3] W. A. Nevin et al., Nature 368 (1994), 529.

[4] Z. Wan et al. Nanosc. Res. Lett. 6 (2011), 129.

[5] H. Schmidt et al., Appl. Surf. Sci. 225 (2005), 1460.

2. Project Achievements (1000 words + figures)

Samples: Non-stoichiometric films with a chemical composition of Si_2C and a thickness of about 0.5 μm were deposited by magnetron co-sputtering of silicon/carbon composite targets on glassy carbon substrates. Crystallization is induced by annealing the samples at 800, 1200 and 1600 °C. Four different samples were characterized by TEM: (1) an as-deposited sample, (2) a sample annealed for 1 h at 800 °C (3) a sample annealed for 2 h at 1200 °C and (4) a sample annealed for 2 h at 1600 °C, respectively.

TEM characterization: Measurements were done using a FEI Titan 80-300 microscope with Cs correction at 300 kV. The samples were investigated in cross-sectional geometry prepared by FIB using BF-TEM, DF-TEM, HR-TEM and STEM-HAADF in combination with SAED, EDX and EELS.

For the as-deposited sample, BF-TEM, STEM and SAED revealed the presence of a homogeneous amorphous film with smooth interfaces. A phase separation in Si and SiC_x rich regions could not be proven.

In contrast to the samples on silicon substrate, annealing at 800 °C in UHV (Fig. 1) does not induce the formation of faceted crystalline silicon nanoparticles at the surface. The film itself is mainly

amorphous with very small, isolated SiC crystallites of about 2-3 nm in the amorphous matrix. Consequently, it can be stated that a silicon substrate will induce an accelerated decomposition of the Si₂C films at low temperatures. The reasons are unclear at the moment.

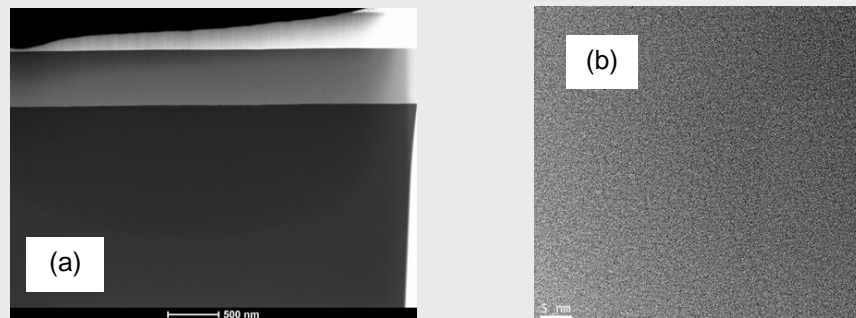


Fig. 1 TEM images of a Si₂C film on a glassy carbon substrate in cross sectional geometry annealed at 800 °C. (a) HAADF-STEM and (b) HR-TEM images.

For annealing at 1200 °C in Ar, the main part of the film deposited on glassy carbon is composed of polycrystalline Si, polycrystalline SiC, and pores, all in the range of some tens of nm. This result is identical to that obtained for samples deposited on silicon substrates (see 2010-005-000416). However, at the surface, crystalline silicon particles with dimensions of about 500 nm are formed, similar to results on samples on silicon substrates annealed at 800 °C in UHV. The carbon substrate seems to shift the onset of this drastic phase separation effect to higher temperatures. This result illustrates that silicon is transferred from the Si₂C film matrix to the substrate interface during annealing. In contrast, for films deposited on silicon substrates a transfer of silicon from the Si₂C film matrix to the substrate interface and an epitaxial growth was observed during annealing at 1200 °C.

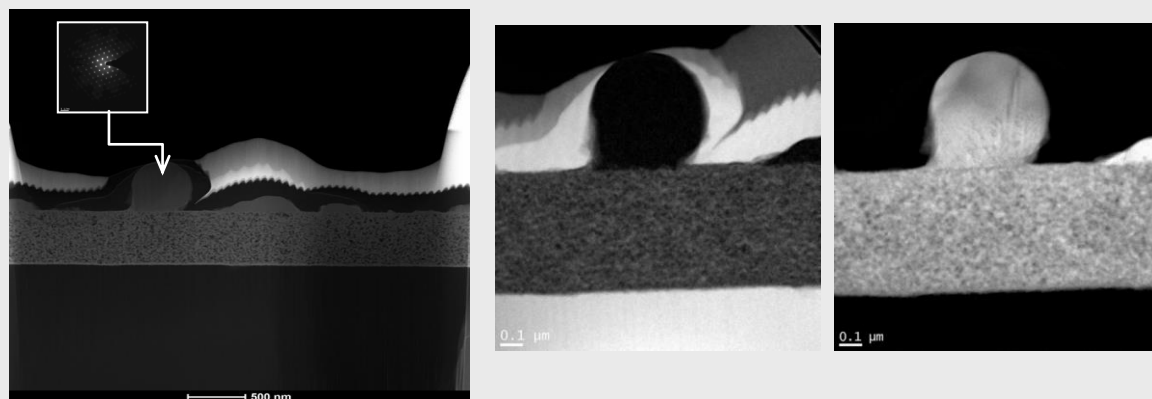


Fig. 2 TEM images of a Si₂C film on a glassy carbon substrate in cross sectional geometry annealed at 1200 for 2 h °C. (a) HAADF-STEM (b) EF-TEM (C map) of the film, and (c) EF-TEM (Si map) of the film.

At 1600 °C the complete film is crystallized to polycrystalline SiC with relatively large grains (50 -100 nm) and with rough surface and interface structures. Large pores are found at the substrate/film interface. Si crystals are no longer present.

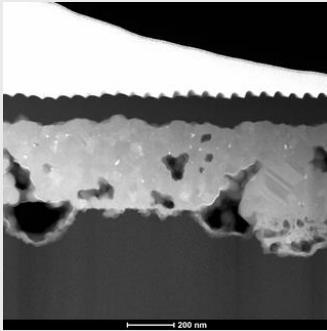


Fig. 3 HAADF-STM image of a Si₂C films in cross sectional geometry annealed at 1200 °C for 120 h.

In conclusion, it can be stated that for Si₂C films deposited on glassy carbon and silicon wafers, respectively, a phase separation and decomposition can be proven at elevated temperatures. Overstoichiometric silicon is transferred by diffusion to interfaces (surface or substrate interface).

3. Instruments Used (comma separated)

Transmission Electron Microscopy, Focused Ion Beam

4. Publications

Please note that the following acknowledgement has to be included in journals, proceedings, presentations and at any other public publications: *"We acknowledge the Karlsruhe Nano Micro Facility (KNMF, www.kit.edu/knmf) of the Forschungszentrum Karlsruhe for provision of access to instruments at their laboratories and we would like to thank x for assistance in using laboratory y."*

to be published	<ul style="list-style-type: none"> H. Schmidt et al., Crystallization of amorphous Si₂C on glassy carbon substrates during thermal annealing.
published	<ul style="list-style-type: none"> R. Gustus, W. Gruber, L. Wegewitz, U. Geckle, R. Prang, C. Kübel, H. Schmidt, W. Maus-Friedrichs, Decomposition of amorphous Si₂C by thermal annealing, Thin Solid Films 552 (2014), 232.

5. Comments (250 words)

The imaging of a new carbon phase by high-resolution electron microscopy

Florian Banhart

Université de Strasbourg

France

Final Report

1. Project goals

The goal of the project has been the study of a new cell-like carbon phase by aberration-corrected transmission electron microscopy. Previous studies by the applicants in Strasbourg showed the appearance of fullerene-like structures around catalytically active metal particles on a graphene substrate. The experiments were carried out in an in-situ experiment at high temperature in an electron microscope. The moderate spatial resolution of the microscope did not allow revealing the structure of these unexpected carbon cells. Therefore, a more detailed study with better resolution became necessary. The availability of the aberration-corrected Titan microscope at the KNMF, equipped with a heating specimen stage, allowed us to repeat the same experiments at higher image resolution. We expected to obtain a detailed picture of the structure, e.g., the diameter and height of the cells, the coherence of the ordered network, and the question whether the structures are related to fullerenes. The results complemented the characterization by scanning transmission electron microscopy in our lab in Strasbourg in an ideal way.

2. Project results

Several days of microscopy experiments by using the Titan instrument have been available. The in-situ experiments on the carbon phase were carried out according to the plans. During the course of the project, a structurally similar phase of silica has been discovered by the applicants in Strasbourg. Due to its close relationship with the carbon phase, the new silica phase was then also included into the project and studied by high-resolution TEM. The in-situ experiments were carried out by heating the substrates with the deposited metal crystals and observing the structural transformations. Numerous exposures of both phases have been taken. Examples of the carbon and silica structures are shown in the figure below.

The carbon phase was produced by depositing metals on graphene layers and heating the system to high temperatures while they are observed in the electron microscope. The aberration-corrected images of the carbon phase show the appearance of cages with a diameter clearly smaller than the diameter of C_{60} and indicate a spherical structure corresponding to the smallest possible fullerenes. This is a surprising result since carbon cages smaller than C_{60} have been considered to be much less stable than graphitic carbon. The reason for the formation of such small carbon cages that nucleate on the surface of catalytically active metals is still unclear. Detailed theoretical studies of the binding energies and the stability of possible carbon clusters are in progress.

The silica phase was produced by depositing metal crystals on an amorphous silica film and heating the system. The appearance of the cellular silica phase was also studied in high image resolution. Since the visibility of the structure is low in plan-view transmission over the metallic substrate, side-view geometries have been selected where the structure appears at the edge of the metal crystal without overlap. Image

simulations show that the structure consists of an ordered monolayer of silica which presents the thinnest possible crystalline silica layer. Such structures could become of interest for applications as tunnel barriers or insulating layers in semiconductor technology.

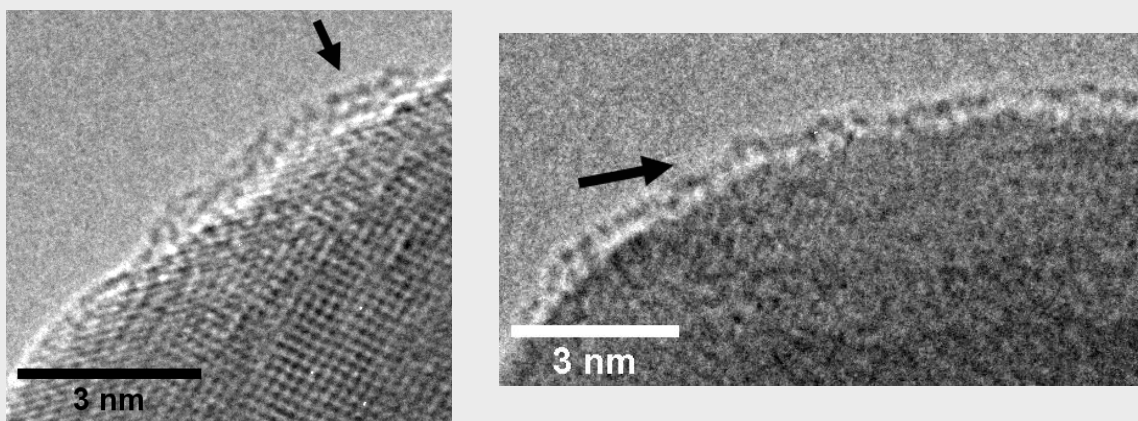


Figure: High-resolution TEM images of carbon cages on Co (left, arrowed) and silica cells on Fe (right), taken with the Titan microscope at the KNMF. Both structures are imaged in side-view at the edge of metal particles. The aberration-corrected images allow the precise measurement of the diameter of the cellular structures.

3. Publications

F. Ben Romdhane, T. Björkman, A. V. Krasheninnikov, F. Banhart, The transformations between one- and two-dimensional silica on metal substrates, submitted to *2D Materials*.

A publication of the results on carbon is under preparation.

4. Comments

The goals of the project have been extended so that not only carbon but also a structurally closely related phase of silica has been studied.

**Multi-period compound gratings with varying
component efficiencies for outcoupling
enhanced OLEDs**

Christian Kluge

Christian-Albrechts-Universität zu Kiel (CAU)

Germany

Final Report

1. Project goals:

This project investigated experimentally a new outcoupling structure for organic light-emitting diodes (OLEDs). Due to waveguiding of the high-index OLED stack, the OLED outcoupling efficiency is limited. Single-period Bragg gratings near the emitting layer can increase the light outcoupling by scattering of guided modes, but lead to strong, wavelength-dependent angular features in the emission spectrum and hence induce a color impression for the viewer. In this project, compound binary gratings, that combine multiple grating components, were studied. We have already shown in a previous project that compound binary gratings scatter each wavelength of a guided mode into multiple directions and thereby reduce the color impression. The aim of this experiment was to design the binary compound gratings in a way that provides control over the intensity of the outcoupling features produced by each component.

2. Project results:

The KNMF fabricated nickel shims that comprised 36 different gratings, providing a large parameter space. The compound binary gratings were designed as the logical disjunction superposition of multiple binary gratings with different periods. In sets of eight compound binary gratings of a particular period combination, the duty cycle of one component was systematically varied. Each grating was of $500\mu\text{m} \times 500\mu\text{m}$ size. The KNMF fabricated the nanostructures by electron beam lithography and transferred them to nickel shims with a grating depth of 50 nm by electroplating. These nickel shims served as master stamps for our nanoimprint lithography process.

By transferring the nanostructures into an organic light-emitting layer and measuring its photoluminescence, we investigated the guided mode outcoupling. Clearly, compound binary gratings scatter a guided mode into multiple directions. In agreement with our theoretical model, we found that the compound binary grating's Fourier coefficients and the waveguide cavity determine the intensity of each scattering direction. We could thus demonstrate that the intensity ratio between the directions can be controlled by changing the duty cycle of a grating component. This result allows to tailor the emission depending on the application in outcoupling-enhanced OLEDs.

3. Publications:

C. Kluge, M. Paulsen, L. T. Neustock, N. Barié, P.-J. Jakobs, J. Adam, and M. Gerken, "Emission tailoring for organic emitter layers with compound binary gratings," accepted for publication in Proc. MRS Spring Meeting Symposium F, San Francisco (2014)

4. Comments:

Altogether, the collaboration with the KNMF team was again valuable and fruitful for us. Thank you!

We were a little disappointed that we haven't been informed about the fact, that the provided labels next to each grating field could not be fabricated. Due to the missing labels, matching of SEM and AFM pictures with the structures as well as further fabrication and characterizations steps were more laborious.

Bimetallic Nanocatalysts: The Gold-Nickel Model System

Adam Fraser

University of Cambridge

United Kingdom

Note: Please fill in this report form and save/print it as a PDF file, then upload it to the KNMF proposal submission system. A cover page containing proposal title, proposer name(s), and technologies selected will be added by the system. A link for the download of the complete report as a PDF file will be displayed in the system.

Final Report

1. Project goals (max. 1.800 characters):

To identify the chemical composition of Au-Ni and Co-Fe nanoparticles, and Au/Pd aggregates
To identify the structure of Au-Ni and Co-Fe nanoparticles

2. Project results (max. 7.000 characters + figures):

2.1.1 Experimental Procedure for AF18

Ni(NO₃)₂·6H₂O was added to anhydrous ethylene glycol (120 mL). P4VP (1.100 g) was added and the resulting mixture was stirred magnetically. The solution was cooled and NaAuCl₄·2H₂O in distilled water (50 mL) was added to the reaction mixture. The resulting mixture was heated for 2 hours. One equivalent of NaBH₄ was added - the colloidal suspension produced was deep red. Acetone (500 mL) was added to precipitate the nanoparticles overnight.

2.1.2 Results for AF18

Analysis by TEM shows the successful synthesis of nanoparticles in the desired size regime (sub 10 nm), with larger Au nanoparticles and (Figure 1a). Bimetallic nature was difficult to verify due to contamination and size constraints.

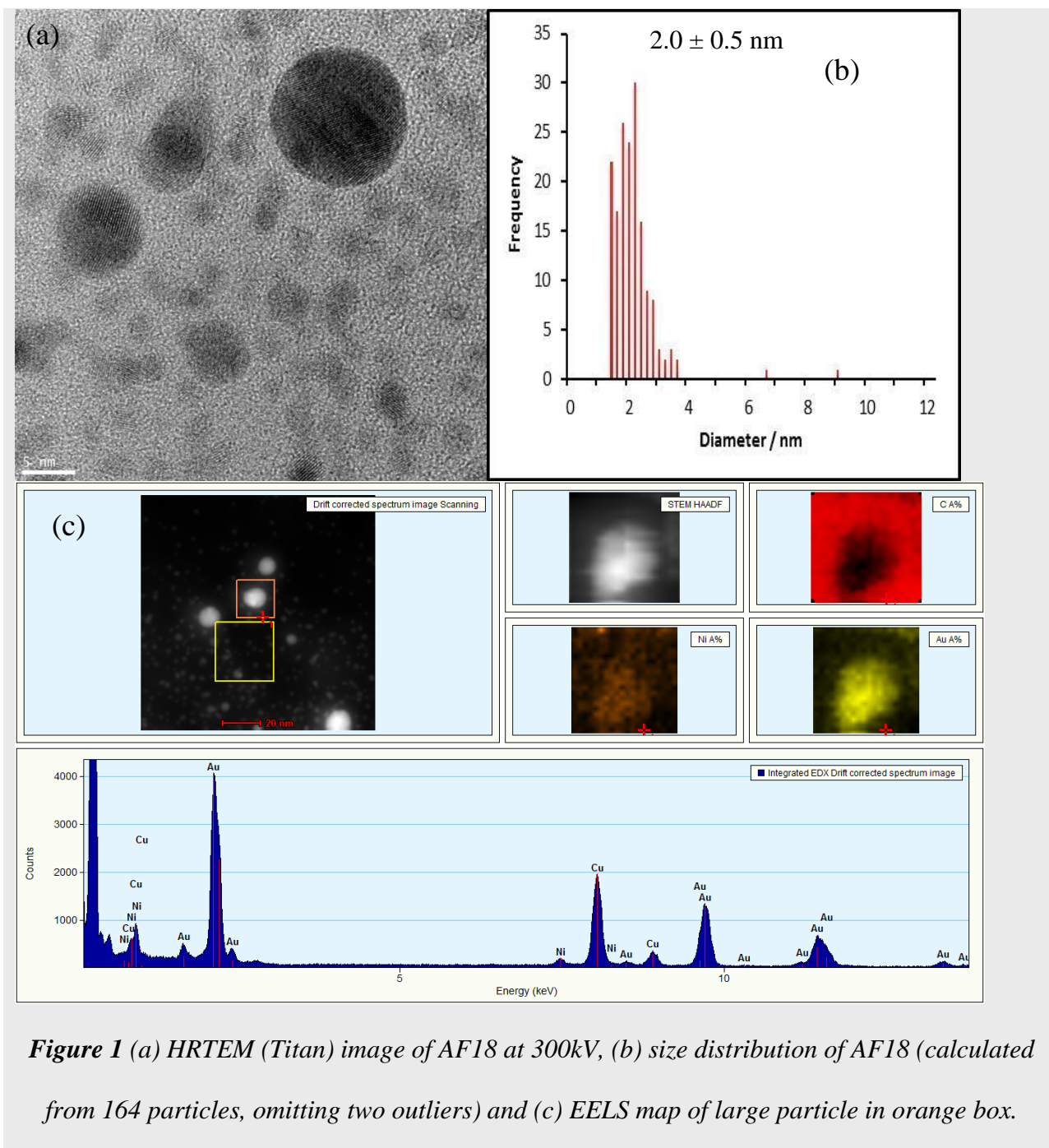


Figure 1 (a) HRTEM (Titan) image of AF18 at 300kV, (b) size distribution of AF18 (calculated from 164 particles, omitting two outliers) and (c) EELS map of large particle in orange box.

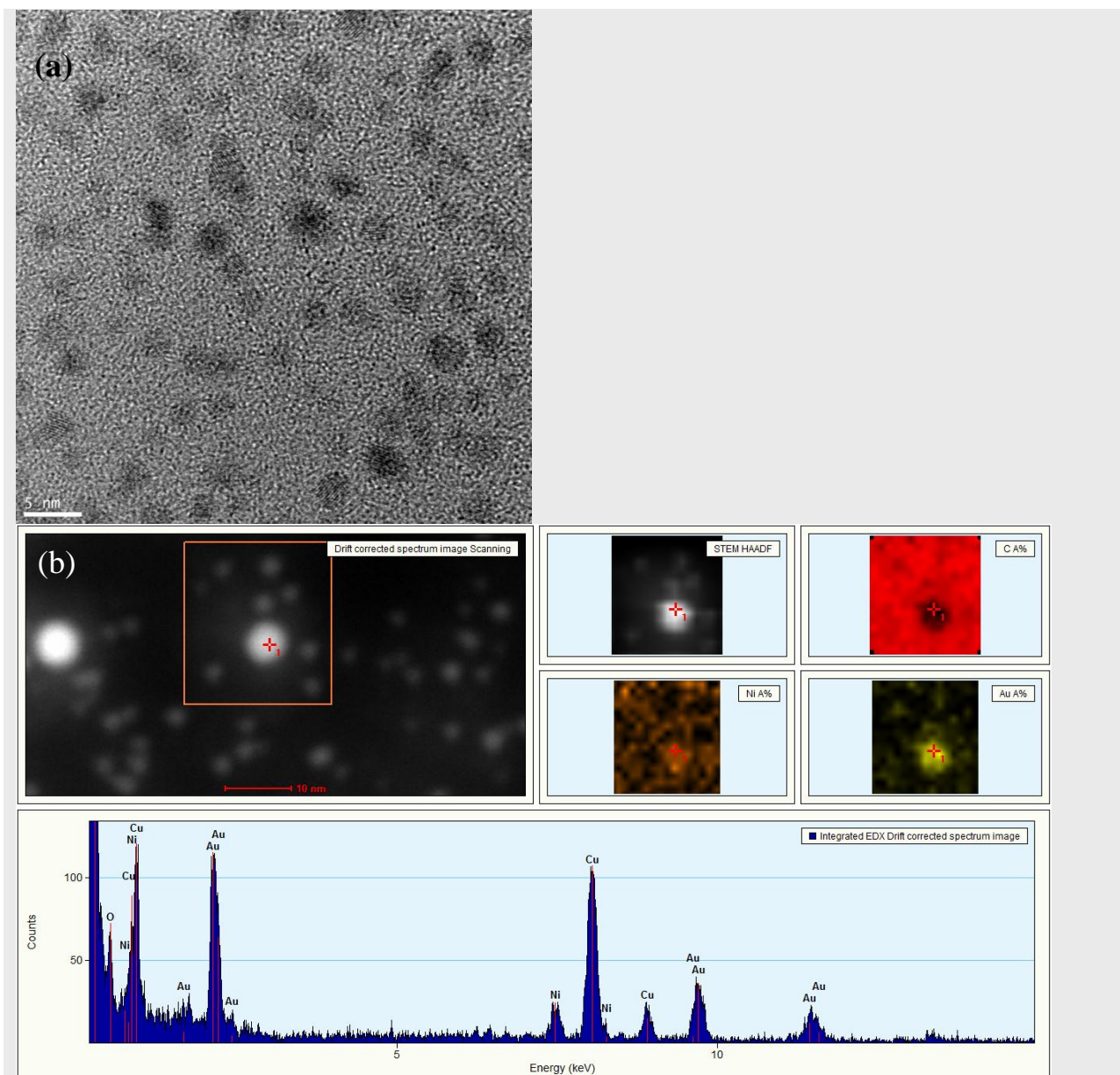


Figure 2 (a) HRTEM (Titan) image of AF18 at 300kV and (b) EDX map of particles in orange box.

HAADF Z-contrast imaging allowed for STEM micrographs to be transformed into a binary image, allowing huge numbers of particles to be analysed rapidly using ImageJ© software with a

TIA reader plug-in. If the two outliers are removed, the nanoparticles are narrowly dispersed: 2.0 ± 0.5 nm. These values are rounded to the nearest Å to not overestimate the accuracy of the instrument. The presence of outliers would normally suggest non-uniform nanoparticle nucleation, giving rise to a bimodal or broad distribution. However, this is not the case, and instead there are simply a few large particles (6-10 nm) amongst a vast majority of smaller particles (1-3 nm). Figure 2 shows a region of the sample AF18 sample with no outliers present. Further analysis using EELS (Figure 1c) and EDX (Figure 2b) mapping suggests that the larger nanoparticles may be bimetallic in nature. As for the smaller particles, the extremely low interaction volume for sub 5 nm particles and the presence of P4VP contamination in the sample make it very hard to distinguish low concentrations of Ni against the background.

The analysis of small and large particles by EDX confirmed the presence of Au and Ni in almost all instances (Figure 3). However, to reiterate, these signals are weak due to low interaction volume and are not exhaustive evidence of bimetallic nanoparticle formation, especially for the larger particles, where the Ni signal is sometimes very low, albeit well above the background. One possible factor could be the presence of a Ni salt background, which may interact with particles more strongly than the carbon grid, thus creating an artificial difference between the background and the particles where the Ni salt concentrates itself around the large particles.

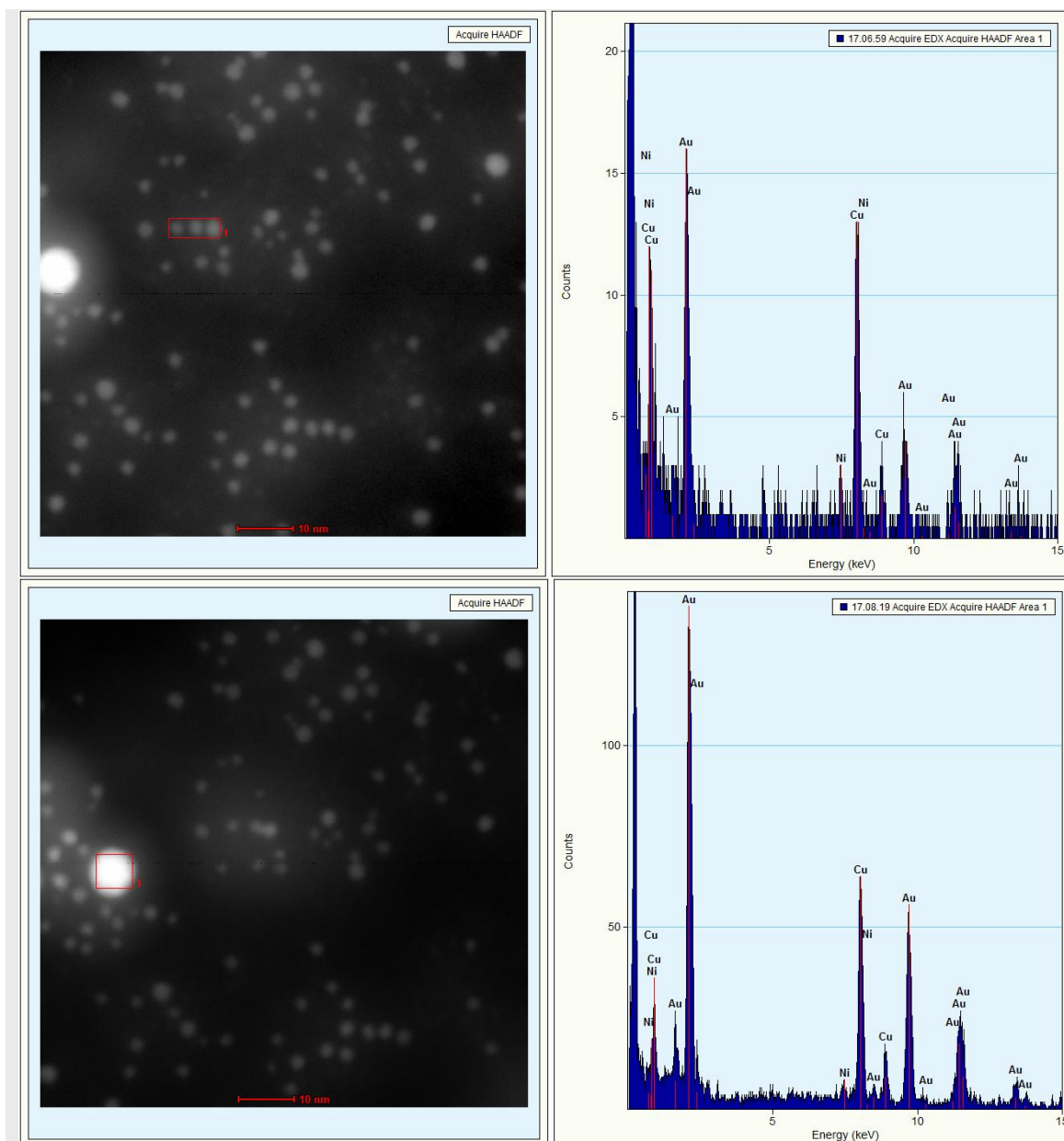


Figure 3 HAADF Z-contrast imaging (Titan) of AF18 at 100kV and associated EDX spectra of red boxes.

2.2.1 Experimental Procedure for AF30

Bimetallic Au-Ni nanoparticles have been successfully synthesised by She *et al.* in the size range of 40-70 nm using a seed-based approach.¹ The synthesis of AF30 aimed to produce smaller Au-Ni nanoparticles by forming smaller Ni seeds and reducing the reaction temperature. The synthesis of Ni nanoparticles in the size range 2-9 nm was attempted following the work of Carencio *et al.*², followed by reduction of Au.

For the synthesis of Ni seeds: Ni(acac)₂ (2.00 g, 7.80 mmol) was added to 78.0 mmol of oleylamine (20.8 g, 10 equiv) and 6.24 mmol of trioctylphosphine (2.30 g, 0.8 equiv) in 12 mL of 1-octadecene. The mixture was degassed at 100 °C and then heated at 220 °C for 2 h, giving a black solution.

For the attempted synthesis of Au-Ni nanoparticles: 2.3 mmol of NaAuCl₄·2H₂O was dissolved in 1 mL of dibenzyl ether and transferred to the Ni seed solution. The reaction mixture was heated to 70 °C for 30 min and then cooled to room temperature. The mixture was centrifuged after addition of 40 mL of acetone to give a black product. The nanoparticles were redispersed in 10 mL of dry hexane.

2.2.2 Results for AF30

Performing EDX analysis on a relatively large area of the sample gives an overall picture of the composition. This reveals that Au and Ni are present, along with some Si contamination from vacuum sealant used during the synthesis, but no other impurities exist (Figure 4).

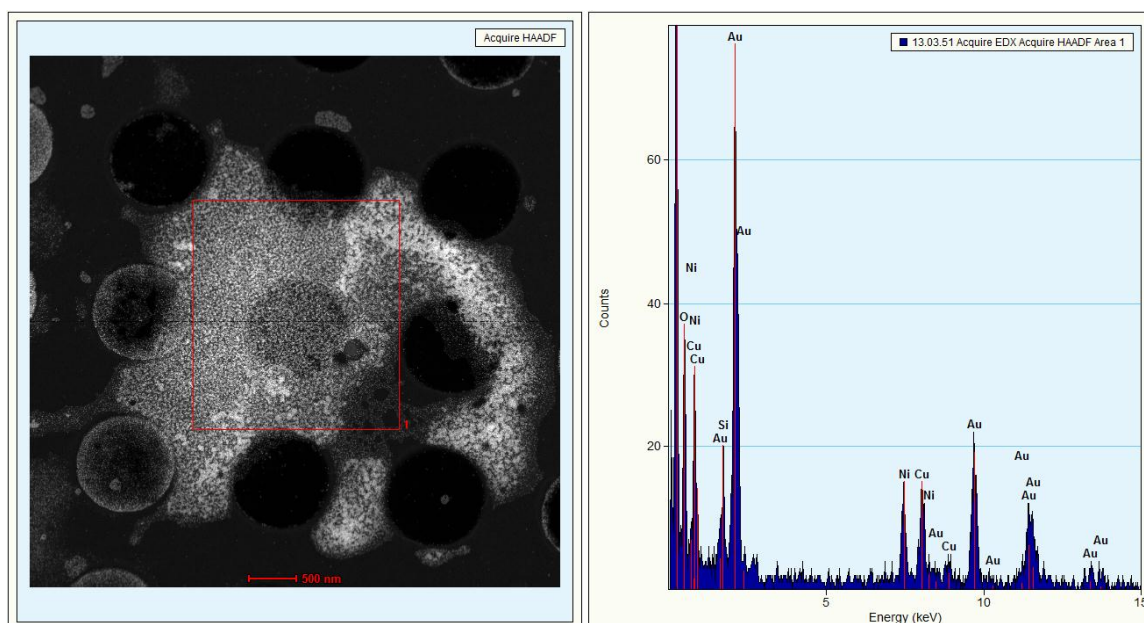


Figure 4 HAADF Z-contrast imaging (Titan) of AF30 at 100kV and associated EDX spectrum of red box.

However, HAADF Z-contrast imaging of the sample indicates that it consists of a physical mixture of monometallic species (Figure 5,6). The presence of smaller grey Ni nanoparticles and larger bright Au nanoparticles, as revealed by selected area EDX, shows the attempt at bimetallic nanoparticle formation was unsuccessful. This could be due to insufficient reaction temperature causing the slow formation of Au nanoparticles rather than the coating of Ni seeds. This argument suggests that fast reaction kinetics are needed to dominate over the low thermodynamic stability of Au-Ni alloys.

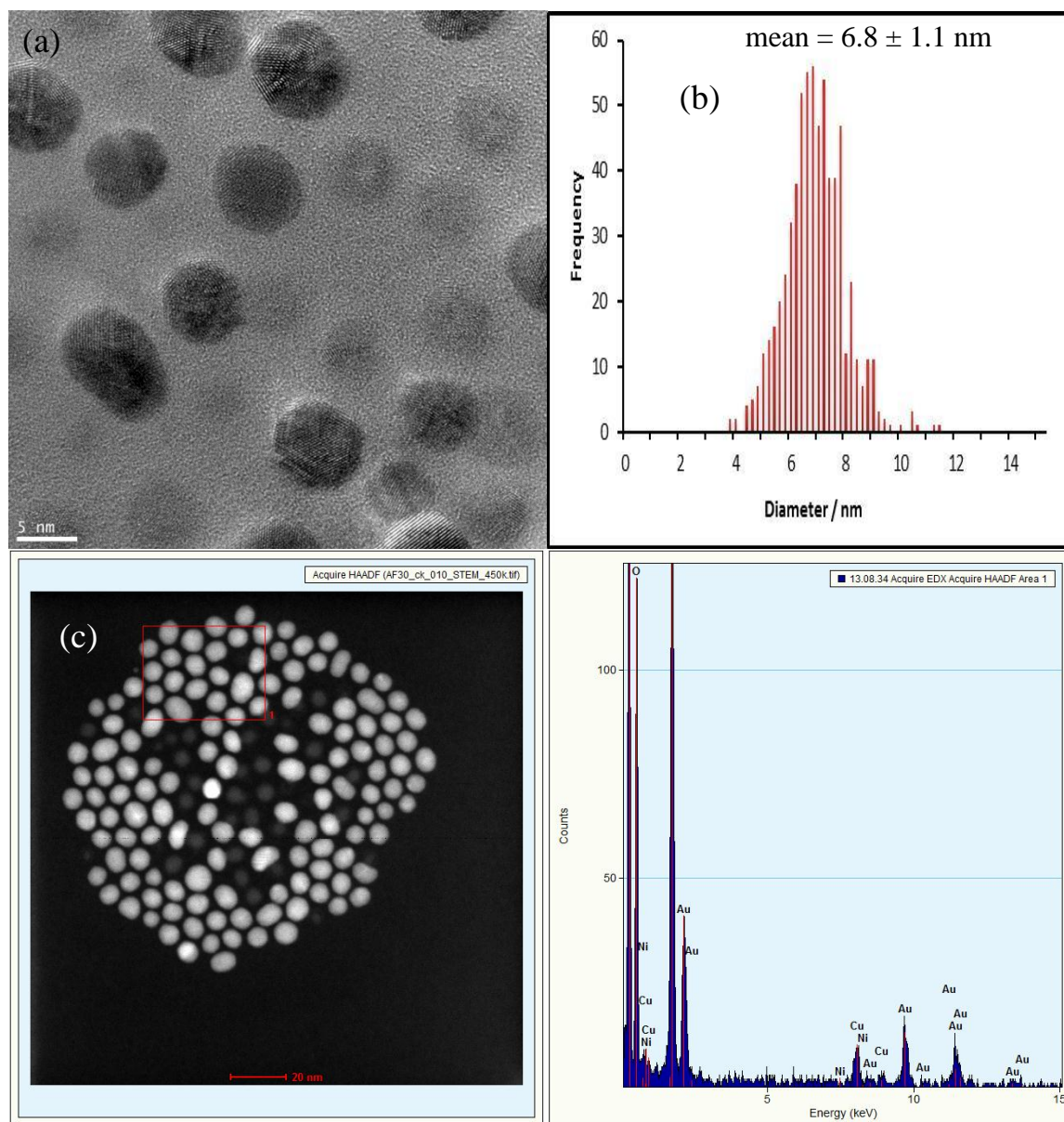


Figure 5 (a) HRTEM (Titan) image of AF30 at 300kV, (b) size distribution of AF30 (calculated from 658 particles) and (c) HAADF Z-contrast imaging (Titan) of AF30 at 100kV and associated EDX spectrum of red box.

A possible explanation for the failure of the synthesis is two-fold: 1) Ni and Au possess a large miscibility gap at low temperature, with solid solubility only occurring **between 800 and 950 °C**, and 2) studies that succeed in core-shell synthesis of Au and Ni either use much larger Ni seeds, or use large stabilising dendrimers³ or microemulsion techniques⁴, which may use fast stabilisation kinetics to overcome the unfavourable thermodynamics of the system.

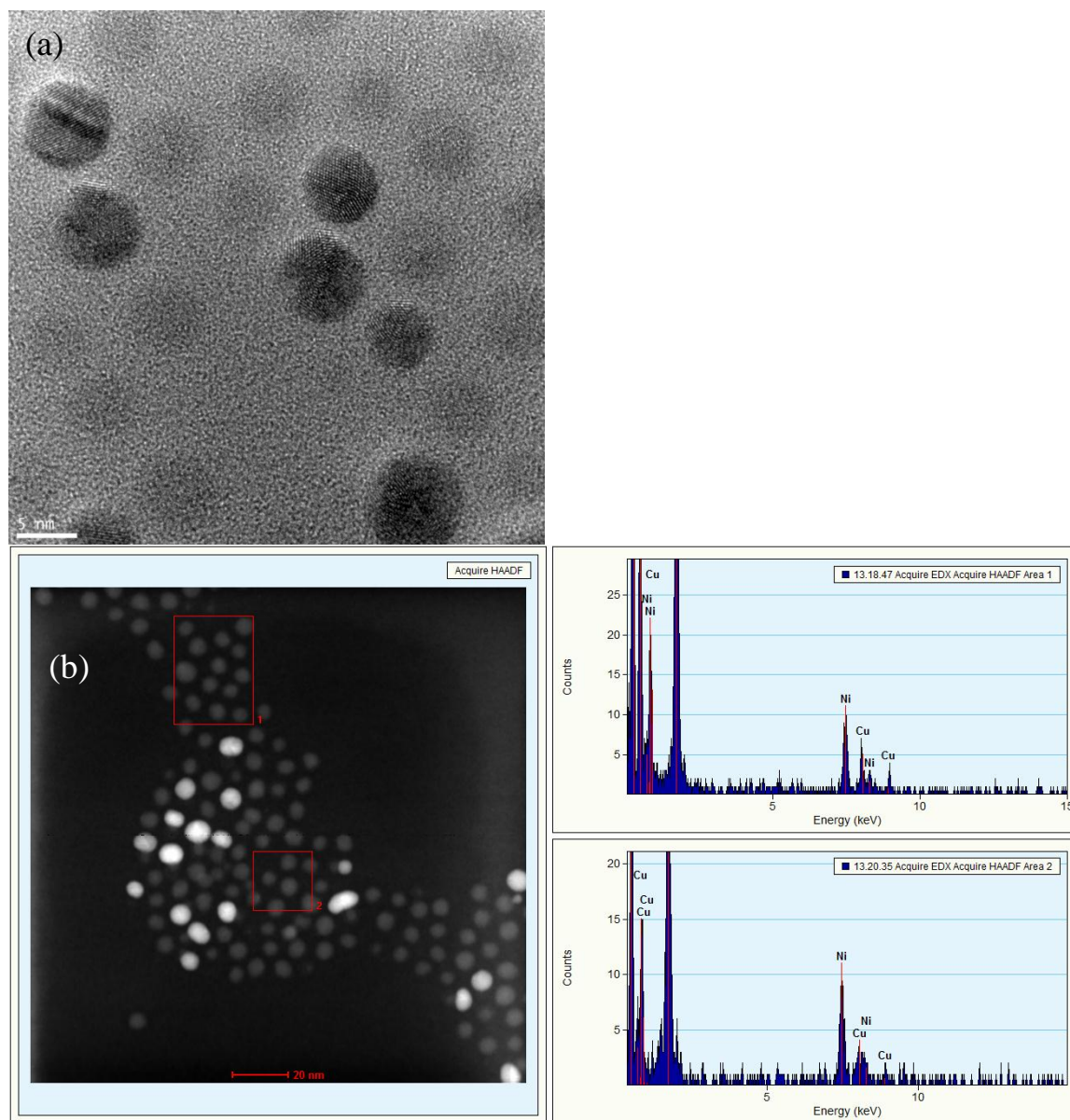


Figure 6 (a) HRTEM (Titan) image of AF30 at 300kV and (b) HAADF Z-contrast imaging (Titan) of AF30 at 100kV and associated EDX spectra of red boxes.

One interesting finding from the AF30 sample was the assembly of Au and Ni nanoparticles in superlattices with two sets of distinct fringes (Figure 7). This is rarely seen unless the nanoparticles

are allowed to settle slowly over time into these self-assembled structures. However, in this case the assembly occurred extremely quickly – in the time taken for a drop to be cast onto the TEM grip and then immediately dried against filter paper. Such superlattices have interesting optical properties and the potential for application in many and various fields.⁵

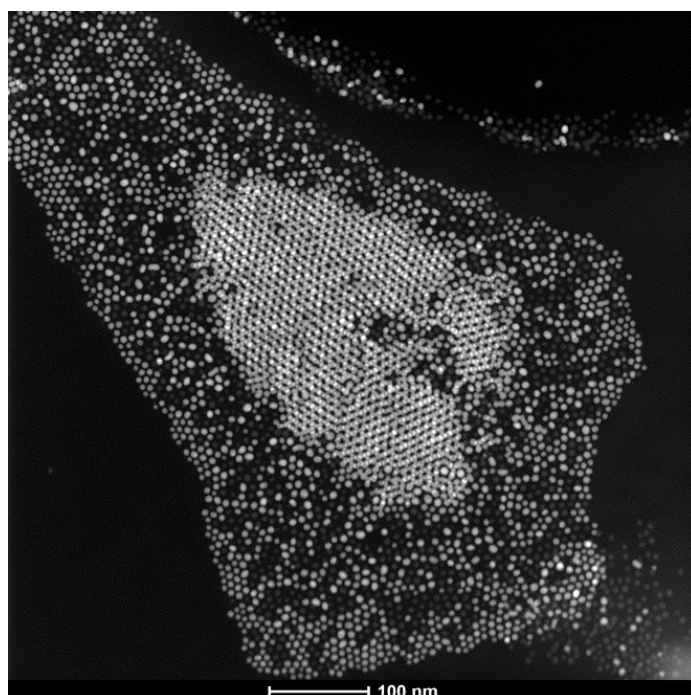


Figure 7 HAADF Z-contrast imaging (Titan) of AF30 at 100kV; brighter pixels represent higher atomic number, Z.

2.3.1 Experimental Procedure for AF33

This was the same as AF30, except the amount of $\text{NaAuCl}_4 \cdot 2\text{H}_2\text{O}$ added to the Ni seeds was doubled to 4.6 mmol.

2.3.2 Results for AF33

The AF33 sample showed a few peculiar results. Increasing the concentration of Au causes a broadening of the size distribution, but more importantly, the Ni nanoparticles appear to adopt a different structure under the new conditions (Figure 9). EDX analysis shows that, despite the presence of bright dots in several Ni nanoparticles, the smaller, dull nanoparticles are still composed entirely of Ni. However, the shape of the Ni nanoparticles is clearly different than in AF30 and much more irregular as opposed to spherical. The Au concentration has clearly increased, as Ni nanoparticles cannot be seen at all in several images (Figure 8). Upon closer inspection, however, the Ni is still present but in a much less defined way, with Ni particles clustering around Au nanoparticles like a support. Such structural changes initiated by the addition of a second metal have been documented in the literature.⁶

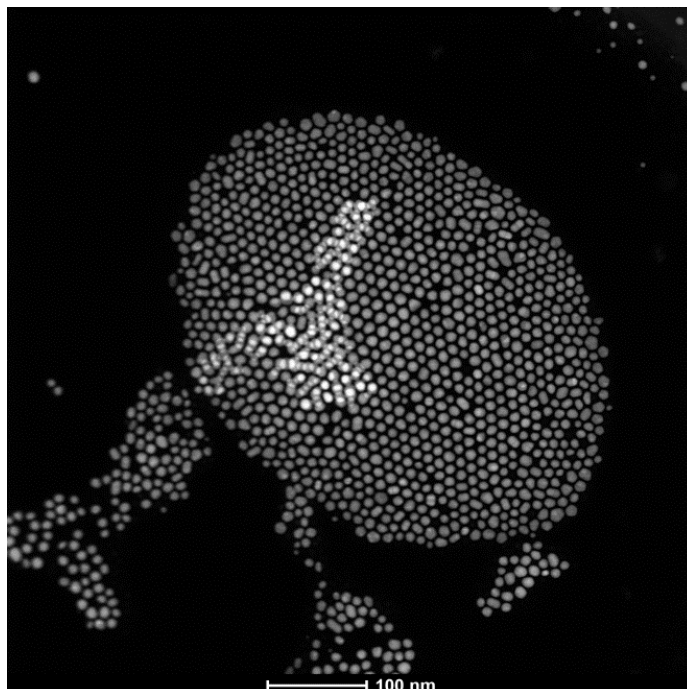


Figure 8 HAADF Z-contrast imaging (Titan) of AF33 at 100kV.

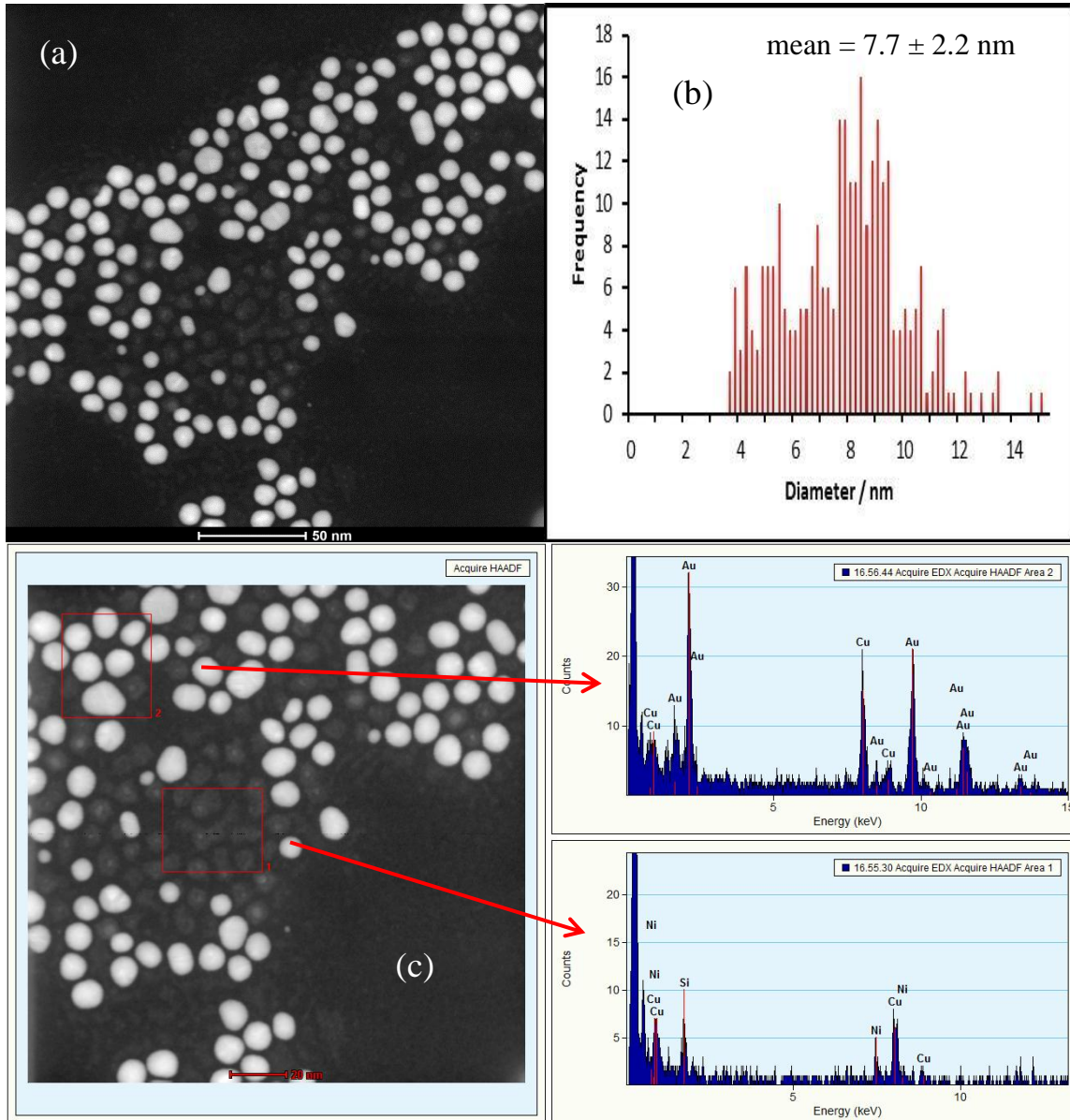


Figure 9 (a) HAADF Z-contrast imaging (Titan) of AF33 at 100kV, (b) size distribution of AF33 (calculated from 288 particles) and (c) HAADF Z-contrast imaging (Titan) of AF30 at 100kV and associated EDX spectra of red boxes.

2.4.1 Experimental Procedure for BK01

In a typical experiment, $\text{Co}_2(\text{CO})_8$ (2 mmol, 0.68 g) was dissolved in 1,2-dichlorobenzene (DCB, 5ml) and injected into a solution of oleic acid (0.65 ml, 2.0 mmol), also in DCB (40 ml) at 60 °C. After initial effervescence subsided, the solution was heated to 185 °C for 30 minutes, and then left to cool.

The cobalt seeds were then heated to 120 °C and $\text{Fe}(\text{CO})_5$ (0.18 mol, 0.9ml) was added. After 30 minutes, the temperature was increased to 180 °C at a rate of 2-3 °C/min, and was then kept at this temperature for an additional 30 minutes. The temperature was then increased to 250 °C for 15 minutes, before allowing it to cool to room temperature. The nanoparticles were purified by precipitation in excess ethanol, followed by re-dispersion in the minimum volume of hexane (4-5ml) followed by a second precipitation. The resulting particles were dispersed in hexane (10 ml).

2.4.2 Results for BK01

The sample showed a clear core-shell structure in HRTEM images, with a darker core region surrounded by a shell of lower contrast material (Figure 10). These materials can be confirmed as Co and Fe_3O_4 using SAED images (Figure 10b) and d-spacings.

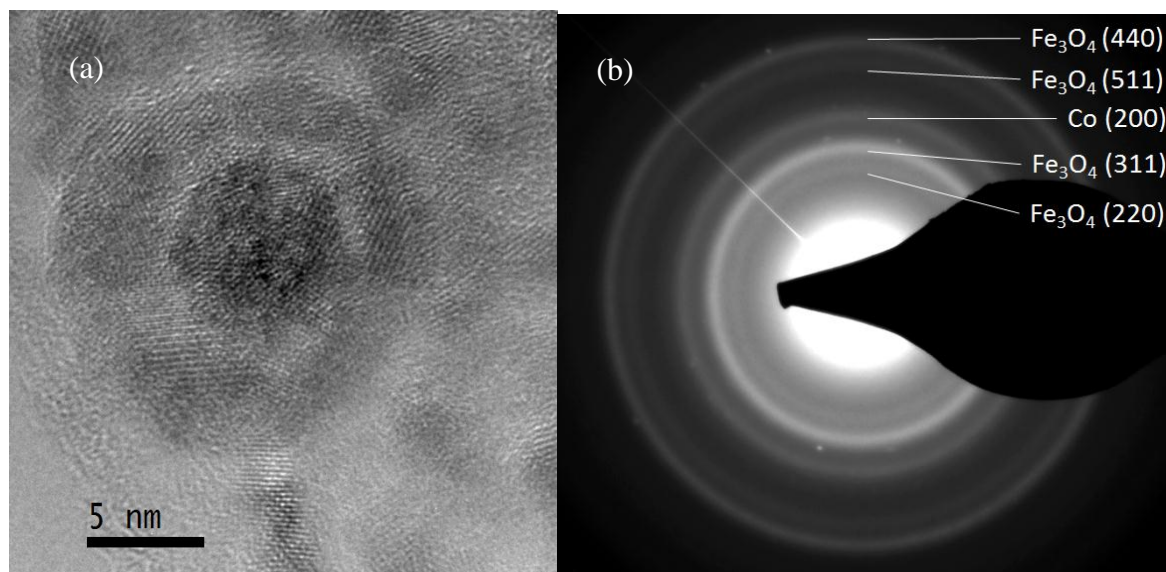


Figure 10 (a) HRTEM image of a BK01 core-shell particle at 300kV, (b) SAED image of Co@Fe₃O₄ nanoparticles with phases assigned to the signals.

An FFT of an individual particle was recorded, and shows signals for most of the phases identified in the SAED in Figure 10. This particle was subjected to a masking procedure identifying the regions of the image which generated the FFT signals. This is shown in Figure 11. The arrows drawn from the FFT to regions of the nanoparticle are spatially accurate.

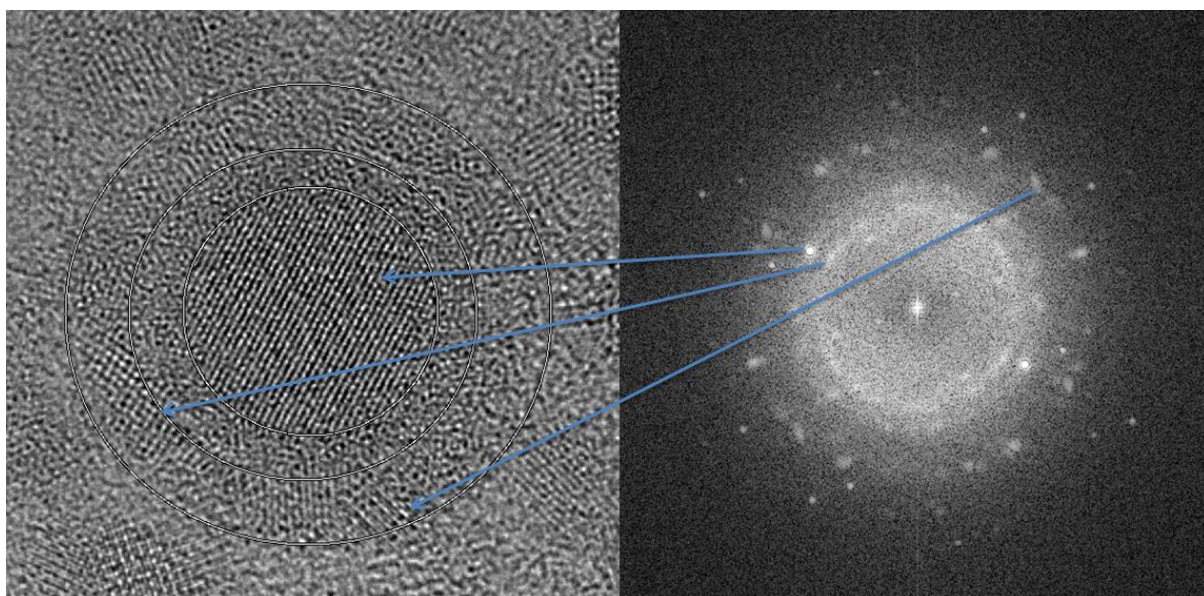


Figure 11 HRTEM image of a BK01 core-shell nanoparticle, with corresponding FFT. The three rings on the FFT correspond to the 3 major rings in the SAED image in Figure 10b.

This is good evidence of a Cobalt core with an Fe_3O_4 shell, however d spacings as measured from fringes in TEM images are subject to errors in lens magnification, due to hysteresis effects. Further evidence was obtained from energy filtered (EF)TEM imaging. Here, signals from Co and Fe were isolated by selecting only the electrons which correspond to the electron energy loss of the respective metal. In this manner, images can be taken of the same region of sample which show different intensities relating to specific elements.

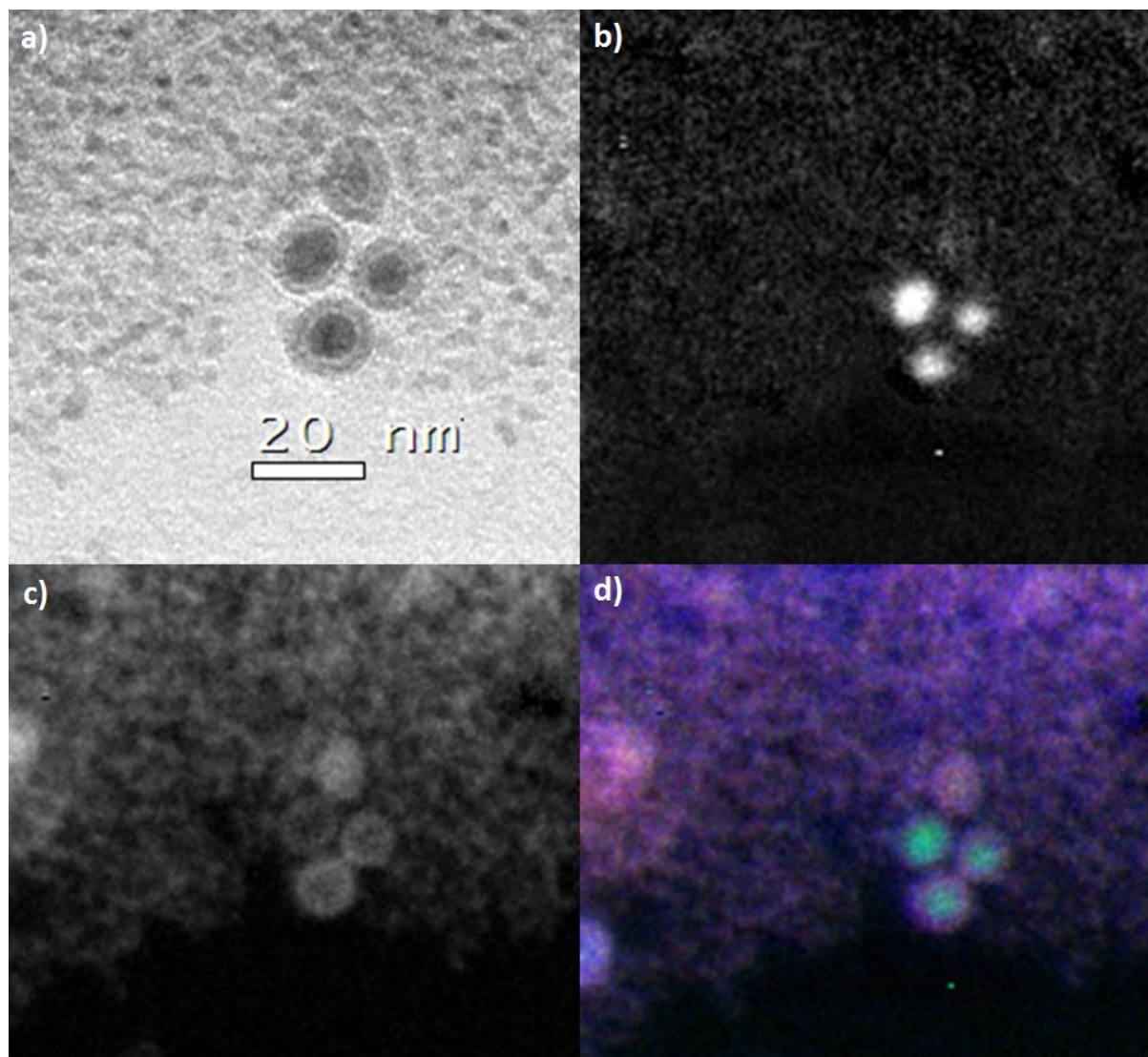


Figure 12 EFTEM images of Co@Fe particles - a) bright field HRTEM image; b) cobalt map; c) Fe map; d) overlay of the Fe and Co maps, with Co in green, Fe in orange and O in blue.

The images in Figure 12 clearly show that the particle has a core-shell structure, and that the core is comprised of cobalt with an iron shell. The oxygen map matches closely with the iron map, agreeing with the previous indications that the shell is indeed an oxide of iron.

The techniques used above give convincing evidence that the particles synthesised are indeed core-shell, and similar results have been obtained using other microscopes. The lattice spacings measured from fringes are reinforced by the SAED data, meaning that the phases are readily identifiable using techniques other than XRD which to date has given very poor uncharacterisable patterns for this sample.

2.5.1 Results for AFEN-01

Au-Pd aggregates were prepared using aqueous methods to produce large Au particles (~20 nm) and smaller Pd particles (~6 nm) (Figure 13).

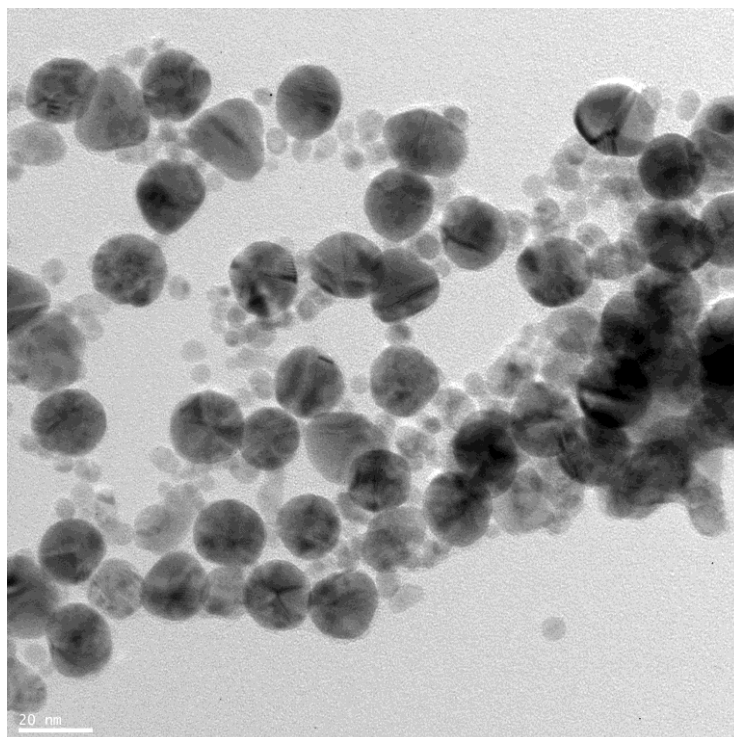


Figure 13 BFTEM image of Au-Pd aggregate at 115kV.

EDX analysis shows that the larger particles consist of Au and the smaller particles consist of Pd (Figure 14). However, the smaller Pd particles contain some Hg-contamination, possibly due to a cracked thermometer which leaked into the reaction mixture during synthesis. A large-scale EDX of AFEN-01 showed almost no signal for Hg, suggesting that the amount of contamination was small (Figure 15).

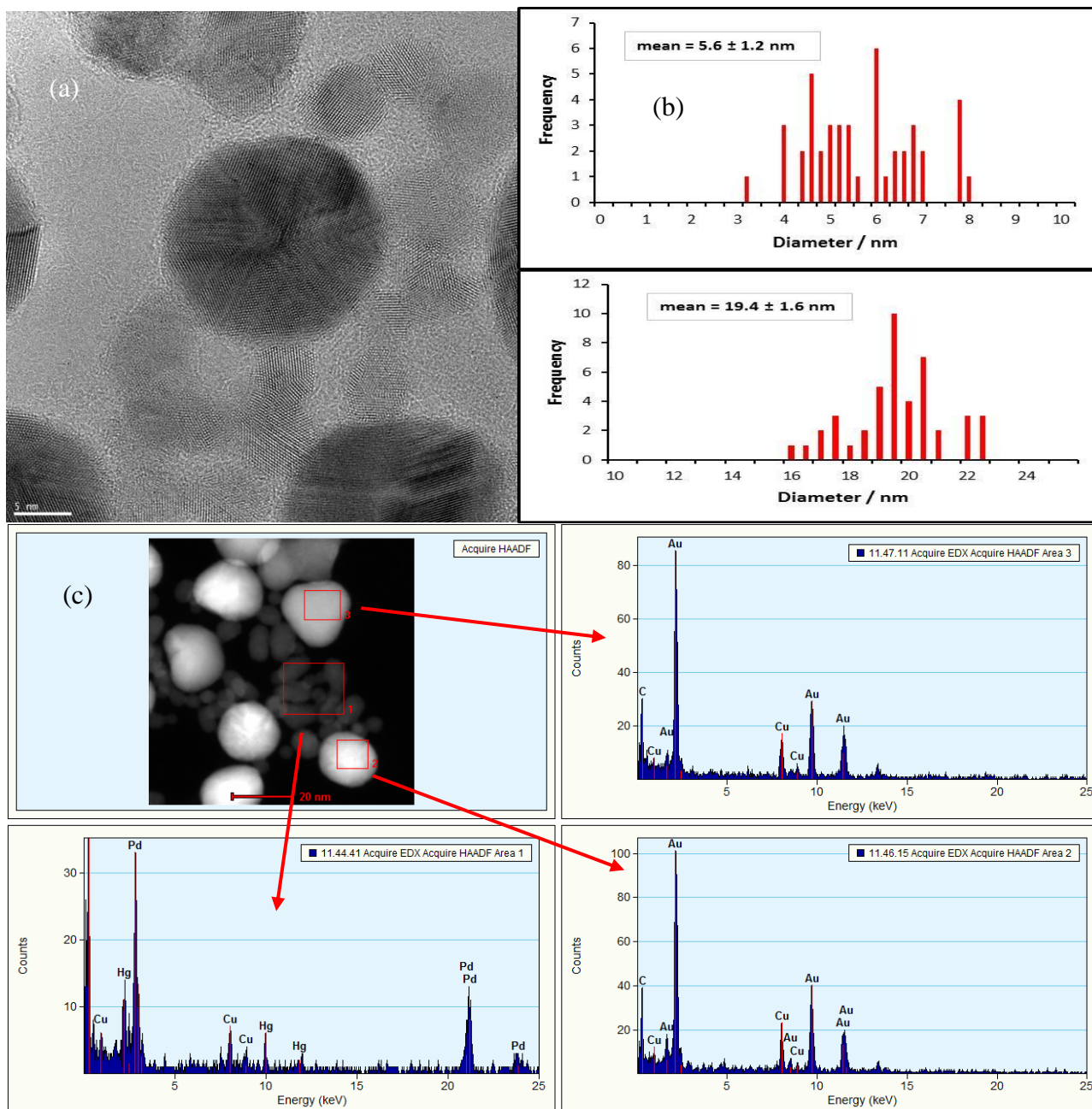


Figure 14 (a) HRTEM image of AFEN-01 at 300 kV, (b) size distributions of Pd (top) and Au (bottom) nanoparticles calculated from 44 particles each, and (c) EDX of AFEN-01.

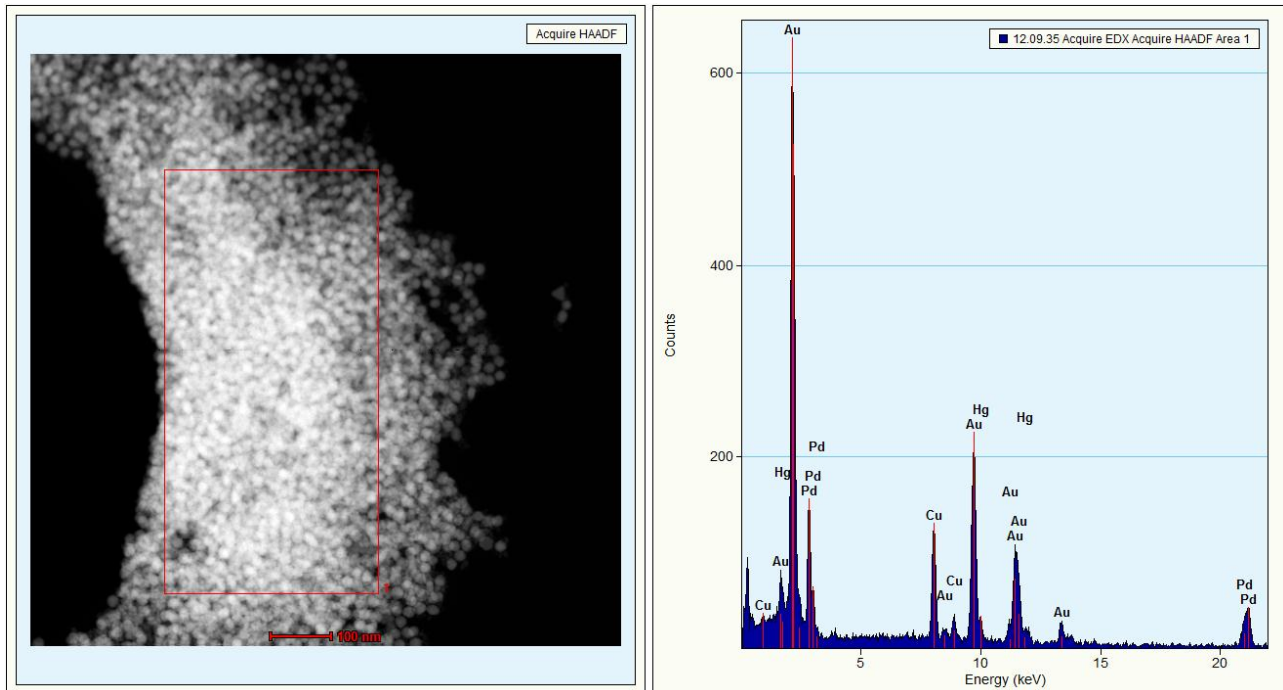


Figure 15 Large-scale EDX of AFEN-01

2.6.1 Supporting Information

- BK01 (1) EELS and (2) EDX mapping

(1)

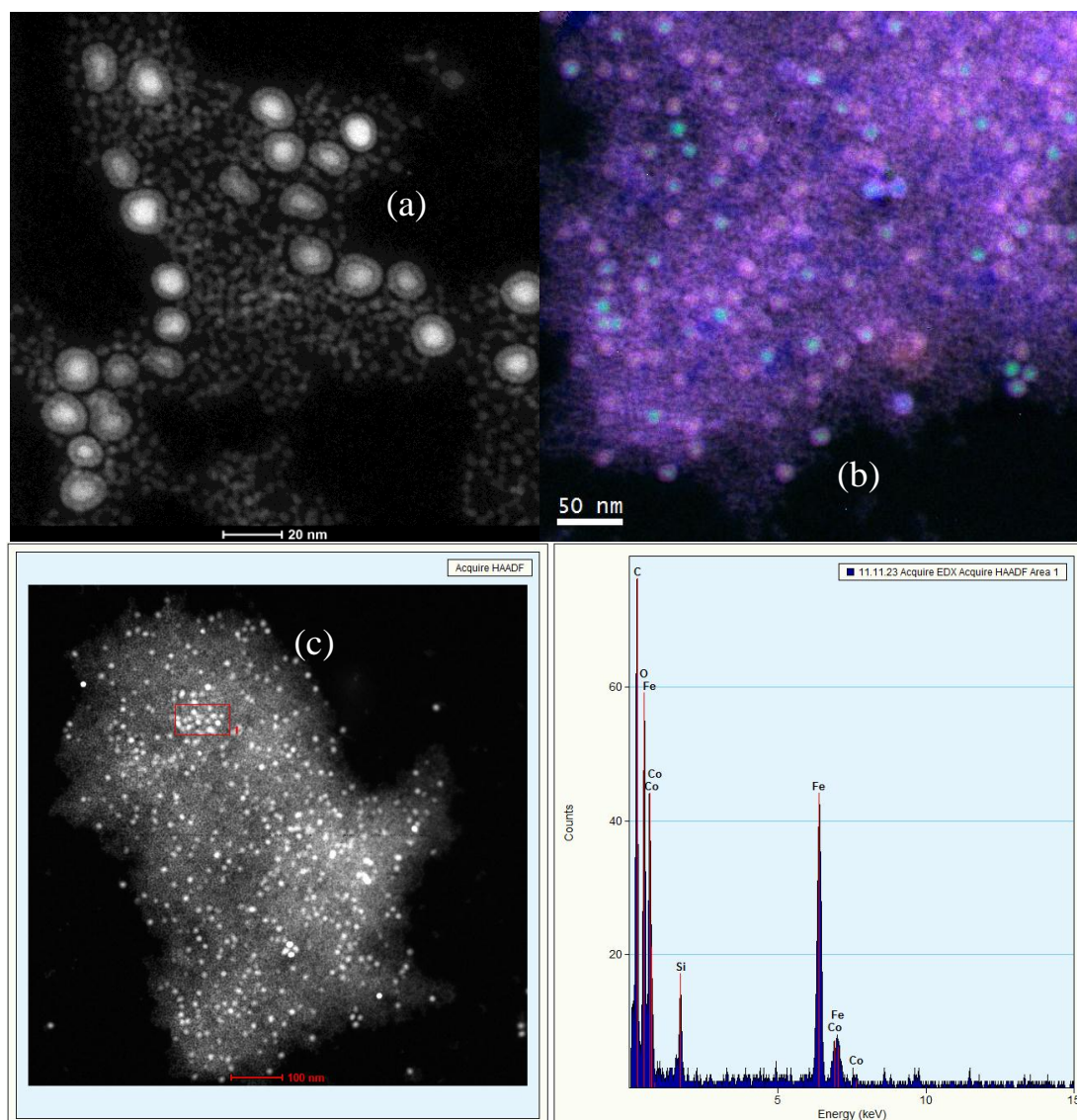


Figure 16 (a) HAADF image of BK01, (b) EELS mapping of BK01 (Co = green, Fe = orange, O = blue), and (c) EDX of BK01.

(2)

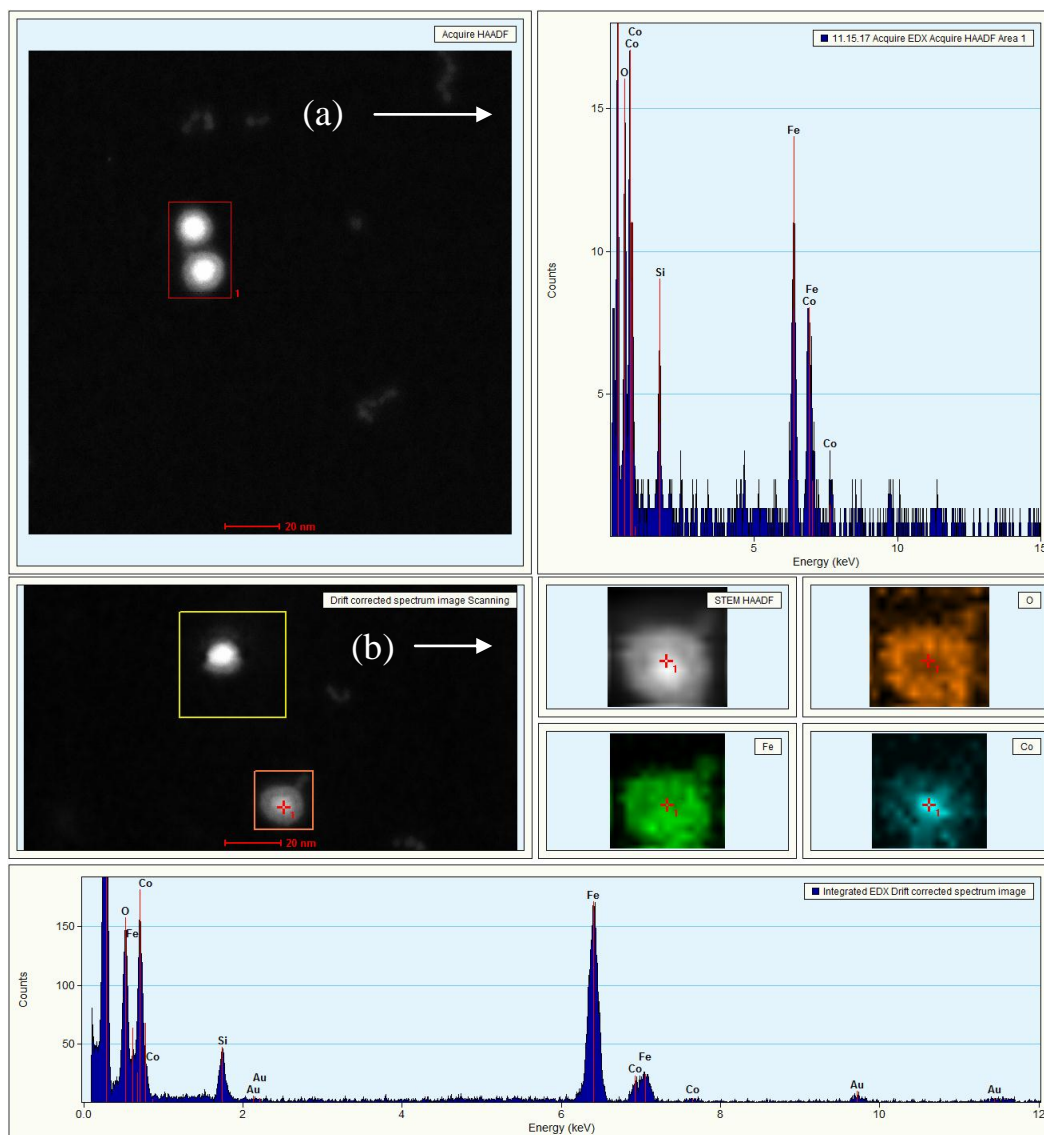


Figure 17 (a) EDX of two core-shell BK01 nanoparticles, and (b) EELS map of a core-shell nanoparticle (in orange box).

3.1 XPS Data

The XPS data showed the complete removal of carbon from the following samples, using an RF-activated ozone plasma etcher (Femto Diener):

- FeMo in PS-b-P4VP micelles
- Ni in PS-b-P4VP micelles
- AuNi in PS-b-P4VP micelles

The etching rate of PS-b-P4VP is currently under investigation.

3. Publications (please stick to the user guidelines for publications and acknowledgements on www.knmf.kit.edu):

Currently working on the following publications:

- 1) Electron Microscopy of Co@Fe core@shell bimetallic nanoparticles – Nanoscale Publication – Currently accepted but publication date “to be determined”
- 2) Plasmonic interactions in Au/Pd aggregates – Currently in progress

4. Comments (max. 1.800 characters):

The synthesis of bimetallic Au-Ni nanoparticles using oleylamine reduction and oleic acid capping agents is unsuccessful (samples AF30 and AF33).

-
- ¹ She, H., Chen, Y., Chen, X., Zhang, K., Wang, Z., & Peng, D.-L. (2012). Structure, optical and magnetic properties of Ni@Au and Au@Ni nanoparticles synthesized via non-aqueous approaches. *Journal of Materials Chemistry*, 22(6), 2757. doi:10.1039/c1jm14479k
 - ² Carenco, S., Boissière, C., Nicole, L., Sanchez, C., Le Floch, P., & Mézailles, N. (2010). Controlled Design of Size-Tunable Monodisperse Nickel Nanoparticles. *Chemistry of Materials*, 22(4), 1340-1349. ACS Publications. doi:10.1021/cm902007g

-
- ³ Auten, B. J., Hahn, B. P., Vijayaraghavan, G., Stevenson, K. J., & Chandler, B. D. (2008). Preparation and Characterization of 3 nm Magnetic NiAu Nanoparticles. *Journal of Physical Chemistry C*, 112(14), 5365-5372. doi:10.1021/jp076982c
- ⁴ Chiu, H.-K., Chiang, I.-C., & Chen, D.-H. (2009). Synthesis of NiAu alloy and core-shell nanoparticles in water-in-oil microemulsions. *Journal of Nanoparticle Research*, 11(5), 1137-1144. Springer Netherlands. Retrieved from <http://www.springerlink.com/content/4m8nj1v738824154/>
- ⁵ Labastide, J. A., Baghgar, M., Dujovne, I., Yang, Y., Dinsmore, A. D., G Sumpter, B., Venkataraman, D., et al. (2011). Polymer Nanoparticle Superlattices for Organic Photovoltaic Applications. *The Journal of Physical Chemistry Letters*, 2(24), 3085-3091. American Chemical Society. doi:10.1021/jz2012275
- ⁶ Harada, M., Asakura, K., & Toshima, N. (1993). Catalytic Activity and Structural Analysis of Polymer-Protected Au/Pd Bimetallic Clusters Prepared by the Successive Reduction of HAuCl₄ and PdCl₂. *Society*, 97(19), 5103-5114.

Out of Plane High Aspect Ratio Micro Wires as Suspension Elements in Inertial Sensors

Felix Greiner

Technische Universität Darmstadt

Germany

Final Report

1. Project goals:

Micro- and nanowires with high aspect ratios, arranged as slim and tall standing metal pillars offer promising features for micro systems. The general goals are the same as in preceding proposal 2010-004-000365:

- 1st fabrication of high aspect ratio out of plane metal wires next to low aspect ratio metal blocks,
- 2nd multilayer material link of these structures,
- 3rd realization and characterization of an acceleration sensor applying these structures.

The KNMF services refer to the fabrication of aligned templates made by X-ray lithography, referred by *X-ray template* (1st point), followed by Ni electroforming (2nd point), and support during planarization (3rd point). The remaining process steps as well as Cu electroforming and planarization of most samples are to be processed at Technische Universität Darmstadt (TUD), see Fig. 1.

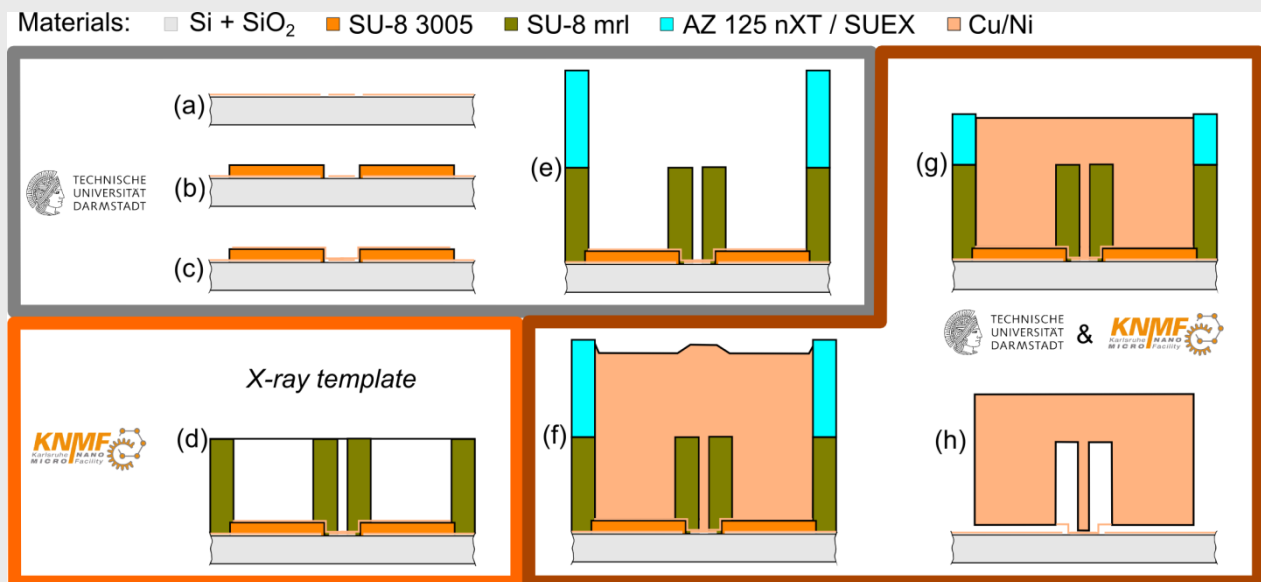


Fig. 1: Process flow: (a) - (c) UV litho at TUD; (d) Aligned X-ray litho at KNMF; (e) UV litho at TUD; (f) electroforming at TUD/KNMF; (g) planarization at TUD/KNMF; (h) photoresist removal at TUD.

For the 1st goal, the high aspect ratio templates (*X-ray template*) provide vertical cylindrical holes with aspect ratios from 16 to 33 next to template openings with low aspect ratios (Fig. 1 d). X-ray lithography is the only technique suitable for the fabrication of these templates.

For the 2nd goal, structures beneath and above the *X-ray template* are necessary. Beneath, there are structured circuit paths (Fig. 1 a), sacrificial layers (Fig. 1 b), and seed layers (Fig. 1 c). Above, there is a low aspect ratio electroforming template (Fig. 1 e). All these layers contribute to the functional integration of all structures into an electroformed accelerometer MEMS (Fig. 1 f).

For the 3rd goal, the wafers are to be planarized for a defined structural height (Fig. 1 g), cut into dies, the electroforming templates and the sacrificial layers are to be removed (Fig. 1 h), the dies are to be connected to evaluation electronics and a sensor characterization is to be executed.

2. Project results:

Major project results have been published in a journal article [1], have been presented at an international workshop [2] and more details have been published in a phd thesis [3].

For the 1st goal, an intermediate mask and an expensive working mask for aligned exposure have been fabricated in the precedent proposal 2010-004-000365 (Fig. 2). With respect to project runtime and costs, the same working mask has been used for this proposal 2012-008-00970. Like every technical realization, the working mask shows small production errors.

First, the metal structures of the mask are approximately 1 μm smaller than designed, resulting in 1 μm smaller diameters of the vertical cylindrical holes in the X-ray templates and subsequently 1 μm smaller diameters of the vertical cylindrical metal wires. The smaller diameters of the metal wires emphasize the stability issue of the metal MEMS accelerometers. Due to project runtime and costs, the approach to ease this issue is reducing mass load by planarization of the top metal layer (Fig. 1 g).

Second, the mask's features are minimally distorted in the lateral dimension in comparison to CAD definition. This is probably due to the demanding production process of the mask with the separation of the X-ray transparent foil from a carrier substrate and the subsequent etching step for opening the alignment structures (detail of Fig. 2). In addition, the mask heats up during several minutes of X-ray exposure, potentially resulting in some drifting of feature positions. This impreciseness exceeds the one of UV masks but still stays in between the planned tolerances of $\pm 20 \mu\text{m}$. Thus, the scheduled process flow can be executed using the existing working mask.

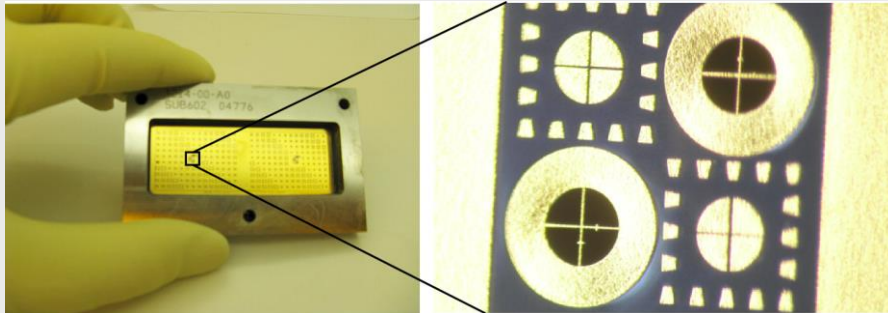


Fig. 2: Working mask in its frame with 20 mm x 60 mm exposure field, detail: alignment structures with dark black openings and golden microstructures clamped across the openings for optical alignment.

For the 2nd goal, the fabrication of circuit paths has been optimized in comparison to the precedent proposal (Fig. 3 b). The copper circuit paths now show good adhesion to the substrate and now show no spikes at their outer edges. The circuit paths are thickened for a better conductivity during electroforming of the large structures (Fig. 1 f). The sacrificial layer processing has also been optimized. Its defect density has been minimized by the use of a double layer process with SU-8 3005. After the project runtime, the defects have been completely eliminated by the use of a new charge of SU-8 3005 material which has not been stored at below 15°C. The seed layer's design has been adapted, so a final etching step is no longer necessary (Fig. 3 a). There has been much effort to find good Cu electroforming conditions (Fig. 3 f), while a single test with Ni electroforming at KNMF has shown, that standard parameters are not very suitable.

For the 3rd goal, the planarization has been investigated. Residues of lapping slurry can cover the whole structure (Fig. 1 h, and prevent its movement. Therefore, a successful final cleaning step with ultrafine abrasive paper has been introduced by KNMF.

Project Report

Proposal-ID: 2012-008-000970

Date: 2013-12-16

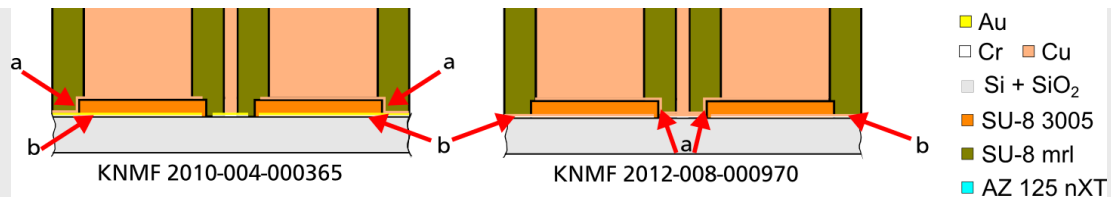
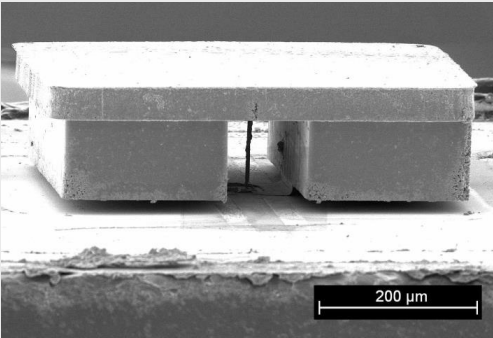
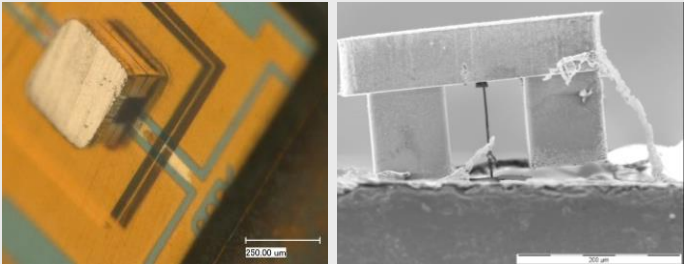
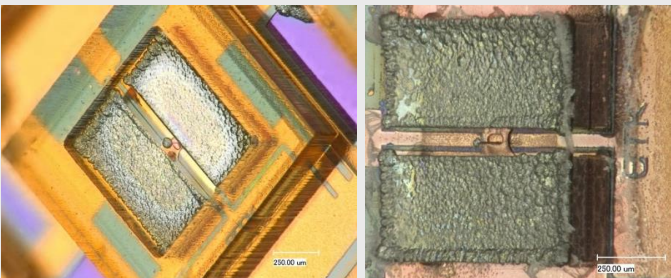


Fig. 3: Changes in mask designs from old (left) to new (right):
 (a) Seed layer connecting the top of the sacrificial layer from outer edges to inner edges.
 (b) Circuit path material from Au (150 nm) to Cu (300 nm + thickened regions of 3 μm),

Table 1 shows results of 9 wafers that have been processed according to Fig. 1. 3 additional process runs have been started, but have early been stopped due to quality issues of SU-8 3005 (Fig. 1 c). 3 further wafers have been stopped after realization of X-ray template (Fig. 1 d) due to project runtime.

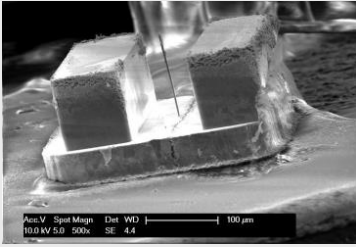
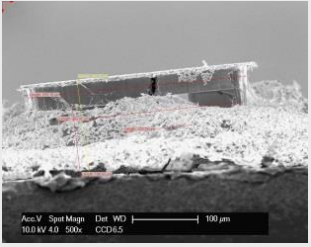
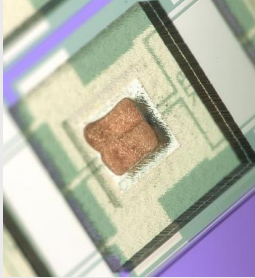
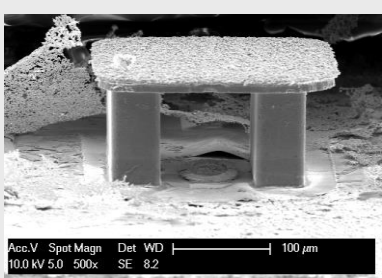
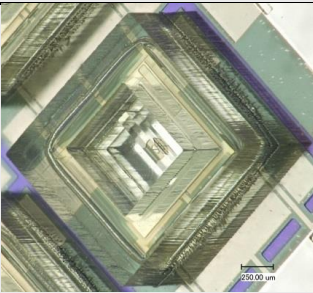
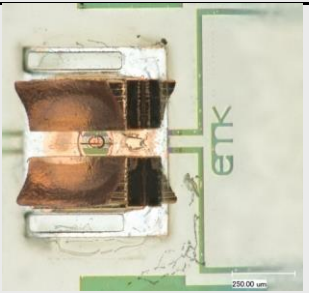
Tab. 1: Wafers and their status sorted by their processing order (process step names referring to Fig. 1).

Wafer	Status
FG342	<ul style="list-style-type: none"> • a-c: excellent results • d (X-ray template): good results • e: good results with AZ 125 nXT • f: good Cu deposition • g: minimal residues due to ultrafine abrasive paper at TUD some wires are sheared off, maybe this is due to a too abrupt force application during handling with the abrasive paper • h & chip separation: good results 
FG340	<ul style="list-style-type: none"> • Similar to FG337, but: <ul style="list-style-type: none"> - mistake in Cu plating solution → large fields stay inhibited from deposition - g: additional AZ 125 nXT applied to fill up the gaps between the structures for better adhesion during lapping → no improvement
FG337	<ul style="list-style-type: none"> • a-c: excellent results • d (X-ray template): good results • e: good results with AZ 125 nXT • f: better Cu deposition, but still not all wires electroformed • g: lapping at TUD, polishing with ultrafine abrasive paper at KNMF • h & chip separation: good results 
FG336	<ul style="list-style-type: none"> • a-c: excellent results • d (X-ray template): good results • e: good results with AZ 125 nXT • f: Ni deposition at KNMF defects in SU-8 3005 layer → Ni grows at wrong positions → Ni deposition stopped too early 

Project Report

Proposal-ID: 2012-008-000970

Date: 2013-12-16

FG335	<ul style="list-style-type: none">• similar to FG334, but lapped too long → nearly no Cu left over		
FG334	<ul style="list-style-type: none">• a-c: good results• d (X-ray template): good results• e: good results with AZ 125 nXT• f: too high current density → porous Cu wires• g: residues after lapping• h & chip separation: good results		
FG322	<ul style="list-style-type: none">• similar to FG320, same results		
FG321	<ul style="list-style-type: none">• a-c: old design, good results• d (X-ray template): good results• e: realized with AZ 125 nXT with minimal soft bake• f, h: good adhesion to layers beneath → far better than SUEX approach but mistake in Cu plating solution → large crystals / no growth• g: planarization with slurry residues		
FG320	<ul style="list-style-type: none">• a-c: old design, good results• d (X-ray template): good results• e: realized with laminated SUEX dry film• f: bad adhesion of SU-8 mrl to SU-8 3005, possibly due to lamination stress → Cu grows at wrong positions → Cu deposition stopped too early		

3. Publications:

- [1] F. Greiner, S. Quednau, F. Dassinger, R. Sarwar, H. F. Schlaak, M. Guttmann, and P. Meyer, "Fabrication techniques for multiscale 3D-MEMS with vertical metal micro- and nanowire integration," *Journal of Micromechanics and Microengineering*, vol. 23, no. 2, p. 025018, Feb. 2013.
- [2] F. Greiner, M. Guttmann, P. Meyer, and H. F. Schlaak, "Fabrication of 3D-MEMS with High Aspect Ratio Micro Wires," in *Book of Abstracts on 10th International Workshop on High Aspect Ratio Micro and Nano System Technology HARMNST 2013*, Berlin, 2013, pp. 19–20.
- [3] F. Greiner, "Micro Nano Integration for Metallic Microsystems applying Vertically Integrated Suspension Elements," phd thesis, Technische Universität Darmstadt, 2013, <http://www.tuprints.ulb.tu-darmstadt.de/3640>.

4. Comments:

Karlsruhe Nano Micro Facility (KNMF)
Karlsruhe Institute of Technology (KIT)
Hermann-von-Helmholtz-Platz 1
76344 Eggenstein-Leopoldshafen
Germany

User Office
Phone: +49 (721) 608-23123
Fax: +49 (721) 6082-26273
Email: knmf-useroffice@kit.edu
Web: www.knmf.kit.edu

Project Report

Proposal-ID: 2012-008-000970

Date: 2013-12-16



A KNMF project could profit from a scholarship for the person in charge, similarly to projects running at GSI Helmholtz Center of Heavy Ion Research in cooperation with Johann Wolfgang Goethe University of Frankfurt or Technische Universität Darmstadt.

Actin Myosin Interaction in Functionally Structured Micro/Nano-Domains

Matias Mosqueira

Ruprecht-Karls-Universität Heidelberg

Germany

Note: Please fill in this report form and save/print it as a PDF file, then upload it to the KNMF proposal submission system. A cover page containing proposal title, proposer name(s), and technologies selected will be added by the system. A link for the download of the complete report as a PDF file will be displayed in the system.

Final Report

1. Project goals (max. 1.800 characters):

The aims of this project are (I) to demonstrate spatially control over the arrangement of motor proteins on surfaces in arbitrary defined geometries, (II) to study the effect of geometrical constraints in size and form on the sliding of myofilaments on these structures and (III) to study on the nano-scale the activity of the actomyosin complex from different type of muscles in presence of key regulatory protein of the cross-bridge cyclin such as troponin-I and troponin-C activated by caged-Ca₂₊ and/or caged-ATP. In a first step we request a short term project (6 month) to establish the basic experimental setup and showing the functionality of the actomyosin complex on DPN generated structures. After accomplishing this first aim proposed here, we would extend our proposal in the next KNMF call to study the actin/ myosin interactions in detail on the DPN structures.

2. Project results (max. 7.000 characters + figures):

No results were obtained.

3. Publications (please stick to the user guidelines for publications and acknowledgements on www.knmf.kit.edu):

None

4. Comments (max. 1.800 characters):

Although the first trial was satisfactory with promising perspective, the following trial was not successful. The main reason for unaccomplished aims of this proposal was due to several technical issues that cannot be solved during the time-frame, listed below:

- 1) The main approach was to link the myosin to the DPN surface via biotinylation. This approach resulted to be very unspecific and not reliable. Myosin never was only present in the DPN surface, having more artefact signal than proper results. Several biotinylation kits from different companies were used without any improvement.

2) The DPN showed an intense background signal that did not allow observing and quantifying the velocity of actin. Different approaches were taken in consideration, but none of the resulted in a satisfactory final result.

The two major technical issues observed during set-up period prevented a success continuity of this proposal.

**A Self-reluctant Against Shear Stress of
Anode Materials for High Electrochemical
Performance Lithium-Ion Battery**

Joong-Kee Lee

Korea Institute of Science and Technology

South Korea

Note: Please fill in this report form and save/print it as a PDF file, then upload it to the KNMF proposal submission system. A cover page containing proposal title, proposer name(s), and technologies selected will be added by the system. A link for the download of the complete report as a PDF file will be displayed in the system.

Final Report

1. Project goals (max. 1.800 characters):

The scientific goal is to gain a better understanding of the effects of the volume expansion of anode materials during electrochemical cycling. By adjusting the size of the laser-generated surface structures an optimal design which allows improved cycling stability can be obtained. In this study, a laser microstructuring process was successfully applied to prepare patterned fluorine-doped tin oxide ($\text{SnO}_2\cdot\text{F}$, FTO) films. A study of the characteristics of a plasma-treated microstructured anode for lithium-ion batteries was carried out in order to investigate the effect of microstructuring of FTO.

2. Project results (max. 7.000 characters + figures):

Title (First): Electrochemical behavior of a laser microstructured fluorine doped tin oxide anode layer with a plasma pretreatment for 3D battery systems

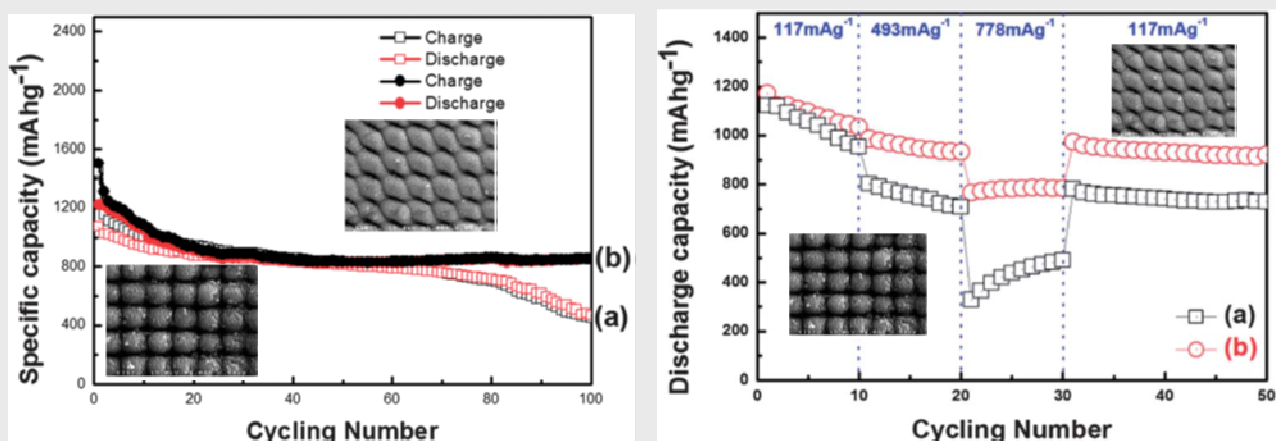


Fig. Electrochemical performance of (a) microstructured FTO film and (b) plasma treated microstructured FTO film as anode electrodes between 3.0 V and 0.01 V at a current density of 117 mA g⁻¹.

Fluorine-doped tin oxide (FTO) films with a thickness of about 3 micrometers were prepared by electron cyclotron resonance-metal organic chemical vapor deposition (ECR-MOCVD) under 800 W of microwave power, with tetra-methyl tin (TMT) as a tin precursor. The dome-shaped micro-patterned FTO layer was prepared on a copper current collector using a KrF excimer laser micromachining system for application as an anode for 3D lithium-ion batteries. Mild ECR plasma treatment at 600 W was carried out on the surface of the microstructured FTO anode, and the electrochemical characteristics were investigated with regard to the

plasma treatment effects. The results show that physical properties such as the smooth and dense surface morphology and reduced surface oxygen functional groups of the plasma-treated samples enhanced the specific capacity, rate capability, and capacity fading. This was probably due to the reduction of side reactions, which may be closely related to the plasma treatment of the microstructured FTO layer. The ECR plasma treatment plays an important role in reducing the charging transfer resistance. In the experimental range studied, a higher specific capacity of 1425 mA h g^{-1} at a current density of 117 mA g^{-1} was observed, with capacity fading of 37.8% after 100 cycles for the plasma-treated microstructured FTO anode.

3. Publications (please stick to the user guidelines for publications and acknowledgements on www.knmf.kit.edu):

RSC Adv., 4 (2014) 4247-4252. (Publication)

Acknowledgments

This work was supported by research grants of NRF (NRF-2012M1A2A2671792) funded by the National Research-Foundation under the Ministry of Science, ICT & Future, Korea. This work was also supported by the K-GRL program of the Korea Institute of Science and Technology (KIST). Finally, the support for laser processing by the Karlsruhe Nano Micro Facility (KNMF, <http://www.knmf.kit.edu/>) a Helmholtz research infrastructure at the Karlsruhe Institute of Technology (KIT) is gratefully acknowledged.

4. Comments (max. 1.800 characters):

This is our first output as the result of cooperative work between KIT IAM-AWP and KIST AEMPL. KIST starts grafting KIT's technologies to 3D batteries and KIT understands KIST's core technologies too. It will lead to synergetic effect for the boosting the cooperative work. We have common objectives and will move to our target to the higher impact journal.

Evaluation of Talbot-Lau based X-ray imaging for medical applications

Gisela Anton

Friedrich-Alexander-Universität Erlangen-Nürnberg

Germany

Final Report

1. Project goals (max. 1.800 characters):

X-ray grating interferometry has been made applicable at low brilliance sources by introduction of the Talbot-Lau method to the X-ray regime [1] [2]. The method delivers three kinds of images: the absorption, the differential phase-contrast and the dark-field image.

The focus of most experiments at medical X-ray sources laid on low-energy applications like mammography, but an increase of the design energy of the Talbot-Lau set-up is urgently needed to investigate morphological structures at state-of-the-art medical imaging X-ray energies.

Therefore, the goal of this project was to produce a high quality set of gratings specified for a design energy of 40keV. The envisaged thickness of the gratings was expected to deliver a high visibility even with spectra up to 60kVp or higher.

2. Project results (max. 7.000 characters + figures):

After installing the proposed set of gratings in our lab set-up and an appropriate calibration, a set of basic measurements was carried out, including the analysis of the resulting visibility map of the grating, which is a main quality criterion of a Talbot-Lau grating set-up.

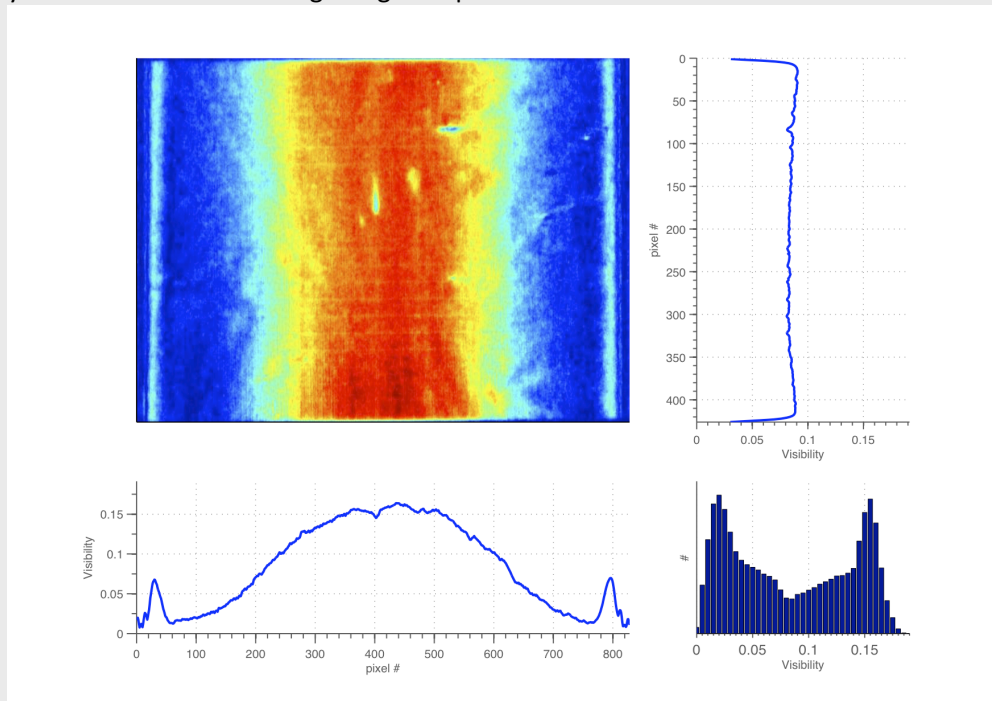


Figure 1: Visibility map of the Talbot-Lau interferometer set-up used (top left). The projection of the visibility along the y-axis (top right) shows a homogeneous distribution. Along the x-axis (bottom left), an expected reduction of the visibility due to shadowing is observed. The histogram of all values is shown right in the bottom row.

We performed measurements at 60kV tube acceleration voltage and achieved the results presented in Fig. 1. Due to the unbent gratings and the compact set-up design, a severe loss in visibility can be observed at the left and right side of the field-of-view.

Later on, further measurements using this set-up were performed. One major project was the investigation of energy-weighting methods for X-ray phase-contrast and especially dark-field imaging. The main results have been published recently [3].

Therefore, the Dosepix detector, a hybrid photon-counting pixel detector with a 16×16 pixel matrix and a pixel pitch of $220 \mu\text{m}$ was used. The Dosepix detector was bump bonded to a 1 mm thick cadmium telluride (CdTe) sensor layer by the Freiburger Materialforschungszentrum (FMF) to achieve a quantum efficiency reasonably high even at photon energies up to 60 keV, necessary for this experiment. Furthermore, the Dosepix detector is capable to compare the deposited energy of the incident photon to 16 digital thresholds and increment only the one of its 15 counters per pixel with the energy interval corresponding to the deposited photon energy. By this procedure, the energy deposition spectrum of the incident photon spectrum is sampled by 15 bins. Further information about the specifications of the Dosepix detector can be found in [3].

Setting the digital thresholds of the counters to values equivalent to energies from 15 keV to 60 keV in 3 keV steps, the first measurement performed was to analyse the spectral behaviour of the set-up's visibility. These results are shown in Fig. 2.

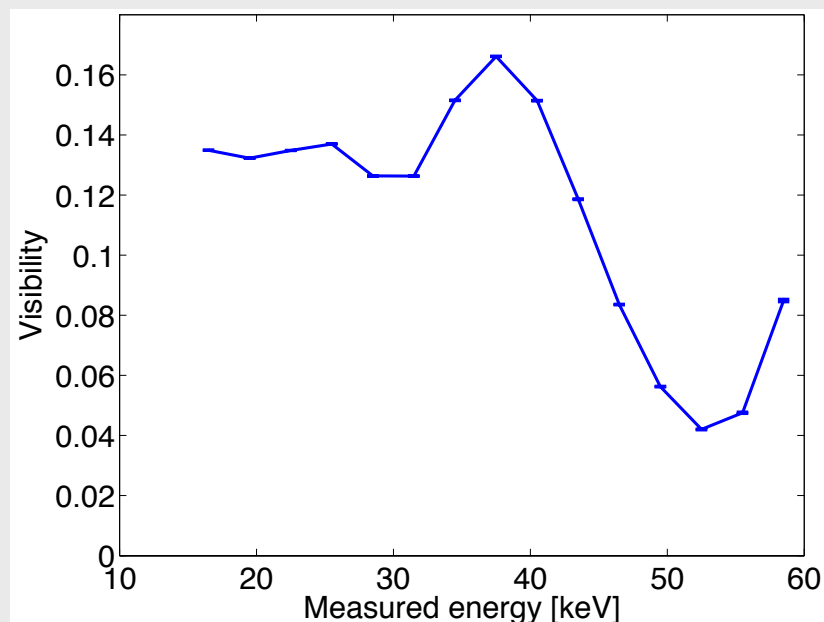


Figure 2: Measured visibility against the measured photon energy.

As expected, the maximum visibility can be found at approximately 40keV, the design energy of the set-up. The small deviations are due to fabrication tolerances of the gratings and misalignment of the set-up.

To investigate the performance of energy-weighting techniques to increase the contrast-to-noise ratio (CNR) in the X-ray dark-field 100 repetitions of a melamine sponge of 2.7mm thickness compared to air was performed. From these datasets, CNR optimized dark-field values were deduced using an ansatz similar to [4], but with an a-priori unknown spectral exponent called k . The optimization of k revealed a maximum CNR of 10.7 ± 0.1 at $k = -0.77$ compared to a CNR value of 9.4 ± 0.1 for a non-weighting counting detector.

A further analysis of the data showed that the increase in CNR due to energy weighting mainly arises from noise reduction.

In conclusion, with this technique we were able to reduce the patient dose necessary to 77% of the original radiation dose needed without loss in image quality.

3. Publications (please stick to the user guidelines for publications and acknowledgements on www.knmf.kit.edu):

- [1] C. David et al., Appl. Phys. Lett. 81, 3287-3289 (2002)
- [2] F. Pfeiffer et al., Nature Mat., 7, 134-137 (2008)
- [3] G. Pelzer et al., Opt. Ex., (2014), accepted, in press
- [4] G. Pelzer et al., Opt. Ex., 21(22), (2013)

**3D imaging and analysis of mesopores in
hierarchical pore structures by electron
tomography**

Daniela Stoeckel

Justus-Liebig-Universität Gießen

Germany

Note: Please fill in this report form and save/print it as a PDF file, then upload it to the KNMF proposal submission system. A cover page containing proposal title, proposer name(s), and technologies selected will be added by the system. A link for the download of the complete report as a PDF file will be displayed in the system.

Final Report

1. Project goals (max. 1.800 characters):

This project aims at the understanding of the fundamental relationship between the porosity on the nanoscale in porous materials and its relationship to integral physical properties, in particular mass transport through porous media, focusing on porous monolithic silica structures.

Porous silica in monolithic form is used in chromatography and catalysis as an alternative to other fixed bed structures. Silica monoliths are prominent representatives of the group of materials which can be prepared featuring a hierarchical pore system, containing mesopores of ~ 10 nm and macropores of ~ 2 μm average size. Beyond a basic characterization of the two pore categories, the monolith's disordered pore structure has remained largely unknown until recently, when the morphology at the macropore scale became accessible through 3D imaging methods (e.g., CLSM). [1] Resolving the much smaller mesopore network in this respect has never been tried previously. This lack of understanding results from the fact that the mesopores do not possess a defined shape and, furthermore, are probably randomly distributed. Techniques such as physisorption and SAXS were used to get average values for the pore size, but are unsuitable techniques to determine the shape and mutual connection of these mesopores. Standard TEM and SEM analyses are not able to provide reasonable information either.

The goal of this project was, therefore, the 3D reconstruction of the mesopore space in monolithic silica by STEM-tomography, aiming at revealing the shape, size and local connectivity between the mesopores. The targeted 3D model should provide the interconnectivity of the mesopore system and in turn enable us to qualitatively and semi-quantitatively relate the separation performance in HPLC to the mesopore structure.

For similar reasons the 3D reconstruction of the macropore space was intended using FIB-SEM technique. Thus, the 3D reconstruction of both, meso- and macropore space was a major goal, which can then be used for a model independent, statistical analysis and comparison of pore spaces on both length scales.

¹ S. Bruns, T. Hara, B. M. Smarsly, U. Tallarek, *J. Chromatogr. A*, **2011**, 1218, 5187.

2. Project results (max. 7.000 characters + figures):

A silica monolith was prepared according to a standardized synthetic route, reported previously (Fig. 1).^[2] Part of the silica rod was embedded in polydivinylbenzene for the FIB-SEM analysis, to avoid charging effects and enhance the skeleton/pore-contrast (Fig. 2). The residual unmodified silica rod was used for TEM tomography.

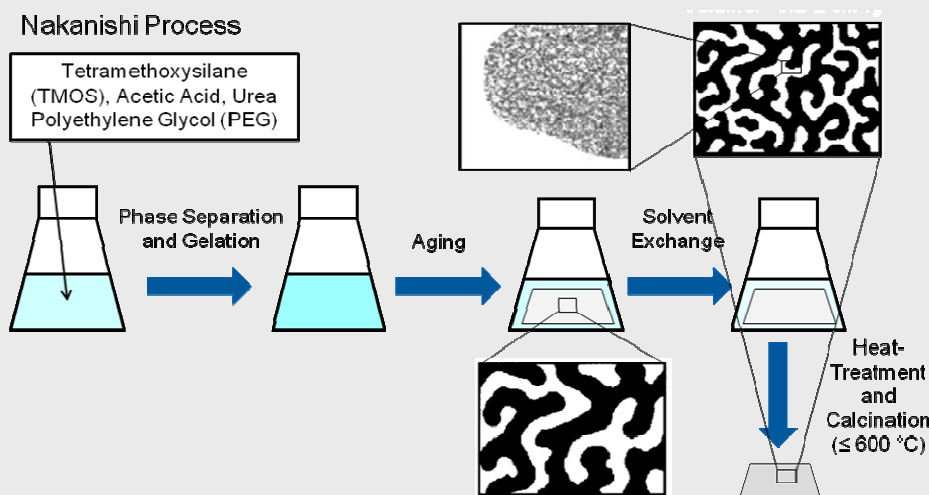


Fig. 1: Generation of the monolithic pore structure according to the Nakanishi Process.^[3]

A 3D model of both pore spaces was obtained from 3D FIB-SEM and high resolution STEM (Fig. 2) Based on the acquired 3D reconstructions we then analyzed the morphology of both pore spaces using chord length distributions (CLDs). The tomography of monolith morphology and the CLD analysis yielded information related to key structural properties, e.g., mean pore sizes and pore size distributions, as well as porosity and tortuosity. The combined application of these techniques and their resolution (~10 nm/pixel, FIB-SEM; ~0.5 nm/pixel, STEM) allowed assessing structural properties on submicron scale of interskeleton macropores and on nanometer scale of intraskelton mesopores. The mean pore sizes of macro- and mesopore space are derived from CLD analysis, which neither makes nor requires assumptions about the shape and topology of the pore space.

² T. Hara, S. Mascotto, C. Weidmann, B.M. Smarsly, *J. Chromatogr. A*, **2011**, 1218, 3624.

³ K. Nakanishi, *J. Porous Mater.*, **1997**, 4, 67–112.

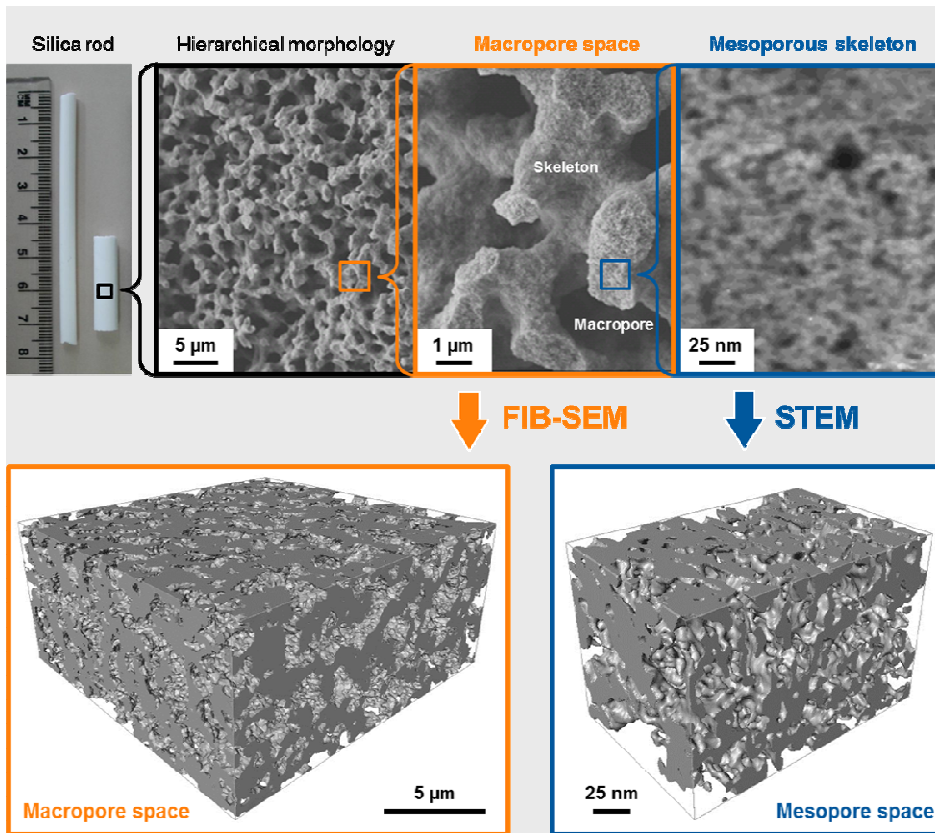


Fig. 2: The hierarchical structure of a silica monolith, reconstructed via FIB-SEM (macropore space) and STEM tomography (mesopore space). The characteristic length scales of macropores ($\sim 1 \mu\text{m}$) and mesopores ($\sim 10 \text{nm}$) determine the mass transport regime in each pore space as well as the imaging method used for its reconstruction. In the interskeleton macropore space transport is advection-dominated, whereas in the intraskeleton mesopore space transport is diffusion-limited. The macro- ($\epsilon_{\text{macro}} = 0.51$) and mesoporosity ($\epsilon_{\text{meso}} = 0.64$) were calculated as the fraction of void pixels in the respective image stack.

The chord length distributions of the macro- and mesopore space were calculated by collecting 10^6 randomly distributed chords (skeleton-to-skeleton distance) in the segmented 2D image stacks. The CLD concept is theoretically applicable to any porous medium representation that provides segmented information. Also, its evaluation principle is not subject to any size restrictions, therefore it can be applied for both macro- and mesopore space. Results were displayed in a histogram (Fig. 3). A mathematical description of the normalized CLDs is achieved by fitting the histograms with a scaled k-gamma function. For the macropores the mean chord length was found to be $1.21 \mu\text{m}$ and 16.23nm for the mesopores. The dimensionless k-value, defining the statistical dispersion of the distribution function, lies at 2.61 for the macro- and 1.82 for the mesopores. This value has proven to be an eligible indicator of the structural homogeneity, with larger k-values portending increased morphological homogeneity. A direct comparison of both CLDs is achieved by scaling them with the corresponding value for the mode, as shown in Fig. 3c. This figure quantifies the relative heterogeneity of the intraskeleton mesopore space with respect to the interskeleton macropore space. Importantly, this comparison is achieved by using only the physically reconstructed (FIB-SEM and STEM based) void spaces and the straightforward CLD analysis, without involving any assumptions about void space morphologies.

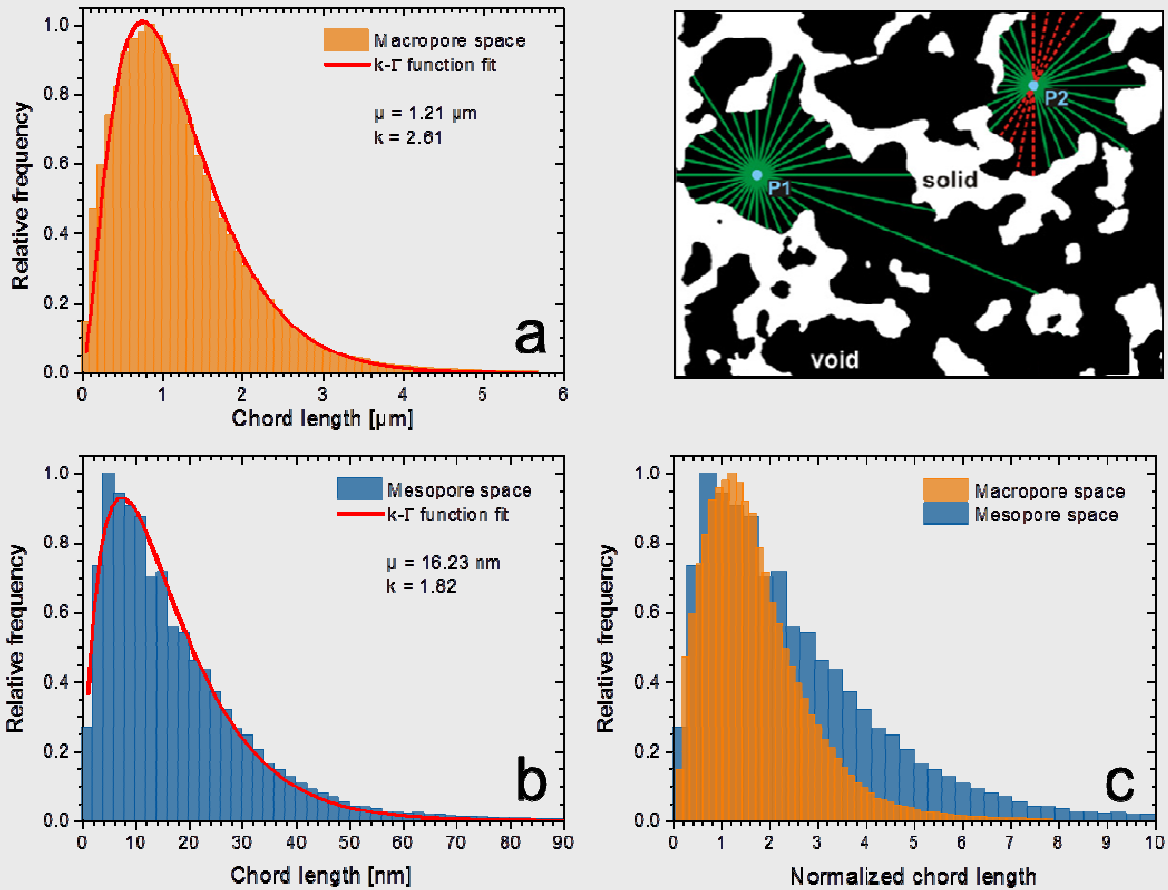
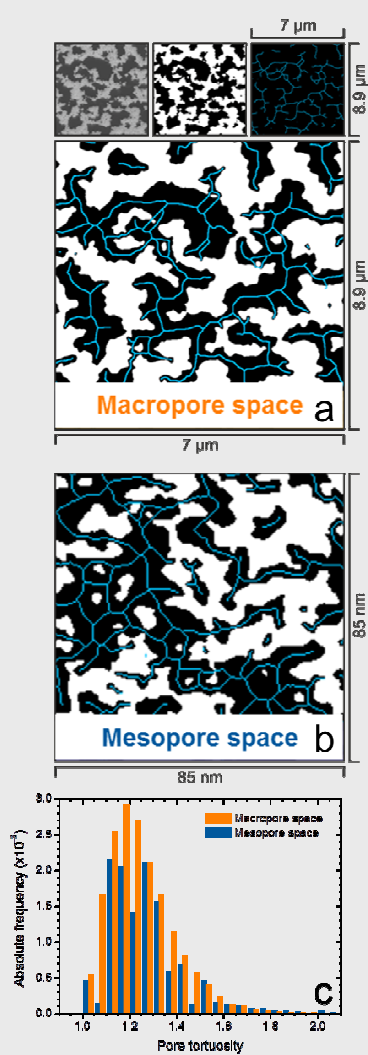


Fig. 3: CLDs for macro- (a), mesopore (b) space together with the best fits of the k - Γ function, $f(l_c) = A \cdot k^k / \Gamma(k) \cdot l_c^{k-1} / \mu_c^k \cdot \exp(-k \cdot l_c / \mu_c)$, to the data. The k - Γ function gives a mathematical description of the normalized CLDs by fitting the histograms. l_c denotes the chord length and μ_c is the mean chord length. The parameter k is defined by the mean and the standard deviation σ as $k = \mu_c^2 / \sigma^2$. As illustrated, a CLD consists of straight skeleton-to-skeleton distances in the macropore or mesopore space, collected by scanning the complex geometry of the solid-void border through 1D chords. Chords are generated by sprouting pairs of opposing vectors from randomly chosen points (P_i) in the void space; from each point vectors are extended equiangularly in several directions until they hit solid. The distance spanned by a vector pair is a chord length. Chords that reach beyond the image boundary are rejected (dashed red lines). (c) Comparison of CLDs normalized by the respective mode.

Based on this comparison the mesopore space appears much more heterogeneous than the macropore space, as indicated by the pronounced tail of its CLD toward longer chords. This finding is surprising taking into account that the **macropores** are created in a spinodal demixing process within the system water/ethanol- polymer- SiO_2 precursors, and that the polymer (PEG) possesses a broad molecular weight distribution. The heterogeneity in the **mesopore** space can thus be attributed to the etching process (applying basic pH conditions), which seems to attack the silica matrix quite viciously.

Furthermore, it reveals, as one major result of this study, the presence of a significant number of macropores inside the “mesoporous” skeleton (i.e. pores larger than 50 nm). This small fraction of larger mesopores is hardly detectable by standard methods (N₂ physisorption or Hg intrusion), but of high relevance for separation and transport in these pore structure. The origin of these relatively large pores is important to clarify, because they can be critical to the skeleton’s mechanical stability. How this wide distribution of intraskeleton pore sizes translates into the effective diffusion properties of small and large analytes, and whether the intraskeleton transport properties should be improved (and how), is addressed by pore scale simulations in the real morphology.



When comparing the mesopore size evaluated from STEM with nitrogen physisorption (performed at 77 K), which is **THE** standard routine technique for the determination of mesopore size distributions, the STEM-based analysis provided a larger average mesopore diameter. Although a general conclusion is aggravated by the fact that only one singular part of the sample was studied, this apparent contradiction can be attributed to the unexpectedly broad mesopore distribution, which cannot be easily resolved by N₂ or Ar physisorption. As a quite important result, our experiments thus suggest that the mesopore size distribution of such monolithic silicas, determined by standard N₂ physisorption analysis, should be handled with care and critically re-assessed. Our results can therefore be the starting point for bench-testing the validity of N₂ physisorption as routine analysis for mesopore sizes and therefore provide a valuable contribution to the field of characterizing mesoporous materials. Furthermore the tortuosity of the pore space was evaluated using a skeletonization process (Fig. 4). The pore tortuosity is defined as the branch length of a pore divided by the Euclidean distance between pore entrance and exit. Applying such analysis, the tortuosity factors are similar for both pore spaces in the silica monoliths (Fig. 4c). This finding is surprising, because the two pore systems are generated by completely different processes and also generated at different stages during the synthesis – and these results are at variance with the larger heterogeneity of the mesopore space. This apparent contradiction is based on the larger distribution of pore sizes in the mesopore size. In the future, such findings can – for the first time – help to tune the porosity on both length scales based on rational strategies, not only on trial-and-error-based synthesis. These insights into the morphology and topology were only possible by the advanced electron microscopy experiment applied.

Fig. 4: Illustration of the topological skeleton (in 2D) for selected regions from the interskeleton macro- (a) and the intraskeleton mesopore space (b). The skeletal network (blue lines) was statistically evaluated in terms of pore-level tortuosities (c). The tortuosity is defined as branch length of a pore divided by the Euclidean distance between pore entrance and exit.

Elucidating the peculiar mesopore morphology is thus a significant step towards a complete understanding of the structural details of silica monoliths. The reconstructed model will be also useful as a starting point in simulations of flow and mass transport,^[4] which aim at a fundamental understanding of the mass transport properties of silica monoliths. Consequently, this approach will enable material scientists to distinguish the adsorbents morphological features leading to poor separation efficiencies, and to successively improve the meso-/macropore structure to achieve optimal separation results.

3. Publications (please stick to the user guidelines for publications and acknowledgements on www.knmf.kit.edu):

A manuscript of the results is in preparation. Since the results are outstanding we plan to publish them in a high-ranking journal (probably *Angewandte Chemie*). The results were presented at the EUROMAT conference 2013 in Sevilla and will also be shown at the COPS meeting (“Characterization of Porous Solids”) in Grenada (Spain), which is the most important international conference in this field.

4. Comments (max. 1.800 characters):

We gratefully acknowledge the excellent technical and friendly support of the KNMF team, especially Dr. Kübel, both during the measurement and also afterwards during the data treatment and evaluation. The setup at KNMF fits perfectly our requirements.

⁴ D. Hlushkou, S. Bruns, A. Höltzel, U. Tallarek, *Anal. Chem.* **2010**, *82*, 7150–7159.

High-resolution x-ray grating interferometry in a laboratory setting

Anna Burvall

KTH Royal Institute of Technology

Sweden

Final Report

1. Project goals (max. 1.800 characters):

We aim to use grating-based phase contrast in combination with a liquid-metal-jet x-ray source, to get laboratory-based high-resolution phase-contrast imaging. This can be used in biomedical and small-animal imaging, with special interest in angiography and tumor demarcation. KNMF has supplied gratings for this arrangement. The gratings themselves are standard, the uniqueness lies in the combination of grating interferometry with the source, and in possible applications.

Among laboratory-based systems, as opposed to synchrotron facilities, the source [Larsson et al., Rev. Sci. Instr. **82**, 123701 (2011)] is unique in its small size and high flux. The source spot size of roughly 5 μm allows for grating interferometry without a source grating, thus allowing higher resolution than normal x-ray tubes. The relatively high flux gives the best exposure times provided by microfocus sources, though this is still an issue and source development continues for improved flux. We already use the source for high-resolution propagation-based phase-contrast imaging inside thick tissue [e.g. Lundström et al., Phys. Med. Biol. **57**, 2603-2617 (2012)], but grating-based phase contrast extends the applicability to a different range of samples and applications.

The first steps are performed in collaboration with the groups of Marco Stampanoni and Christian David at PSI, using gratings that they have previously obtained from KNMF.

2. Project results (max. 7.000 characters + figures):

We are currently in the process of creating an arrangement for grating-based phase-contrast imaging, using the gratings provided to us by KNMF in June 2013. At present, we have not results obtained using those gratings.

However, as part of our collaboration with the groups of Marco Stampanoni and Christian David at PSI, we have already tested grating-based phase contrast in combination with the liquid-metal-jet source. Gratings supplied to those groups by KNMF were used, and KNMF acknowledged in the resulting two publications. Also, several conference contributions are underway. As those publications cannot be formally be listed as results of this project, they are instead listed here:

- [1] T. Thuring, T. Zhou, U. Lundström, A. Burvall, S. Rutishauser, C. David, H.M. Hertz, and M. Stampanoni, "X-ray grating interferometry with a liquid-metal-jet source," Appl. Phys. Lett. **103**, 091105 (2013).
- [2] T. Zhou, U. Lundström, T. Thuring, S. Rutishauser, D.H. Larsson, M. Stampanoni, C. David, H.M. Hertz, and A. Burvall, "Comparison of two x-ray phase-contrast imaging methods with a microfocus source," Optics Express **21**, 30183--30195 (2013).

From these experiments and simulations, several interesting conclusions can be drawn. In the first paper, we confirm that the liquid-metal-jet source has sufficient spatial coherence for the task, and perform

tomography on a phantom and on a rat brain. The results are also compared to those using a conventional microfocus source, showing a substantially higher SNR for the liquid-metal-jet source at similar exposure times.

The second paper compares grating-based phase-contrast imaging to propagation-based phase-contrast imaging, using the liquid-metal-jet source for both. The comparison concentrates on dose, comparing the dose required to view objects of different sizes for the two methods. This is highly relevant to high-resolution dose-sensitive applications, such as in vivo small-animal imaging.

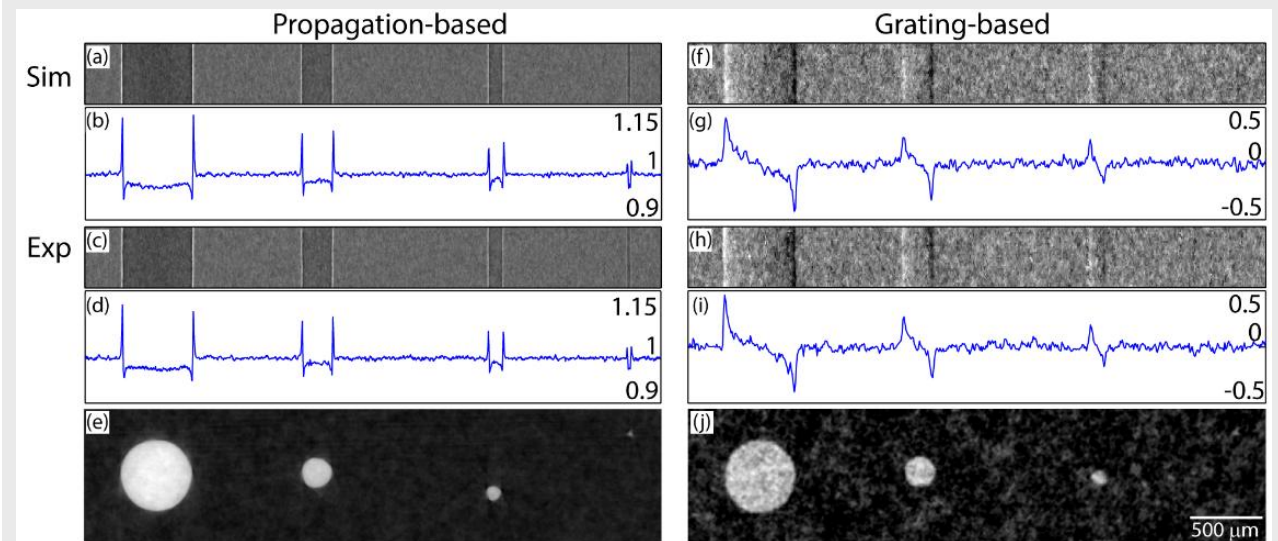


Figure 1. Simulated and experimental results of using the propagation-based and grating-based phase-contrast methods at similar doses. Figure from T. Zhou et al., *Optics Express* **21**, 30183--30195 (2013).

Figure 1 shows imaging of PET monofilaments of diameters 494, 213, 100, and 23 μm using both grating-based and propagation-based phase contrast. Observation of the image quality supports the conclusions reached from extensive simulations. For the ideal case of monochromatic illumination and perfect gratings, propagation-based imaging requires the lower dose for the highest resolution, while grating-based imaging requires the lower dose for somewhat lower resolution. If the polychromatic radiation inherent to laboratory sources is taken into account, the required dose increases for both methods. This increase, however, is much larger for the grating-based method, which also suffers from imperfect gratings. Including both these effects, the propagation-based method requires the lower dose for all resolution levels tested.

3. Publications (please stick to the user guidelines for publications and acknowledgements on www.knmf.kit.edu):

See section 2, "Project results"

**Characterization of binding process of
Oligonucleotides, and Lipids on
microlithographed TiO₂ substrates**

Ruy Sanz

Nanoate

Spain

Final Report

1. Project goals (max. 1.800 characters):

We have used energetic (MeV) heavy ion-beam combined with lithography mask to create patterned surfaces on TiO₂ rutile single crystals. This process generates changes in the nanotopography and may induce compositional changes as well, and then, a chemical contrast between ion irradiated (patterned) and non-irradiated (not patterned) areas. The chemical differences between patterned and not patterned surfaces are strongly marked after the exposition to UV light.

The project goals were:

- 1.-Quantitative data on the composition and chemical state the damaged TiO₂ of the micro-wells.
- 2.-Determination of the role of UV and hydrocarbons on the chemical reactivity of damaged TiO₂.
- 3.-Qualitative and Quantitative data of the efficiency of the adsorption of oligonucleotides and lipids. In order to evaluate the possibilities of employing the substrates as platform for biomedical applications.

2. Project results (max. 7.000 characters + figures):

Phospholipids, 99% 1,2-di-(9Z-octadecenoyl)-*sn*-glycero-3-phosphocholine (DOPC)+ 1%Rhodamine-PE, and Oligonucleotides were successfully deposited into microwells and outside them as a control. See Fig 1, for examples of deposited Phospholipids. Deposited oligonucleotides were not marked with fluorescent dye.

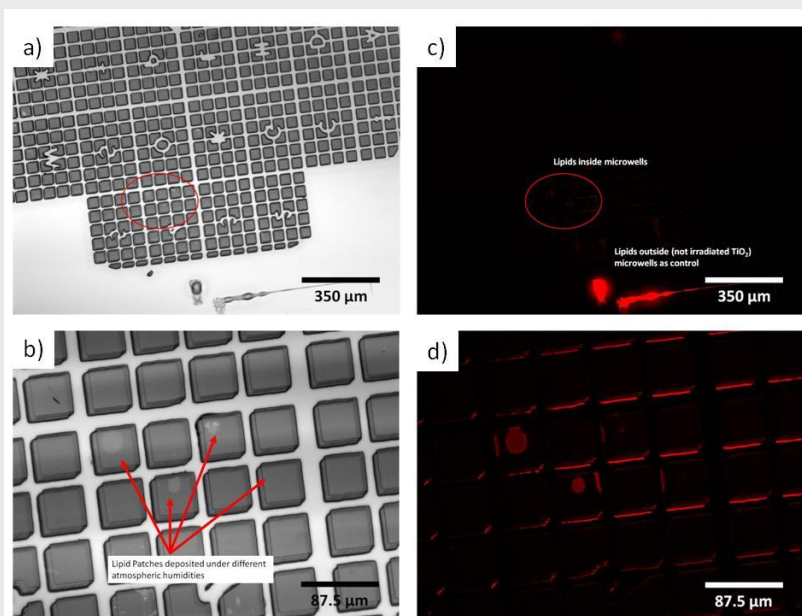


Figure 1: Micrographies of a patterned substrate with deposited phospholipids. a) and b) General and detailed view. c) and d) Fluorescent image of a) and b).

Since the base material of the substrate is an insulator(TiO_2), it was expected some charge problems for μ -NEXAFS. Therefore the time assigned for the experiment was taken as a preliminary test.

The preliminary results were as follows:

Charging was substantial and required the primary beam intensity to be chosen much lower than "normal" to reduce the effects to manageable levels.

- The Ti 2p and O 1s signal points to a small doping effect in the microwells.
- Lipid layers in the appropriate microwells were thin but easily identifiable.
- However, no trace of the oligonucleotides could be found in the microwells. If present at all it might perhaps be in some residual "droplets" _between_ some of the microwells. If true, this would indicate that the writing process for the oligonucleotides was perhaps a bit "off".

3. Publications (please stick to the user guidelines for publications and acknowledgements on www.knmf.kit.edu):

4. Comments (max. 1.800 characters):

No detailed or additional report has been provided from WERA scientist until now.

**Micro-machining of a glass coverslip
implanted for high resolution imaging of
mouse brain**

Yajie Liang

Eberhard-Karls-Universität Tübingen

Germany

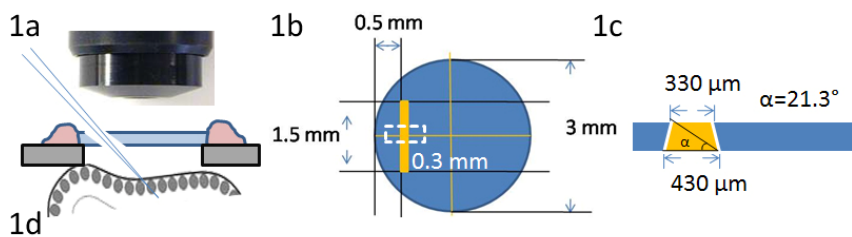
Note: Please fill in this report form and save/print it as a PDF file, then upload it to the KNMF proposal submission system. A cover page containing proposal title, proposer name(s), and technologies selected will be added by the system. A link for the download of the complete report as a PDF file will be displayed in the system.

Final Report

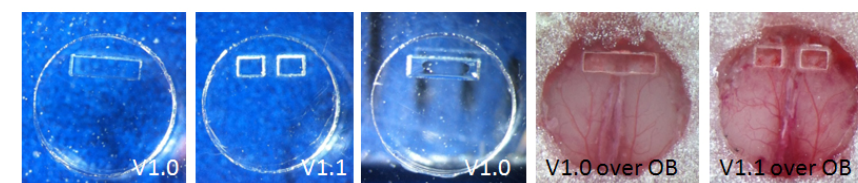
1. Project goals (max. 1.800 characters):

Glass coverslips have been used to make cranial windows in mice, through which brain function could be visualized *in vivo* by the two-photon microscope (Holtmaat, et al., 2009). However, once the cranial window is installed, there is no more access to the observation area for glass capillary intending to apply dyes or drugs. This is especially problematic for longitudinal study of brain function. The goal of this project is to micro-machine thin glass coverslips so as to obtain access to the mouse brain through a slit in the chronic cranial window over the brain. For this purpose the femtosecond (fs) laser material processing of the user facility (KNMF) was applied in order to enable a crack-free and almost debris-free microstructured glass surface.

2. Project results (max. 7.000 characters + figures):

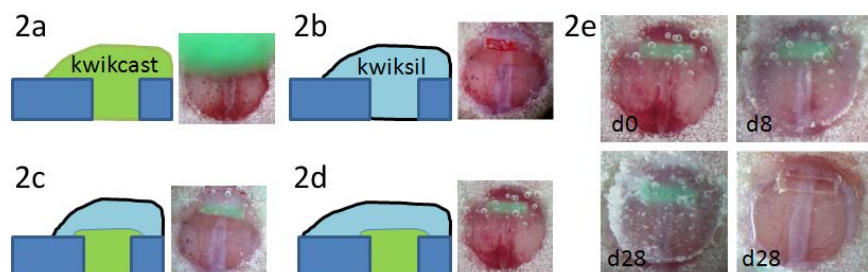


To design a slit in glass coverslips through which micro-pipettes could be inserted for access of the brain (Fig 1a), we made via fs laser machining a 1.5 mm long slit in the front part of the 3 mm glass coverslip (Fig 1b). The cross section of the slit is a trapezoid (Fig 1 c) so as to allow convenient insertion of pipette from lateral side. The actual images of the

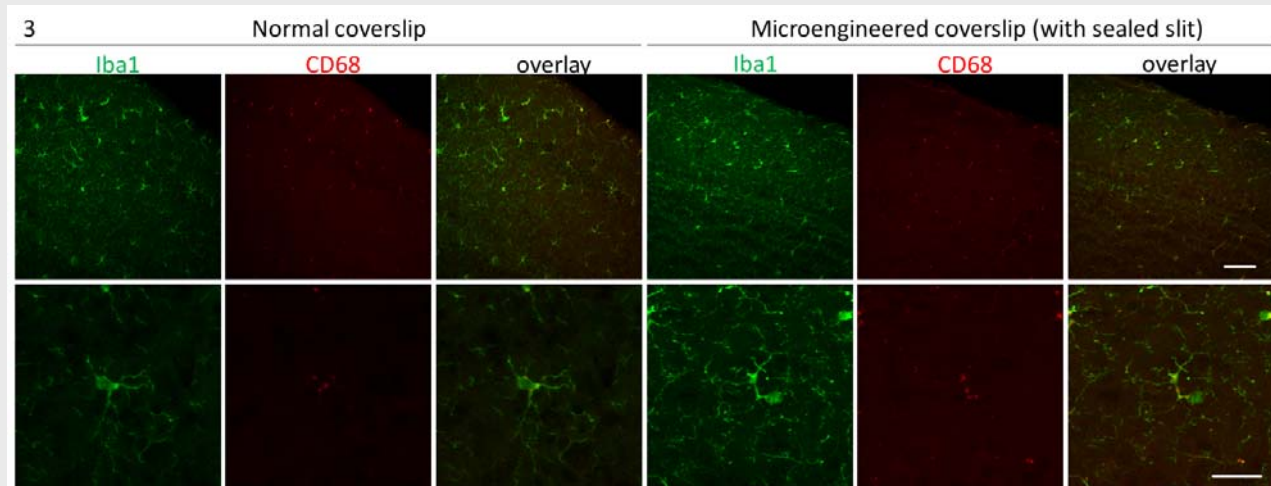


microengineered coverslip are displayed in Fig 1d. The slit in version 1.1 is split into two parts with a bridge of 0.3 mm in between. Then the microengineered coverslips were installed on the olfactory bulb (OB) of live mice (Fig 1 d, right images).

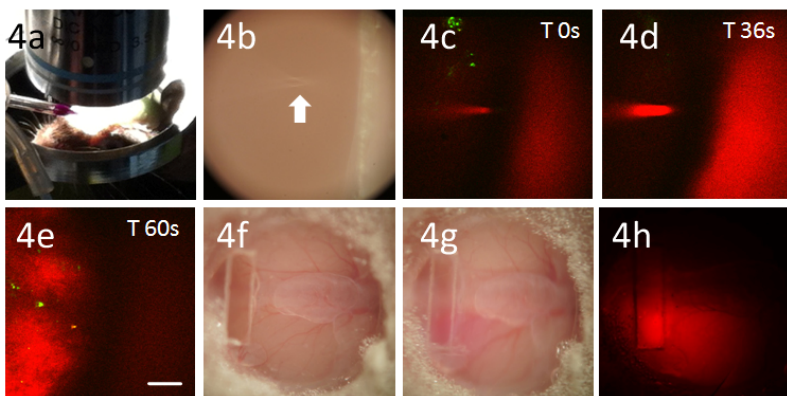
The open slit in the cranial window poses the risk of infection and thus has to be sealed. For effective sealing, four application methods were tested: a. biocompatible adhesive Kwik-cast was applied



to seal the slit (Fig 2a, right inset shows how the brain look like after the application of adhesives); b. biocompatible adhesive Kwik-sil was applied (Fig 2b). 3. Kwik-cast for filling the slit plus Kwik-sil covering the slit (Fig 2c); 4. Similar to method 3, but the Kwik-sil covers the whole coverslip (Fig 2d). It turns out that method 4 confers the most effective and long lasting seal without apparent side effects. The adhesive stayed in the slit even 4 weeks after the filling (d28, Fig 2e), with good window quality below the adhesive (Fig 2e, d28, right panel).



Then we evaluated the inflammation in the brain covered by microengineered coverslip, in comparison with that under normal coverslip (not micro-engineered) 4 weeks after their installation. The OB sections were immunostained by anti Iba1 and CD68 antibodies (markers of microglia, the inflammation cell in the brain). We found that the inflammation level in the two groups were quite comparable, all displaying typical morphology of resting microglia (Fig 3, scale bar in upper row is 50 μ m, in lower row is 20 μ m). This means that our sealant worked well in preventing the OB from infection through the slit.



Next we sought to inject dyes into the OB through the slit. In our setup, the mouse with a microengineered coverslip was anesthetized by ketamine/xylazine, and its OB was approached by a micropipette (filled with sulforhodamine 101, a red dye) angled at 40 degree under direct visualization of two-photon microscopy (Fig 4a). Under bright light, the slit and pipette (arrow) could be observed (Fig 4b). Then we switched to two photon imaging and targeted the pipette and the edge of the slit (Fig 4c). The injection process was monitored by time-lapse imaging (Fig 4d and 4e, scale bar is 50 μ m). By 60 seconds after start of imaging, the injection procedure was finished as evidenced by bright red color in tissue. The successful injection of the dye could also be demonstrated by the presence of red tissue under bright field view (Fig 4g) in comparison with that before injection (Fig 4f), or by presence of bright fluorescence in the left OB under epifluorescent illumination (Fig

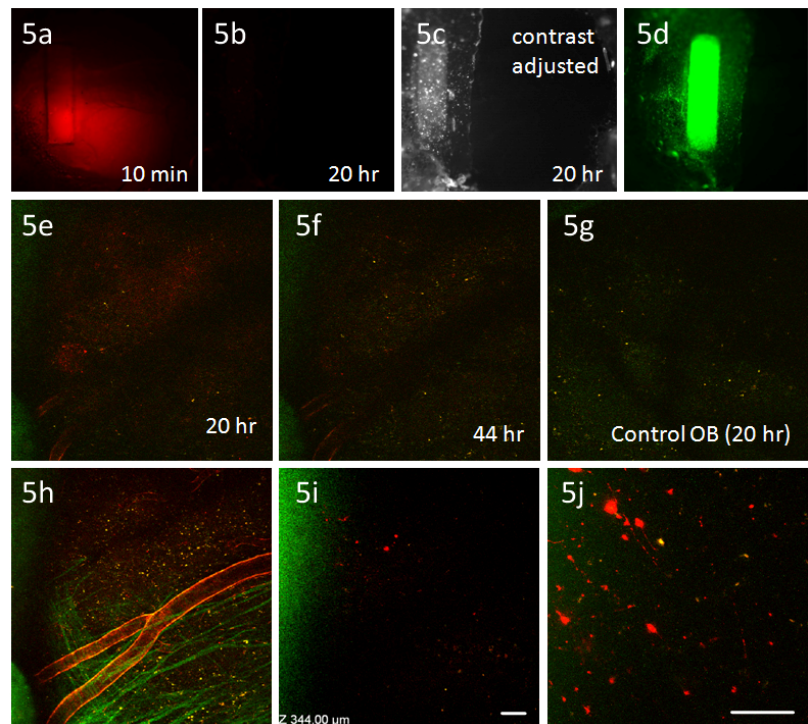
4h). The injection process was monitored by time-lapse imaging (Fig 4d and 4e, scale bar is 50 μ m). By 60 seconds after start of imaging, the injection procedure was finished as evidenced by bright red color in tissue. The successful injection of the dye could also be demonstrated by the presence of red tissue under bright field view (Fig 4g) in comparison with that before injection (Fig 4f), or by presence of bright fluorescence in the left OB under epifluorescent illumination (Fig

4h). These results prove that we have established the platform to deliver dyes through the microengineered coverslip.

The dye-loading paradigm in our setting occurs in a closed *in vivo* system, different from that under acutely prepared mice where there is a constant perfusion in the chamber covering the exposed brain. Therefore, it is important to find out the kinetics of the dye, i.e. decay time. So we monitored the fluorescence from the injected dye 10 minutes after injection (Fig 5a) and 20 hours after injection (Fig 5b), and found that by 20 hours, there was very weak fluorescent signal. Fig 5c is the same image with Fig 5b, but was adjusted to optimize contrast. In the mean time, we found that Kwik-cast was fluorescent under 488 nm excitation light (Fig 5d). Then we scanned the OB tissue close to the injection sites, and also found a huge drop of red fluorescent signal from 20 hours after injection (Fig 5e) to 44 hours after injection (Fig 5f) at the same position (and focal plane). The absence of red fluorescence in control bulb (Fig 5g) indicates that by 44 hours after injection, the dye has not been completely cleared. As for the structures stained by the dye, we have found big blood vessel with strong red fluorescence (Fig 5h), and astrocyte-like cells below mitral cell layer (Fig 5i). The zoom-in image showed the morphology of these stained cells (Fig 5j, scale bar is 50 μm for 5e-5j), which are very likely to be astrocytes according to literature (Nimmerjahn, et al., 2004). There has been a recent study investigating the perfusion system in the mouse brain (Ilyff, et al., 2012). Our results have established the clearing rate for the injected dye in the microengineered coverslip brain and set up the basic for further tests of application of this technology.

Reference

- Holtmaat, A., Bonhoeffer, T., Chow, D. K., Chuckowree, J., De Paola, V., Hofer, S. B., Hubener, M., Keck, T., Knott, G., Lee, W. C. A., Mostany, R., Mrsic-Flogel, T. D., Nedivi, E., Portera-Cailliau, C., Svoboda, K., Trachtenberg, J. T., and Wilbrecht, L., 2009. Long-term, high-resolution imaging in the mouse neocortex through a chronic cranial window. *Nature Protocols* 4, 1128-1144.
- Ilyff, J. J., Wang, M. H., Liao, Y. H., Plogg, B. A., Peng, W. G., Gundersen, G. A., Benveniste, H., Vates, G. E., Deane, R., Goldman, S. A., Nagehus, E. A., and Nedergaard, M., 2012. A Paravascular Pathway Facilitates CSF Flow Through the Brain Parenchyma and the Clearance of Interstitial Solutes, Including Amyloid beta. *Science Translational Medicine* 4.
- Nimmerjahn, A., Kirchhoff, F., Kerr, J. N. D., and Helmchen, F., 2004. Sulforhodamine 101 as a specific marker of astroglia in the neocortex *in vivo*. *Nature Methods* 1, 31-37.



3. Publications (please stick to the user guidelines for publications and acknowledgements on www.knmf.kit.edu):

4. Comments (max. 1.800 characters):

We have successfully demonstrated that our micro-engineered coverslip could allow access to the brain covered by chronic cranial window, and we have found a way to effectively seal the coverslip for more than 4 weeks, without induction of inflammation in the brain tissue under its cover. By using this microengineered coverslip, we injected a dye (sulforhodamine 101 into the brain) and observed brightly stained astrocytes, validating further exploration of the application of this microengineered coverslip. For publication in a high ranked journal, a more detailed study in terms of more animal number and additional applications is necessary. Thus an ongoing KNMF project is needed in which fs laser machining will be applied in order to produce microengineered coverslips made of glass. We also plan to explore the possibility of manufacturing materials other than glass, such as plastics, for convenient manipulation of coverslips.

**Using FIB-SEM to determine the influence of
support morphology on the structure and
performance of low-temperature fuel cells**

Benedikt Peter

Technische Universität Darmstadt

Germany

Note: Please fill in this report form and save/print it as a PDF file, then upload it to the KNMF proposal submission system. A cover page containing proposal title, proposer name(s), and technologies selected will be added by the system. A link for the download of the complete report as a PDF file will be displayed in the system.

Final Report

1. Project goals (max. 1.800 characters):

Goal of the project was to correlate the structures on the nanoscale of gas diffusion cathodes for use in PEM fuel cells, with their performance in real test conditions.

The first main issue was to prepare chemically identical support materials and decorate them with platinum nanoparticles with similar size and size distribution. This is quite difficult as the decoration with platinum nanoparticles is strongly dependent on the surface of the support material, which changes with different morphology (Sevjidsuren et al., 2010). We decided to use polyaniline, a conductive polymer which is easy to prepare in different morphologies, decorate it with platinum and carbonize it afterwards (Peter, Melke, Muench, Ensinger, & Roth, 2014). Thereby much attention was given to prove the chemical identity of the materials used.

Gas diffusion cathodes were prepared from these materials and showed significant differences in full cell performance depending on morphology (see Figure 1).

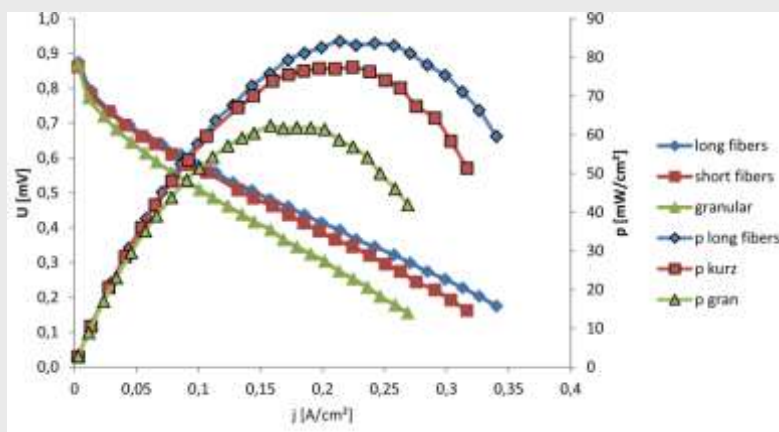


Figure 1: Polarization and power density curves of the MEAs employing three different support morphologies.

The second issue was not possible to solve without the KNMF. The performance of these devices is strongly dependent on porosity, homogeneity, Pt distribution and accessibility. FIB-SEM was applied to image the electrode structure and to define parameters, which can be correlated with the electrochemical activity.

2. Project results (max. 7.000 characters + figures):

The FIB-SEM data acquisition and evaluation of the slice&view was a success. For the first time the real 3-D-structure of fuel cell cathodes composed of support materials differing only in the morphology could be visualized (Figure 2). No difference in porosity (MEA_{long} : 63.6 %, MEA_{short} : 66.8 %) and connectivity (>99,9 % for both samples) was observed. Only the specific surface area showed differences (MEA_{long} : $8.2 \cdot 10^6 \text{ m}^2 \text{ m}^{-3}$, MEA_{short} : $10.6 \cdot 10^6 \text{ m}^2 \text{ m}^{-3}$). But the MEA with the higher performance showed a lower specific surface, which is in agreement with the electrochemically active surface (MEA_{long} : $52 \pm 2 \text{ mC}$, MEA_{short} : $19 \pm 2 \text{ mC}$). Therefore we were able to conclude, that the difference in performance must be due to the electrodes structure.

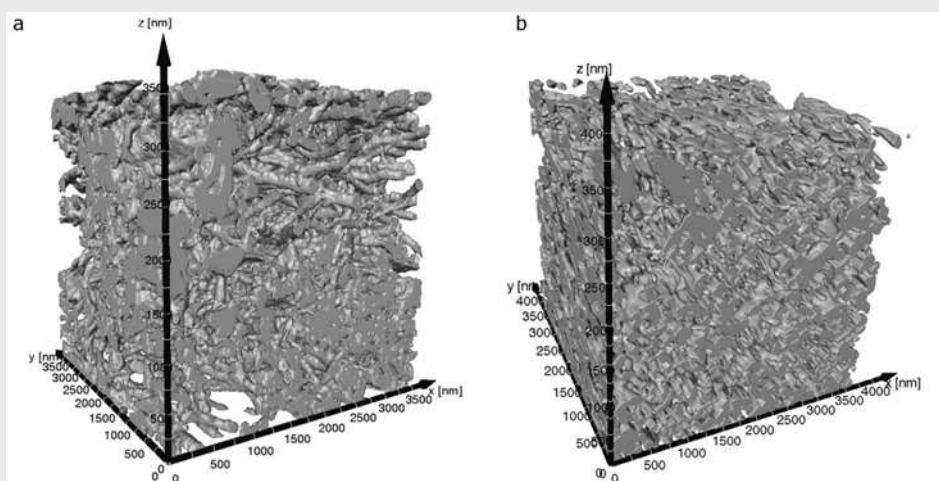


Figure 2: 3D reconstruction of the cathodes having different support morphologies, (a) long fibers, (b) short fibers.

To get an impression of the structure a chord-length distribution (CLD)-analysis was performed in collaboration with the Group of Prof. Smarsly based on the work of Bruns et al. (Bruns, Hara, Smarsly, & Tallarek, 2011). The CLD of the electrodes is depicted in Figure 3.

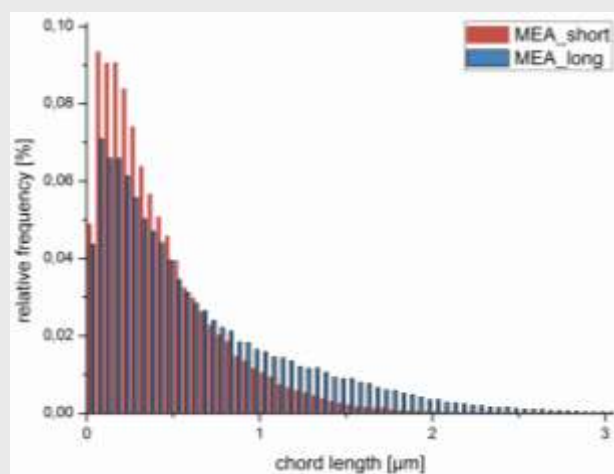


Figure 3: Chord length distribution of pore space from MEA_{long} and MEA_{short}

Both samples show a homogeneous distribution with a sharp increase for small particles with a maximum in the second interval (interval size: 50 nm). Obviously there are more large pores in MEA_{long} compared to MEA_{short}. This pore network has an influence on water management of the fuel cell which is crucial for the performance (Fuller & Newman, 1993).

Further collaboration using simulations to learn more about the creation and flow of water in the cathodes is planned.

3. Publications (please stick to the user guidelines for publications and acknowledgements on www.knmf.kit.edu):

This work has not been published yet. A conference talk was given at the ECS spring meeting 2014 in Orlando.

A publication is submitted to the Journal of Power Sources since 29.07.20014 (Manuscript number: POWER-D-14-02802) Title: "Morphology influence of chemically identical carbon supports on Polymer-Electrolyte-Membrane-Fuel-Cell performance", B. Peter, D. Stoeckel, T. Scherer, C. Kuebel, C. Roth

In addition, the results will be part of a PhD thesis which is planned to be finalized in 2014

4. Comments (max. 1.800 characters):

The cooperation with the KNMF was constructive and full of results. We enjoyed a number of interesting discussions. After the measurements it was always possible to contact the KNMF members to ask for support in the data handling and evaluation. Especially the contact to the group of Prof. Smarsly (Gießen), which was provided by Dr. Kuebel, gave us the opportunity for further data analysis using the CLD-Methode.

3. References:

- Bruns, S., Hara, T., Smarsly, B. M., & Tallarek, U. (2011). Morphological analysis of physically reconstructed capillary hybrid silica monoliths and correlation with separation efficiency. *Journal of Chromatography. A*, 1218(31), 5187–94. doi:10.1016/j.chroma.2011.05.090
- Fuller, T., & Newman, J. (1993). Water and thermal management in solid polymer electrolyte fuel cells. *Journal of the Electrochemical Society*, 1218–1225. Retrieved from <http://jes.ecsdl.org/content/140/5/1218.short>
- Peter, B., Melke, J., Muench, F., Ensinger, W., & Roth, C. (2014). Stable platinum nanostructures on nitrogen-doped carbon obtained by high-temperature synthesis for use in PEMFC. *Journal of Applied Electrochemistry*. doi:10.1007/s10800-014-0664-4
- Sevjidsuren, G., Zils, S., Kaserer, S., Wolz, a., Etingshausen, F., Dixon, D., ... Ganzorig, C. (2010). Effect of Different Support Morphologies and Pt Particle Sizes in Electrocatalysts for Fuel Cell Applications. *Journal of Nanomaterials*, 2010, 1–9. doi:10.1155/2010/852786

Replacement of Noble Metal Catalysts for the Hydrogenation of Polar Multiple Bonds

Robert Langer

Philipps-Universität Marburg

Germany

Note: Please fill in this report form and save/print it as a PDF file, then upload it to the KNMF proposal submission system. A cover page containing proposal title, proposer name(s), and technologies selected will be added by the system. A link for the download of the complete report as a PDF file will be displayed in the system.

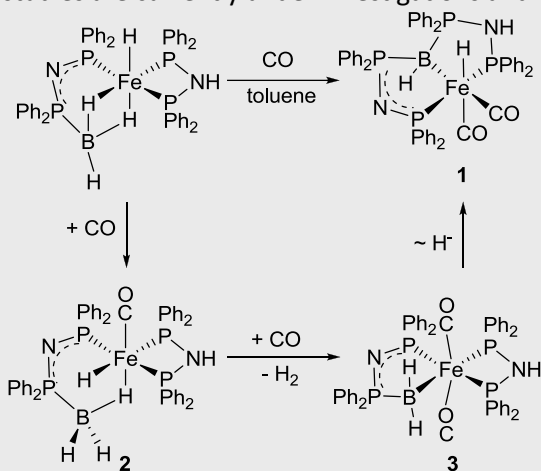
Final Report

1. Project goals (max. 1.800 characters):

With the present project we are aiming to design well defined iron-based catalysts for the reactions involving dihydrogen, that are showing sufficient productivity and activity to replace known noble metal analogues. For this reason we are studying the reactivity of iron(II)- and iron(0)-complexes with different kinds of ligands. One important analytic technique to analyze isolable compounds is single crystal X-ray diffraction, which is often problematic in the present case and requires state-of-the-art machines, such as the STOE STADIVARI with a DECTRIS PILATUS detector.

2. Project results (max. 7.000 characters + figures):

Within this project we were trying to synthesize and characterize various iron hydride complexes, before we investigate their catalytic properties. For several pre-catalysts the molecular structure was determined by single crystal X-ray diffraction, using the STOE STADIVARI device of the Karlsruhe Nano Micro Facility. So far the synthesis of an unusual iron phosphine borane complex has led to the publication of one paper. Furthermore, the synthesis of the unique pincer-type complex **1** was investigated in detail. This complex turned out to be very productive pre-catalyst for the dehydrogenation of primary alcohols, a very useful reaction, which is unprecedented for iron-based catalysts. The scope of this catalyst as well as mechanistic studies are currently under investigations and will be published soon.



Scheme 1. Formation of pre-catalyst **1**.

In Addition, the molecular structure of *cis*-[(Ph₂PH)₄Fe(H)₂] has been determined. As this complex was dynamic in solution, it was not possible to identify a structural model based on NMR spectroscopy. So far we have evidence that this complex is an active catalyst for the dehydrogenation of formic acid to carbon dioxide and hydrogen. These investigations are currently in progress and will lead to a publication soon.

3. Publications (please stick to the user guidelines for publications and acknowledgements on www.knmf.kit.edu):

- [1] "Formation of an iron phosphine-borane complex by formal insertion of BH₃ into the Fe–P bond" N. Frank, K. Hanau, K. Flosdorf, R. Langer*, *Dalton Trans.* **2013**, 42, 11252-11261.
- [2] "A PBP-pincer iron complex for the acceptorless dehydrogenation of primary alcohols" L. Vondung, N. Frank, R. Langer*, (*in preparation*).
- [3] "Simple iron complexes with secondary phosphine ligands as active catalysts for dehydrogenation of formic acid" W. Xu, K. Flosdorf, R. Langer*, (*in preparation*).

4. Comments (max. 1.800 characters):

Surface texturing for hybrid contact tribological applications

Mengyan Nie

University of Southampton

United Kingdom

Note: Please fill in this report form and save/print it as a PDF file, then upload it to the KNMF proposal submission system. A cover page containing proposal title, proposer name(s), and technologies selected will be added by the system. A link for the download of the complete report as a PDF file will be displayed in the system.

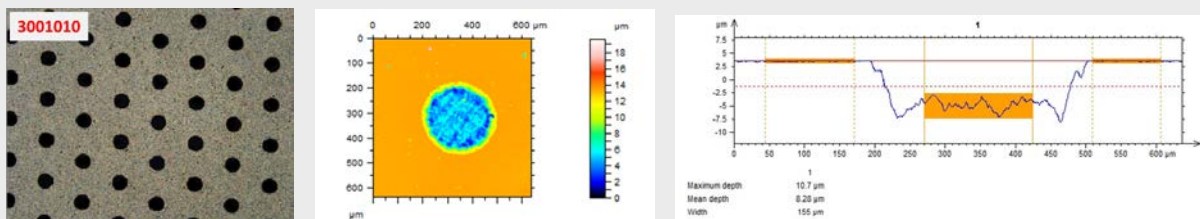
Final Report

1. Project goals (max. 1.800 characters):

In a former EUMINAFab project, and the supports from Laser Material processing group in KIT, we have manufactured some surface patterned silicon nitride discs and investigated tribological performance of those textured silicon nitride discs against bearing steel pins with our pin-on-disc test rig, which produced some preliminary and promising results for tribological performance enhancement for lubricated hybrid sliding contacts by surface texturing. However, due to the rotation speed limitation of the used pin-on-disc test rig, the effect of surface texturing on hybrid sliding contacts cannot be fully understood in the full speed spectrum for all the potential operational conditions of hybrid sliding contacts. In order to fully understand the surface texturing effect on tribological performance of hybrid contacts as well as to finalize our manuscripts with enhanced scientific quality, we need to process more textured surfaces to perform further essential tribo-tests with our another test rig TE-77 in a wide range of sliding speeds especially in boundary lubrication regime.

2. Project results (max. 7.000 characters + figures):

- 1) With ultrafast laser radiation (femtosecond laser), high quality circular dimples with diameter of 50 μm to 300 μm , depth of 2.5 μm to 15 μm , and area densities of 5% to 20%, were fabricated on the large areas of silicon nitride discs as well as silicon nitride plates. Typical processed circular dimple samples as seen below.



- 2) Tribological performance of femtosecond laser textured silicon nitride discs was measured against bearing steel pins with pin-on-disc test rig in the linear speed range of 0.1 m/s to 5 m/s under nominal contact pressure of ca. 0.5 GPa. For femtosecond laser processed discs with dimple diameter of 150 μm and depth of 10 μm , significant (ca. 50%) friction reduction was observed for the discs covered with area density of 5% at ca. 0.1 m/s of the boundary lubrication regime.
- 3) Further tribo-tests with femtosecond laser processed plates with dimple diameter of 150 μm and 50 μm in the area density coverage of 5% to 20% were performed in the speed range of 0.05 m/s to 0.6 m/s with TE-77 reciprocating sliding test rig, but no friction reduction was observed.
- 4) A complicated effect of surface texturing on tribological performance was observed for lubricated hybrid sliding contacts between silicon nitride and bearing steels. The influence of the size (depth, diameter, and aspect ratio) and the coverage of dimples as well as dimple roughness is being analysed based on the all the obtained results in order to establish theoretical models.

3. Publications (please stick to the user guidelines for publications and acknowledgements on www.knmf.kit.edu):

Two invited talks have been given in the workshops using some data from these projects, and KNMF supports were acknowledged. The details for the talks are:

1. G. MacAulay, Quantifying surface topography-function relationships. *Predicting Function From Surface Topography Measurement*, Coventry, UK, 6 November, 2013.
2. L. Wang, Surface texturing to improve bearing performance – a review. *Predicting Function From Surface Topography Measurement*, Coventry, UK, 6 November, 2013.

An abstract based on the tribo-testing results on the textured silicon nitride surfaces has been accepted for oral presentation on STLE annual conference, detailed as

3. M. Nie, L. Wang, S.K. Purackal, M. Gee, R.J.K. Wood, Effect of surface texturing on oil lubricated sliding contact between silicon nitride and steel. STLE 2014-69th Annual Meeting & Exhibition, Florida, USA, May 2014.

In addition, two and three full papers are in preparation for the publication in the ISI journals.

4. Comments (max. 1.800 characters):

**Development of 3D topography in laser-
printed LiFePO₄ cathodes by femtosecond
laser structuring**

Alberto Pique

US Naval Research Laboratory

USA

Final Report

1. Project goals (max. 1.800 characters):

The aim of this project was to apply a new type of three-dimensional (3D) electrode design suitable for integration in lithium-ion microbatteries. Therefore, femtosecond laser processing of laser-printed LiFePO₄ composite cathodes was developed to form high aspect ratio grid structures into the cathode. The combination of both techniques allowed the set-up of a novel 3D electrode design while LiFePO₄ was chosen as cathode material with high capacity and safety. A detailed investigation of the electrochemical properties as a function of the surface design enabled the optimization of the laser-printed electrode. The main project goals were defined as follows in accordance to the proposed work plan:

- Laser-printing of porous LiFePO₄ composite electrodes with three different thicknesses (30, 80, 200 μm)
- Calendering of laser-printed LiFePO₄ composite electrodes for improvement of particle contact
- Ultrafast laser structuring of LiFePO₄ composite electrodes with different thicknesses for formation of 3D grid structures with high aspect ratio
- Electrochemical testing of unstructured ("laser-printed/calendered") and laser structured ("laser-printed/calendered/laser structured") LiFePO₄ electrodes with three different thicknesses (30, 80, 200 μm) for quantification of an optimal 3D design for micro-battery application

2. Project results (max. 7.000 characters + figures):

First, the cathode ink was prepared at NRL by mixing 90 wt.% or 91 wt.% LiFePO₄ (MTI Corporation), 4 wt.% graphite (KS6, Timcal) and 2 wt.% carbon black (Super P, Erachem) in a solution of 4 wt.% or 3 wt.% PVDF-HFP (Kynar 2801, Elf Atochem) in DBE or NMP solvent. Secondly, a small amount of ink was uniformly spread onto a 7.5 cm diameter UV transparent quartz wafer (ribbon) and the cathode inks were laser-printed from the ribbon onto 50 μm thick aluminium (Al) current collectors while the number of laser-printing passes was varied in order to achieve different film masses/thicknesses. The graphite (KS6) was added to the ink to improve the electric conductivity and the carbon black (Super P) was added to increase the porosity in the electrode films. The PVDF-HFP binder was added to form a flexible and mechanically reinforced cathode film. Laser-printed LiFePO₄ composite cathodes were dried after the printing process in a vacuum oven at 120 °C to remove the solvent and any absorbed water.

Calendering of laser-printed LiFePO₄ composite films was carried out at KIT using a compact hot rolling press (Precision 400 Hot Rolling Press/Calender, MTI Corporation, USA). The calendering process was repeated up to five times for each roller distance to counter thickness relaxation of the composite electrodes. The rolling speed was 8 mm/s and the roller temperature was 55 °C. By applying the calendering process to laser-printed cathodes, three different LiFePO₄ composite film thicknesses could be adjusted and were classified into a) 30 μm, b) 80 μm and c) 200 μm thick films (Fig.1).

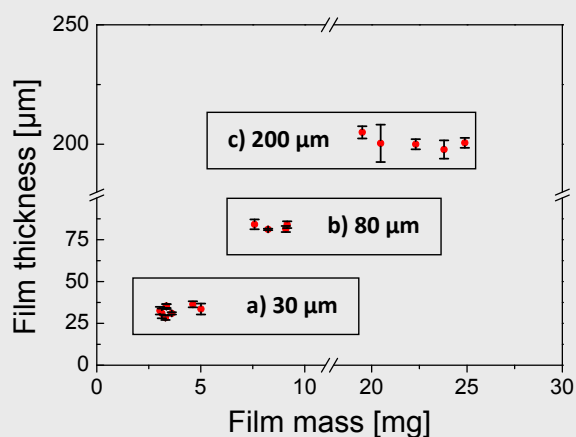


Fig.1: LiFePO₄ composite film thickness in dependence of the film mass after calendaring.

Ultrafast laser structuring of laser-printed and calendared LiFePO₄ composite films was performed using a micromachining workstation (PS450-TO, Optec, Belgium) equipped with a tunable fiber laser (Tangerine, Amplitude Systemes, France) with an average power of 20 W, a maximum pulse energy of 100 µJ at 1030 nm (TEM₀₀ with M² < 1.3), a variable pulse repetition rate (single pulse to 2 MHz) and tunable laser pulse duration (330 fs up to 10 ps). The laser structuring process for 30 µm thick films was performed using the second harmonic generation (SHG, 515 nm), a repetition rate of 1 MHz, a laser power of 0.36 W, a pulse duration of 350 fs and a scanning velocity of 400 mm/s. The laser beam was scanned over the sample surface three times for each scanning path with a pitch in between two scanning paths of 50 µm to process 3D grid structures into the LiFePO₄ composite films (Fig.2, a). In order to achieve high aspect ratio 3D microstructures in 80 µm thick and 200 µm thick electrodes (Fig.2, b-c), the composite material was removed from the laser material interaction zone by varying the numbers of laser passes (three passes for 30 µm thick films and 12 passes for 200 µm thick films) while all other laser process parameters were kept constant.

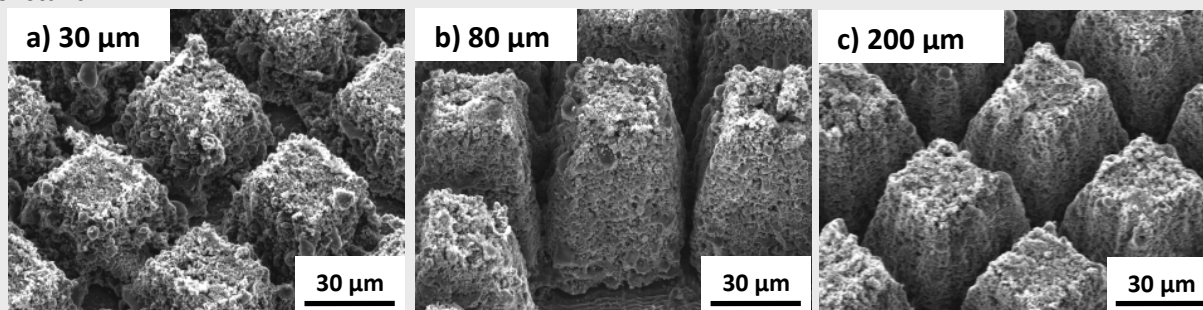


Fig.2: SEM images of ultrafast laser structured LiFePO₄ composite films. All samples were structured using 515 nm, 1 MHz, 0.36 W, 350 fs and 400 mm/s. The numbers of laser passes were (a) 3, (b) 5 and (c) 12.

Electrochemical cycling of unstructured (“laser-printed/calendered”) and laser structured (“laser-printed/calendered/laser structured”) LiFePO₄ composite electrodes was carried out using the Swagelok® cell design. Therefore, all samples were heated for about 24 h at 130 °C under vacuum and afterwards immediately transferred to an Argon-filled glove-box. Each cathode film was placed inside a Swagelok® cell body together with lithium metal as counter electrode and a glass-fiber separator (GF/A filter, Whatman

company) for preventing internal shorting. 100 μl of EC/DMC mixed in a 1:1 ratio with 1M LiPF_6 conducting salt (BASF) was used as the electrolyte.

Electrochemical testing was carried out using an Arbin Instruments BT2000 battery cycler and the testing procedure listed in Tab.1 was applied. First, three cyclic voltammograms (CV) were recorded with a scan rate of 0.02 mV/s. The electrode capacity was measured from the third CV cycle and applied for C-rate calculation for further galvanostatic testing. The charging rates were C/10 and C/5 while the discharging rates were continuously enhanced from C/10 to 1 C (Tab.1). The voltage window for all experiments was set to 2.5 V - 4.2 V.

Tab.1: Electrochemical cycling procedure for LiFePO_4 cells.

cycle number	3	5	10	10	10	10
charge rate	0.02 mV/s	C/10	C/5	C/5	C/5	C/5
discharge rate	0.02 mV/s	C/10	C/5	C/2	1 C	C/5

In Fig.3, the cyclic voltammograms for unstructured and laser structured electrode films are presented.

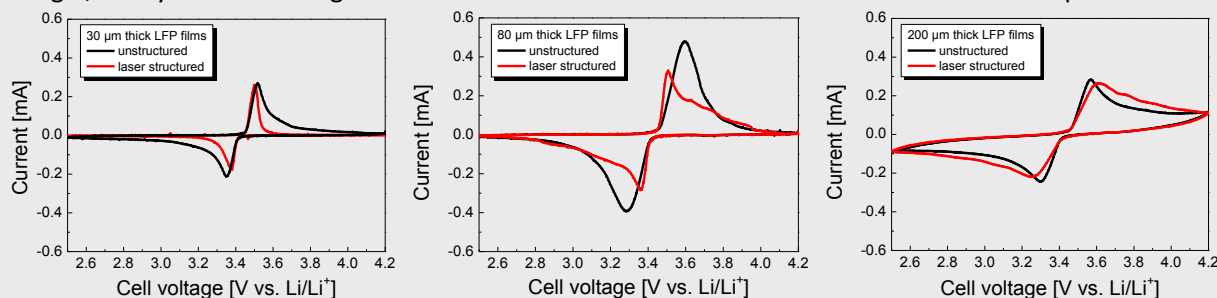


Fig.3: Cyclic voltammograms recorded within the third cycle for unstructured and laser structured LiFePO_4 films.

Three distinctive CV features could be observed (Fig.3):

- 1) Well-separated redox reactions were achieved for laser structured 30 μm thick films. Charge transfer was completed in a narrow voltage range and the peak currents shifted to slightly lower (charge) and higher (discharge) voltage values compared to those of unstructured films. The peak currents of unstructured and laser structured LiFePO_4 films exhibited similar values indicating improved lithium-ion diffusion properties of 3D micro-grids in 30 μm thick LiFePO_4 cathodes.
- 2) The voltage gap of the peak currents (oxidation and reduction reaction) of laser structured 80 μm thick films was reduced in comparison to an unstructured film but a "shoulder" appeared indicating charge transfer over a wide voltage range.
- 3) For 200 μm thick films, the voltage range of charge transfer for unstructured and laser structured films was observed to be very similar. Furthermore, the peak currents decreased compared to 80 μm thick films indicating low lithium-ion diffusion properties of thick LiFePO_4 films.

The characteristic CV features were reflected in the voltage curves obtained through galvanostatic cycling of the cells with a charging/discharging rate of C/10 (Fig.4). The most promising cycling behaviour was observed for 30 μm thick laser structured LiFePO_4 films due to flat voltage profiles while the voltage gap between the charge and discharge curve counts ~ 50 mV indicating good reversibility within galvanostatic charge and discharge.

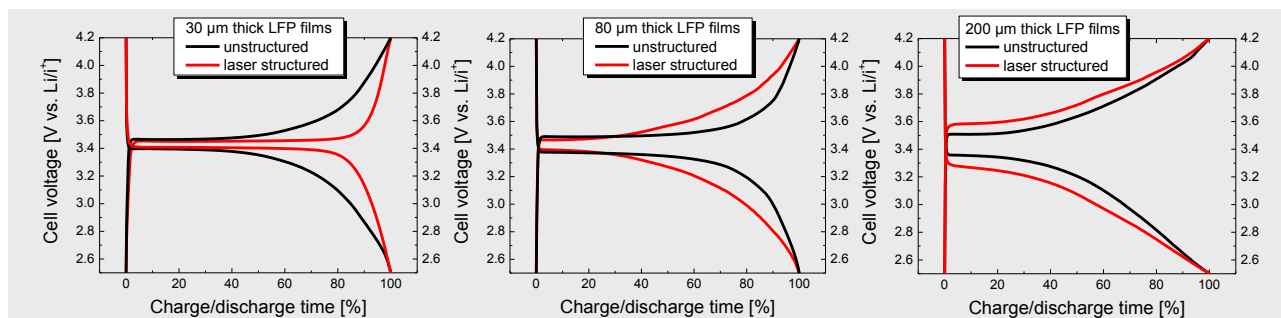


Fig.4: Charging and discharging curves (2^{nd} cycle) obtained from a C/10 rate for unstructured and laser structured LiFePO_4 films.

Well separated CV peaks (Fig.3, laser structured 30 μm thick film) in combination with flat voltage curves (Fig.4, laser structured 30 μm thick film) both imply good reversibility during charge and discharge at higher C-rates which could be confirmed within the C-rate dependent galvanostatic measurements (Fig.5).

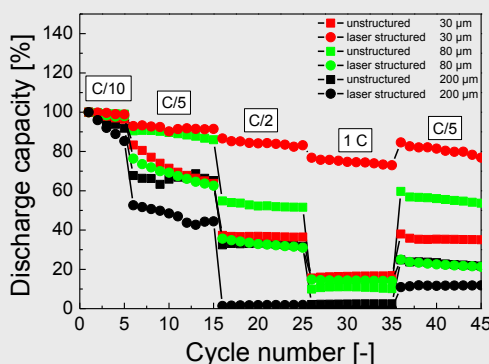


Fig.5: Discharge capacities for unstructured and laser structured LiFePO_4 composite films.

By combining NRLs laser-printing technique and KNMFs know-how in ultrafast laser processing of battery materials, it could be demonstrated that 3D topographies with high aspect ratio were successfully formed in LiFePO_4 composite electrodes with thicknesses of 30 μm - 200 μm . By taking into account the narrowest observed interspace between two microstructures of about 5 μm in 80 μm thick LiFePO_4 films (Fig.2 b), an aspect ratio of 16 was calculated. This demonstrates the strengths of both techniques for forming novel 3D microstructures in even thick battery materials. The combination of laser-printing of composite electrode inks onto current collectors and subsequent composite electrode material removal by using femtosecond laser pulses allowed for the establishment of a unique processing chain for setting-up novel 3D batteries. We further want to apply KNMFs ultrafast laser material processing in the field of lithium-ion batteries to establish both techniques (Laser-printing, laser structuring) as a standard in the development of future 3D microbatteries and large-scale 3D batteries.

In summary, the scientific findings within this KNMF project were as follows:

- 1) LiFePO_4 composite electrodes with thicknesses of 30 μm - 200 μm were laser-printed onto 50 μm thick Al substrates. It was shown that laser transfer of LiFePO_4 inks containing fine active powder particles result in highly porous and dense electrode films.
- 2) 3D grid structures were formed in 30 μm - 200 μm thick LiFePO_4 electrodes. Electrode material removal down to substrate for 200 μm thick LiFePO_4 electrodes could not be achieved due to possible shielding of

laser pulses by ejected material vapor.

- 3) Melt formation in LiFePO_4 electrodes was observed and therefore, not completely suppressed by ultrafast laser processing with a 1 MHz repetition rate. It is expected that increased melt formation within laser structured LiFePO_4 electrodes with thicknesses of 80 μm - 200 μm counter proper lithium-ion diffusion, resulting in the shift of the voltage positions of the peak currents and voltage plateaus as well as decreased high C-rate behavior within galvanostatic cycling. Further XRD analysis for determining possible phase changes due to laser structuring of LiFePO_4 are currently under investigation and exhibit a unique scientific extension to this KNMF project.
- 4) Distinctive redox reactions were achieved for laser structured 30 μm thick films within CV and galvanostatic measurements indicating most promising high C-rate cycling behavior due to improved lithium-ion diffusion kinetics in cells with 3D LiFePO_4 micro-grids.
- 5) All proposed milestones and work packages were fulfilled without delay.
- 6) We plan to publish the scientific findings from this project in an ISI journal.
- 7) Further investigations were performed as an extension of the proposed project such as laser-printing of LiFePO_4 pouch cell geometries and LiFePO_4 circle electrodes for demonstration of flexibility of both technologies, e.g. for 3D micro-battery development for medical devices and long lifetime pouch cells.

3. Publications (please stick to the user guidelines for publications and acknowledgements on www.knmf.kit.edu):

J. Pröll, H. Kim, A. Piqué, H.J. Seifert, W. Pfleging: Laser-printing and femtosecond-laser structuring of LiMn_2O_4 composite cathodes for Li-ion microbatteries, *Journal of Power Sources* 255 (2014) 116-124.

H. Kim, J. Proell, R. Kohler, W. Pfleging, A. Piqué: Laser-Printed and Processed LiCoO_2 Cathode Thick Films for Li-Ion Microbatteries, *Journal of Laser Micro/Nanoengineering* 7(3) (2012) 320-325.

J. Pröll, H. Kim, M. Mangang, H.J. Seifert, A. Piqué, W. Pfleging, Fs-laser microstructuring of laser-printed LiMn_2O_4 electrodes for manufacturing of 3D microbatteries, *Proc. of SPIE Vol. 8968* (2014) 896805-1-896805-6, doi: 10.1117/12.2039902, ISBN: 978-0-8194-9881-6.

H. Kim, T. E. Sutto, J. Pröll, R. Kohler, W. Pfleging, A. Piqué, Laser-printed/structured thick-film electrodes for Li-ion microbatteries, *Proc. of SPIE Vol. 8968* (2014) 89680L-1-89680L-9, doi: 10.1117/12.2037287, ISBN: 978-0-8194-9881-6.

4. Comments (max. 1.800 characters):

- This work lead to novel scientific findings regarding laser processing of promising LiFePO_4 cathode material for 3D lithium-ion microbatteries and additional experiments to investigate this cathode material should be conducted.

- This project resulted in a very fruitful cooperation with respect to fulfilling the proposed working plan and towards the development of future ongoing studies. Among the areas being considered for future investigation is the implementation of electrodes comprised of carbon coated LiFePO_4 particles.

**Biomimetic lipid-based research platform for
studying antibody-membrane interactions**

Stefan Zauscher

Duke University

USA

Note: Please fill in this report form and save/print it as a PDF file, then upload it to the KNMF proposal submission system. A cover page containing proposal title, proposer name(s), and technologies selected will be added by the system. A link for the download of the complete report as a PDF file will be displayed in the system.

Final Report

1. Project goals (max. 1.800 characters):

The objective of this research collaboration is to visualize binding interactions between HIV-1 antigen (MPER656) and neutralizing antibodies (2F5 and 4E10) to lipid membranes that mimic the native HIV-1 envelope. Completion of this objective is focused on achieving three specific aims: **Aim 1:** Use vesicle fusion techniques to create model HIV-1 supported lipid bilayers. **Aim 2:** Use dip-pen nanolithography (DPN) to write an array of lipid bilayers with complex lipid compositions that mimic the native HIV-1 lipid envelope. These lipid compositions include (i) high cholesterol content (from 0 to 50 mol %) and (ii) phase separating lipid mixtures that create lipid domains within bilayers. **Aim 3:** Image supported lipid bilayers and lipid-DPN arrays with atomic force microscopy (AFM) before and after the addition of HIV-1 neutralizing antibodies and HIV-1 antigens. AFM imaging will be performed in liquid and will use a heating stage to observe temperature effects on lipid patch structure, bilayer formation, and domain formation.

2. Project results (max. 7.000 characters + figures):

Aim 1 was completed by using alpha-helical peptide induced vesicle fusion to create supported lipid bilayers that mimic the composition of the native HIV-1 envelope. However, while progress was made on Aim 2, ultimately the DPN technique proved ineffective at creating an array of lipid bilayers to be screened with antigen and antibodies. The major obstacle was the stability of the lipid arrays in liquid. Once the array was submerged in buffer, the lipids would spread on the substrate and lose their array shape. Current work is now focused on increasing the stability of the arrays in liquid by using blocking techniques and the use of physical barriers. Since Aim 1 was successful, Aim 3 was still completed using the supported lipid bilayers to screen antigen and antibody interactions.

Our results showed that localized binding of HIV-1 antigens (MPER₆₅₆) and NAbs were observed to interact preferentially with the most fluid membrane domain. Figure 1 shows an AFM topography image of antibodies binding to a phase-separated SLB. The taller (brighter) areas are the gel phase while the lower (darker) areas are the liquid-disordered phase. The small, bright dots are locations of bound antibody which are only found in the liquid-disordered areas. This supports the theory that neutralizing antibodies may interact with regions of low lateral lipid forces that allow antibody insertion into the bilayer. Presence of antigen within gel-liquid disordered bilayers prevented coalescence of gel domains while antigen within the model HIV-1

bilayer prevented observable domain formation altogether.

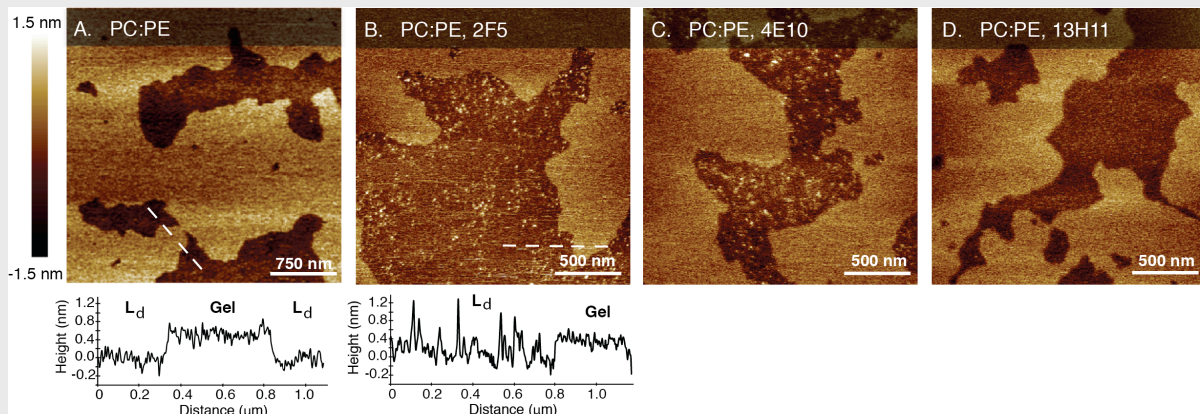


Figure 1. AFM height images of gel-Ld phase separated SLBs consisting of POPC:POPE 1:1 **(A)** Neat POPC:POPC SLB. Height cross-section given under the image. The brighter areas are the taller, gel domains, while the darker area is the lower, Ld phase. **(B)** Addition of NAb, 2F5 (4.7 μM) to the POPC:POPE SLB. Bright dots are peaks in topography and indicate presence of antibody. Height cross-section below image shows antibody peaks forming exclusively in the Ld phase. **(C)** Addition of NAb, 4E10 (4.7 μM) to the POPC:POPE SLB. **(D)** Control antibody, 13H11, (4.7 μM) added to SLB.

3. Publications (please stick to the user guidelines for publications and acknowledgements on www.knmf.kit.edu):

In progress: HIV Antibodies and Vaccine Antigen Selectively Interact with Lipid Domains

4. Comments (max. 1.800 characters):

Our research is significant in that it will help understand how vaccine antigen, MPER, is distributed in SLBs that model vaccine liposomes and the HIV envelope. It will also help understand the lipid environment most favorable for membrane-antibody interactions in the absence of antigen; which occurs during the first step of 2F5/4E10's proposed neutralizing mechanism.

**TEM observation of the initial growth stage of
carbon nanotubes synthesized in low
temperature plasmas**

Eva Kovacevic

Université d'Orleans

France

Note: Please fill in this report form and save/print it as a PDF file, then upload it to the KNMF proposal submission system. A cover page containing proposal title, proposer name(s), and technologies selected will be added by the system. A link for the download of the complete report as a PDF file will be displayed in the system.

Final Report

1. Project goals (max. 1.800 characters):

The TEM observations should give an insight in the first moments of the CNT formation. Measurements should be obtained at the seeds of CNTs obtained (systematically) in the first seconds of their growth. Although nowadays we can find a numerous works in the field of CNTs, as well as broad range of applications, the information about the growth /formation mechanism is coming mostly from the theoretical work (examples for experimental work: M. Gaillard *et al.*, Appl. Surf. Scie. 258 (2012) 9237-9241). The subject is thus interesting for fundamental research but also for applications.

In our case the application (in the framework of a national project) is correlated with microelectronics and nanopackaging and we observed clearly how stability of our CNT deposits depend strongly on this first moments. In our case the main question is the initial stage of formation of carbon nanotubes. The initial stage of growth is very often discussed and explained in theory, however the experimental observations, specially for our deposition type, are just a very few (see eg: S. Hofmann *et al.*, Nano letters, 7, 602-8(2007) and references therein). This first step is also decisive for the stability of the CNT carpets in applications (eg in our case nanopackaging) By initial stage we consider the first nuclei of carbon, first "seed" of CNTs and CNT carpets, from different sources. For this first step observation the high resolution microscopy, as existing at KNMF is necessary to obtain the needed precision.

The results that would be obtained from selected samples will be compared with the result from same formation stage by means of NEXAF and high resolution XPS analysis at BESSY II.

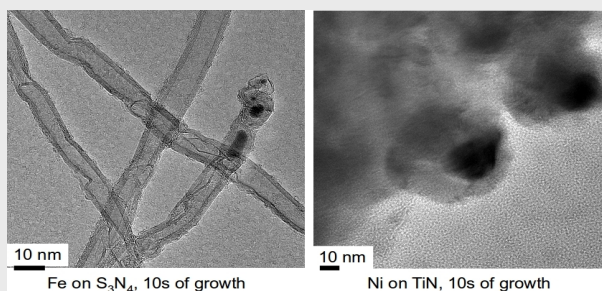
2. Project results (max. 7.000 characters + figures):

In the frame of this project, we analyzed 4 samples of CNT grown from Fe and Ni catalysts deposited on Si₃N₄ and TiN barrier layers (on Si wafers). We followed in this measurements the time behavior of the growth and analyzed mostly the first instants of the growth.

Several interesting results have been found: first, the HRTEM observations confirmed the very different growth kinetics between Fe catalysts on Si₃N₄ surface and Ni catalysts on TiN surface. The latter system is much slower as seen in the Figure1:

within 10 sec of growth, there are already nanotubes with Fe catalyst, but still only the seeds of graphitic walls around Ni catalyst nanoparticles. This supports the assumption about the initial moments of growth for our experimental parameters, as suggested in M. Gaillard *et al.* JVST B 31(3) (2013) 031805.

Fig. 1



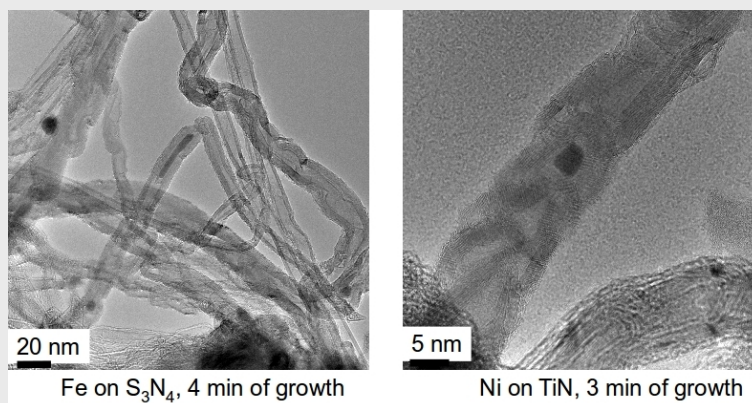
Second, it has been also observed that already after 10 seconds of growth with Fe as catalyst, the nanostructures have exactly the same kind of morphology as the final structures after tens of minutes of growth: same number of walls, same graphitization level... This is a very important information because it shows clearly that in the case of PECVD growth (low temperature plasmas plus catalyst annealing), the structures are defined already after 10s.

However, more observations are necessary to precise the importance of different experimental parameters on the initial growth stage (other catalysts, other substrates, variation of PECVD parameters).

Furthermore, the reshaping of the catalyst nanoparticles at the very beginning of the growth for the iron catalyst is much more pronounced than for the nickel catalyst. After 10 sec, the Fe catalyst nanoparticles are already clearly elongated, but those of Ni are still round.

After few minutes of growth (Fig. 2), the structures are the same as those obtained after longer growth time, indicating that the nanotubes are structured at the beginning and then only their length can varied (comparison for longer CNT from previous TEM - analysis at KIT).

Fig. 2



Last sample was obtained after applying a modified growth procedure with the goal of development and use of novel in-situ Raman spectroscopy. This technique is used to follow the formation of CNT walls in real time. Since our PECVD procedure results in strong optical emission in the region where Raman spectra should be obtained, it is necessary to sequentially switch the plasma on and off during the growth of CNTs: plasma-off mode during the time that Raman spectra is taken and plasma-on mode for the growth of CNTs. It was thus necessary to check whether this modified procedure influences the final structure, and if it is comparable with the results from the standard PECVD procedure. For optimized parameters (on and off time) TEM images showed that this production method results in the structure that is fully similar to the one obtained by continuous PECVD process.

3. Publications (please stick to the user guidelines for publications and acknowledgements on www.knmf.kit.edu):

Thibault Labbaye *et al.* E-MRS Spring Meeting, Lille-France, April 2014, *Real-time laser diagnostic of CNTs growth : In-situ Raman spectroscopy*

Thibault Labbaye *et al.* E-MRS Spring Meeting, Lille-France, April 2014, *Surface property modification of carbon nanotube carpet by plasma*

C. Boulmer-Leborgne *et al.* 26th Symposium on Plasma Physics and Technology, Prague-Czech Republic, June 2014, *Plasma Based Growth and Functionalization of Carbon Nanotubes from First Steps to Technological Applications*

4. Comments (max. 1.800 characters):

We faced several difficulties during these measurements and thus the analysis was not fully accomplished. For example: TEM grids with carbon membranes without the holes, that were used here, reduce drastically the contrast. Also the catalyst nanoparticles are in the range of nanometers and thus difficult to find on the grids during the given TEM-time.

In-depth profiling of amino acid coupling efficiency on polymeric surfaces

Volker Stadler

PEPperPRINT GmbH

Germany

Final Report

1. Project goals:

The scope of the project was to obtain a deeper insight into the coupling process of amino acids deposited within a polymeric matrix on the synthesis surfaces for the peptide synthesis in the array format. Especially yields of the coupling and the maximum depth where coupling still occurs within the polyethylene-glycolmethacrylate(PEGMA)-methylmethacrylate(MMA)-copolymers were of particular interest.

For future applications, it was also necessary to determine whether after cleavage of the finished peptides from the surface (e.g. with gaseous ammonia), all of the peptides from all depths of the film are able to diffuse out of the polymeric layer and if cleavage is comparably quantitative throughout the depth of the film. Also, XPS and ToF-SIMS are able to measure the cleavage rate, which is especially important if a large number of copies should be produced out of a single array. This information is crucial to promote the concept of in situ transfer of peptide arrays to a commercial application.

2. Project results:

First, the coupling depth of the amino acid derivatives was investigated with ToF-SIMS. For the sputtering, the C60 ion gun was used while the Bi-Liquid metal ion gun(Bi-LMIG) was used to generate secondary ions. Figure 1 compares the poisson-corrected trityl⁺ ToF-SIMS intensity standardized to the number of total ion counts of two samples. Sample 1, black circles, was prepared by solution based coupling of Fmoc-Cys(Trt)-OPfp to the substrate using a 0,2 M amino acid active ester solution in DMF. The preparation of sample 2, shown in red, demanded the production of Fmoc-Cys(Trt)-OPfp loaded, polymer based micro particles, which were deposited on the substrate, and heated to 90°C for 90 min under argon-atmosphere to induce coupling.

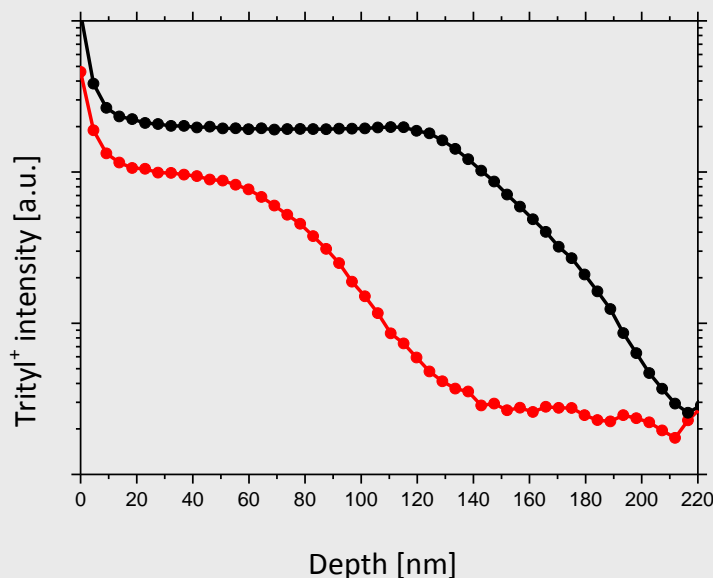


Figure 1 Poisson-corrected trityl⁺ ToF-SIMS intensity, standardized to the number of total ion counts. Samples consisting of Fmoc-Cys(Trt)-OPfp ester coupled to a 100% PEGMA synthesis film, functionalized with three β-alanine. Sample 1 (black) coupled from a 0,2 M solution of Fmoc-Cys(Trt)-OPfp in DMF under argon at room temperature (black). Sample 2 (red) was prepared by coupling Fmoc-Cys(Trt)-OPfp from polymer micro particles at 90 °C for 90 min under argon-atmosphere (red).

Between 0-10 nm both graphs were affected by surface destruction related to the sputtering process during the dynamic ToF-SIMS depth profiling, and therefore lacked in significance. Reaching a synthesis-film-depth of 130 nm, the trityl⁺-signal of sample 1 decreased according to the synthesis yield of the solution based coupling reaction (figure 1, black graph). The coupling performance of sample 2 already decreased at a film-depth of 60 nm (figure 1, red graph).

This result showed that the liquid polymer particle matrix material mediates the immobilization of the Fmoc-Cys(Trt)-OPfp ester in the depth of the synthesis film less efficiently compared to commonly used solvents like DMF. One consequence is to adjust the thickness of the polymer film on the solid support to 60 nm or less. The penetration depth of an alternative matrix material and the influence of a less compact polymer film on the immobilization performance will be investigated in future experiments.

A fundamental understanding of the rate of cleavage is essential to accomplish the multiple transfers necessary to create cheap copies of peptide arrays.

For a rough estimation, a sequential deprotection of beta-alanine-glutamine dipeptide coupled to a polyethylenglycolmethacrylate(PEGMA)-functionalized glass slide was used. First, the Fmoc-protection group was removed to determine the amount of epitope before cleavage. Afterwards, the slides were incubated with gaseous ammonia for 10 days at room temperature. After the incubation, the slides were thoroughly washed to remove cleaved peptides. To determine the amount of dipeptides still coupled to the surface, the sidechain protecting group of Gln, a Methyltrityl-group, was removed and detected with a photometer. This yielded a cleavage efficiency in the range of 5-15% within 10 days.

For a more detailed analysis however, XPS and ToF-SIMS measurements were necessary. As labels, we

used dipeptides again. For the XPS-measurement, we coupled the dipeptide beta-Ala-Phe to the surface, with 5 F-atoms at the benzyl-residue of the Phe. The measurement was conducted using monochromatic AlK α -X-rays while peak fitting was performed using Voigt profiles. For ToF-SIMS, the trityl protection group was monitored as in the previous experiments. The samples were incubated for a certain amount of days, thoroughly washed with DMSO and then read out. Figure 2 shows the results of the XPS measurements. The reference was set to 100% for better visualization.

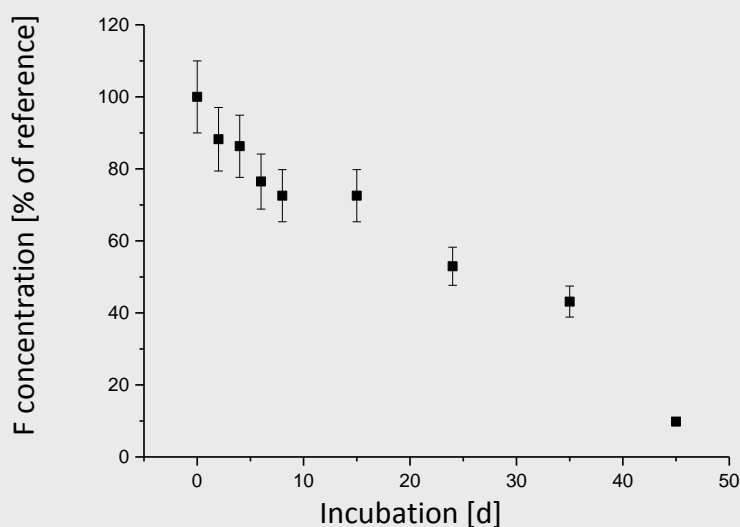


Figure 2: F concentration over incubation time based on F 1s XPS measurements.

For each sample, up to three measurements were made. The error bars were set to 10% of the measured value in accordance to calibrations done by the operator, which also seemed reasonable when comparing individual measurements on the same sample. However, it is to be noted that the error correlating with 45 days is very likely higher than depicted, due to the low concentration of the label left on the sample. The ToF-SIMS measurement, again performed using the Bi-LMIG showed a similar result, as depicted in Figure 3. Again, the reference value was set to 100%.

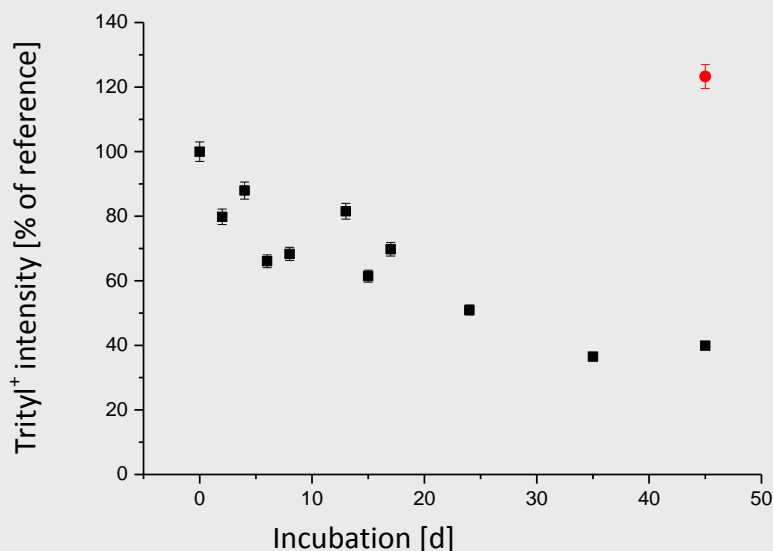


Figure 3 Trityl⁺ intensity over incubation time obtained with ToF-SIMS-measurements.

The red dot marks the measurement of the last sample prior to the washing step. After applying the washing protocol used for all the other measurements, the 45 d sample was washed again for 2 h with DMSO and measured again. No further reduction could be observed, proving that the washing procedure was sufficient to remove peptide adsorbates. The error was determined by calculating the standard deviation of 10 measurements on the reference. During the measurement, dust impurities were found to have a huge impact on signal stability, which are responsible for the scattering seen in Figure 3. However, as the experiment was designed to show actual laboratory conditions, we did not repeat the measurement under clean room conditions. Combined, both experiments give roughly the same magnitude of cleavage, and should therefore suffice for demonstrating the very slow kinetics of the reaction.

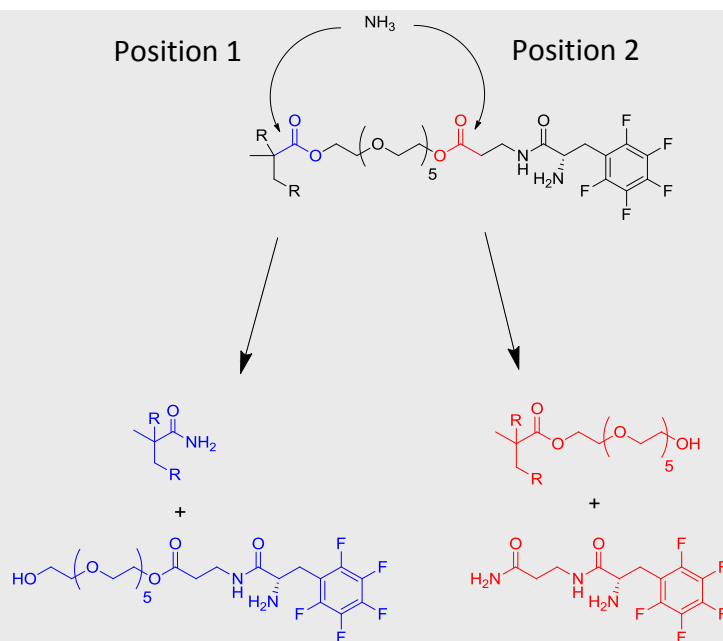


Figure 4 Possible cleavage sites in the polymer.

Another important aspect is the cleavage position. Theoretically, two cleavable sites are present in a subunit of the functionalized polymer, as shown in Figure 4. Position 1 would be undesirable, because a PEG-chain on the C-terminal end of a transferred peptide could possibly impair its binding properties. Therefore, the CO-correlated C 1s XPS signal and the PEG-related ToF-SIMS-peaks, C₂H₅O⁺ and C₂H₅O₂⁺ were also investigated using the experimental parameters mentioned above.

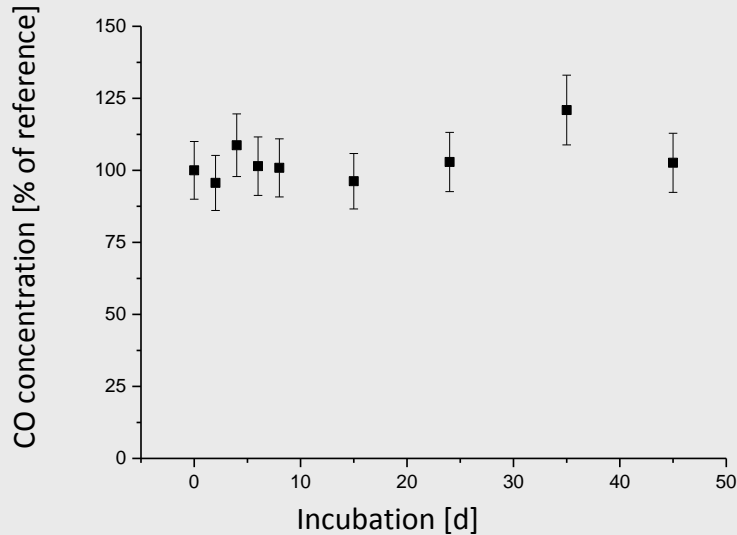


Figure 5 CO concentration over incubation time based on C 1s XPS-measurements.

Within the error range of the measurements, there is no detectable decay of the C 1s signal. In fact, a slight rise, which was expected due to the relative increase in the C-specimen yielding the signal, is observed. The ToF-SIMS measurement showed a similar result (Figure 6).

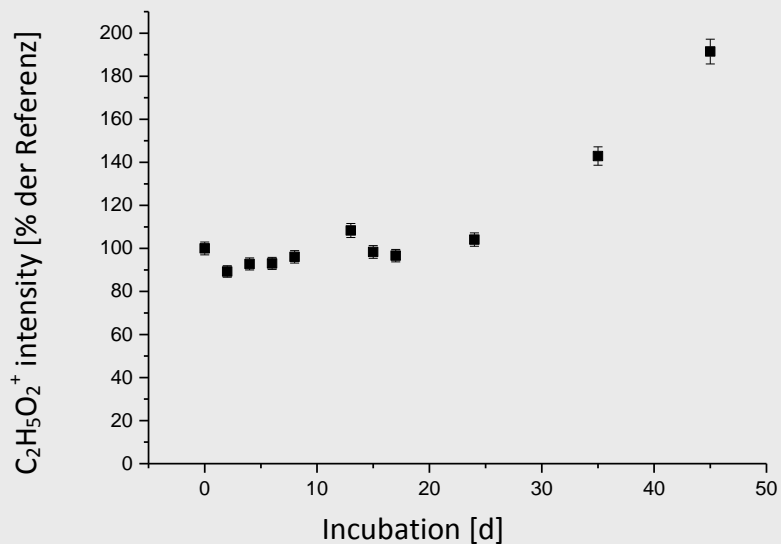


Figure 6 C₂H₅O₂⁺ intensity over incubation time obtained with ToF-SIMS-measurements.

A rising tendency is clearly visible, even more than in the XPS-measurement. Therefore, both measurements indicate a preference of the cleavage in position 2 shown in Figure 4.

3. Publications:

A publication of the obtained results is currently prepared. We will try to submit it to Advanced Materials.

4. Comments:

The project paved the way to a novel method to read out coupling efficiencies in situ, improving the quality of the synthesized peptide arrays. Furthermore, the cleavage rate using gaseous ammonia was investigated and the resistance of the polymeric layer to the incubation condition shown to be likely.